

From the Institute of Biomedical Optics  
of the University of Lübeck  
Director: Prof. Dr. rer. nat. Alfred Vogel

and

The Wellman Center for Photomedicine  
Massachusetts General Hospital  
Director: Prof. R. Rox Anderson, MD

**Quantitative Optical Coherence Tomography  
for Imaging Healthy and Emphysematous  
Pulmonary Alveoli *In Vivo***

**Dissertation**  
for Fulfillment of  
Requirements  
for the Doctoral Degree  
- Dr. Ing. -  
of the University of Lübeck

from the Department of Natural Sciences

Submitted by

**Carolin Unglert**  
from Munich

Lübeck, 2012



First referee: Prof. Dr. Reginald Birngruber  
Second referee: Prof. Dr. Guillermo Tearney  
Third referee: Prof. Dr. Steven Jacques

Chairman: Prof. Dr. Achim Schweikard

Date of oral examination: March 18, 2013

Approved for printing: Lübeck, October 31, 2013



Gewidmet meinen Eltern,

Denen ich meine Neugier, meinen Mut, und meine Lebensfreude verdanke.



## Acknowledgments

First and foremost I would like to thank my primary supervisor Professor Guillermo J. Tearney who continually supported this work with his time, creativity and strategic foresight and whom, more importantly, I owe everything I understand about academic research. His enthusiasm and guidance have enabled me to grow as a researcher and to pursue the work that I was passionate about.

I am deeply indebted to Professor Reginald Birngruber for his transnational scientific supervision. This work would not have been possible without his unique insight into both research worlds, his continuous encouragement, and astute scientific advice. I am tremendously grateful for the crucial edits to the manuscript and the honest career advice provided along the way.

I could not be more grateful for the generous funds provided by Air Liquide that enabled my work on this project. I would like to express my deeply felt thanks to Professor Gabriela Apiou whose advice convinced me to pursue a PhD and whose foresight and efforts enabled its success. And I would like to sincerely thank Linda Myrick who continued to actively support my work and who has been a true mentor and role model.

My path was accompanied by exceptional advisors and colleagues on both sides of the ocean, whom I would like to sincerely thank:

It was an honor for me to start this project in Boston with Eman Namati, who patiently exposed me to all aspects of the lab work from splicing fibers to excising lungs and encouraged me to find my own path and research questions. His teaching influence remained apparent and crucially important throughout my thesis work.

The second part of this thesis work was critically supported by Bill Warger, who taught me about optics and the fine details of written communication with a great sense of humor. I am also deeply indebted to Bill for editing the manuscript. Thank you for making the endless animal studies so much fun! I will truly miss our collaborative work!

Throughout the years, I was extremely fortunate to receive additional continuous support from my colleagues, friends, and mentors at Air Liquide, Medical Gases R&D in Les-Loges-en-Josas. Georges Caillibotte and his team, in particular, provided absolutely crucial support and fruitful scientific discussions throughout the entire work. Ira Katz was a terrific mentor and teacher and I am infinitely grateful for his time and effort editing the early manuscript.

At the Wellman Center for Photomedicine, I would like to first express my sincere gratitude to Professor Brett E. Bouma, who always had an open door for my earliest and most naïve technical questions and for his invaluable unbiased personal advice. I would also like to express special thanks to Melissa Suter, Lida Hariri and Jacque Namati for sharing advice and passion for pulmonary imaging, to Bill Farinelli, Joe Gardecki, Dongkyun Kang, and Hao Wang for digging out equipment that no one knew we had, to Yukako Yagi, Jenny Zhao, Peggy Sherwood and the Photopathology Team for crucial support with histology processing, to Jocelyn Eckert for help with the segmentation, to Yaron Bromberg, Egidijus Aukorius, Martin Villiger and the whole team for helpful discussions about optics and science and for making work enjoyable day-after-day, and last but not least to Michalina Gora for her most beautiful OFDI figure for my manuscript, for continuous encouragement during the thesis writing and for being a true friend.

Absolutely essential to the success of this work were also my friends and family. I am thankful to Pat Cox and the S. Russell Street crew for providing me with a home abroad. My sincere thanks go particularly to Chris for facilitating my arrival in the American world of research and for all the cakes and favors over the years, and to my roommate Anke for her generous support in all stages of work and life, and for the numerous biscotti that made the manuscript writing sweeter. I would not have wanted to do this without you! Lastly, I would like to thank the love of my life Antoine for his patience, his continuous moral and active housekeeping support and my beloved brother Peter and parents Mathilde and Werner, who have always supported my craziest ideas and endeavors and to whom I dedicate this thesis.

## Summary

The presented work describes the successful development of an optical imaging method to visualize and quantify subpleural alveolar sizes in healthy and emphysematous swine *in vivo*.

Lung diseases involving the distal alveoli include chronic obstructive pulmonary disease (one of the leading causes of death world-wide) and acute lung injury with high mortality rates. Despite a good understanding about the macro-architecture and whole organ mechanics of the human lung, the structure-function relationship at the alveolar level is still poorly understood limiting an improved management of these patients. Similarly, models of gas exchange and aerosol deposition lack quantitative *in-vivo* data, and pathophysiologic changes of lung tissue over time or the effect of potential pharmaceutical agents cannot be adequately assessed with the commonly used lung function tests or destructive methods, like histology. Visualization and quantification of alveolar movement is inherently difficult due to their small size ( $\sim 100 - 300 \mu\text{m}$  in humans) and constant motion ( $\sim 15$  breaths per minute in humans) within the natural environment. Available imaging tools for the non-destructive assessment of the alveolar structure include X-ray computed tomography, Synchrotron radiation based tomography, and intra-vital fluorescence microscopy. These techniques are all either limited by a long acquisition time, inadequate resolution or visualization of only two dimensions.

The presented technical development focused on optical techniques with the goal to provide four-dimensional visualization and quantification of air-filled pulmonary alveoli. This goal was achieved through three specific aims:

- 1) Three high-resolution optical-imaging modalities, namely Fourier-domain optical coherence tomography (FDOCT), spectrally encoded confocal microscopy (SECM) and full-field optical coherence microscopy (FFOCM), were evaluated *ex vivo* on water-immersed fixed lung tissue. The visualized outlines of individual alveoli and blood vessels (visualized by all techniques),

type II pneumocytes within the alveolar epithelium (SECM and FFOCM), and crenated red blood cells (FFOCM) were validated through histopathology.

2) Because FDOCT was found to provide the most adapted specifications for dynamic alveolar imaging, the technique was integrated into a light-weight (12 g), miniaturized (23 mm diameter) cylindrical contact probe to sit upon the lung and follow the natural dynamic movement during the ventilation cycle. An optimization study of the focal parameters (numerical aperture and depth location of the focus) suggested the usage of high numerical apertures (0.2) to leverage improved lateral resolution (3  $\mu\text{m}$  diffraction limited) at no significant cost to imaging depth, which was found to be limited to one layer of alveoli (~ 100 - 200  $\mu\text{m}$ ) by the inherent optical properties of the air-filled lung tissue.

3) In order to validate quantitative measurements of pulmonary alveoli in FDOCT images, it was crucial to investigate the effects of refraction at the tissue-air interfaces. Measurements of fixed, air-filled swine alveoli obtained from FDOCT were compared to measurements from micro-CT images (minimally influenced by refraction) of identical alveoli. Alveolar cross-sectional area, perimeter, volume, and surface area were evaluated and measurements from the two techniques were found highly correlated ( $R^2 > 0.9$ ) for all size parameters. However, the absolute values were systematically underestimated by FDOCT compared to micro-CT, independent of alveolar size. The mean average underestimation was 27% (area), 7% (perimeter), 46% (volume), and 25% (surface area). In addition to the described experimental comparison, a ray-tracing model was developed that confirmed the observed error in FDOCT size measurements and provided scaling factors to correct the initial FDOCT measurements to successfully approximate the absolute average micro-CT values.

The developed methodologies then enabled the first visualization and quantification of alveolar structure and motion in three healthy and one emphysematous swine *in-vivo*. In addition to a large heterogeneity between individual alveoli in both cases, emphysematous alveoli in this preliminary assessment were found larger (5-fold median volume increase, 3-fold median surface area increase) and more compliant on average (3-fold increase in

compliance, 2-fold decreased relative expansion) with less variation between airspaces compared to healthy alveoli.

Future development of automated segmentation algorithms and less invasive imaging probes is especially merited.

In conclusion, the presented work opens new avenues for studying pulmonary physiology and patho-physiology at the alveolar level with great promise to improve models of gas exchange and aerosol deposition, to advance the current understanding of lung diseases, and to accelerate the development of protective ventilation strategies.



## TABLE OF CONTENTS

<b>1</b>	<b>INTRODUCTION .....</b>	<b>1</b>
<b>2</b>	<b>MEDICAL BACKGROUND .....</b>	<b>3</b>
<b>2.1</b>	<b>Basic structure and function of the lung and the alveolar unit .....</b>	<b>3</b>
2.1.1	Anatomy of the human lung .....	3
2.1.2	Alveolar structure .....	6
2.1.3	Mechanics of breathing .....	8
<b>2.2</b>	<b>Clinical motivation .....</b>	<b>11</b>
2.2.1	Improving phenotyping of COPD patients .....	11
2.2.2	Accelerating the development of protective mechanical ventilation strategies .....	13
2.2.3	Complementing models of gas exchange and aerosol deposition .....	15
<b>3</b>	<b>MATERIALS &amp; METHODS .....</b>	<b>17</b>
<b>3.1</b>	<b>Animal models and lung tissue preparations .....</b>	<b>18</b>
3.1.1	Background: Mammalian pulmonary structure and function	18
3.1.2	Instillation fixed lung samples .....	20
3.1.3	Freshly excised lung tissue .....	22
3.1.4	<i>In-vivo</i> swine model .....	24
3.1.5	Elastase emphysema model .....	27
<b>3.2</b>	<b>Optical reflectance techniques for imaging alveolar structure .....</b>	<b>28</b>
3.2.1	Introduction of three high-resolution optical reflectance techniques .....	29
3.2.2	Specific challenges in alveolar optical imaging .....	39
3.2.3	Evaluation of FDOCT, SECM, and FFOCM for imaging fixed, fluid-immersed peripheral rat lung tissue .....	54
<b>3.3</b>	<b>Swept-source Fourier-domain optical coherence tomography for imaging alveolar structure and function .....</b>	<b>64</b>
3.3.1	Imaging depth and image quality in fluid-filled <i>versus</i> air-filled alveoli .....	64
3.3.2	Optimization of the focal parameters for imaging air-filled alveoli .....	65
3.3.3	MEMS imaging probe for dynamic <i>in-vivo</i> imaging .....	77
3.3.4	Air space segmentation and measurement in four-dimensional <i>in-vivo</i> images .....	80
<b>3.4</b>	<b>Techniques to investigate the quantitative representation of alveolar size and shape in optical coherence tomography images .....</b>	<b>82</b>

3.4.1	Refractive index measurement .....	82
3.4.2	Comparison of FDOCT to micro-CT images .....	83
3.4.3	Ray-tracing model to investigate the influence of refraction effects .....	88
3.4.4	Statistical analysis to assess the agreement of FDOCT with micro-CT measurements of alveolar size .....	96
3.4.5	Statistical analysis to assess the agreement of scaled FDOCT with micro-CT measurements of alveolar size.....	102
<b>4</b>	<b>RESULTS .....</b>	<b>105</b>
<b>4.1</b>	<b>FDOCT images of pulmonary alveoli .....</b>	<b>105</b>
4.1.1	Three-dimensional visualization of mammalian alveoli across species.....	105
4.1.2	Four-dimensional visualization of healthy alveolar motion <i>in-vivo</i> .....	106
4.1.3	Four-dimensional visualization of emphysematous alveolar motion <i>in-vivo</i> .....	108
<b>4.2</b>	<b>Validation of two- and three-dimensional measurements of subpleural alveolar size by optical coherence tomography .....</b>	<b>112</b>
4.2.1	FDOCT <i>versus</i> micro-CT comparison of segmented alveolar sizes .....	112
4.2.2	Modeled influence of refraction.....	117
4.2.3	Correction of alveolar size measurements.....	119
<b>4.3</b>	<b>Preliminary quantitative studies of uncorrected alveolar structure and motion <i>in vivo</i> .....</b>	<b>123</b>
4.3.1	Healthy alveolar airspace sizes in a swine model during continuous mechanical ventilation .....	123
4.3.2	Emphysematous alveolar structure and motion in an elastase swine model .....	126
<b>5</b>	<b>DISCUSSION .....</b>	<b>133</b>
<b>5.1</b>	<b>Validation of two- and three- dimensional measurements of subpleural alveolar size by optical coherence tomography .....</b>	<b>133</b>
5.1.1	Summary of results .....	133
5.1.2	Differences between <i>in-vivo</i> and fixed subpleural alveolar tissue .....	134
5.1.3	<i>In-vivo</i> measurements of uncorrected subpleural alveolar size .....	135
5.1.4	Correction of FDOCT measures of subpleural alveolar size .	136
5.1.5	Alternative segmentation to obtain absolute alveolar sizes	140
5.1.6	Applicability to non-subpleural alveoli .....	143

---

<b>5.2 Preliminary quantitative studies of subpleural alveolar structure and motion <i>in-vivo</i> .....</b>	<b>143</b>
5.2.1 Assessment of uncorrected <i>versus</i> corrected sizes and size changes.....	144
5.2.2 Translation of results into models simulating airflow in human alveoli .....	151
<b>5.3 Future opportunities and challenges for FDOCT imaging of pulmonary alveoli .....</b>	<b>151</b>
5.3.1 New pathways to studying alveolar physiology and pathophysiology.....	152
5.3.2 Development of automatic segmentation methods.....	154
5.3.3 Future probe developments to image alveoli in a closed chest .....	156
5.3.4 Sample size .....	158
5.3.5 Clinical relevance .....	158
<b>6 SUMMARY AND CONCLUSION .....</b>	<b>161</b>
<b>7 DISSEMINATION OF RESULTS .....</b>	<b>166</b>
<b>8 BIBLIOGRAPHY .....</b>	<b>168</b>

## TABLE OF ABBREVIATIONS

ALI	Acute Lung Injury
bpm	Breaths per minute
COPD	Chronic Obstructive Pulmonary Disease
CS	Cross-sectional area
CT	Computed Tomography
ET	Endo-Tracheal
FDOCT	Fourier-Domain Optical Coherence Tomography
FEV1	Forced Expiratory Volume in 1 <sup>st</sup> Second
FFOCM	Full Field Optical Coherence Microscopy
FOV	Field Of View
fps	Frames per second
FRC	Functional Residual Capacity
FWHM	Full Width at Half Maximum
H&E	Hematoxylin & Eosin
ID	Inner Diameter
MDF	Multi-Depth Focusing
MEMS	Micro-Electro-Mechanical Systems
P	Perimeter
PBS	Phosphate Buffered Saline
PEEP	Positive End-Expiratory Pressure
PFT	Pulmonary Function Test
PIP	Peak Inspiratory Pressure
PPE	Porcine Pancreatic Elastase
PSF	Point Spread Function
RR	Respiratory Rate
RV	Residual Volume
SA	Surface Area
SD	Standard Deviation
SE	Standard Error
SECM	Spectrally Encoded Confocal Microscopy

---

SR	Spherical Radius
TLC	Total Lung Capacity
V	Volume
VC	Vital Capacity
VILI/VALI	Ventilator Induced Lung Injury/Ventilator Assisted Lung Injury
V <sub>T</sub>	Tidal Volume



## 1 INTRODUCTION

Lung diseases are among the most prevalent, costly and morbid pathologies in the world. Chronic obstructive pulmonary disease (COPD), for example, has been predicted to become the third leading cause of death worldwide by 2020 and direct yearly costs have been estimated to be several million Euros in Spain and almost 15 billion Dollars in the US (1, 2). Additional clinical challenges related to the lung include the high mortality rate of mechanically ventilated patients with acute lung injury (3-5), and the hindered development of accurate models of airflow and aerosol deposition throughout the lung to accelerate the development of new therapies (6, 7). The primary cause for these challenges is the inherent difficulty to image the smallest features of gas exchange (alveoli) that are under constant motion within the natural environment, which has resulted in an incomplete understanding of pulmonary physiology and pathophysiology.

The majority of the existing knowledge about alveolar structure and function has been obtained indirectly *via* lung function tests or the use of destructive methods such as casts and histology. Currently available imaging tools for non-destructive assessment of alveolar structure have become more popular in recent years, including X-ray computed tomography (CT), Synchrotron Radiation based X-ray Tomographic Microscopy (SRXTM), video microscopy, and magnetic resonance imaging (MRI). All of these techniques, however, are limited by the field of view, long acquisition times and/or inadequate spatial resolution. While these tools have provided invaluable information about the lung, a complete understanding cannot be obtained for the natural environment without a dynamic visualization with adequate resolution in all spatial and temporal dimensions. Therefore, the goal of this thesis was the successful development of a methodology to visualize and quantify the motion of individual pulmonary alveoli during physiologic ventilation cycles *in vivo* to provide new insights for studying alveolar physiology and pathophysiology.

This goal was achieved through three specific aims. First, three high-resolution optical-imaging modalities, namely Fourier-domain optical coherence tomography (FDOCT), spectrally encoded confocal microscopy (SECM) and full-field optical coherence microscopy (FFOCM), were assessed to image water-immersed fixed lung tissue *ex vivo*, with the structural results validated through histopathology. Sections 3.1 and 3.2 describe the lung tissue preparation, background of the optical techniques and results from the study. Because FDOCT was found to provide the most adapted specifications for dynamic alveolar imaging, section 3.3 describes the optimization of the focal parameters with a bench-top FDOCT system and the development of a miniaturized contact probe that was fabricated to image subpleural air-filled alveoli within an *in-vivo* ventilated swine model. Lastly, the quantitative measures of alveolar size obtained from FDOCT images were validated through a combination of experimentation and ray-trace modeling in section 3.4. Optical images of fixed, air-filled swine lung samples were compared to micro-CT images of the same field of view to confirm the validity of relative alveolar size measurements. A ray-trace model was established to simulate FDOCT image reconstruction and create quantitative correction factors for the deduction of absolute alveolar sizes.

Following the demonstration that the FDOCT technique could acquire accurate measures of alveolar size, the methodology was utilized in a live swine model to provide the first quantitative four-dimensional measures of healthy and emphysematous alveolar dynamics during uninterrupted ventilation. The results from this study are provided in chapter 4, and are further discussed in chapter 5 with respect to their potential and limitations to answer clinical questions.

## 2 MEDICAL BACKGROUND

This chapter provides the biological and medical background necessary to understand the context, constraints and motivation of this work. Basic anatomy and physiology of the respiratory system is explained within the first section. The second section provides an overview of distinct clinical problems that could be alleviated by techniques developed for dynamic visualization and quantification of pulmonary alveoli.

### 2.1 Basic structure and function of the lung and the alveolar unit

The primary function of the lung is to deliver oxygen to and extract carbon dioxide from the blood for sustaining cell metabolism and maintaining acid-base balance throughout the body. The lung achieves gas exchange through a diffusion process such that maximum efficiency requires a large surface area with thin separation between the air and blood. The gross structure of the lung, the specific structure of the alveolar unit and the mechanics of breathing are uniquely designed to achieve this goal and are described in the following subsections, respectively.

#### 2.1.1 Anatomy of the human lung

In order to provide the largest surface area between the air in the lung and the blood, the lung is organized in a tree structure. Air entering the mouth or nose conducts through the trachea at generation 0. The trachea then branches into the two main stem bronchi for the left and right lung, and the airways continue to branch dichotomously to progressively smaller diameters for approximately 23 generations. Much like the larger branches of a tree do not have leaves branching off directly, approximately the first 15 airway generations are not alveolated and provide minimal contribution to gas exchange. These airways are therefore named the conducting zone of the lung or anatomic dead space. The volume of the anatomic dead space is on the order of 150 ml (8). The first alveolated airways are called respiratory bronchioles and the alveolated region

is named the respiratory zone, which will often be referred to as the peripheral regions of the lung throughout this work. Figure 1 illustrates the idealized branching pattern.

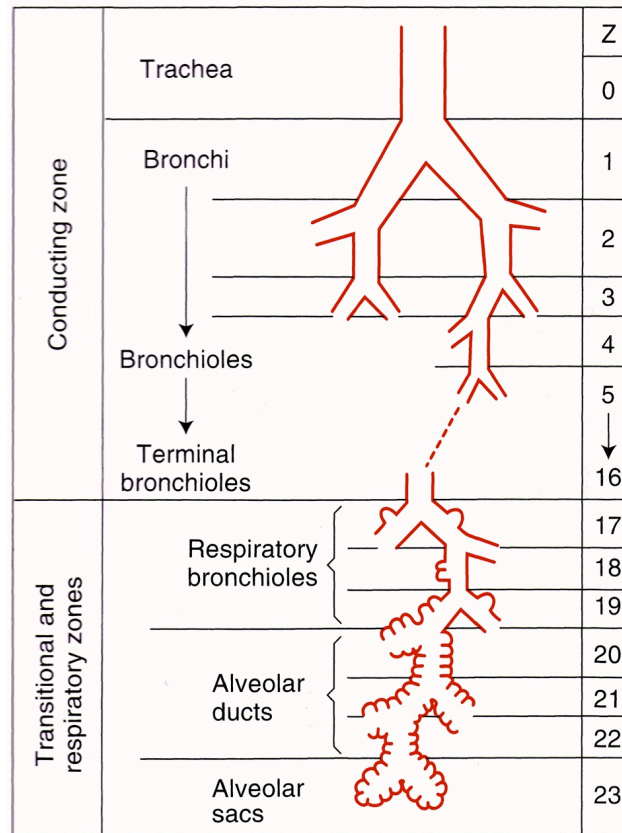


**Figure 1: Idealization of the human airway branching pattern established by Weibel (9).**

It has been estimated that there are approximately 480 million alveoli in the human lung (range of 275-790 million from 6 lungs) (10). The volume of the alveolar region within a healthy person depends primarily on the stage in the respiratory cycle and the respiratory maneuver, and also on the size, weight and gender of the person. Typical volumes during tidal breathing at rest are on the order of 2.5 – 3 l (8). Figure 2 shows exemplary lung volumes of an average healthy 29-year old female during a breathing manoeuvre of maximum inhalation and exhalation following and preceding two normal (tidal) breaths at rest illustrating important terms characterizing lung volumes. The vital capacity (VC) describes the maximum volume one can breathe to reach total lung capacity (TLC) following a full exhalation to residual volume (RV). In the given example in Figure 2, the TLC could be 6.99 l. The tidal volume ( $V_T$ )

describes the cyclically inhaled and exhaled volume and depends on the size and metabolic needs of the person. For example, the  $V_T$  could be on the order of 500 ml per breath at rest, increase to over a liter during exercise, and decrease to approximately 250 ml during sleep. The volume of air remaining in the lung during tidal breathing is referred to as functional residual capacity (FRC).

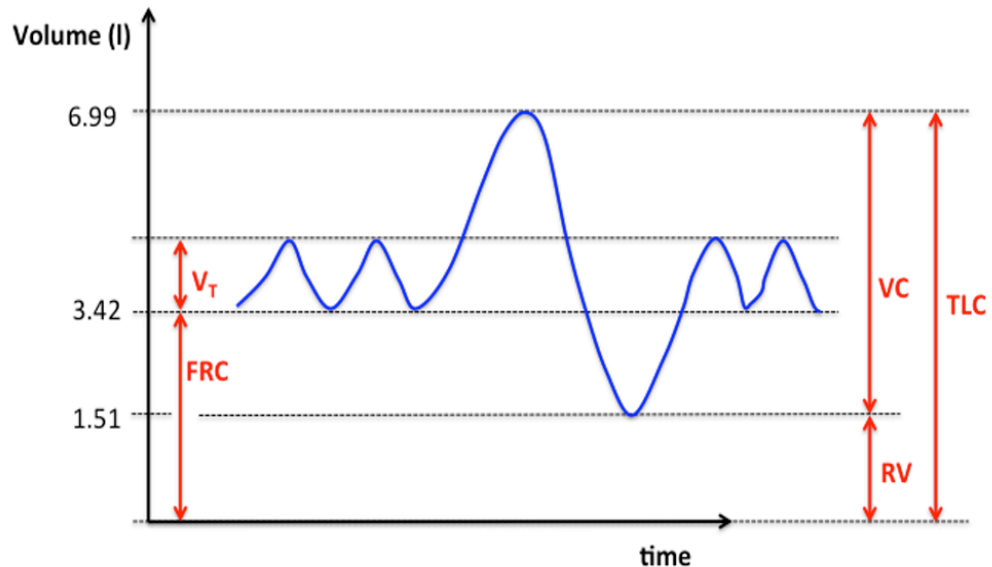


**Figure 2: Illustration of important terms describing lung volumes. TLC = total lung capacity, VC = vital capacity, RV = residual volume,  $V_T$  = tidal volume, FRC = functional residual capacity. (Further explanation in the text.) Numerical values are exemplary plethysmography results of a healthy 29-year old female.**

The surface area available for gas exchange in the previously mentioned example of an average healthy person could be grossly approximated assuming a fixed number of 480 million spherical alveoli and an anatomic dead space of 150 ml (Table 1). At RV and TLC, the average alveolar radius would then be 88  $\mu\text{m}$  and 150  $\mu\text{m}$ , and the total alveolar surface area would be 46  $\text{m}^2$  and 136  $\text{m}^2$ , respectively. In spite of the simplified assumptions regarding alveolar number and shape (see subsections 2.1.2 and 2.1.3 for further information regarding these assumptions), the estimated values for alveolar size and total surface area correspond well to established literature citing an alveolar diameter of 200  $\mu\text{m}$  (10) and a surface area of 50 to 100  $\text{m}^2$  (8). Note the efficiency of the lung's anatomic structure in creating a large surface area,

comparable to half a tennis court (98 m<sup>2</sup>), within the comparably small volume of the chest cavity within the human body.

**Table 1: Numerical example estimating the increase in gas exchange surface area assuming a constant number of  $N_a = 480$  million spherical alveoli and anatomic dead space volume  $V_{ds} = 0.15$  l when inhaling from 1.51 l of lung volume to 6.99 l.**

Lung volume	Alveolar volume	Alveolar radius	Alveolar surface area	Total surface area
$V_l$	$V_a = \frac{V_l - V_{ds}}{N_a}$	$R_a = \left(\frac{3V_a}{4\pi}\right)^{1/3}$	$SA_a = 4\pi \cdot R_a^2$	$SA_{total} = SA_a \cdot N_a$
<b>1.51 l</b>	2.8 nl	88 $\mu\text{m}$	0.097 mm <sup>2</sup>	46 m <sup>2</sup>
<b>6.99 l</b>	14.3 nl	150 $\mu\text{m}$	0.28 mm <sup>2</sup>	136 m <sup>2</sup>

The described anatomy has specific consequences for this thesis work. First, the pulmonary alveoli are the site of gas exchange and have a central importance for respiratory physiology. The destruction of their walls (as in emphysema) or their flooding with exudate (such as in acute lung injury) can significantly lower the surface area available for gas exchange. In these cases, patients may rely on supplemental oxygen and possibly positive pressure ventilation. Visualizing individual alveoli could therefore not only improve the current understanding of their function, but also impact the diagnosis of disease and the monitoring of therapy. Specific clinical questions will be discussed in more detail in section 2.2. Secondly, because of their small size, the commonly used clinical technologies (such as computed tomography or magnetic resonance tomography) are not capable of resolving individual alveoli and as such, this work focused on developing optical technologies that provide high resolution ( $\sim 10 \mu\text{m}$ ) to visualize individual alveoli.

### 2.1.2 Alveolar structure

In addition to a large surface area, efficient gas exchange also requires the diffusion distance to be as short as possible. The entire alveolar wall is 7 to 10  $\mu\text{m}$  thick, includes the capillaries and is shared between two adjacent alveoli. The blood-gas barrier can then be as small as 0.3  $\mu\text{m}$  in some places. The thinness of this blood-gas barrier together with efficiently designed oxygen

carriers (hemoglobin) in the cytoplasm of the red blood cell achieves oxygen saturation in a healthy person in approximately a quarter of a second.

Figure 3 shows a schematic of the structures of the alveolar wall. The blood-gas barrier is comprised of simple squamous alveolar epithelium, an interstitial space, and the capillary endothelium. In addition to the flat type I pneumocyte covering 95% of the surface of the alveolar wall, the alveolar epithelium contains a second cell type, the cuboidal shaped type II pneumocyte, which synthesizes surfactant to reduce the surface tension of the alveoli, and gives rise to type I cells to repair alveolar epithelium (11). The interstitial space includes elastin fibers and collagen bundles that influence the elastance/compliance of the alveoli and the lung, in regard to the expansion and contraction as a function of the applied pressures (12). An interesting property of the elastin fibers is also their autofluorescence at 488 nm, which has led to confocal imaging studies of the alveolar elastin network in humans *in vivo* (13).

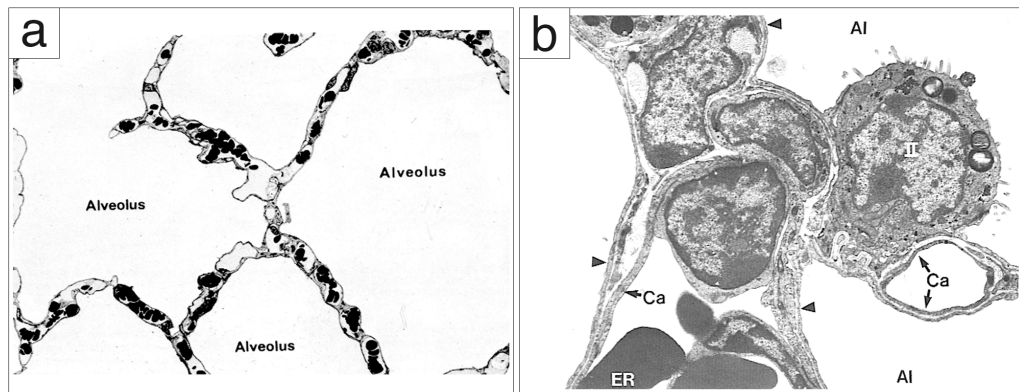


**Figure 3: Transmission electron micrographs showing alveolar wall microstructure. (a) Alveolar walls shared by two airspaces. (b) Micrograph showing type II pneumocyte (II), capillary endothelium (Ca), alveolar airspace (Al), and erythrocyte (ER). [Adapted from (14).]**

Consequently for this work, an imaging technique to visualize the thickness of the alveolar wall with proper sampling should provide a spatial resolution superior to  $5 \mu\text{m}$ . Also, due to the different inherent structures (squameous type I cells, cuboidal type II cells, capillary network), the thickness of the alveolar wall can be expected to vary by several microns.

The general alveolar shape is believed to be hexagonal with a honey-comb like arrangement of alveolar networks (9); an arrangement that guarantees the most

efficient use of space. However, note that previous knowledge about the alveolar shape and structure was primarily derived from casts and fixed lungs. Dynamic *in-vivo* shape changes of specific alveoli have only been visualized recently using optical techniques presented within this work.

### 2.1.3 Mechanics of breathing

The third prerequisite for gas exchange with the blood is a regular exchange of the gas contained within the lungs. To keep the lungs open, in spite of their natural tendency to collapse, surface tension allows the visceral pleura to slide along the parietal pleura of the chest wall separated only by a few ml of intrapleural fluid. The pressure in the intrapleural space at rest is approximately  $-5 \text{ cmH}_2\text{O}$ . The volume at which the inward recoil of the lung is balanced by outward recoil of the chest wall is named FRC. To achieve a more efficient exchange than provided by simple diffusion along a concentration gradient, the lung volume changes in a cyclic fashion for the delivery of fresh gas and the elimination of the used gas. For inhalation, the diaphragm descends and the intercostal muscles pull the chest wall outward creating negative pressure in the pleural space, which expands the lungs and lowers the pressure inside the lungs below atmospheric pressure, drawing fresh air in. To achieve higher volumes than approximately 70% TLC, the inspiratory muscles must work against inward recoil of both the lungs and the chest wall. The inspired volume therefore depends on the strength of the respiratory muscles as well as the stiffness of the chest wall and the stiffness of the lung tissue. The reciprocal of the stiffness is named compliance, and is frequently used to characterize pathologies of the lung and chest wall. Figure 4 illustrates the relative contributions of the lung and the chest wall to the compliance of the overall respiratory system. Figure 5 shows exemplary alterations in compliance for fibrotic lungs with increased elastic recoil and emphysematous lungs with decreased elastic recoil and increased compliance. So far, only overall lung compliance could be measured *in vivo* using indirect methods like pulmonary function tests. A tool that quantifies the volume change of specific alveoli would allow an assessment of alveolar compliance and could provide insights into regional differences of compliance within a lung. In contrast to inspiration,

expiration is passive during quiet breathing. As the respiratory muscles relax, the lung and chest wall return to their equilibrium position at FRC.

Another interesting property of lung expansion and contraction is the hysteresis of the pressure-volume (PV) curve (Figure 6). The change in lung volume for a given pressure difference acting on the respiratory system differs depending on whether the lung is inflating or deflating and the lung volume at any given pressure is larger during deflation than during inflation. This hysteresis can be explained in part as a consequence of the special properties of pulmonary surfactant. Several hypotheses of alveolar recruitment and de-recruitment have evolved suggesting that alveoli completely collapse and reopen at critical pressures during the breathing cycle (15, 16) or that the alveolar mouth closes on deflation (17). However, these mechanisms could not be visualized in four dimensions with current imaging techniques (18). Further development of a high-resolution, high-speed imaging technique such as Fourier-domain optical coherence tomography (FDOCT) has the potential to answer this and other important questions about alveolar structure and function during the breathing cycle.

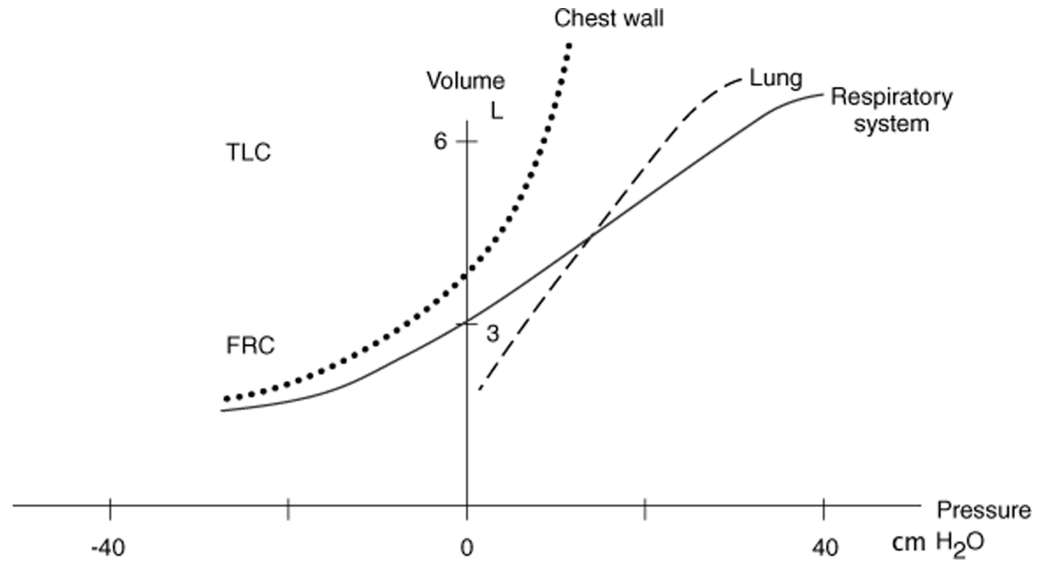


**Figure 4: The graph demonstrates the elastic contribution of the lung (dashed line) and relaxed chest wall (dotted line). The solid line represents the resultant elastic properties of the respiratory system. [Reproduced from (19).]**

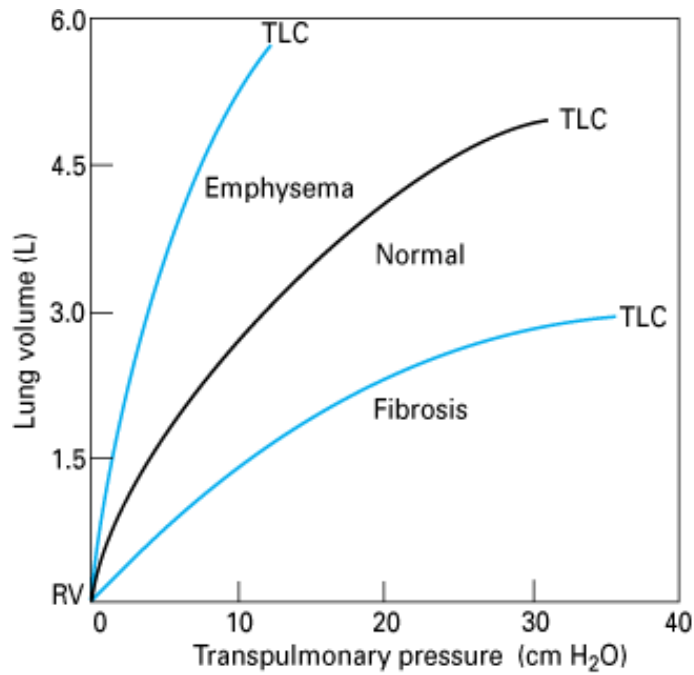


**Figure 5: Representative static pulmonary compliance curve for normal lungs, fibrotic lungs, and emphysematous lungs. [Reproduced from (19).]**

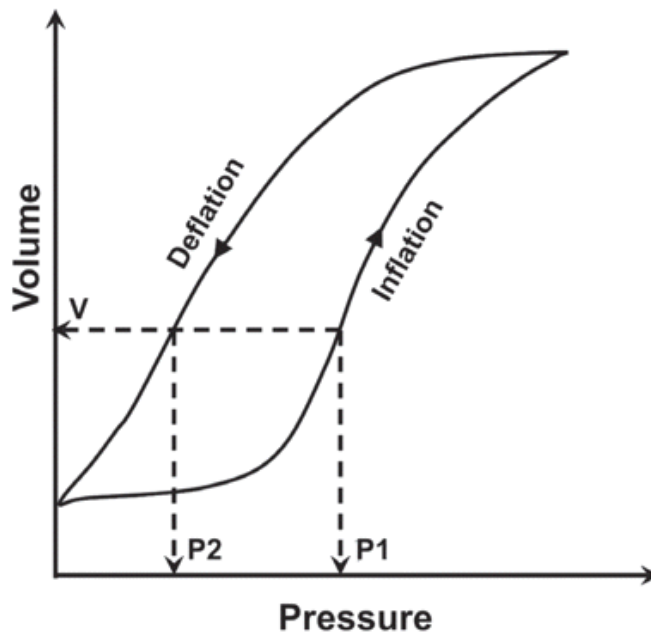


**Figure 6: Schematic showing the hysteresis of the pressure-volume curve of the respiratory system. A given lung volume V is achieved at different pressures P1 and P2 during inflation and deflation, respectively. [Reproduced from (20).]**

## 2.2 Clinical motivation

This subsection reviews the rationale for initiating the work presented within this thesis and for subsequent continued research efforts, namely open clinical questions that the developed technology could potentially answer. Three exemplary unanswered clinical challenges are introduced in the following subsections.

### 2.2.1 Improving phenotyping of COPD patients

Chronic obstructive pulmonary disease (COPD) is characterized by a fixed (non-episodic and irreversible) airflow limitation, and is currently the fourth leading cause of death in the world (21). COPD usually develops as a result of cumulative exposure to direct or indirect cigarette smoke, occupational dust or chemicals, and air pollution, being additionally influenced by genetic effects. Therefore, the diagnosis of COPD can often be made on the basis of the patient's medical history, but will be supported by a pulmonary function test (PFT). This test quantifies the maximum volume a patient can forcibly exhale in one second following a full inhalation (FEV1) in addition to the total volume expired during the maneuver (FVC). An FEV1/FVC ratio  $< 0.7$  in spite of bronchodilator use indicates the diagnosis of COPD (21). Further classification of patients is commonly made on the basis of the FEV1 value compared to a healthy individual of the same age, height, and sex. However, FEV1 only correlates slightly with the impact of the disease for the patient ( $R = -0.23$ ,  $p < 0.0001$ ), which in turn is predictive of mortality (22). Moreover, two COPD patients may present with different patterns. While one may be hypoxemic and present with cough, productive sputum, and distinct breath sounds, another extreme may have normal blood gases at rest, no cough, but only distant breath sounds and possibly an overinflated chest. Lastly, the underlying mechanism for airflow obstruction may differ significantly from patient to patient, but a precise diagnosis would have to be made at the alveolar level, which is difficult in a living patient. The current literature distinguishes between emphysema and chronic bronchitis as the primary, not mutually exclusive, causes for the symptoms (23).

In chronic bronchitis, the airways are partially blocked by excessive secretions, reducing the lumen diameter  $r$  and increasing the resistance  $R$  to (laminar) flow ( $\dot{V}$ ) (24):

$$R \propto \frac{1}{r^4} \quad (2.1)$$

Emphysema is characterized by the destruction of alveolar walls leading to enlarged air spaces and loss of elastic recoil  $P_{EL}$ , which also limits airflow:

$$\dot{V} \propto \frac{P_{EL}}{R} \quad (2.2)$$

Late stages of emphysema and chronic bronchitis can be observed on chest X-Ray or X-Ray Computed Tomography (CT), and is characterized by the loss of attenuation (black lungs) and an increase of X-Ray attenuation (“dirty” lungs), respectively (24). Early detection is impossible with current clinical imaging techniques due to the small structures of the air spaces in the peripheral lung.

Current treatment options for COPD patients include smoking cessation (25) and administration of bronchodilators and inhaled or oral corticosteroids. Supplemental oxygen can also be given and has been shown to increase survival in severely hypoxemic patients (oxygen saturation  $\leq 88\%$ , or  $\text{PaO}_2 \leq 55$  mmHg) (26). More invasive and novel surgical therapies, such as lung volume reduction (through resections or one-way valves), or bronchial fenestration (creation of bypass airways between the proximal airways and emphysematous regions) promise increased lung function, but come at the risk of increased morbidity (27-30).

Phenotyping COPD patients is therefore critical to assure each patient receives the most adapted therapy and that novel therapies are tested on the right patients, so that their benefit can be proven clearly. Because of the complexity of the disease and the variety of clinical presentations, classification of COPD patients based on FEV1 and/or disease impact, seems unsatisfactory. Phenotyping based on the cause of the airflow obstruction rather than its clinical appearance may be more adapted to successful development of personalized therapies. However, a better understanding of these causes would be necessary in addition to a more specific diagnosis of the patient’s pathology at the alveolar level.

An imaging device that visualizes and quantifies pulmonary alveoli in a living animal and/or patient could significantly advance the understanding of the pathogenesis and progression of the disease, allow more specific diagnosis, and accelerate the development of targeted therapies.

### **2.2.2 Accelerating the development of protective mechanical ventilation strategies**

Mechanical ventilation can be life saving for patients with reduced respiratory drive or acute lung injury (ALI). However, no clear consensus on the optimal adjustment of ventilation parameters currently exists and these patients are at the risk of ventilator-induced/ventilator-assisted lung injury (VILI/VALI) (4).

Potential mechanisms of VILI are often classified into barotrauma/volutrauma, biotrauma and atelectrauma (4). Baro-/ volutrauma is believed to be characterized by tissue rupture resulting from a non-physiologically high transpulmonary pressure, which is the pressure difference between the airway opening and the pleural pressure. Inflammation potentially caused by mechanical strain to the tissue is termed biotrauma and atelectrauma could represent injury that results from cyclic opening and collapse of lung units creating pressures at the interface that may be an order of magnitude higher than airway pressures.

Protective ventilation strategies would therefore need to limit the magnitude of mechanical strain to the tissue as well as the frequency of changing its amplitude. Amato *et al.* (3) could show a mortality difference of 71% *versus* 38% in a control study group of mechanically ventilated patients with ALI at 28 days after study enrollment. The study group had been ventilated at approximately half the tidal volume ( $V_T$ ) and twice the positive end-expiratory pressure (PEEP) compared to the control group. Figure 7 shows a simplified pressure-volume curve of the lung and illustrates how ventilation with low  $V_T$  and specific PEEP could be protective by avoiding potential cyclic collapse and reopening of lung units below the lower inflection point (LIP), as well as overdistension and rupture of lung tissue at high transpulmonary pressures.

Later studies have also investigated the effect of low *versus* high tidal volumes at constant PEEP in ALI, and although benefit could be shown, the mortality improvement was less striking (31, 32). Further, no specific damaging

threshold or optimized value for the tidal volume could be established in these studies, which is difficult due to the rapidly increasing complexity of randomized controlled studies with increasing numbers of test-variables. The current recommendation states a tidal volume of 6 ml/kg of predicted body weight (31) to adjust for overall lung size. However, especially in ALI, which by definition is characterized by bilateral infiltrates, only a portion of lung tissue is recruited and participates in ventilation. A personalized adjustment of the tidal volume as a function of the lung volume available for ventilation rather than the predicted body weight could be more adapted for protective ventilation, but is difficult to assess (4).

The potential benefit (increased oxygenation and reduced mortality) of individualized PEEP adjustment guided by each patient's transpulmonary pressure, rather than the airway pressure as previously performed, has been shown recently (5). However, only two strategies of adjusting the PEEP were compared instead of investigating an optimal PEEP value.

Further, the role of the respiratory rate (RR) in mechanical ventilation remains unclear. A recent study evaluated the influence of the RR and PEEP on oscillations of the arterial partial pressure of oxygen as an indicator for the amount of cyclic recruiting/derecruiting (R/D) in a swine model of ALI (33). The authors found decreased R/D with increased RR, however, at the cost of lower oxygenation compared to adequate adjustments of PEEP.

Lastly, the relationship between ventilation strategies in healthy *versus* diseased lungs remains insufficiently understood. It is unclear whether healthy lungs behave similar to recruited parts of the lungs in ALI, and clinical studies are difficult to perform, because the difference between patients with healthy and acutely injured lungs is often based solely on radiologic findings of bilateral infiltrates although both patients may be similarly hypoxemic (4). David *et al.* have evaluated healthy *versus* diseased swine lungs and found cyclic changes between atelectasis and hyperinflation to be susceptible to the PEEP level in the healthy, but not in the injured lungs (34).

In summary, the potential benefit of protective ventilation strategies has been proven, but the exact mechanisms and their interdependence remain incompletely understood and are subject of ongoing clinical and animal

studies. Further, optimal values and potential damaging thresholds for tidal volume, PEEP, and RR have not been determined and are likely to depend on the specific patient. An imaging tool that could visualize and quantitatively characterize individual pulmonary alveoli under different ventilation settings could significantly advance the current understanding of normal and diseased alveolar mechanics and accelerate the development of safe ventilation strategies to reduce the occurrence and severity of VILI and improve patient outcome.

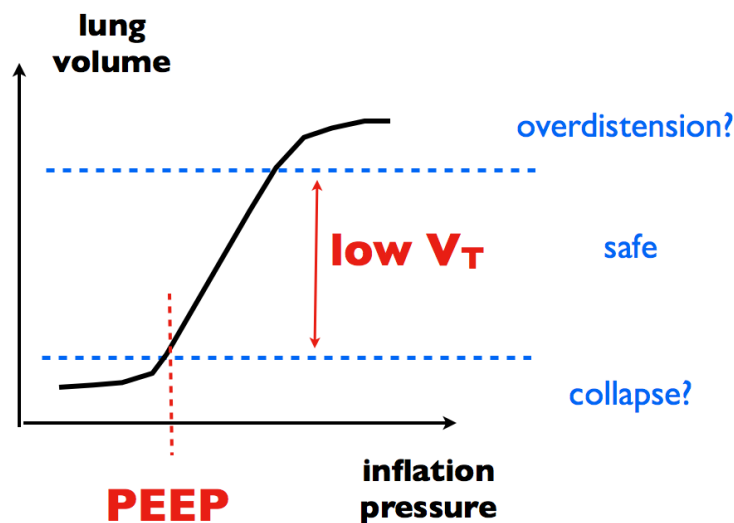


**Figure 7: Simplified pressure-volume curve of the lung illustrating how mechanical ventilation with low tidal volume ( $V_T$ ) and specific positive end-expiratory pressure (PEEP) could avoid potential collapse of lung units below the lower inflection point (LIP) as well as overdistension of pulmonary alveoli at high transpulmonary inflation pressures.**

### 2.2.3 Complementing models of gas exchange and aerosol deposition

Computational models that are able to precisely predict gas and particle flow in a patient of given respiratory system anatomy and pathophysiology could provide a personalized improved treatment of that patient. The choice of adapted gas mixtures and/or aerosolized medication for mechanical ventilation could, for example, be personalized and the optimal deposition location could potentially be targeted (35, 36).

Analytical and numerical fluid-dynamic models calculating the flow conditions and particle deposition in the airways have been developed and can be

validated, often with the help of imaging techniques, such as single photon emission computed tomography (SPECT) and X-ray computed tomography (CT) (7, 37-39). Modeling the alveolar region, however, poses a particular challenge, due to the lack of clinical technologies capable of providing dynamic images of breathing alveoli. Therefore, available quantitative data about alveolar sizes has primarily come from studies involving fixed and static lung casts and two-dimensional histology slides (9, 40). On the other hand, the influence of the alveolar wall movement on gas and particle flow in the alveolar region of the lung has been modeled and the difference in airflow compared to models of static alveolar walls was found to be significant (6, 41). This work, therefore, has aimed to develop optical techniques for dynamic imaging of alveolar movement in the most physiologic scenario possible to complement models of gas exchange and aerosol deposition.

### 3 MATERIALS & METHODS

The following chapter describes the various materials and methods utilized during the course of this work. The preparation of the different *ex-vivo* and *in-vivo* lung samples is reported first, followed by an overview of three optical reflectance techniques that were evaluated for their potential to visualize the fine structure of the peripheral lung in fixed, fluid-immersed *ex-vivo* samples. As a result of this evaluation, Fourier-domain optical coherence tomography (FDOCT) was chosen as the most promising technology to visualize alveolar dynamics *in vivo*. FDOCT was therefore developed further and section 3.3 shows the image quality difference in fluid- versus air-filled images, the optimization of the focal parameters for imaging air-filled alveoli, the design of a novel MEMS (micro-electro-mechanical systems) imaging probe that enabled *in-vivo* imaging with the technology, and how the images were segmented to obtain quantitative information. In the fourth section, the techniques to investigate the quantitative representation of alveolar size and shape in FDOCT images are explained. Since refraction and total internal reflection influence the visualization of pulmonary alveoli in FDOCT, the refractive index of lung tissue was measured. To isolate the effects of refraction, FDOCT images were also compared to micro-CT images, which are minimally subject to refraction artifacts and could serve as a gold standard to visualize the alveolar structure. Further, a 2D ray trace model was established to investigate and explain the experimentally observed difference in alveolar shape and size. Using this model, correction factors were suggested to account for the effect of refraction in FDOCT images of pulmonary alveoli. The chapter closes with a detailed description of the statistical analysis performed to compare the measurements from FDOCT *versus* micro-CT and to evaluate the suggested correction of FDOCT measurements.

### 3.1 Animal models and lung tissue preparations

This section describes the type and preparation of tissues used in this study. The first subsection provides background comparing the human lung to the studied tissues from mammalian animal models. The subsequent subsections then focus on the tissue preparations that were the basis of most of the studies performed. Fixed rat lung tissue was used to evaluate three optical reflectance techniques for their potential for lung imaging, fixed rabbit lungs were used for the optimization of focal parameters for FDOCT of air-filled alveoli, and fixed swine lungs were used for a comparison of FDOCT and micro-CT images of subpleural alveoli. The refractive index of fresh and fixed rat lung tissue was determined later and the dynamics of fresh swine lungs were studied *in vivo*. All animal experiments were approved and carried out in accordance with the regulations set forth by the Massachusetts General Hospital Subcommittee on Research Animal Care.

#### 3.1.1 Background: Mammalian pulmonary structure and function

Animal models are crucial to answer clinically relevant questions in human medicine, because of the ethical limits to experiments on humans. In order to allow the translation of obtained results to humans, however, a basic understanding of the main differences between different animal models and between animals and humans is critical.

This work focuses on the structure and dynamics of the most distal, functional unit of the lung, the pulmonary alveoli. In general, absolute alveolar sizes scale with animal size. At lung volumes close to total lung capacity (TLC) the literature indicates a diameter of 35–45  $\mu\text{m}$  for various strains of mice (42), 100  $\mu\text{m}$  for rats and rabbits (43, 44), and 250–300  $\mu\text{m}$  for large animals and humans (9). However, the alveolar wall thickness ( $\sim 10\mu\text{m}$ ) and corresponding constituents, namely the alveolar epithelium (type I and type II pneumocytes, liquid lining layer, etc.), interstitial space (collagen and elastin), capillary endothelium, blood plasma, and erythrocytes are similar across all mammalian species. Qualitative morphologic differences do occur for the larger acinar airways (45). For example, while humans have several orders of branching respiratory bronchioles following the non-alveolated terminal bronchioles,

those are rarely found in healthy rodents and the terminal bronchioles directly end into alveolar ducts (46). Also, the relatively symmetric, dichotomous airway branching pattern found in man (9), is not consistent with the monopodial branching in most species as shown in Figure 8 (47).

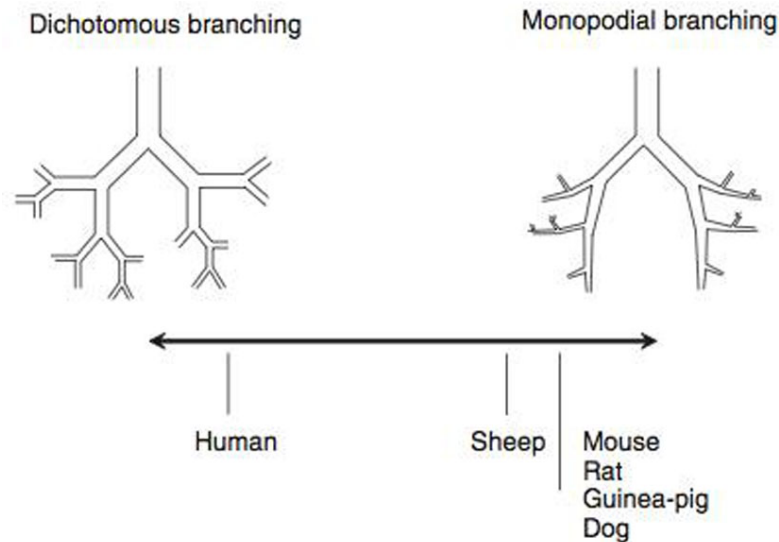


**Figure 8: Schematic representation of the difference in branching patterns between humans and several animal models. Humans present mainly dichotomous branching, where the daughter airways are similar in size compared to monopodial branching, where one of the daughters is larger than the other. [Reproduced from (47).]**

Further, while humans present with 3 lobes in the right lung and 2 lobes in the left lung, swine have an accessory cranial lobe on the right side, which branches off directly from the trachea proximal to the main bifurcation of the main bronchi (48). In rodents, the number, type and arrangement of lobes and lobules depends significantly on the strain (49). It is interesting to note, that most of the current knowledge about the morphology of the mammalian lung has been derived from casts and small sample sizes. As newer imaging and segmentation technologies become available (50), the data on morphologic differences is expected to become more precise and to cover a greater number of species.

In addition to the morphological differences, physiological parameters should also be considered. The physiologic pressure ranges that inflate and deflate lungs between FRC and TLC are very similar across species. However, differences exist for example in terms of the amount of occurring collateral

ventilation, that is gas exchange between different alveoli or lung units that does not exclusively employ the conducting airways. In the case of obstructive diseases, this effect could potentially play an important role. While humans have the ability for collateral ventilation between and within lobules, swine have very limited ability and dogs have comparably increased collateral ventilation to both humans and swine (46).

Lastly, animal models for studying pathologic conditions must be well chosen, since most human pathologies do not occur spontaneously in animal models and often symptoms or mechanisms can only be partly reproduced. One of the goals of this work, for example, was to investigate emphysema as one of the underlying pathologies of COPD. An elastase emphysema swine model was chosen as discussed in subsection 3.1.5.

### **3.1.2 Instillation fixed lung samples**

Fixed lung samples were crucial throughout the development and validation of FDOCT for alveolar imaging. Currently, no gold standard exists for fixing lung tissue, such that the method must be optimized according to the study goals (51). For this work, the most important criterion was for the samples to dry in a morphologically stable manner to allow imaging the same air-filled alveoli over a period of days to weeks for comparison of the same field of view with different imaging technologies. Therefore, an instillation technique (Figure 9) using a fixation solution containing polyethylene glycol was chosen, referred to as the modified Heitzman technique (52, 53). The most significant drawback of instillation fixation is its inability to preserve the liquid lining layer of the lung parenchyma compared to perfusion fixation (51). While the liquid layer is a critical aspect of alveolar stability *in-vivo*, the alveolar surface lining was not a subject of the presented investigation. In turn, perfusion fixation does not preserve capillary blood, which affects the refractive index of the alveolar wall, an important component of all of the optical studies considered herein.

Whole rat, rabbit, and swine lungs were fixed according to the following protocols, respectively (54-56):

Adult Sprague-Dawley rats ( $n = 3$ , approximately 350 g) were weighed and anesthetized with an intramuscular injection of Ketamine-Xylazine. Once a surgical plane of anesthesia was reached, the abdominal aorta was transected to

exsanguate the animals. The trachea was then exposed and catheterized with an 18G catheter. The lungs were instillation fixed *in situ* at 20 cmH<sub>2</sub>O pressure through a gravity feed system using a modified Heitzman solution consisting of 10% formaldehyde solution (Fisher Scientific), 10% ethanol (Fisher Scientific), 25% polyethylene glycol 400 (Post Apple Scientific) and 55% laboratory distilled water (52). After 30 min, the lungs were carefully excised and then immersed within the Heitzman solution while connected to the feed system at the same inflation pressure for a minimum of 48h. The lungs were then disconnected from the fixation apparatus and air-dried for a minimum of 2 days in a 60 °C drying oven while pressurized with air at 20 cmH<sub>2</sub>O. Finally, the dry inflated lungs were cut into 1-2 mm thick sections, immersed in phosphate buffered saline (PBS) and degassed for imaging. After three-dimensional images were obtained with all three imaging modalities on the same sample, each was placed in formalin and processed for paraffin-embedded histopathology by using standard methods. Hematoxylin and eosin (H&E) stained histopathology slices (5  $\mu$ m thick) showing nuclei in blue and cytoplasm in pink/red were obtained, and slides were digitized with a full-slide scanner (ScanScope CS, Aperio Technologies, Inc, Vista, Calif).

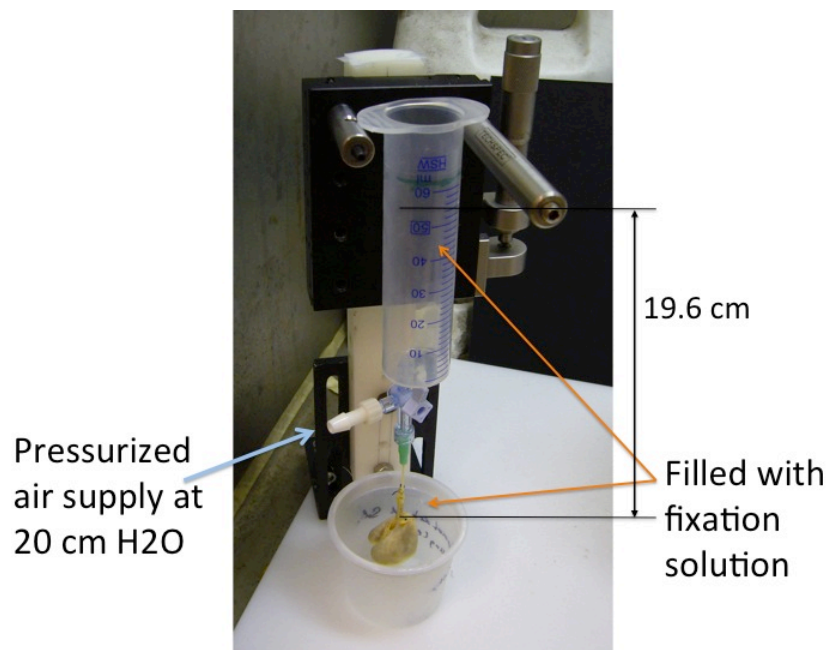


**Figure 9: Instillation fixation setup shown with excised rat lung. The fixative solution will fill the syringe up to a pressure of 20 cmH<sub>2</sub>O. Later, the trachea is disconnected from the solution and connected to a pressurized gas supply at the same pressure until dry.**

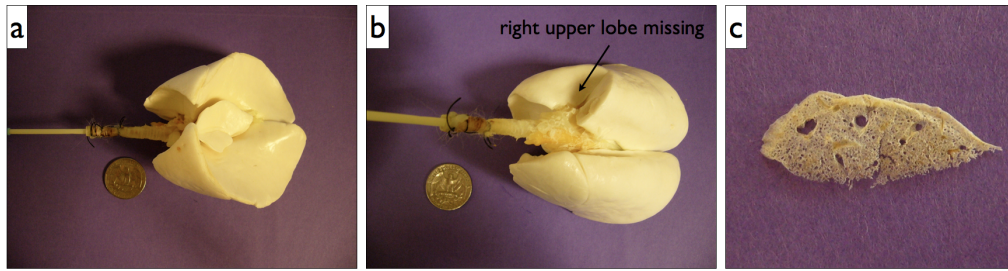


**Figure 10: Images of a fixed and dried rabbit lung and rat lung slice. (a) Rabbit ventral and (b) dorsal, with the right upper lobe cut out; (c) rat lung slice, thickness is approximately 500  $\mu\text{m}$ .**

One adult female rabbit (2.5 kg) and male Yorkshire swine lungs ( $n = 4$ , 30-35 kg) were fixed in a similar way at 20 cmH<sub>2</sub>O pressure, but after careful excision from the chest and samples were not immersed in PBS to keep the alveoli air-filled. In contrast to the rats and rabbit, swine were subject to 2-5 hours of mechanical ventilation with anesthesia maintained using 1-3% inhaled isoflurane before euthanization.

The instillation fixation technique proved to be most successful when initially started *in situ* with a closed chest as done in the rats compared to fixation after excision from the chest as done for rabbit and swine as shown in Figure 9. However, specific approval had to be obtained for *in-situ* fixation and it could not be performed when fixation followed *ex-vivo* experiments. Figure 10 shows an example of a fixed rabbit lung and a slice of fixed rat lung.

### 3.1.3 Freshly excised lung tissue

Certain research questions are best answered with freshly excised lungs. Compared to fixed lungs, a specific alveolar region can be imaged at various inflation states. Furthermore, in terms of development of *in-vivo* devices, the refractive indices are well matched. At the same time, any region of the lung is accessible for imaging and experiments can be performed in a non-surgical laboratory, avoiding the complexity of monitoring the animal during an *in-vivo* experiment. Freshly excised tissue was used for a first qualitative investigation of alveolar size changes during step-wise inflation and deflation of the lung.

Similar to the preparation of fixed tissue, animals were weighed and anesthetized with either an intramuscular injection of Ketamine-Xylazine (80-90 mg/kg of Ketamine + 10 mg/kg Xylazine for rats, 35-50 mg/kg Ketamine +

5-10 mg/kg Xylazine for rabbits) or Telazol/Xylazine at 4.4 mg/kg / 2.2 mg/kg followed by 1-3% isofluorene once intubated (swine). After a surgical plane of anesthesia was reached, the abdominal aorta was transected to exsanguinate the animals. The trachea was exposed and catheterized with an 18G catheter (rats), 4 mm diameter tube (rabbit), or 7 mm ID ET tube (swine). The lungs were then carefully excised. It is important to note that best results can be expected, if lungs are excised in a well-recruited stage (at approximately 20 cmH<sub>2</sub>O) with the endotracheal tubing clamped to prevent collapse. Figure 11 shows an example image of a freshly excised rat lung.

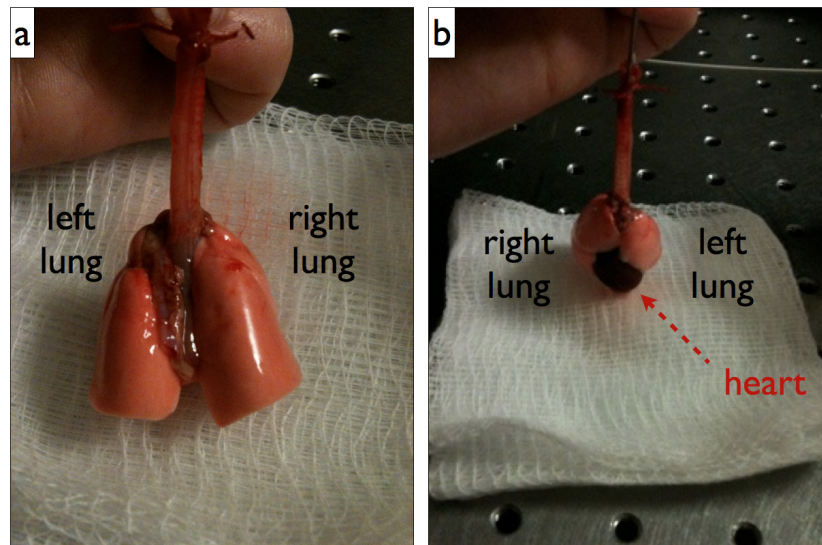


**Figure 11: Images of a freshly excised rat lung, dorsal (a) and ventral (b).**

There are several constraints of experiments with freshly excised lungs that are especially important in the context of optical imaging. Outside of the body and exposed to room air, lung tissue will dry and become more transparent. Therefore, in order to ensure a refractive index similar to the *in-vivo* case, it is crucial to keep the lung hydrated. Secondly, when evaluating quantitative alveolar sizes, it is essential to control the volume history of each lung before the acquisition of data and to control the overall time of the experiment (15). A specific number of several recruitment cycles of a completely collapsed lung should precede any experiment. As shown in Figure 12, the inhaled volume of the collapsed lung will increase gradually from cycle to cycle although the same pressure differences may be applied for inflation and deflation. Eventually, the volume changes will reach a temporary steady state. In addition to the pressures and the number of cycles, the cycle time should be controlled.

If exposed to a constant inflation pressure over time, the lung tissue may relax and the inhaled volume may be increased such that two cycles using the same pressure difference but different cycle times may result in different lung volumes. Lastly, the lung is also sensitive to overall time of the experiment and temperature changes. The hysteresis between the inflation and deflation limb of the pressure-volume curve was shown to be wider in non-perfused excised lungs, than in *in-vivo* lungs (57). The compliance (volume change per change in transpulmonary pressure) decreases with decreasing temperature and increasing time of the experiment (58) indicating a stiffening lung at low temperatures and over time.

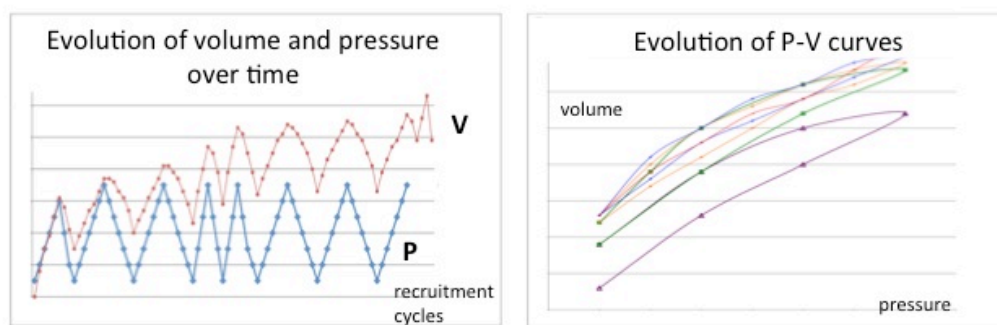


**Figure 12: Recruitment of a freshly excised, completely collapsed rabbit lung: The lung volume (V) increases over time when ventilated with constant pressure (P) changes.**

### 3.1.4 *In-vivo* swine model

Experiments to study lung physiology and clinically relevant questions about alveolar dynamics should be performed in a living model. Alveolar sizes during the breathing cycle are a function of many complex and intertwined parameters including the inflation volume and flow rate, airway resistance and the elastic properties of the lung and chest wall, the alveolar liquid lining layer (surfactant), the pulmonary circulation, the species, strain, age and weight of the subject, and gravitational forces. In this work, results are shown from *in-vivo* experiments led by Eman Namati and Bill Warger (54) on 30 – 35 kg healthy, male Yorkshire swine ( $n = 3$ ). As stated previously, FDOCT images should be provided that allow visualization and quantification of alveolar sizes during ventilation and providing results on alveolar expansion and contraction that were the closest to a physiologic situation in humans. However, few main

differences between the ideal case scenario and the performed experiments must be discussed:

First, the experiments were performed in a swine model. This species was chosen because of the relatively close resemblance in lung morphology to the human lung.

Further, during the experiment, the swine were not breathing spontaneously, but were anesthetized, intubated and mechanically ventilated. In spontaneous breathing, inspiration happens as the respiratory muscles including the diaphragm pull outward creating a negative pressure in the pleural space that expands the lung and lowers the pressure inside the lung below atmospheric. As a result, ambient air is drawn in to equilibrate the pressures. In mechanical ventilation, the lung and chest wall are both expanded by positive pressures that are applied to the airway opening or the endotracheal tube by the ventilator. Therefore, the forces expanding the lung parenchyma are opposite in sign. Potential differences on the lung mechanics between positive and negative pressure mechanical ventilation have been studied with conflicting results (59, 60). However, in the context of the studied lungs in this work (either healthy or emphysematous but non-occluded), it is reasonable to assume that there is no difference between positive and negative pressure ventilation at the same absolute value of transpulmonary pressure, that is the pressure difference between the pleural space and the airway opening (59).

Lastly, imaging with the contact-MEMS probe (subsection 3.3.3) required partial removal of the chest wall (thoracotomy). As soon as air enters the pleural space, the outward recoil of the chest wall no longer assists in keeping the lung inflated and the lung volume (in mechanical ventilation) depends solely on the airway opening pressure, airway resistance, and lung compliance during both inspiration and expiration. This is especially important when comparing pressure-volume curves to subjects with a closed chest wall. Further, the shape of subpleural alveoli might be influenced, as their expansion is no longer limited by the boundary chest wall. It is also important to note, that any surgery that intrudes the pleural space has to be performed with extreme caution, because of the fragility of the lung. Best results are obtained when the first cut into the pleural space is made at a low lung volume.

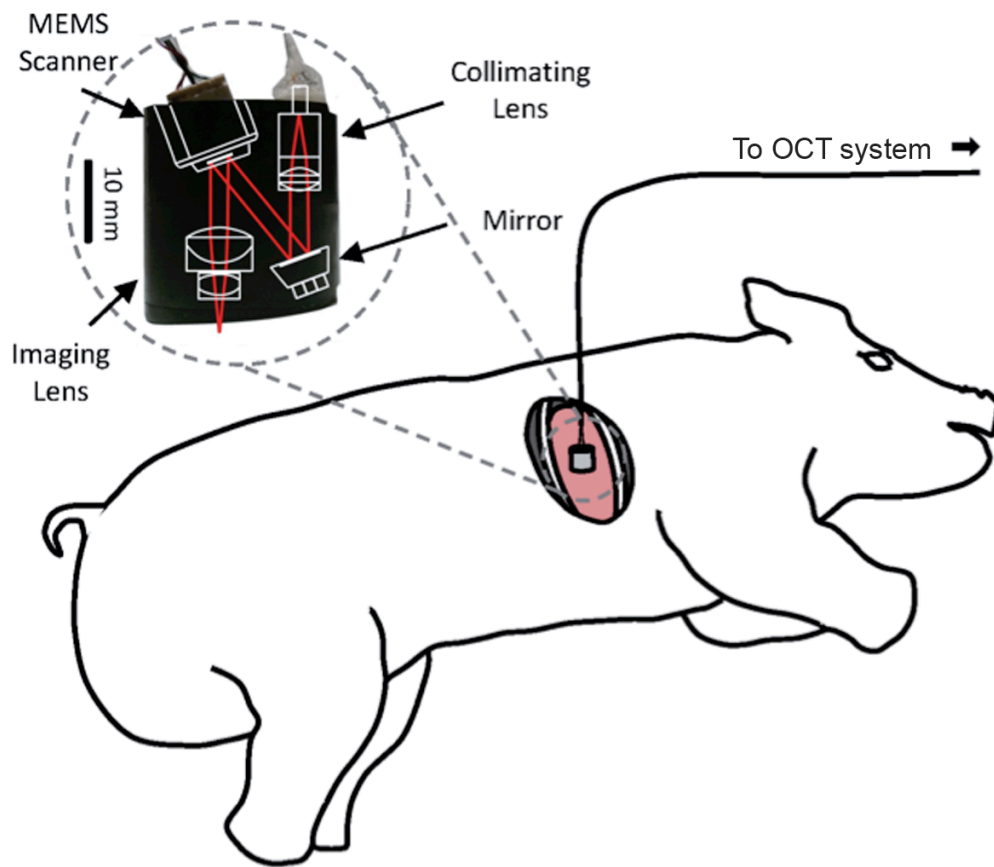


**Figure 13: Picture of the MEMS probe with a diagram of the primary components within the MEMS probe and the positioning on the right middle lobe of live swine on mechanical ventilation. [Reproduced from (54).]**

The following protocol and figure of the performed *in-vivo* experiments are reproduced from (54): Male Yorkshire swine ( $n = 3$ ) weighing 30-35 kg were initially sedated with a mixture of Telazol 4.4 mg/kg and Xylazine 2.2 mg/kg, intubated using a 7 mm inner diameter cuffed endotracheal tube, and placed on mechanical ventilation with anesthesia maintained using 1-3% isoflurane. Buprenorphine 0.3 mg/kg was also administered intravenously for additional pain management. Electrocardiographic output, blood pressure, pulse oximetry, and temperature were monitored for assessment of anesthesia, pain, and distress. Swine were ventilated with a tidal volume of 10 ml/kg, 20 bpm, and 20 cmH<sub>2</sub>O peak inspiratory pressure (PIP). Once a surgical plane of anesthesia had been met, the swine were positioned on their left side and a right thoracotomy was performed to reveal the right middle lobe. Warm saline was applied to the pleural surface periodically to ensure the tissue retained moisture. The lightweight probe was placed at various locations on the right

middle lobe in Figure 13, and continuous volumetric datasets were acquired over a minimum of three breaths at various ventilation settings (10 bpm, 1-3 cmH<sub>2</sub>O peak expiratory end pressure (PEEP), 11-20 cmH<sub>2</sub>O PIP). A pressure sensor positioned at the proximal tip of the endotracheal tube recorded the intratracheal ventilation parameters during image acquisition such that each frame could be related to the intratracheally-applied pressure. Once the imaging procedure was completed, the animal was euthanized *via* exsanguination, the endotracheal tube was clamped to keep the lungs inflated, and the lungs were carefully excised.

### 3.1.5 Elastase emphysema model

Emphysema is one of the major pathologies underlying COPD. In this work, it should be shown that FDOCT is capable of visualizing alveolar dynamics in emphysema and emphysematous alveolar sizes during the breathing cycle should be provided. The ideal model would have had a pulmonary anatomy similar to that of humans, and the same mechanisms behind the lesion, all while being produced in a short period of time (45).

The swine model was chosen for its similarity in lung morphology to humans, and to have the ability to compare the generated results to the previously obtained data in healthy swine. Since approximately 80% of smokers get COPD, smoke-induced animal models have been developed and are preferred by many (45). However, these models are time consuming, expensive, and the pathogenesis is unclear. It remains unknown, for example, why only 30-40% of smokers develop COPD. Emphysema has also been correlated to genetic  $\alpha$ 1-antitrypsin deficiency. This has led to the hypothesis that the destruction of the alveolar wall is caused by a protease/anti-protease imbalance and elastase induced emphysema models have been widely used (61-63). Other possibilities include genetic models, endotoxin-, and starvation- induced models (45, 64), but none of those models replicates better the characteristics of human emphysema in swine at a comparable time and cost as the elastase model.

Therefore, a porcine pancreatic elastase (PPE) model similar to Noma et al. (62, 63), was developed with elastase purchased from Elastin Product Company. Three male Yorkshire swine (30-35kg) have undergone a first survival procedure of elastase instillation to the left lung followed by a second

non-survival imaging procedure of both the left and right lungs three weeks after the application of the elastase. Also, the left lung of three healthy controls was assessed with the same protocol as described in the previous subsection.

In the first procedure, swine were put on mechanical ventilation as described previously. A 3-mm outer diameter bronchial blocker (Uniblocker, Fuji Systems Corporation) was inserted into the left main bronchus. Positioning of the balloon was confirmed visually using a bronchoscope. Through the bronchial blocker 2 mg/kg PPE diluted with 5 ml/kg saline were instilled during a period of approximately 20 min. The applied pressures were monitored closely to stay below 20 cmH<sub>2</sub>O to prevent pneumothorax. After administration, the animal remained on mechanical ventilation for 45 minutes to allow the solution to be absorbed. Upon removal of the bronchial blocker, only a few bubbles of possible backflow of elastase solution into the right bronchus were observed through the bronchoscope.

The imaging procedure was performed three weeks after the instillation of the elastase according to the same protocol as outlined in the previous subsection, except that the left lung was imaged first followed by the right lung, which had not been exposed to the elastase. The left chest wall was closed with sutures before turning the animal. Moreover, X-ray projection images were obtained after excision of the fresh lung and after instillation fixation according to subsection 3.1.2. Computed tomography (CT) volume images were also acquired post-fixation.

### 3.2 Optical reflectance techniques for imaging alveolar structure

This section discusses the specific challenges for developing optical reflectance techniques for imaging pulmonary alveoli and presents the rationale for choosing FDOCT for the further development to image alveolar dynamics *in-vivo* (55).

The first subsection briefly introduces three optical reflectance techniques, namely Fourier-domain optical coherence tomography (FDOCT), spectrally encoded confocal microscopy (SECM), and full field optical coherence microscopy (FFOCM).

Secondly, the specific challenges of alveolar imaging are discussed and related to the basic principles of the presented techniques for a better understanding of their capabilities and limitations. Lastly, each technology was evaluated for its potential to visualize both gross architecture as well as cellular detail in fixed, PBS-immersed rat lung tissue.

**Table 2: FDOCT, SECM, and FFOCM system parameters used to image PBS-immersed rat lung tissue.**

Parameter	FDOCT	SECM	FFOCM
Numerical aperture	0.08	1.2	0.45
Transverse resolution ( $\mu\text{m}$ )	12	1.3	1
Axial resolution ( $\mu\text{m}$ )	7	2.4	1
Acquired volumes (mm x mm x mm)	2 x 2 x 5 <sup>1</sup>	2 x 2 x 0.2	0.25 x 0.25 x 0.25
Acquisition time (min)	0.07	30	60

<sup>1</sup> The ranging depth in PBS is 5 mm.

### 3.2.1 Introduction of three high-resolution optical reflectance techniques

FDOCT, SECM, and FFOCM all allow three-dimensional imaging of biological samples utilizing the tissues' light scattering properties without the need for ionizing radiation or contrast agents. Their spatial resolution (1-10  $\mu\text{m}$ ) is typically several orders of magnitudes finer than the commonly used clinical imaging technologies such as ultrasound, X-ray computed tomography, or magnetic resonance tomography (100  $\mu\text{m}$  - 1mm). In addition, because they do not rely on transmission of the signal through the sample, but detect the backscattered light, their spatial resolution and its decay with increasing penetration depth in the tissue is independent of the sample size. However, all three techniques are based on different principles and may supply

complimentary information due to their range of contrast, and spatial and temporal resolutions. This subsection briefly introduces the basic functionality and system components of each technique. The characteristics of each imaging modality as used for a comparative study on fixed, PBS-immersed rat lung tissue are summarized in Table 2.

### **Fourier domain optical coherence tomography (FDOCT)**

Optical coherence tomography (OCT) can be considered the optical analogue to ultrasound, as it measures echoes of light along the depth of a given sample to reconstruct its internal structure (A-scan). In contrast to the speed of sound ( $\sim 3 \cdot 10^2$  m/s in air,  $\sim 15 \cdot 10^2$  m/s in water), the speed of light ( $\sim 3 \cdot 10^8$  m/s in vacuum) is outside the limits of electronic detection, and OCT generally employs low-coherence interferometry to detect the echo time delay between different backreflecting or backscattering structures within the sample (65). The intensity of the backscattered signal is then mapped onto a grey scale to create the sample's image.

Figure 14 illustrates the principle of low-coherence interferometry utilized by OCT. A beam splitter (BS) separates the light from the source into sample and reference paths. The light in the reference arm travels a known distance and time before it is backreflected from a mirror. The light incident on the sample is backscattered and backreflected from internal structures at various unknown depths. Both returning beams recombine at the BS and their interference signal is detected. Constructive interference occurs when the optical path length difference between the reference and sample paths is matched within the coherence length of the light source. The key to high axial resolution in OCT is the use of a short coherence-length light source to discriminate small differences in depth in the sample of various scattering events. The use of a long coherence length in Figure 14 will result in all of the scattering events within that length to interfere with little difference in the interference signal. For example, it would be impossible to differentiate two scattering events 10 cm apart with a HeNe laser of a typical coherence length of more than 20 cm. However, the use of a laser diode with a coherence length of  $10 \mu\text{m}$  will only provide an interference signal when scattering events exist within  $\pm 5 \mu\text{m}$  from the reference arm optical path length. Consequently, the depth locations of

scattering structures in the sample arm can be inferred from the time-of-flight of the light in the reference arm, and the coherence length of the light source primarily determines the axial resolution.

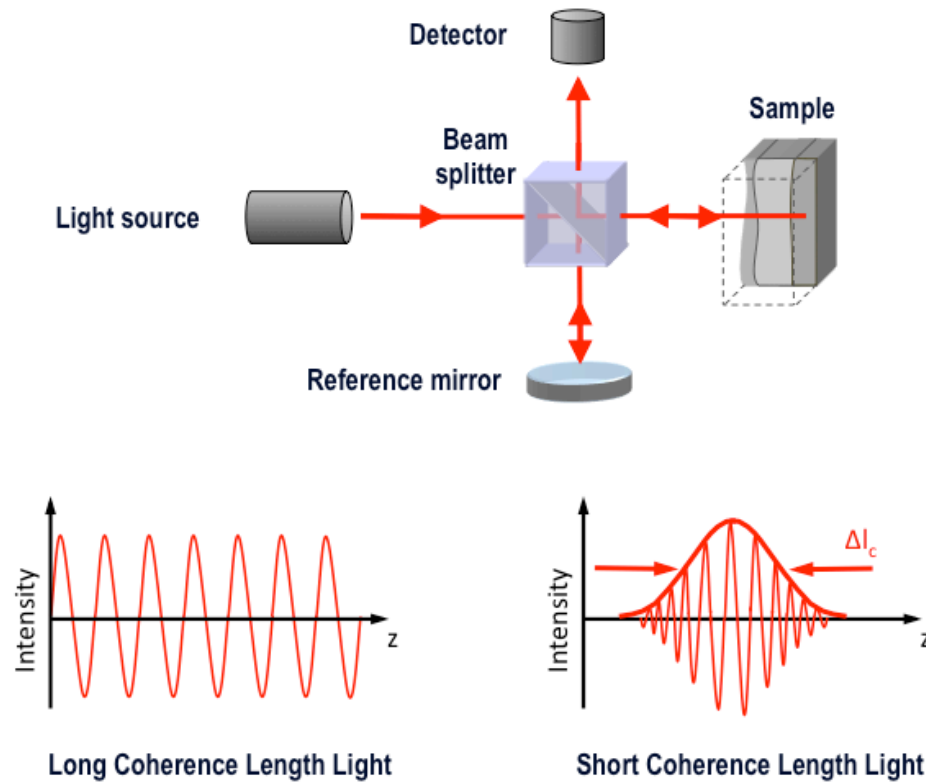


**Figure 14: Schematic illustrating the principle of low coherence interferometry to measure the location of scatterers or tissue interfaces in a given sample. A beam splitter (BS) splits light into a reference and sample beam. While the reference beam is backreflected from a mirror, the sample beam propagates into a sample or tissue. Light that is backscattered from structures and interfaces within the tissue is then recombined with the reflected sample arm beam at the BS to create the interference signal that is detected to reconstruct the depth at which the scattering events occurred. Constructive interference occurs when the path length difference of both beams is within the coherence length ( $\Delta l_c$ ) of the light source. A low coherence length is therefore key to obtaining fine axial resolution.**

An important underlying assumption of the technique is then that the returning light from the sample has undergone a single scattering event and that the light is returned from structures along the straight A-line. This may not always be the case, however, such that multiple scattering and refraction of light can cause artifacts.

In order to reconstruct two- (B-scan) or three-dimensional (C-scan) images, a scanner, such as a galvanometric scanner that translates the illumination beam in a raster pattern, is required to sample A-lines throughout a region of the tissue. Figure 15 shows a generic OCT imaging system setup.

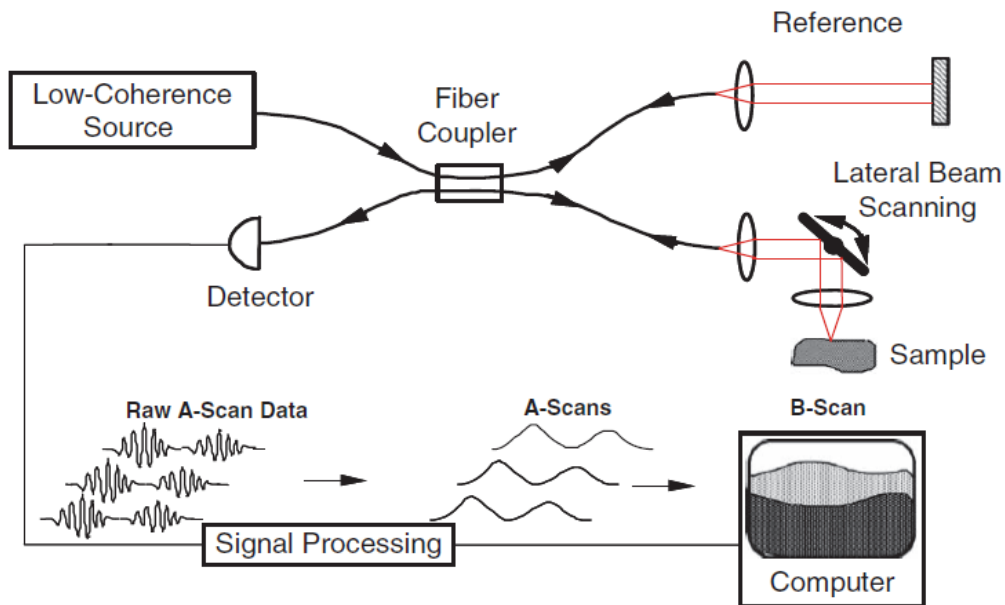


**Figure 15: Schematic illustrating a generic OCT scanner setup. The sample beam providing depth information along an A-line is scanned transversely over the sample to reconstruct a two- or three-dimensional image (B-scan). Bold lines represent fiber-optic paths, red lines represent free-space optical paths, and thin lines represent electronic signal paths. [Reproduced from (66).]**

Different OCT technologies can be further specified according to employed strategies for detecting and processing the interference signal. In time-domain OCT (TDOCT), the reference arm mirror physically translates along the axial direction to scan the depth of the sample for matching path lengths between the mirror position and tissue interfaces/scatterers. The position of the reference mirror then directly provides the depth location (in optical path) of the internal structures within the sample. In Fourier-domain or frequency-domain OCT (FDOCT), the reference mirror is stationary and the spectral modulation of the interference signal as a function of frequency is detected and further processed to obtain the depth location of the tissue structures. FDOCT is often referred to as a second generation OCT and in addition to eliminating mechanical scanning of the reference mirror, it provides a significant sensitivity advantage compared to TDOCT, which is especially crucial for high-speed imaging

applications (67). In practice, FDOCT can be performed by either separating the interference signal into multiple spectral components at the detection following simultaneous broadband illumination of the sample (referred to as spectral FDOCT) or by modulating the frequency output of the light source to illuminate the sample with one frequency (wavelength) at a time (swept-source FDOCT). In spectral FDOCT, a broadband light source illuminates the sample and the entire spectral interference is acquired simultaneously, but as a function of wavelength using a spectrometer. Rescaling the spectrometer output from wavelength to wave number ( $k \propto 1/\lambda$ ) and then Fourier transforming the interference signal provides the depth location of the scattering events (65). In swept-source FDOCT or optical frequency domain imaging (OFDI), a wavelength-swept source with a narrow linewidth and broad tuning range, illuminates the sample and a single photodiode detects the interference signal from each wavelength separately (67-70). Fourier transforming the resultant interferogram from one complete sweep of the laser bandwidth provides the reflectivity profile as a function of depth (A-line) within the tissue (Figure 16). Note that the work presented in this thesis is entirely based on swept-source FDOCT, which will simply be referred to as FDOCT.

The axial resolution of FDOCT is dependent on the bandwidth of the swept-source laser (70) and is decoupled from the lateral resolution (71), which is dependent on the numerical aperture (NA) of the imaging lens (0.08 NA, 30 mm focal length, Thorlabs). The FDOCT system used throughout this work has a 62.5 kHz wavelength-swept source, with a 110 nm bandwidth centered at 1310 nm, providing fast (>100 cross-sectional B-scans/s) imaging with high isotropic resolution ( $\sim 10 \mu\text{m}$ ) over large depths in isotropic tissue (1-2 mm). The principles governing spatial and temporal resolution as well as imaging depth are explained in detail in the following subsection. In this first study comparing images of fixed, PBS-immersed rat lung samples, a bench top raster-scanning setup was used to obtain fields of view of 2 x 2 mm (512 x 512 pixels) over a ranging depth of 5 mm (in water) in 4s.

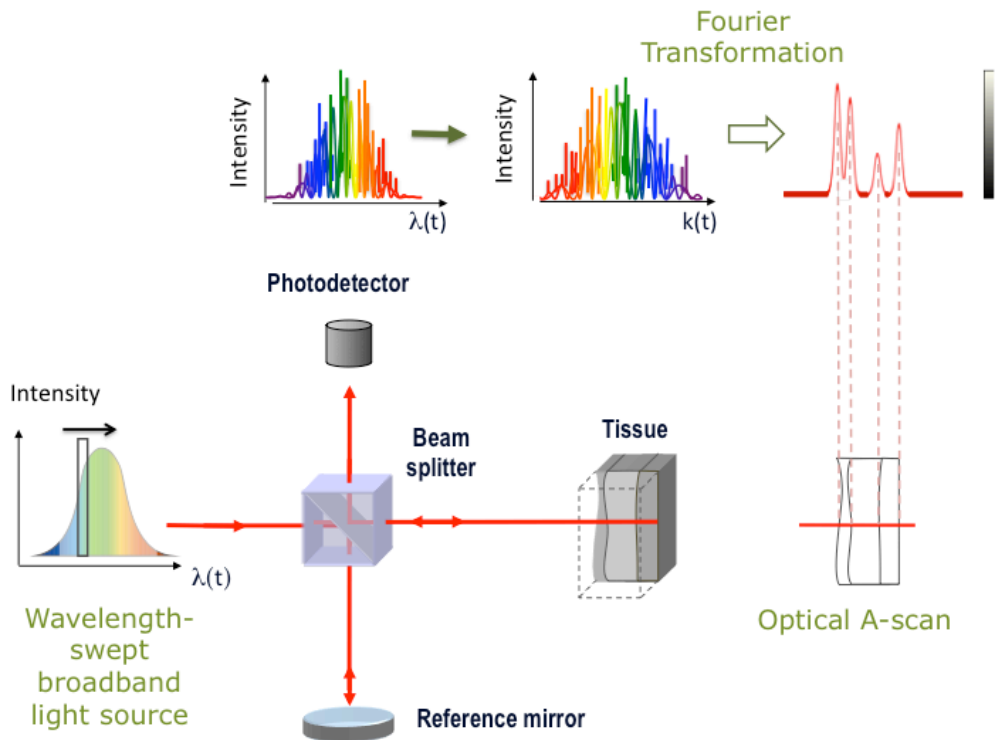


**Figure 16:** Schematic illustration of the principles of swept-source Fourier domain optical coherence tomography. The reference mirror is fixed and light from a wavelength-swept source illuminates the interferometer (and tissue) one wavelength at a time. A photodiode detects the interference signal intensity for each wavelength resulting from backreflected and backscattered light from the sample and reference arm. The resultant interferogram from one complete sweep of the laser bandwidth is mapped from the wavelength- into  $k$ -space and Fourier transformed to reconstruct the reflectivity profile as a function of depth (A-line) within the tissue.

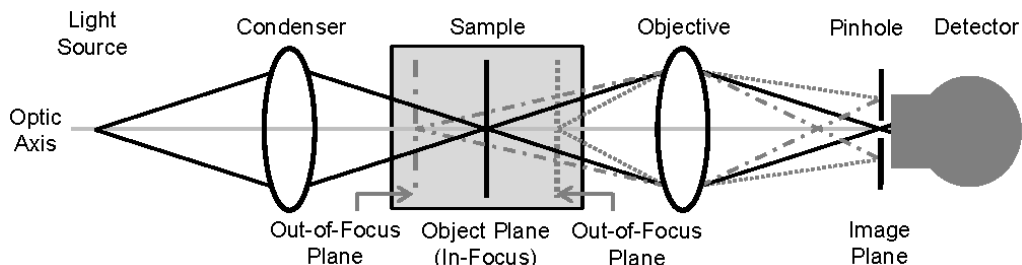


**Figure 17:** Confocal transmission imaging system. A condenser lens provides point illumination of the sample and an objective lens directs the scattered light to the detector. A pinhole in front of the detector assures rejection of most of the out-of-focus scattered light. [Reproduced from (72).]

### **Spectrally encoded confocal microscopy (SECM)**

In conventional wide-field light microscopy (typical microscopy), the entire field of view of a sample is illuminated and the resultant full-field image is detected. As a result, the contrast from the light at one specific depth focal plane is reduced by light scattered from other planes that blurs across the detector. Confocal microscopy uses point illumination and a pinhole in front of the detector to block most of the out-of-focus scattered light from depths outside of the focal plane resulting in increased contrast for the specific plane of interest. Figure 17 illustrates how the objective lens and pinhole only allow the in-focus scattered light from the focal plane (optical section) to pass to the detector for reconstruction of the image (72). Compared to conventional microscopy, confocal microscopy achieves high-contrast images of a focal spot, but requires the beam to be scanned in all dimensions within the sample to provide two- and three-dimensional images.

Confocal reflectance microscopy uses the same principle to select backscattered/ backreflected light from a specific optical section. Therefore, the light source and detector are placed on the same side of the sample and a beam splitter is typically used to direct the illumination light from the source to the objective lens and the returning light from the lens to the detector (compared to a transmission geometry in Figure 18). To a first approximation, the size of the focal spot is determined by the angle with which the light beam focuses onto the sample. In order to create a three-dimensional image, the focal spot must then be scanned in both transverse and axial directions.

Spectrally encoded confocal microscopy (SECM) (73, 74) is a reflectance confocal microscopy technique that uses optical scanning in the transverse direction to increase image acquisition speed. In SECM, broadband light illuminates a diffraction grating-lens pair to focus a line of spectrally dispersed light into the sample, where each point along the line illuminates the sample with a different wavelength as shown in Figure 18. Light reflected from the sample returns back through the grating-lens pair and then through an aperture, which provides the optical sectioning. The simultaneous detection of all wavelengths along the spectrally-encoded line eliminates the need for a mechanical scanning mechanism within the spectrally encoded dimension, and

a single scanner sweeps the line to provide a two-dimensional image. Large fields of view are obtained by mosaicing the scan pattern with a stage scanner and three-dimensional images are obtained by adding a scanning mechanism in the depth direction.

The system used in this study (75) utilizes a wavelength-swept source with a 1320 nm center wavelength, 70 nm bandwidth, and a 5 kHz repetition rate. The combination of an 1100 lines/mm transmission diffraction grating and a 3 mm focal length objective lens (Olympus 60x, 1.2 NA in water, 350  $\mu\text{m}$  working distance) provided a 0.12 mm spectrally encoded line. Translation stages in the transverse and axial directions scanned the sample to image a 2 x 2 x 0.2 mm volume (4000 x 4000 x 40 pixels) in approximately 30 min. SECM was integrated in this study because it can provide high spatial resolution (1.3  $\mu\text{m}$  transverse and 2.4  $\mu\text{m}$  axial) over a large field of view (73, 76).

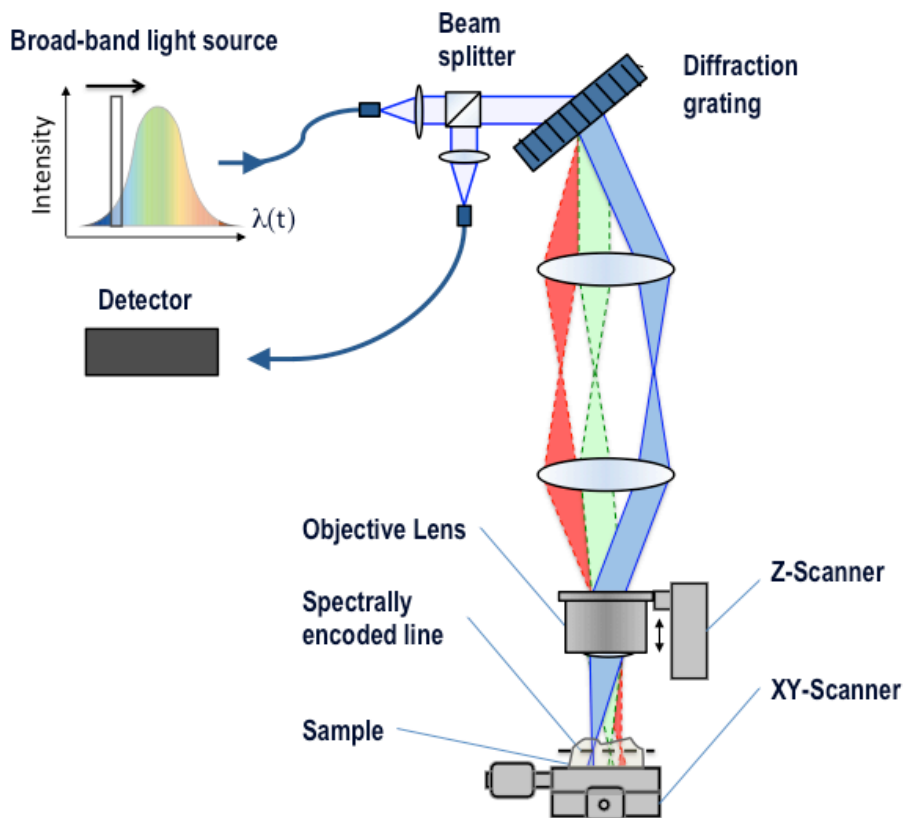


**Figure 18: Schematic showing the setup of a bench-top spectrally encoded confocal microscopy (SECM) system using a wavelength-swept broadband light source. During one sweep of the light source, the transmission diffraction grating-lens pair focuses a line of spectrally dispersed light into the sample and thus performs optical scanning of the line image.**

### Full field optical coherence microscopy (FFOCM)

Full field optical coherence microscopy (FFOCM) (77, 78) is based on conventional wide-field light microscopy and provides *en face* images. FFOCM, however, is also capable of optical sectioning due to an additional reference arm that enables processing of an interference signal. Figure 19 illustrates a basic FFOCM setup. Broadband, spatially and temporally low coherent illumination light is delivered by a multi-mode optical fiber and split into a reference and a sample arm, which contain identical microscope objective lenses to focus the light on a mirror and three-dimensional sample, respectively. The backreflected and backscattered light from both arms is then recombined and interference occurs between photons that traveled the same path-length in both arms. At a fixed path length of the reference arm, the interference thus optically selects an *en-face* image from a specific depth in the specimen. In order to extract the interference fringe envelope, the reference arm position (and thus the phase in the interferometer) is modulated in the axial direction. The *en-face* image is reconstructed by processing the resultant interference patterns from the backscattered light at discrete reference arm lengths with a phase-shifting algorithm (77). Similar to distinguishing different depth locations with temporal coherence of the light source, the spatially low coherent light allows distinguishing between scatterers separated in the transverse directions. Thus, the entire *en-face* field of view of the sample is acquired without transverse scanning. Three-dimensional datasets are obtained by scanning the sample relative to the reference mirror along the z-axis.

The FFOCM system used in this study (79) uses a broadband Xenon arc lamp (450-750 nm) that illuminates the reference arm mirror and sample through two identical water-immersion objective lenses (Olympus 20x, 0.45 NA in water, working distance 3 mm). The resultant interference pattern is detected by a high-speed CMOS (complementary metal oxide semiconductor) area scan camera (1M150, Dalsa, peak response at 600 nm). A motorized stage (Picomotor 8302, New Focus) was used to scan the sample along the z-axis (depth) every 0.25  $\mu\text{m}$ . Volumes of 0.25 x 0.25 x 0.25 mm (512 x 512 x 1000 pixels) were obtained within approximately 60 min. FFOCM was integrated in

this study to visualize sub-cellular structures in the peripheral lung with isotropic  $1\ \mu\text{m}$  resolution.

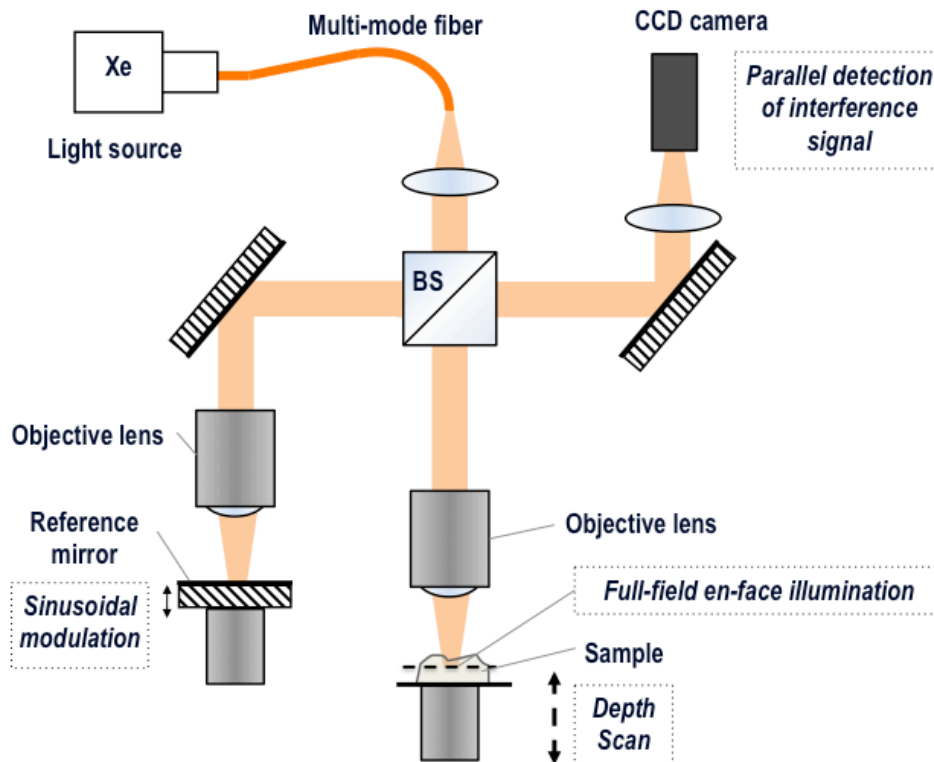


**Figure 19: Schematic setup of a full field optical coherence microscopy (FFOCM) system.** A broad-band, spatially incoherent light source is transmitted through a multi-mode fiber and illuminates a Linnik interferometer (containing two identical objective lenses). Backreflected and backscattered light from the reference mirror and the sample's *en face* field of view is recombined at the beam splitter (BS) and the interference signal is detected by a camera for the entire *en face* view at a distinct reference mirror position and thus depth in the tissue. The reference mirror position is sinusoidally modulated and the interference signal is integrated over different phase intervals to extract the fringe envelope and obtain the optically sectioned image data. *En-face* images at different depths can be acquired via translating the sample relative to the objective lens and reference arm. Xe = Xenon arc lamp.

### 3.2.2 Specific challenges in alveolar optical imaging

High spatial and temporal resolution, miniaturized probe design, and minimal artifacts from high refractive index changes are specifically important for imaging pulmonary alveoli. Because these parameters are interdependent, they cannot all be optimized at the same time and the conflicting tendencies must be understood, such that they can be optimized for a specific application. This subsection discusses the specific requirements for optical imaging of the alveoli and describes their interdependence in the context of each of the technologies assessed.

High spatial resolution independent of the sample size is one of the key arguments for using optical reflectance techniques for imaging pulmonary alveoli because the better the resolution, the more detailed the structures that can be investigated. However, high resolution may come at the cost of slower imaging speed and/or imaging depth. Imaging speed is especially crucial for limiting motion artifacts during *in-vivo* imaging within this organ, which is in constant movement due to the breathing itself and the underlying cardiac motion. Moreover, in order to assess the dynamics of pulmonary alveoli, several data sets must be acquired during each inflation - deflation cycle. Another challenge arises from the fragility of the lung and its well-protected location within the body. Optical reflectance imaging of internal organs generally requires the illumination and collection of light to occur in close proximity (within several hundred  $\mu\text{m}$  to a few cm) to the region of interest. Therefore, miniaturized probes are crucial to gain access during a minimally invasive procedure to prevent damage to the organ and to provide information about the physiologic and pathophysiologic environment. Lastly, compared to most organ systems, the pulmonary alveoli present especially large refractive index changes between the alveolar tissue ( $n \sim 1.4$ ) and the air filling ( $n = 1$ ) which leads to strong reflection and refraction and decreased imaging depth. In this study assessing the potential of different imaging technologies, the alveoli were fluid-filled to minimize refraction artifacts. Sections 3.3.1 and 3.3.2 show the difference in images of fluid- *versus* air-filled alveoli and investigate the effects on image quality and imaging depth.

### Spatial resolution

a. Transverse resolution:

FDOCT, SECM, and FFOCM achieve high lateral resolution (along  $x$  and  $y$ ) by focusing the light to a small spot with an objective lens. The angle with which the light focuses upon the sample is an important parameter and can be expressed as the numerical aperture (NA):

$$NA = n \cdot \sin \phi \quad (3.1)$$

where  $n$  is the refractive index of the medium between the lens and the focal spot and  $\phi$  is the half-angle of the light cone (Figure 20).<sup>1</sup>

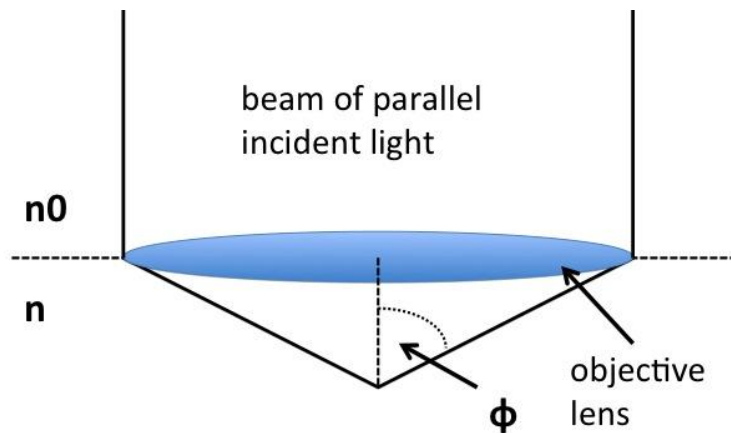


**Figure 20: Schematic illustrating the definition of the numerical aperture ( $NA = n \cdot \sin \phi$ ).  $n$  is the refractive index of the medium between the lens and the focal spot, which may be the same or different compared to the surrounding ( $n_0$ ).  $\phi$  is the half-angle of the cone of light.**

The NA and the wavelength of light ( $\lambda$ ) determine the maximum possible (diffraction limited) resolution:

$$\delta x = k \frac{\lambda}{NA} \quad (3.2)$$

where  $k$  is a constant factor that varies slightly between systems. For example, the lateral resolution in the tested FFOCM system can be compared to that of a conventional microscope with  $k = 0.61$  (72). Both the SECM and FDOCT systems use single mode fibers and can with respect to lateral resolution be

---

<sup>1</sup> Note that the geometric maximum of the NA is reached with  $\phi = 90^\circ$ , corresponding to an  $NA < 1$  for air-,  $NA < 1.3$  for water-, and  $NA < 1.5$  for oil immersion.

considered confocal systems with pinholes the size of the fiber core. Using a pinhole for illumination and detection,  $k$  can theoretically be reduced to a value of 0.44 (72). When computing diffraction-limited resolution, however, it should be kept in mind that this equation contains several simplifying assumptions. In reality, the pinhole size in a confocal system is not infinitely small,  $\lambda$  is not constant when using a broadband source, and the sample itself alters parameters such as the NA with increasing light penetration, to name just a few. In the case of a broadband source, the center wavelength  $\lambda_c$  is often assumed to compute approximate resolution. Although diffraction-limited resolution measurements are often smaller than what is experimentally observed (generally within a factor of 2), it becomes clear that in order to achieve small values (high lateral resolution), a larger NA and a shorter wavelength are preferred.

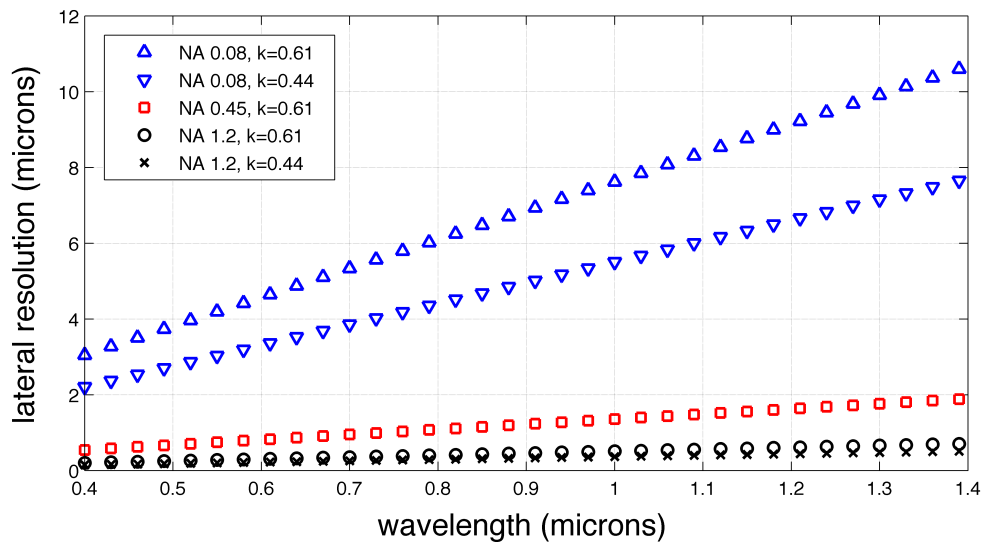


**Figure 21: Overview of the influence of NA,  $k$  and  $\lambda$  on the theoretical lateral resolution.**

In the present case, the FFOCM system ( $\lambda_c = 0.6 \mu\text{m}$ ,  $\text{NA} = 0.45$ ) could provide a diffraction-limited transverse resolution down to  $0.8 \mu\text{m}$ , the SECM system ( $\lambda_c = 1.32 \mu\text{m}$ ,  $\text{NA} = 1.2$ ) down to  $0.5 \mu\text{m}$ , and the FDOCT system ( $\lambda_c = 1.31 \mu\text{m}$ ,  $\text{NA} = 0.08$ ) down to  $7 \mu\text{m}$ . Note the large influence of the NA and that FDOCT could achieve the same high transverse resolution as SECM if a similar objective lens was used. However, higher NAs entrain also a decreased depth of focus as discussed in detail in subsection 3.3.2, which can limit the

imaging depth in FDOCT and is therefore not beneficial for most applications. In general, the NA should be optimized for a specific application. Lower NA objective lenses provide larger, more convenient working distances. In SECM, usage of a lower NA lens would lower the transverse resolution, but would decrease image acquisition time for a given field of view as less of the larger focal points would need to be acquired to cover the field of view. Figure 21 provides an overview of the influence of the parameters  $k$ , NA and  $\lambda$  on the diffraction-limited transverse resolution values.

In the presented SECM system, two additional parameters must be considered when calculating the transverse resolution along the spectrally encoded line ( $x$ ).<sup>2</sup> The best achievable resolution will be the larger of: the previously described optical resolution, the linewidth of the wavelength-swept source, and the spectral resolution provided by the diffraction grating. In an optimized system, the spectral resolutions of the light source and grating should approximately match the optical resolution. The utilized light source provided a less than 0.1 nm line width, which is much smaller than the optical resolution. The spectral resolution of the grating can be calculated for the first diffraction order as:

$$\delta\lambda_G = \frac{\lambda_c \cdot \Lambda}{D} \quad (3.3)$$

where  $\lambda_c$  is the center wavelength of the source,  $\Lambda$  is the period of the diffraction grating often given as the reciprocal of the number of lines per mm, and  $D$  is the beam diameter incident on the grating (73). In order to provide high spectral resolution, a narrow line-width source, small wavelength, high groove-density grating, and large beam diameter are all beneficial. In the utilized system ( $\lambda_c = 1.32 \mu\text{m}$ ,  $\Lambda = 0.91 \mu\text{m}$ ,  $D = 12 \text{ mm}$  (80)) the spectral resolution provided by the grating was 0.1 nm, again much smaller than the optical resolution.

---

<sup>2</sup> Similar discussions apply to any transverse scanning or sampling mechanism that extends a point image to a 1D or 2D image. This discussion is omitted to keep the focus on the most fundamental concepts limiting lateral resolution.

### b. Axial resolution

In SECM (current implementation), the axial resolution and optical sectioning capability can be calculated exactly analogous to a conventional confocal microscope. The ability to resolve two points in the axial direction is the larger of the axial resolution and optical sectioning, both of which are inversely proportional to  $NA^2$ , with the constants  $c \sim 1.52$  and  $c \sim 1.36$ , respectively (72):

$$\delta z_{confocal} = c \frac{n\lambda}{NA^2} \quad (3.4)$$

Again, higher NAs and shorter wavelengths are able to resolve smaller structures. It is important to note, that the numerical aperture of the objective lens governs both the transverse ( $x, y$ ) and the axial ( $z$ ) resolution in conventional SECM. Hence, one cannot be modified without the other. Further, while the lateral resolution is inversely proportional to the NA (equation (3.2)), the axial resolution is inversely proportional to the squared NA (equation (3.4)). Using higher numerical aperture lenses then results in a faster improvement in axial resolution compared to lateral resolution. In the utilized system ( $\lambda_c = 1.32 \mu\text{m}$ ,  $NA = 1.2$ ), the theoretical resolution is  $1.8 \mu\text{m}$  in water ( $n = 1.3$ ).

In swept-source FDOCT, the axial resolution is mainly determined by the coherence length of the system and can be calculated according to (70):

$$\delta z_{OCT} = \frac{2 \ln 2}{\pi} \frac{\lambda_c^2}{n \Delta \lambda} \quad (3.5)$$

where  $\Delta \lambda$  is the full width at half maximum (FWHM) of the spectral envelope (tuning range), and  $n$  is the group refractive index of the sample. The ratio  $\lambda_c^2/\Delta \lambda$  is of central importance. Better axial resolution can be obtained with larger bandwidth sources or imaging with shorter wavelengths. In the presented FDOCT system ( $\lambda_c = 1.31 \mu\text{m}$ ,  $\Delta \lambda = 0.11 \mu\text{m}$ ), the diffraction-limited axial resolution in water ( $n = 1.3$ ) is  $5.3 \mu\text{m}$ . In this equation, the NA of the focusing lens has no influence on the axial resolution, thereby decoupling the lateral and axial resolution (71), such that one can be adjusted without modifying the other. However, using high NAs could further improve the axial resolution. The combined effect may be approximated according to (81):

$$\delta z = \left[ \frac{2n(1 - \cos\phi)}{\lambda} + \frac{n\pi}{2 \ln 2} \frac{\Delta\lambda}{\lambda_c^2} \right]^{-1} \quad (3.6)$$

Figure 22 shows the influence of the coherence and the aperture effects in a sample of refractive index 1.3 and confirms that for the 0.08 NA of the FDOCT system, the axial resolution is governed by the coherence effect alone.

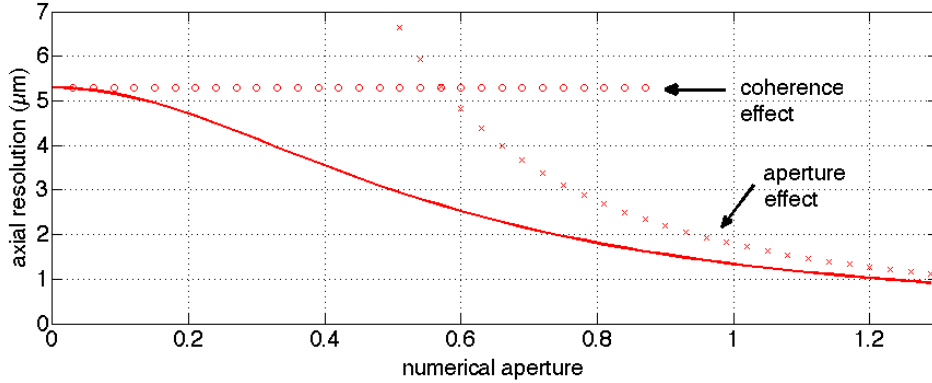


**Figure 22:** Graph showing the influence of high NAs on the axial resolution in coherent imaging systems. The solid line shows the NA dependence of the axial resolution for a system with bandwidth  $0.11 \mu\text{m}$  centered at  $1.31 \mu\text{m}$  and a medium of refractive index  $n = 1.3$ , the dotted lines delineate the coherence and aperture effects [recalculated according to (81)].

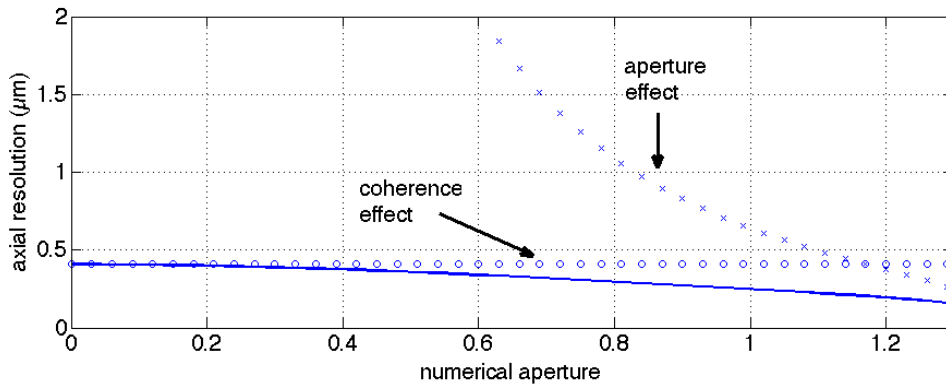


**Figure 23:** Graph showing the axial resolution of the FFOCM system. The solid line shows the NA dependence for the system with bandwidth  $0.3 \mu\text{m}$  centered at  $0.6 \mu\text{m}$  and a medium of refractive index  $n = 1.3$ , the dotted lines delineate the coherence and aperture effects.

The axial resolution in FFOCM is governed by the same principles as in FDOCT and is proportional to  $\lambda_c^2/\Delta\lambda$ . For the source-detector combination used in this setup, the center wavelength  $\lambda_c$  is approximately  $0.6 \mu\text{m}$  (or a

factor of  $\frac{1}{2}$  compared to the FDOCT system) with a spectral bandwidth  $\Delta\lambda \sim 0.3\mu\text{m}$  (or a factor of 3 compared to the FDOCT system). The ratio  $\lambda_c^2/\Delta\lambda$  of the FFOCM system is therefore about 12 times smaller than that of the FDOCT system and the theoretical axial resolution of FFOCM is  $0.4\mu\text{m}$ . Figure 23 illustrates graphically that ultra-high resolution can be achieved even at moderate numerical apertures because of the very short coherence length. This advantage enables imaging at isotropic high resolution similar to FDOCT and contrary to confocal systems.

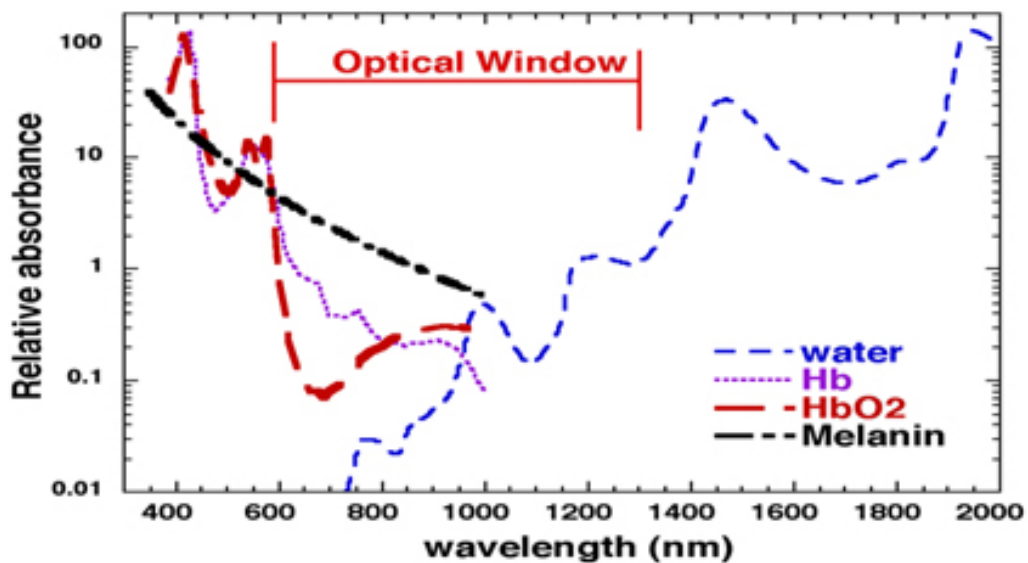


Figure 24: Tissue optical window. Hb: Hemoglobin. HbO2: Oxygenated hemoglobin. [Reproduced from (82).]

### c. Summary

The spatial resolution of an imaging system is key to determine which research question can be answered by the technique. One component of central importance influencing both transverse and axial resolution in optical imaging is the wavelength of light, where shorter wavelengths can achieve higher resolution. However, other factors may also influence the wavelength choice including the optical properties of the tissue and the price and availability of light sources and detectors. For example, wavelengths in the visible and near infrared are chosen because of the low water and blood absorption in this optical window (600 – 1300 nm) (Figure 24). Within this window, longer wavelengths experience less scattering and may lead to increased imaging depth as illustrated in Figure 25. It is interesting to consider what an optimal

wavelength in the case of alveolar imaging could be. One application of optical imaging of the peripheral lung could be to provide structural information about a maximum number of layers of water-filled alveoli beneath the pleura. In this example, penetration depth could be more important than spatial resolution, and choosing a relatively long wavelength in the near-infrared could be beneficial. If however, a research question requires air-filled alveoli, the penetration depth is not influenced by the wavelength choice, but is significantly reduced due to intrinsic refraction effects occurring at the tissue-air interfaces (56, 83). In such a case, one might choose a relatively short wavelength to benefit maximally from the higher resolution. Alternatively, a completely different wavelength window could be considered, such as wavelengths around  $2.8 \mu\text{m}$ , where the refractive index of water (as an approximate for the refractive index of lung tissue) decreases to a value close to 1.14 (84) to better match the refractive index of air. Note, that this imaginary solution is stated as an example, and the particular approach would be accompanied by an increase in the absorption of light limiting the imaging depth to around  $10 \mu\text{m}$  (84).

A second important factor influencing spatial resolution is the numerical aperture of the imaging lens, with higher NAs providing improved resolution. In SECM, the NA governs both the lateral and axial resolutions, where the lateral resolution is inversely proportional to NA and the axial resolution inversely proportional to  $\text{NA}^2$ . In FDOCT and FFOCM, the axial resolution is primarily determined by the coherence length of the source and is somewhat uncoupled from the lateral resolution. In FFOCM, this independence is used to provide isotropic, ultra-high spatial resolution. In FDOCT, the spatial resolution can also be isotropic, but poorer lateral resolution will generally be chosen to allow larger depths of field. The relationship between the lateral resolution and the depth of focus as well as the imaging depth will be discussed in detail in subsection 3.3.2. It will also become apparent that for the particular application of imaging air-filled pulmonary alveoli, the intrinsic optical properties of the tissue-air interfaces are again the primary factor limiting the useful imaging depth, such that high numerical aperture imaging ( $\sim 0.2$ ) may be

beneficial to allow maximum spatial resolution at the intrinsically limited imaging depth.

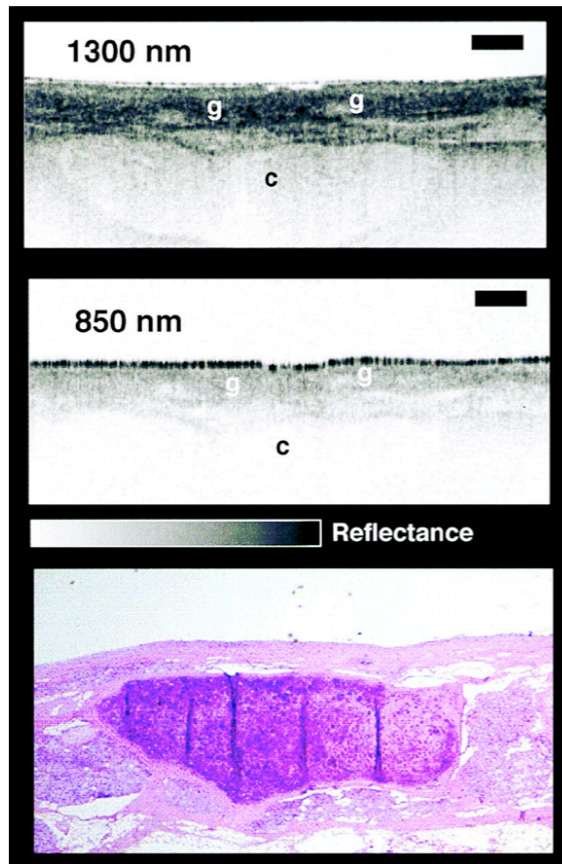


**Figure 25: OCT images of human epiglottis *ex vivo* performed at 850 and 1300 nm illustrating the influence of wavelength on imaging depth. Longer wavelengths are less attenuated by scattering and allow better visualization of the cartilage (c) in this image. Scale bar = 500  $\mu\text{m}$ . [Reproduced from (85).]**

### **Temporal resolution**

Temporal resolution is often defined as the number of frames acquired per unit time. However, the size of the frame has a major influence on the speed at which a frame can be recorded. And in order to acquire three-dimensional images, a scanning mechanism is generally required that further influences the volume acquisition rate in a variety of ways. The temporal resolution must therefore be discussed with respect to the acquired field of view (FOV) and proper sampling.

#### **a. Swept-source FDOCT**

In swept-source FDOCT, the three-dimensional field of view is limited by the imaging depth in the axial direction and by the scanning mechanisms in the

transverse directions. If adequately fast data acquisition and infinitely fast transverse scanning is assumed, then the imaging speed is limited by the speed of the wavelength-swept laser source.

One sweep of the light source represents the range of colors that are focused to approximately the same spot within the sample to provide a 1D image (A-line) along the axial direction ( $z$ ) (Figure 26). The length of the line image can be considered in two different ways. First, the length of the line image of the tissue of interest is in practice generally dependent on the optical properties (absorption and scattering) of the sample. A typical imaging depth for FDOCT systems in isotropic biological tissues is 1 – 2 mm. The specifics about the penetration depth in peripheral lung tissue will be investigated in detail in subsections 3.3.1 and 3.3.2. Secondly, the maximum possible length of the line image in the absence of any tissue sample, namely the ranging depth, depends on the instantaneous line width  $\delta\lambda$  of the source (70):

$$z_{\max} = \frac{\lambda_c^2}{4n \cdot \delta\lambda} \quad (3.7)$$

For the source used throughout this work with  $\delta\lambda \sim 0.06\text{nm}$ , the ranging depth in water is approximately 5 mm. For maximum ranging depth, longer wavelengths and smaller line widths are beneficial, but typically the ranging depth need not be larger than the coherence length of the laser. Note, that the 5 mm ranging depth may seem oversized compared to the 1-2 mm of imaging depth expected in biological tissues. However, large ranging depths may be crucial for imaging tissues with large surface-height variations.

In order to obtain three-dimensional data sets, the axial line must be scanned in the transverse directions  $x$  and  $y$  (Figure 27). The maximum possible *en-face* field of view is then only limited by the scanning mechanism and any potentially induced aberrations. Using a galvanometer-scanning setup and large enough objective lens, a 2 x 2 mm field of view can easily be scanned. The used swept-source currently operates at 62.5 kHz, providing 62,500 full wavelength sweeps per second. A 512 x 512 pixel *en-face* FOV could therefore be scanned in  $(512^2 / 62.5 \cdot 10^3)$  4.19 seconds and a 256 x 256 pixel FOV could be scanned in 1.05 seconds. At a transverse pixel size of 3.9 microns, the acquired and properly sampled volume (pixel size smaller than half the

diffraction-limited resolution) in 4 and 1 second could be 2 x 2 x 1 mm or 1 x 1 x 1 mm, respectively.

This temporal resolution could be considered fast in comparison to other optical technologies or to the breathing frequency of a human (~ 12 breaths/min or 0.2 breaths/sec at rest). However, it could be considered too slow compared to human cardiac motion (~1 beat/sec at rest). The temporal resolution of FDOCT could be increased substantially with the development of new light sources. For example, wavelength-swept sources are now available in the MHz range (86).

#### b. SECM

The presented SECM system also uses a wavelength-swept source, but in contrast to FDOCT, each of the different colors of one sweep focuses to a distinct location in the sample along a 1D transverse line image along  $x$  during the time required to sweep through the bandwidth (Figure 26). The length of the line is dependent on the grating-lens combination and also on the width of the spectral envelope and line width of the source. For example, a 70 nm bandwidth source with 0.1 nm line width could provide the acquisition of (70 / 0.1) 700 pixels along the spectrally encoded line, dependent on the grating/lens resolution. If sampled at 2 pixels per optical resolution, the length of the spectrally encoded line image could be (700 / 2 \* 0.5  $\mu\text{m}$ ) 125  $\mu\text{m}$ . In applications where the spatial resolution may be degraded in favor of large fields of view at constant temporal resolution, the 700 pixels provided by the source could be spread further apart. The maximum 1D FOV is then determined by  $\Delta\theta$ , the maximum angular deviation between the wavelength extremities diffracted from the grating (73) and the focal length of the lens ( $f$ ) because the dispersive grating must be positioned within the pupil plane of the objective:

$$FOV = 2f \tan\left(\frac{\Delta\theta}{2}\right) \quad (3.8)$$

In order to increase the FOV without sacrificing resolution, the number of pixels provided by the source can be increased with larger band-width sources with decreased line widths.

Three-dimensional data sets are acquired by scanning along  $y$  and  $z$  and also along  $x$  to increase the FOV further in the spectrally-encoded direction (Figure 27). This specific transverse scanning pattern (in  $x$  and  $y$ ) to increase the field of view beyond the limitation of the system is often referred to as mosaicing. Scanning can be achieved by displacing either the sample or the beam horizontally and vertically. Mechanical scanning in the axial direction is typically slower than in the transverse direction, because scanning is performed in discrete steps placing high demands on the accuracy of the step size. Further complicating the precision of the scan is a setup as presented here, where heavy components have to be translated such as the objective lens together with the precisely aligned and spaced telescope lenses, grating, beam splitter and collimators. In the present system, the sample was displaced using motorized stages with a fast motor along  $y$  and slower motors along  $x$  and  $z$ , which were the primary limitations to the overall acquisition time of the tissue volume. It is difficult to directly compare the imaging speeds of FDOCT and SECM due to the different scanning patterns and system components. The systems used in this study, for example, differed by the NA of the lenses and the speeds of the wavelength-swept sources. The higher NA lens used in SECM compared to FDOCT results in a shorter working distance, which intrinsically limits imaging depth compared to FDOCT and hinders the comparison of the three-dimensional fields of view provided by the two techniques. At the same time, the spatial resolution is thereby improved in SECM, as previously discussed. Nevertheless, in an attempt to compare the acquisition time of SECM to FDOCT, it can be imagined that a tissue volume of  $2 \times 2 \times 1$  mm must be acquired and the time for mechanical scanning is neglected, such that the imaging time per volume depends solely on the wavelength-swept source and the required spatial resolution. Then, assuming the same swept-source speed as in the FDOCT system, this volume could be acquired using SECM in 32 minutes with a slightly oversampled resolution of  $1.3 \mu\text{m}$ . 16 spectrally encoded lines along  $x$  would need to be assembled ( $2 \text{ mm} / 0.5 \mu\text{m}$ ) and that 4000 times along  $y$  to create a large-field SECM image. Along  $z$ , ( $1 \text{ mm} / 0.9 \mu\text{m}$ ) 1111 of those large-field images would hypothetically need to be acquired for optimal axial resolution. It is important

to emphasize again, that the size of the volume was chosen to provide a direct comparison to the previously mentioned FDOCT example. In the presented SECM images of fixed rat lung tissue, one large-field SECM image was acquired every  $5\ \mu\text{m}$  in the depth direction to approximate the axial resolution of standard histology, where typically one slice is cut every  $5\ \mu\text{m}$ . Further, images were acquired down to a maximum depth of  $200\ \mu\text{m}$  from the surface of the sample, because the contrast was no longer sufficient at this depth.

In summary, SECM encodes several hundred-image points in a spectrally encoded line and is significantly faster than conventional confocal microscopy. SECM technically provides the same number of 1D and 2D image acquisitions per unit time as swept-source FDOCT. However, because of the high resolution and the need for vertical scanning in particular, the acquisition of a similar sized volume is significantly longer compared to FDOCT.

### c. FFOCM

FFOCM captures a complete two-dimensional *en-face* image (full field) of the tissue sample much like a conventional microscope (Figure 26). In addition, however, the low-coherent light allows optical sectioning. Therefore, the reference arm is axially modulated and depending on the phase demodulation algorithm, at least 4 images are usually acquired to obtain one optical section at a fixed depth in the tissue (81). However, the main factor limiting the imaging speed of FFOCM is not intrinsic to the technology, but mainly governed by the limited full-well capacity of current CCD cameras resulting in low sensitivity of each optical section. To achieve reasonable signal-to-noise ratio (SNR), each optical section is acquired tens to hundreds of times and the resultant image is then the average of the acquired sections. In the presented system, one *en-face* image is the result of  $4 \times 100$  acquisitions while the reference arm continually translates between all 400 acquisitions. The *en-face* field of view is generally determined by the size of the image of the multimode-fiber core on the sample. Sensitivity and acquisition time can be improved by binning pixels at the detector, but this comes at the cost of worse resolution and/or smaller field of view. The future development of more sensitive cameras could in principle eliminate the need for averaging the optical sections and significantly increase the imaging speed of the technology.

Three-dimensional data sets are acquired by scanning the sample along the z-axis (Figure 27). In the utilized setup, the sample must be translated, because the focal plane of the objective lens has to match the coherence gate with the reference arm, which increases the complexity of translating the objective with respect to the sample.

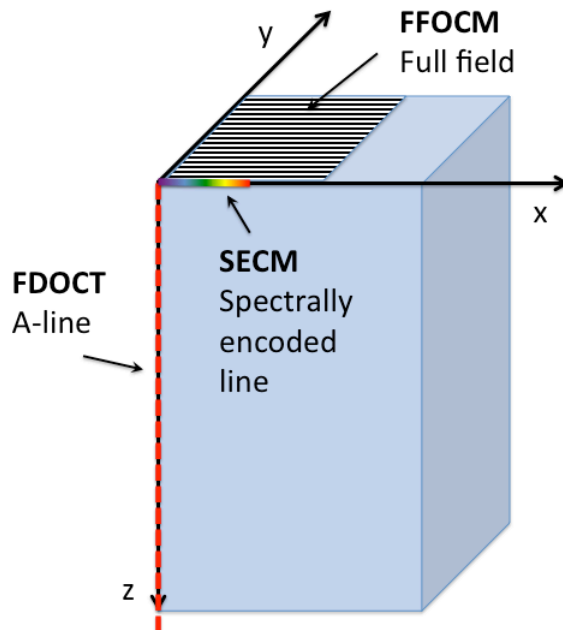


**Figure 26: Cartoon of a rectangular tissue volume illustrating the orientation of the basic 1-D and 2-D images created by FDOCT, SECM, and FFOCM.**

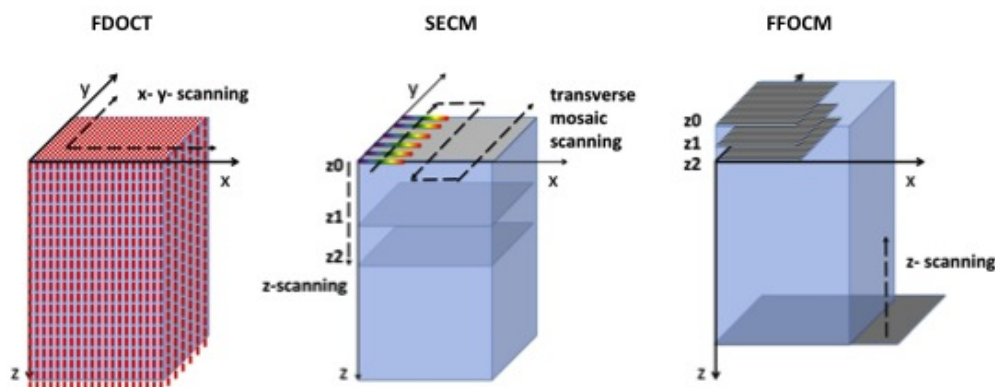


**Figure 27: Cartoon illustrating the mechanisms of scanning to acquire 3-D datasets with FDOCT, SECM, and FFOCM.**

#### d. Summary

Temporal resolution is always dependent on the desired spatial resolution (to provide proper sampling) and/or the three-dimensional field of view. Imaging large volumes with swept-source FDOCT is fast compared to SECM and

FFOCM, because it does not require axial scanning but also provides comparably lower spatial resolution. The acquisition time of swept-source FDOCT and SECM is expected to further increase with the development of new and faster light sources. FFOCM is currently mainly limited by the sensitivity of available detectors.

### **Miniaturized probe design**

Optical imaging requires direct access to the region of interest, which is generally achieved through miniaturized endoscopic probes. The size of the probe is primarily determined by the optical components required for focusing and scanning the light source. Subsection 3.2.3 discusses the current stage of development in detail, while some of the fundamental differences between the techniques are noted here.

FDOCT has the great advantage that depth scanning can be achieved optically outside of the body. Transverse scanning in a tube-like structure can, for example, be performed distally, through a rotating pullback of the probe to create a helical image (87). And FDOCT has the further advantage, that it can utilize small, low numerical aperture lenses.

SECM also scans one dimension of the image optically. However, the technique requires a diffraction grating, which is currently not commercially available at miniature sizes, and a high NA lens. Depth scanning presents a major challenge, but one solution could be a tilted focus as recently described (75). Lastly, because of the tight focus in depth, tissue surface irregularities and movement may require adaptive focusing to provide a larger usable imaging depth, which would introduce more complexity in the probe design (75).

The main disadvantage of FFOCM for *in-vivo* endoscopic imaging may not be related to size, but to stability and signal-to-noise ratio. FFOCM scans two dimensions of the image optically. However, depth scanning is difficult, because the optics, focal length and coherence gate must be precisely matched between the reference and sample arm for the best available spatial resolution. Common path FFOCM reduces aberrations and simplifies the alignment of the reference and sample arms, but is limited in sensitivity (88). One solution could be to use a second external interferometer to select the imaging location

in the sample while compromising lateral resolution in favor of imaging depth (89).

### 3.2.3 Evaluation of FDOCT, SECM, and FFOCM for imaging fixed, fluid-immersed peripheral rat lung tissue

This subsection presents the results of a comparative study between FDOCT, SECM, and FFOCM for imaging fixed, PBS-immersed peripheral rat lung tissue (55). First, FDOCT and SECM images were acquired with a 200  $\mu\text{m}$  thick cover glass between the sample and the focusing optics, and then the cover glass was removed and the sample was imaged with FFOCM. Images from all techniques were compared to each other and to the corresponding histology. Spatial and temporal resolution, imaging depth, and suitability for *in-vivo* probe development were compared to highlight the merits and limitations of each technology for studying respiratory physiology at the alveolar level. The rat lung parenchyma was chosen as a good representation of mammalian lung parenchyma tissue and because it is a popular animal model for pulmonary diseases due to its low price and convenient size for experimental manipulation. (45-47, 90).

#### Fourier domain optical coherence tomography (FDOCT)

Figure 28(a) shows a typical cross-sectional FDOCT image of a fixed, PBS-immersed rat lung slice, where the alveoli appear as dark gaps within the highly scattering tissue under the cover glass. Figure 28(b) shows the orthogonal *en-face* image from the sample with the corresponding H&E histology section shown in Figure 28(c). Single alveoli can be easily distinguished within the FDOCT images up to a depth of approximately 500  $\mu\text{m}$  and the presence of the fixed blood vessels (marked with a V) does not appear to decrease the overall imaging depth significantly. The alveolar wall thickness appears overestimated ( $25 \pm 6 \mu\text{m}$  full width at half maximum (FWHM), mean  $\pm$  standard deviation,  $n = 31$ ) compared to the generally accepted and histologically shown wall thickness of a rat alveolus (7-10  $\mu\text{m}$ ).

It is important to note, that in some histology slides, the structures appear to be distorted or reduced in size compared, which may have been caused by histologic tissue processing required to obtain the hematoxylin and eosin

(H&E) stained slides. Although best efforts were made to ensure that the FDOCT image and H&E section were parallel, there is likely some tilt in the H&E image *versus* the optical image due to the embedding and sectioning process. This was seen for all direct comparisons of optical to histology images.

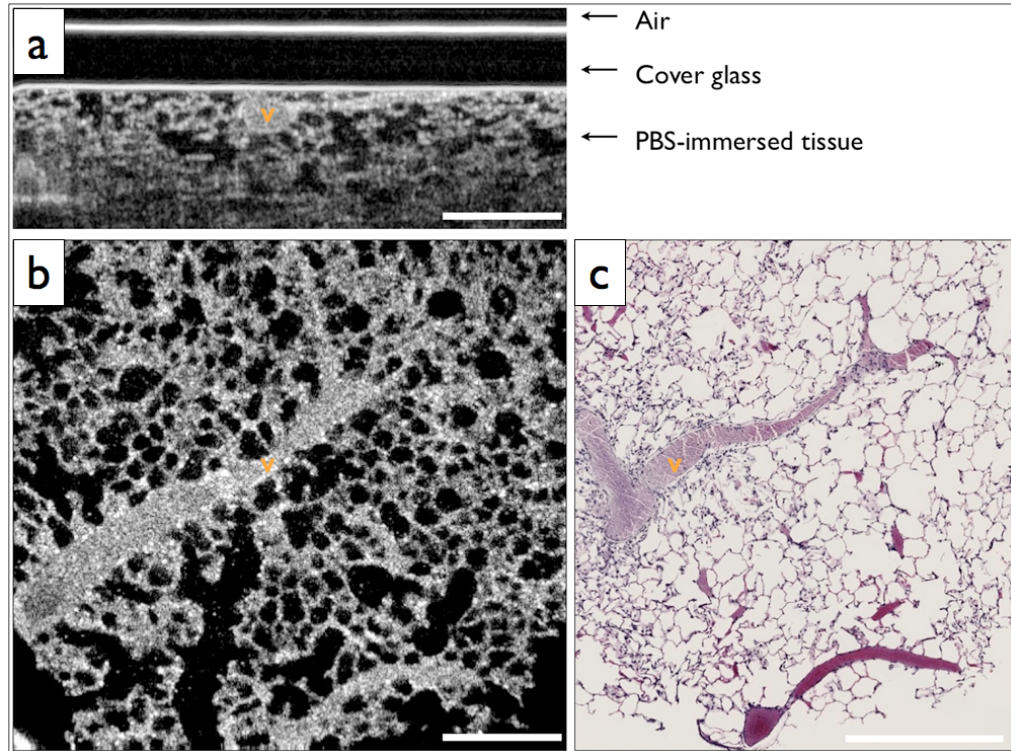


**Figure 28: FDOCT and H&E histology images of PBS-immersed fixed rat lung slice. (a) Axial cross-section and (b) *en-face* FDOCT image at a depth of about 100  $\mu\text{m}$ . (c) Corresponding H&E histology sectioned in *en-face* plane. V indicates a vessel within the tissue. Scale bars, 500  $\mu\text{m}$ .**

### Spectrally encoded confocal microscopy (SECM)

Figure 29(a) shows a wide-field *en-face* SECM image with the corresponding H&E histology (Figure 29(b)) for a rat lung slice approximately 70  $\mu\text{m}$  in depth from the top surface of the slice. The wide-field SECM image demonstrates the ability to visualize relatively large fields of view with cellular-level detail. Figure 29(c)-(d) show a zoomed-in region of a SECM image with corresponding histology to demonstrate how the airway epithelium, vessel endothelium and blood, and aggregations of cell nuclei can be characterized by bright SECM signal. Type II alveolar pneumocytes (arrows) were directly matched between SECM and histology.

The maximum imaging depth was dependent on the structure. Blood-filled vessels and the surrounding collagen matrix provide high contrast up to 150  $\mu\text{m}$  into the specimen, but alveolar walls were difficult to identify for imaging depths greater than 100  $\mu\text{m}$ . 30 randomly chosen alveolar walls were measured with a FWHM thickness of  $5.5 \pm 6.1 \mu\text{m}$  (mean  $\pm$  standard deviation).

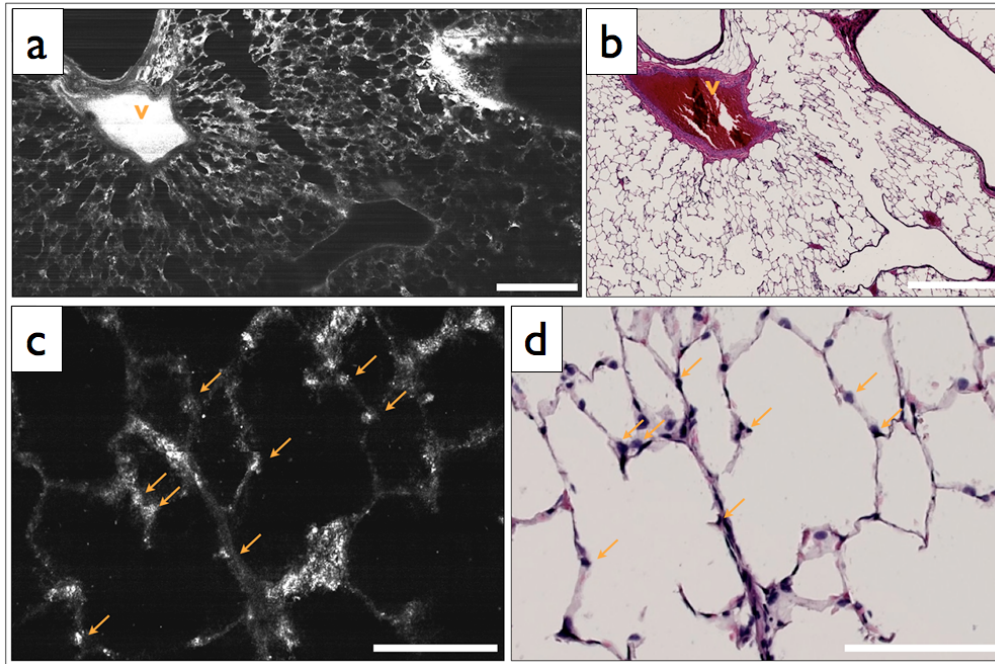


**Figure 29: SECM and H&E histology images of PBS-immersed fixed rat lung slice. (a) *En-face* SECM image 70  $\mu\text{m}$  within tissue and (b) corresponding H&E histology, where V indicates a vessel and scale bar = 500  $\mu\text{m}$ . (c) SECM image in greater detail and (d) corresponding H&E histology, where arrows indicate alveolar type II pneumocytes and scale bar = 100  $\mu\text{m}$ .**

### Full field optical coherence microscopy (FFOCM)

Figure 30(a)-(c) shows images obtained from a rat lung slice with FFOCM from all three spatial planes, with H&E histology from the same sample in Figure 30(d). The alveolar walls can be clearly delineated and the capillary network inside the walls was visible as non-scattering media surrounded by the scattering endothelium (arrows). Cells that are likely to be type II alveolar pneumocytes (stars) are characterized as highly scattering with a relatively large size and shape compared to what would be expected for type I pneumocytes. However, individual type I pneumocytes could not be clearly identified. Blood vessels (V) were identified and their endothelium was

distinguished from the blood content due to high scattering from the nuclei of the endothelial cells. Blood cells could also be visualized with a crenated appearance, likely due to the fixation process. The maximum imaging depth reached beyond 250  $\mu\text{m}$  when imaging through the PBS-immersed airspaces, but the strong blood attenuation limited the imaging depth to less than 50  $\mu\text{m}$  when imaging through blood filled vessels. 30 randomly chosen alveolar walls were measured with a FWHM thickness of  $4.8 \pm 3.3 \mu\text{m}$  (mean  $\pm$  standard deviation).

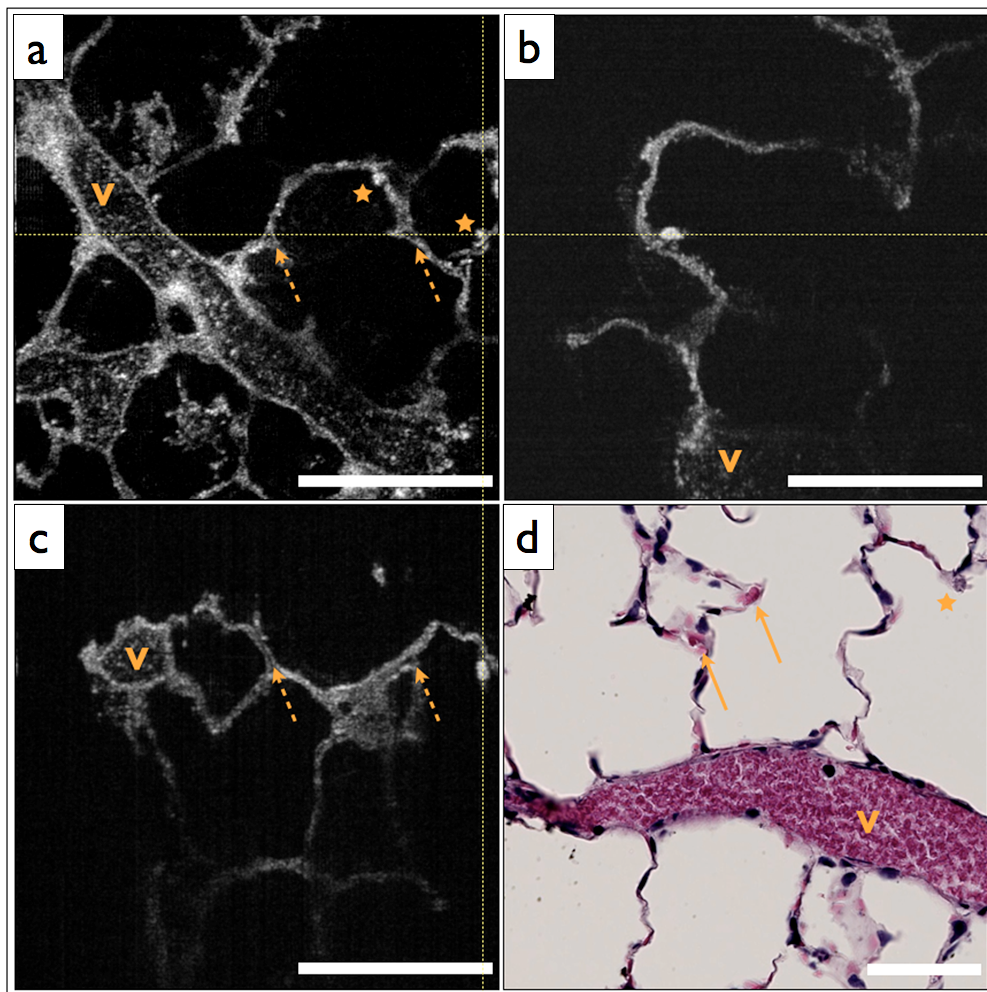


**Figure 30:** FFOCM and H&E histology images of PBS-immersed fixed rat lung slice. (a) *En-face*, (b) axial cross-section, and (c) orthogonal axial cross-section images obtained with FFOCM, where dotted lines show the orientation of axial cross-sections intersecting at a three-dimensional type II pneumocyte. (d) Representative H&E histology slide from nearby location sectioned in *en-face* plane. Stars indicate alveolar type II pneumocytes, V indicates a blood vessel containing crenated blood cells, and dotted arrows indicate capillaries in alveolar walls. Scale bars = 100  $\mu\text{m}$ .

### Comparison of imaging techniques

Figure 31 compares images from all three reflectance-imaging techniques of a fixed PBS-immersed rat lung slice acquired within the same field of view. Figure 31 (a)-(c) show *en-face* FDOCT and SECM sections with the corresponding histology, and Figure 31 (d)-(f) show zoomed-in regions of the FDOCT and SECM images that correspond to the FFOCM field of view. These images illustrate the difference in resolution and expected image quality between the techniques. Table 2 summarizes the performance of FDOCT, SECM, and FFOCM for imaging PBS-immersed, fixed rat lung tissue slices, as described below.

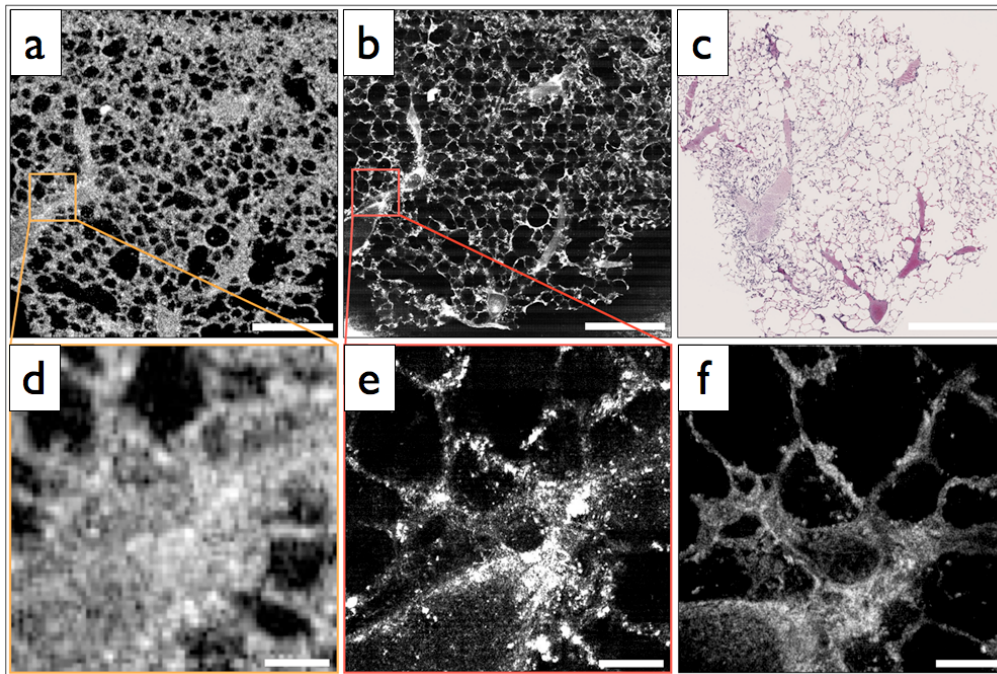


**Figure 31:** FDOCT, SECM, FFOCM and H&E histology images of PBS immersed fixed rat lung slice. (a) FDOCT, (b) SECM, and (c) H&E histology within the *en-face* plane, where scale bar = 500  $\mu\text{m}$ . (d) FDOCT and (e) SECM images in greater detail matched with (f) FFOCM image, where scale bar = 50  $\mu\text{m}$ .

FDOCT provided high frame rates and the largest imaging depth for the specific systems used in this study. The lower transverse resolution of the system resulted in images with thicker alveolar walls, but the majority of the airspaces and vessels were still discernable within the rat lung samples. FDOCT might therefore provide the most practical option for evaluating

alveoli over a relatively large tissue volume. The high acquisition speed may also enable alveolar imaging where motion artifacts hinder current three-dimensional technologies such as micro-CT. FDOCT imaging has already been performed during bronchoscopy and visualized intact alveolar attachments to the small airways (91). As catheters become smaller, more regions surrounding thin walled airways could be reached in a minimally invasive way that limits any changes to the alveolar environment. Currently, 0.8 mm diameter optical catheters are used in the clinical setting to assess coronary arteries (92). However, bronchoscopic access limits the analysis to alveolar features immediately surrounding the airways.

**Table 3: Summary of performance criteria for current FDOCT, SECM, and FFOCM systems to image PBS-immersed rat lung tissue.**

Performance criteria	FDOCT	SECM	FFOCM
Visualized structures	Alveolar walls Blood vessels	Alveolar walls Blood vessels Type II pneumocyte	Alveolar walls Blood vessels Type II pneumocyte Capillaries Crenated erythrocytes
Primary advantage	Imaging speed Imaging depth	High transverse resolution Potential for high imaging speed	High isotropic resolution
Primary disadvantage	Lower spatial resolution	Imaging depth	Imaging speed
Imaging probes	Miniaturized catheter (0.8 mm) and needle probes	Hand held probes at 10 mm diameter	Currently no miniaturized probe

Subpleural alveoli could be evaluated in an open-chest procedure or through an optical window as previously demonstrated in a rabbit model by Meissner et al. (93) or in a swine model by Namati et al. (54). In addition to requiring mechanical ventilation, this route of access currently removes any local effect the chest wall has on the alveolar environment. Lastly, FDOCT-based needle

probes have also been demonstrated (69, 94), (95) to provide access to lung parenchyma that cannot be visualized through the airways or the pleura with optical imaging techniques. However, this route of access comes at the cost of local trauma to the tissue and the possibility of pneumothorax as well as drag artifacts caused by needle movement.

SECM provided much higher resolutions in the lateral ( $1.3 \mu\text{m}$ ), and axial direction ( $2.4 \mu\text{m}$ ) than FDOCT and could visualize type II pneumocytes. The high resolution of SECM could also provide absolute measurements of alveolar wall thickness and identification of inflammatory cells. The usable imaging depth with the current system configuration was  $100 - 150 \mu\text{m}$ , which was the lowest of the three techniques. The potential of SECM for imaging at high speeds may facilitate the acquisition of large fields of view and dynamic imaging, but miniature probes are not currently available. Forward-scanning and helical-scanning probes have been demonstrated at diameters of  $10 \text{ mm}$  (75, 96, 97) with the promise of further reduction of the probe diameter down to  $5 \text{ mm}$  (97). At this development stage, only imaging through a pleural window or an open chest procedure seems possible (98). To enable endoscopic imaging, probe diameters  $\leq 1 \text{ mm}$  would be most practical, allowing the probe to be inserted into the working channel of any adult bronchoscope and reach later generations with thinner airway walls. Confocal fluorescence microscopy has been demonstrated for *in-vivo* alveolar imaging through a bronchoscope and *via* penetration through the distal bronchiolar wall (99). A confocal imaging probe inserted within a 22-gauge needle has also recently been developed for biological tissue (100).

FFOCM provided the best spatial resolution of all three techniques and would be best suited to evaluate absolute alveolar wall thickness in different species and pathophysiologic changes such as wall thickening or inflammatory cell recruitment. The  $1\text{-}\mu\text{m}$  isotropic resolution of FFOCM provides the ability to analyze three-dimensional structures down to a few micrometers, which could potentially be useful for identifying and characterizing individual cells such as alveolar type I or II, macrophages or eosinophils. FFOCM currently provides the slowest acquisition speed of the three imaging systems, however, and the development of miniaturized probes for both *in-vivo* and *ex-vivo* imaging is

still at an early stage. A miniaturized 2 mm diameter probe has recently been demonstrated with a resolution of 3.5  $\mu\text{m}$  and 1.8  $\mu\text{m}$  in the lateral and axial directions, respectively (89). High-speed full-field (that is parallel) acquisition of OCT images, however, has been demonstrated with up to 1.5 million A-lines/s and spatial resolution around 13  $\mu\text{m}$  in air, consistent with classical OCT resolution (101).

### **Study limitations**

This study investigated the use of three reflectance optical imaging techniques to image lung tissue from a single species, the rat. However, the conclusions are expected to translate to all mammalian species, including the ability to visualize cells (where applicable), airspaces, blood vessels, and alveolar walls within the specified imaging depths. The structures of the alveolar regions of the lung are conserved across all mammalian species, with only a change in alveolar size and alveolar interstitial thickness (102).

Here, the advantages and limitations of the different technologies with respect to resolution, field of view and imaging depth were investigated. These parameters are in part specific to the current device configurations. For example, the FDOCT configuration implemented within this study could not resolve alveoli less than 20-30  $\mu\text{m}$  in diameter, which could be limiting in a mouse model. However, this limitation is not intrinsic to the technology as high-transverse resolution FDOCT can be performed with a higher NA lens. It is reasonable to expect improved cellular detail within a decreased imaging depth by implementing a larger NA lens within the FDOCT sample arm probe. SECM, as implemented here, obtained images using a swept-source laser with a 5 kHz line rate, resulting in several minute acquisition times. Newer lasers with rates in the MHz range have been developed (86), and it is likely the combination with high speed detection systems would allow imaging at image acquisition speeds that are 1-2 orders of magnitude greater than video rate. It is also important to note that the field of view of the current FFOCM system might present difficulties when attempting to image multiple alveoli within larger species. Again, this limitation is specific to the imaging system used in the study and not intrinsic to the technique itself.

All samples were filled with PBS and not air, as would be the case in a respiring lung *in-vivo*. Although some alveoli could in principle be fluid filled during various clinical conditions, such as bronchoalveolar lavage, liquid breathing, or edema, additional challenges will arise when translating these technologies for imaging air-filled alveoli *in vivo*. Significant differences in image quality are expected for fluid- *versus* air-filled alveoli as light refracts substantially when encountering the high refractive index differences between tissue and air. The imaging depth of the tested technologies could therefore be greatly reduced when the alveoli are filled with air, as previously demonstrated in ethanol-filled rabbit lungs using spectral-domain OCT (83), which resulted in distorted alveolar shapes.

This study was conducted in fixed lung tissue to allow better comparison of the different imaging technologies. In so doing, the same field of view could be imaged with all three technologies at the same inflation state. Furthermore, the lung could be cut into slices, which allowed the evaluation of any location within the lung compared to limiting the analysis to the alveolar layers directly beneath the pleura. The difference in refractive index between fresh and fixed tissue impacts both the resolution and imaging depth. Fixed tissue has a higher refractive index due to the polyethylene glycol (1.47 at 20°C) and PBS-immersed fresh lungs can be expected to show decreased refraction artifacts and slightly increased imaging depth at the cost of a decrease in contrast and/or resolution. In addition, light scattering by unfixed blood will decrease the imaging depth depending on the size of the vessel within the field of view (103). Subsections 3.3.1 to 3.4.3 will cover in detail the artifacts that arise from the high refractive index changes when imaging air-filled pulmonary alveoli.

A limited number of direct correlations to histology were presented, which does not allow verification of all structures visible in the images. Due to the additional processing cycles between image acquisition and H&E sectioning, the fine structures of the alveolar walls are distorted and difficult to recognize. Often intact histology sections could only be obtained after cutting up to 100  $\mu\text{m}$  from the tissue surface. Correlative histology was also difficult to find due to the limited imaging depth of the technologies. While these difficulties limited the ability to analyze the data, they emphasize the importance of

imaging techniques that provide non-destructive assessment of alveolar structure and function.

### **Conclusion**

It was demonstrated that three reflectance microscopy imaging technologies could visualize the small airways, individual alveoli and blood vessels in fixed, PBS-immersed rat lung slices without administration of contrast agents or radiation exposure. These findings suggest that FFOCM provides the best results for applications where absolute measurements of alveolar wall thickness and the identification of specific cell-types. SECM, with similar resolution and higher acquisition speed, is likely better suited for cellular resolution imaging over larger fields of view. FDOCT has reduced spatial resolution compared with FFOCM and SECM but is still adequate for the observation of relative alveolar sizes or a gross identification of airspaces and vessels. In addition, FDOCT provides high-speed evaluation over very large fields of view and is currently the most promising to be incorporated into an *in-vivo* imaging probe. Compared to histology, the most commonly used method for visualizing alveolar structures, the reflectance imaging methods are non-destructive and do not require embedding, sectioning or staining, which are known to create shrinkage, compression and tearing artifacts (51). Further, no tissue is lost during optical sectioning and the three-dimensional dataset can be virtually sliced and analyzed at oblique angles. Micro-CT does provide comparable resolution to the optical techniques with much greater penetration depth. The acquisition time of micro-CT is dependent on the resolution and sample size, but is much longer than FDOCT and comparable to SECM for the same resolution and size. However, because the resolution of micro-CT decreases with sample size, it cannot currently be translated to whole lung alveolar imaging in species larger than rats. While optical technologies can only obtain images with a penetration depth of a few hundred micrometers, high-resolution images can be acquired from large samples, making these techniques amenable to studying subsurface alveoli in large animals and humans.

### 3.3 Swept-source Fourier-domain optical coherence tomography for imaging alveolar structure and function

Based on the results presented in section 3.2, swept-source Fourier-domain optical coherence tomography (FDOCT) was chosen for further development within the scope of this thesis work. FDOCT emerged as the most promising optical reflectance imaging modality for dynamic visualization of individual alveoli because it provides spatial resolutions on the order of the alveolar wall thickness ( $\sim 10 \mu\text{m}$ ) as well as acquisition speeds well beyond video rate ( $>100$  fps).

This section describes the development steps that were undertaken to turn FDOCT from a promising technology tested on water-immersed samples to a working technique that allows visualization of air-filled pulmonary alveolar dynamics *in-vivo*. At the same time, it illustrates the artifacts that were observed during this development as being specifically important in optical imaging of air-filled alveoli. These artifacts have led to an intensive study investigating the validity of alveolar size measurements in FDOCT images, which will be described in the following sections.

Here, the reduced imaging depth and image quality in air-filled *versus* the previously seen fluid-filled alveoli is shown first. Secondly, a study optimizing the focal parameters is described preparing the development of the MEMS *in-vivo* imaging probe. This probe, developed by Eman Namati (54), enabled imaging specific swine alveoli during expansion and contraction throughout the breathing cycle. Subsection 3.3.3 briefly describes the probe.

#### **3.3.1 Imaging depth and image quality in fluid-filled *versus* air-filled alveoli**

It has been shown previously that FDOCT resolution and imaging depth in air-filled lung tissue is greatly reduced compared to imaging within other organs and compared to imaging within fluid-filled alveoli (83). Other groups investigating alveolar structure and function have pursued the practice of filling alveoli with liquid (index matching) to improve FDOCT image quality and imaging depth (95, 104, 105), which is not representative of normal healthy physiology. This section provides a brief description of the loss in

image quality compared to index matching before exclusively focusing on imaging air-filled alveoli.

Figure 32 shows the difference in image quality and imaging depth for FDOCT of the same field of view within a fixed rat lung slice when the tissue was air- *versus* water-filled. The water-filled sample provides excellent image quality of the alveolar walls at depths up to 240  $\mu\text{m}$ , while the image quality within the air-filled sample decreases dramatically within 100  $\mu\text{m}$  from the surface.

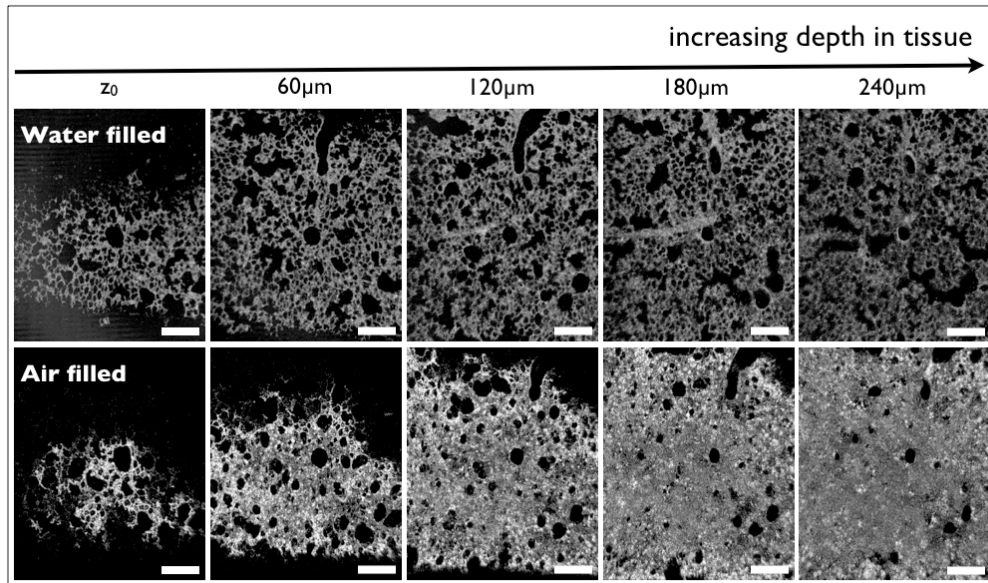


**Figure 32:** *En face* comparison of FDOCT image quality and imaging depth in water- *versus* air-filled, fixed rat lung tissue. Scale bars represent 500  $\mu\text{m}$ .

### 3.3.2 Optimization of the focal parameters for imaging air-filled alveoli

Increasing the imaging depth for FDOCT of the air-filled peripheral lung is critical for studying the interdependence of several layers of alveoli. In most tissues the imaging depth can be increased with longer, less scattering wavelengths and by increasing the depth of focus, as discussed in section 3.2. Because the depth of field depends on the NA, the increase in imaging depth results in a worse resolving capacity of the system or the acquisition of several data sets at different focal depths. It is then crucial to optimize the trade-offs between size, resolution and imaging depth, especially in an *in-vivo* setting, where images must be acquired as quickly as possible and the numerical aperture of the focusing lens may determine the size of the probe.

Secondly, the imaging depth in fresh lung tissue has been shown to be only about  $200\ \mu\text{m}$  (83) compared to more than  $500\ \mu\text{m}$  in fluid-filled tissue. If this limitation were intrinsic to the tissue optical properties as expected, there would be no benefit to sacrificing lateral resolution to increase the depth of focus. For example, a shorter wavelength and a higher numerical aperture could be used to tackle applications where high spatial resolution is critical. Other research questions, that depend heavily on the imaging depth would then require different solutions, such as the suggested index matching of the alveolar filling (83).

The goal of this study was two-fold: First, prepare the development of the *in-vivo* probe, where the optimal numerical aperture must be determined to allow maximum imaging depth while providing sufficient lateral resolution for the visualization of individual alveolar structure. Secondly, the influence of the numerical aperture and focal depth on the maximum possible imaging depth should be investigated to gain a better understanding about the limited imaging depth in FDOCT images of air-filled pulmonary alveoli. Before describing the experimental setup and the study results in detail, the trade-offs between lateral resolution and depth of field, which are expected to limit the imaging depth, are explained.

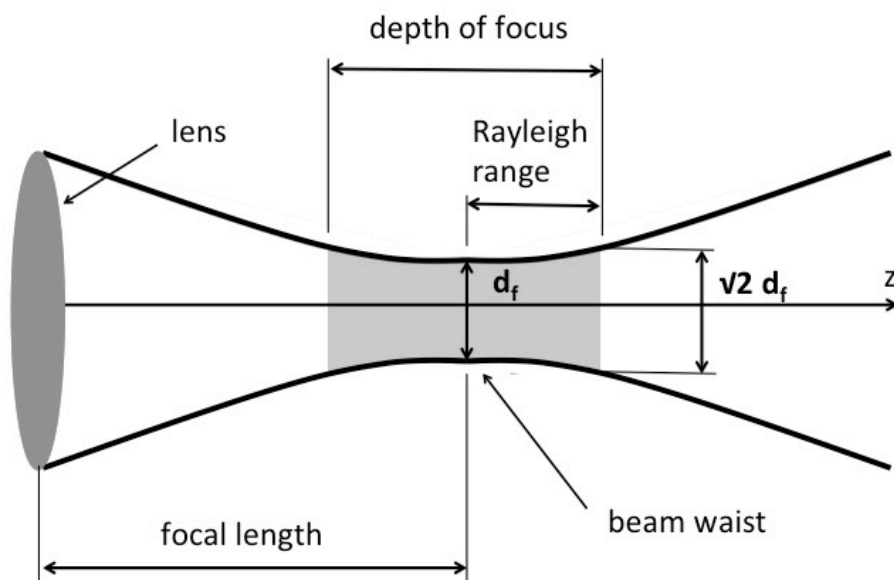


**Figure 33: Depth of focus. The depth of focus is twice the Rayleigh range, which is defined as the distance over which a Gaussian beam diverges from its minimum spot size  $d_f$  to a diameter of  $\sqrt{2} d_f$ .**

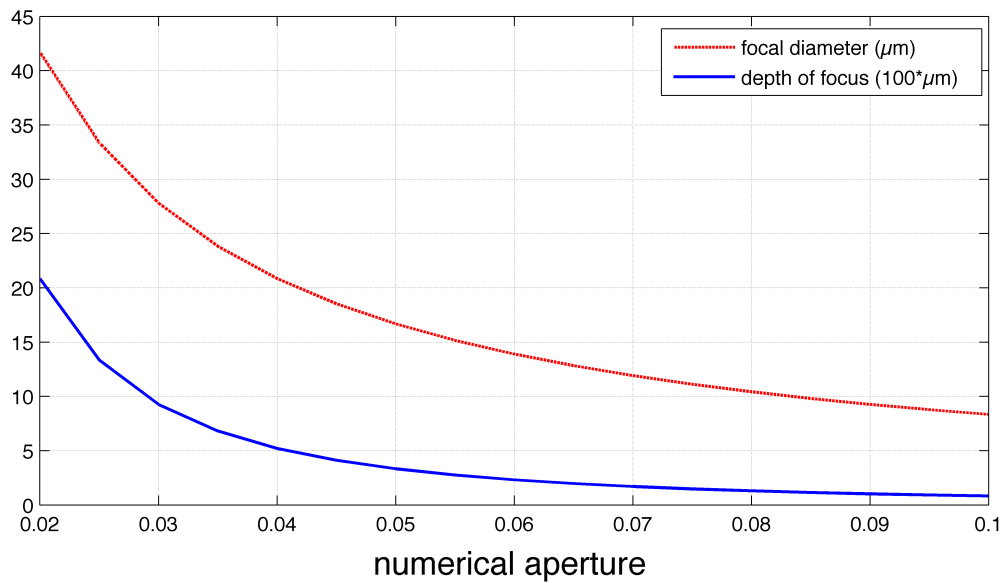


**Figure 34: Graph quantifying the focal diameter (red dotted line) versus the depth of focus (blue full line) as a function of the numerical aperture (calculated according to equation (3.9) and (3.11) for  $\lambda = 1.31 \mu\text{m}$ , objective focal length = 30mm).**

#### **Lateral resolution versus depth of focus**

One factor often limiting the imaging depth is the depth of focus, meaning the distance in which the image of an object appears in focus. The depth of focus, also referred to as the confocal parameter, is twice the Rayleigh range, which is defined as the distance over which a Gaussian beam diverges from its minimum beam waist  $d_r$  to a diameter of  $\sqrt{2} d_r$ . Figure 33 shows the convergence of a beam to its smallest focal diameter and subsequent divergence in order to illustrate the concept of the Rayleigh range and depth of focus. In an imaging system, the depth of focus can therefore be determined by the angle with which the light is focused on the sample (NA). In turn, the NA also determines the focal spot diameter, which determines the lateral resolution such that both quantities are interdependent and the resolving capacity of an imaging system could be sacrificed to achieve a larger depth of focus. The lower the numerical aperture, the larger the focal spot to which the beam is focused, but the slower the focusing/diffraction of the beam prolonging the depth of focus.

Quantitatively, the focal spot diameter  $d_f$  of a Gaussian beam is given by (106):

$$d_f = \frac{2}{\pi} \frac{\lambda}{NA} \quad (3.9)$$

Note that the focal diameter from equation (3.9) is related to equation (3.2) via the factor  $k = 2/\pi \sim 0.64$ .

The depth of focus  $\Delta z_f$  is then defined as (106):

$$\Delta z_f = \frac{\pi}{2} \frac{d_f^2}{\lambda} \quad (3.10)$$

Figure 34 shows the quantitative evolution of the focal diameter and the depth of focus over different NAs for the used imaging system with  $\lambda_c = 1.31 \mu\text{m}$ .

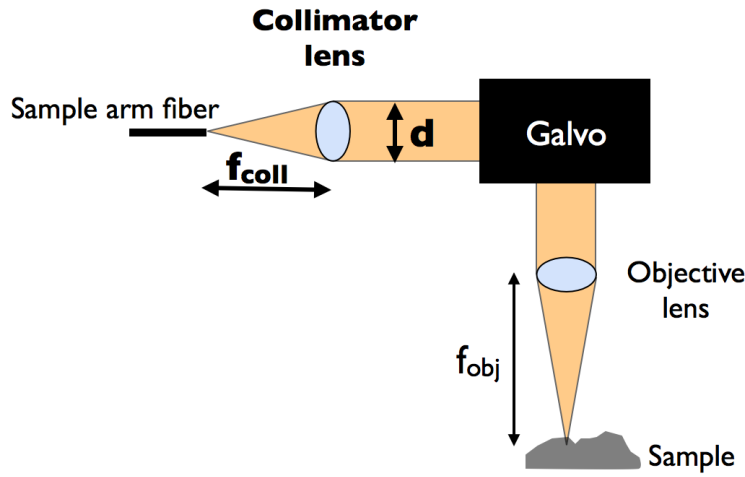


**Figure 35: Schematic of the experimental setup to vary the NA of the focus on the sample. The sample arm light is collimated and the beam is scanned over the sample using a galvanometer scanner setup (galvo). Each collimator has a specific focal length ( $f_{coll}$ ) creating the beam diameter  $d$ , which determines the NA together with the fixed focal length of the objective ( $f_{obj}$ ).**

#### Experimental setup for imaging with different NAs

The performance of four different NAs (0.02, 0.03, 0.08, and 0.1) was evaluated using a fixed focal length objective lens ( $f = 30 \text{ mm}$ ) and varying the beam diameter through changing collimator lenses with a fixed focal length objective lens ( $f = 30 \text{ mm}$ ). The NA of the focus was calculated assuming the paraxial approximation from (106):

$$NA \approx \frac{d}{2f_{obj}} \quad (3.11)$$

where  $d$  is the beam diameter and  $f_{obj}$  the focal length of the objective lens. Note that  $d$  is approximated from the same equation using the NA of the fiber and the focal length of each collimating lens. Figure 35 sketches the experimental setup. Table 4 provides the resultant NA, focal diameter and depth of focus for each tested lens (compare also Figure 34).

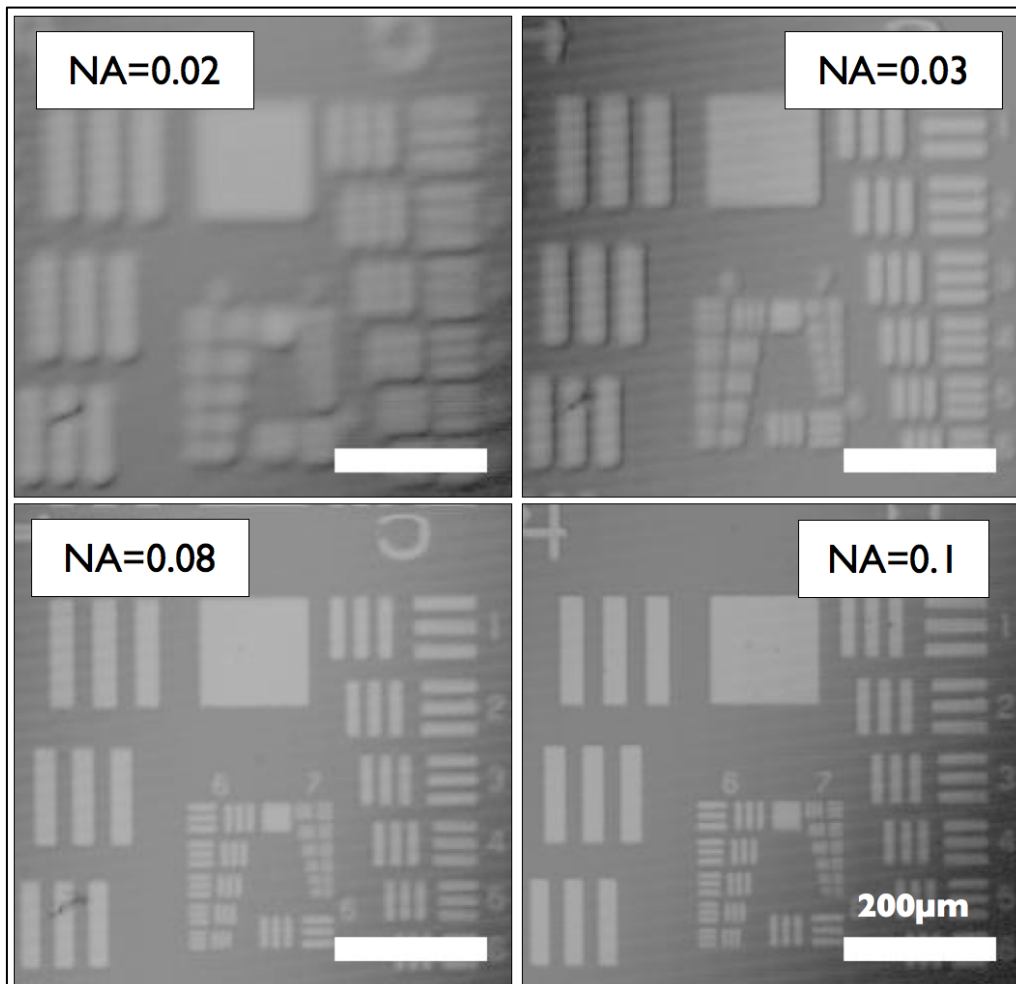
**Table 4: Overview over the four tested collimator lenses with resulting theoretical focal NA, focal diameter, and depth of focus.**

Collimator	1	2	3	4
Focal length (mm)	6.2	11	25	35
Beam diameter (mm)	1.12	1.98	4.5	6.3
NA of focus	0.02	0.03	0.08	0.1
Focal diameter ( $\mu\text{m}$ )	44	25	11	8
Depth of focus ( $\mu\text{m}$ )	2392	760	147	75

Figure 36 illustrates the effect of the four tested numerical apertures on the lateral resolution showing images of the US Air Force (USAF) resolution target. Determining resolution with this target is achieved through visual assessment of the smallest resolvable line pair by the user. This method is therefore often criticized for being subjective. However, it may more closely resemble human vision than more objective methods, such as evaluating point- or edge-spread-functions, which are also prone to variations due to noise. The resolutions determined from the USAF target images were 44  $\mu\text{m}$  (line pair 4-4) for the 0.02 NA, 24  $\mu\text{m}$  (pair 5-3) for the 0.03 NA, 12  $\mu\text{m}$  (pair 6-3) for the 0.08 NA, and 11  $\mu\text{m}$  (pair 6-4) for the 0.1 NA.

The tested range of focal diameters and depths of focus were chosen because a 44  $\mu\text{m}$  focal diameter (0.02 NA) was expected to be just small enough for the identification of air spaces and a 75  $\mu\text{m}$  depth of focus (0.1 NA) would be just large enough to visualize one layer of alveoli for all species from rats to swine, and such the ideal parameter should lie in between these extremes. Note that even the highest evaluated NA (0.1), which provides an 8  $\mu\text{m}$  focal spot

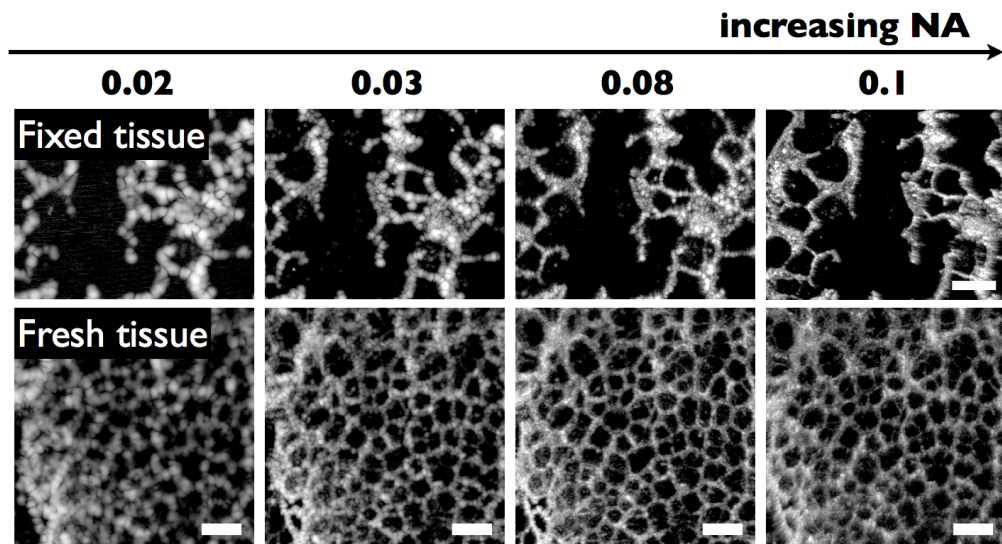
diameter, a diffraction-limited lateral resolution of  $5.7 \mu\text{m}$  (equation (3.2),  $k = 0.44$ ), and an experimentally measured resolution of  $11 \mu\text{m}$  (Figure 36), could only visualize overly thickened alveolar walls, since a realistic alveolar walls, since a realistic alveolar wall thickness is on the same order as the resolution ( $5\text{-}10 \mu\text{m}$ ). In order to provide a more correct visualization of alveolar wall thickness in FDOCT images, the system should be capable of resolving at least 2-3 points per wall. For example, a more appropriate lateral resolution could be  $2.5 \mu\text{m}$ , which would require a focal NA of 0.23 resulting in a depth of focus of only  $16 \mu\text{m}$ . Such a short depth of focus would not cover the expected height of an alveolus ( $\sim 50\text{-}300 \mu\text{m}$ ) and could also be problematic for non-contact probe imaging in the presence of tissue surface variations.



**Figure 36: Images of the US Air Force resolution target acquired with NAs of 0.02, 0.03, 0.08 and 0.1 illustrating the improvement in resolution with increasing NA.**

### NA variations and lateral resolution in FDOCT images of air-filled pulmonary alveoli

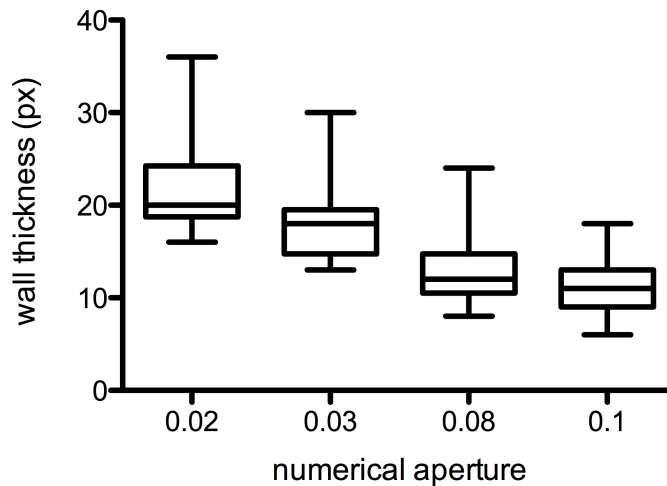
For this study, two rabbit lungs were instillation fixed and dried using a modified Heitzman fixation technique at 20 cmH<sub>2</sub>O pressure, described in subsection 3.1.2, and then cut in 2 mm thick slices. An additional rabbit lung was freshly excised and inflated to 20 cmH<sub>2</sub>O pressure for in-tact fresh tissue imaging. Three-dimensional data sets were acquired with FDOCT from the upper right lobe for each of the focal parameter and the resultant images were analyzed to determine the best compromise between imaging depth and resolution for the visualization of alveolar networks. The rabbit was chosen as an intermediate size between rats and swine expected to provide useful results for all species in this size range.



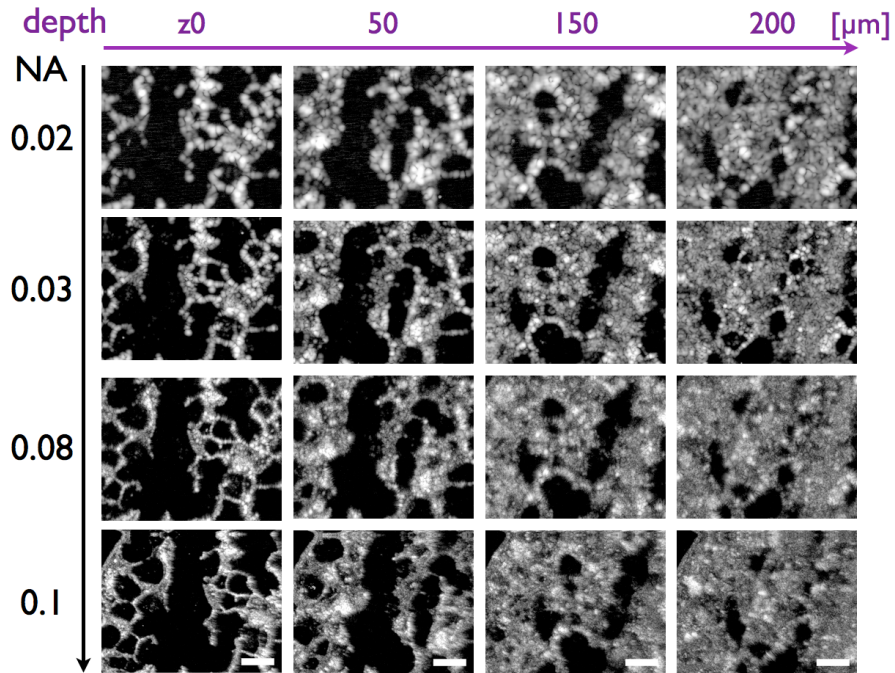
**Figure 37: FDOCT *en-face* images of fixed and fresh, air-filled rabbit lung tissue obtained with four different NAs (0.02, 0.03, 0.08, and 0.1) at the focal depth and about 20  $\mu\text{m}$  below the sample surface. Scale bars = 200  $\mu\text{m}$ .**

Figure 37 illustrates the influence of the NA on the lateral resolution in FDOCT images of an air-filled, fixed lung slice and of subpleural alveoli in a freshly excised lung. In general, the 0.03, 0.08, and 0.1 NAs provide clear identification of all air spaces while the 0.02 NA blurred the alveolar walls such that it was difficult to identify some air spaces. Visually, the image quality increases with higher NA. Quantitatively, the full width at half maximum (FWHM) of a line profile perpendicular to the alveolar walls was

used to quantify the ability to resolve alveolar wall thicknesses. Ten walls were measured in approximately the same location for all of the fixed sample images of Figure 37. Figure 38 shows the distribution of these wall measurements, which were not normally distributed (Shapiro-Wilk normality test) and are therefore compared by median, 25<sup>th</sup> and 75<sup>th</sup> percentile. The median wall thicknesses were 20 pixels (0.02 NA), 18 pixels (0.03 NA), 12 pixels (0.08 NA), and 11 pixels (0.1 NA) demonstrating the improvement in resolution with increasing NA. From these preliminary measurements it appears as a plateau for alveolar wall thickness was not reached with the increasing NAs suggesting that increasing the NA further could result in further decrease in measured wall thickness.



**Figure 38:** Whisker plot (min – max) comparing a measure of alveolar wall thickness (FWHM of the line profile across the wall) as provided by four different NAs. The same walls ( $n = 10$ ) were measured in each of the fixed tissue images of Figure 37.



**Figure 39:** FDOCT *en-face* images at different depths from the surface of a fixed, air-filled rabbit lung slice acquired with different NAs (0.02, 0.03, 0.08, and 0.1). A single three-dimensional image was acquired for each NA with the focal depth fixed at approximately  $z_0$ . Scale bars = 200  $\mu\text{m}$ .

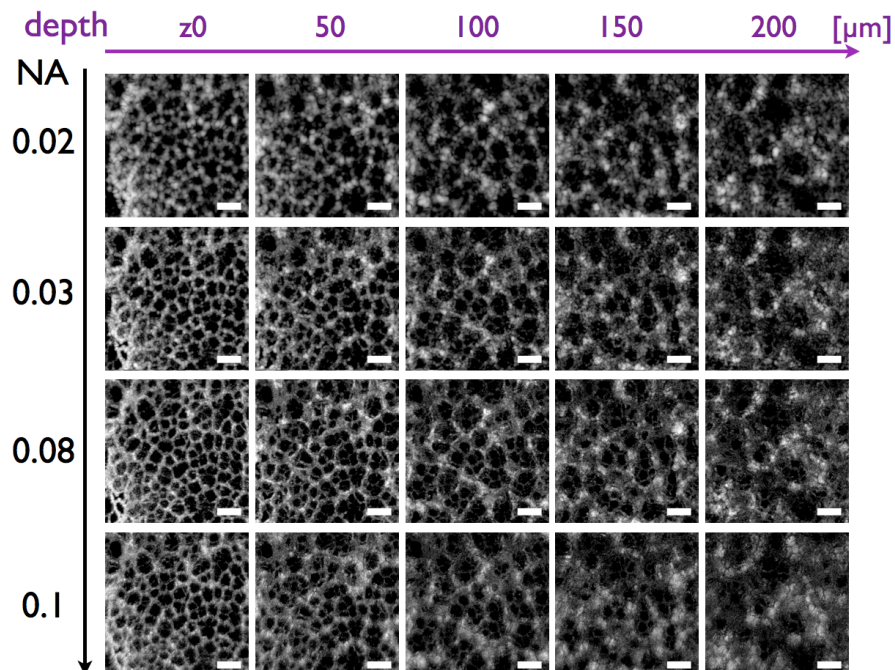


**Figure 40:** FDOCT *en-face* images at different depths starting right below the pleura in an air-filled excised rabbit lung. One image stack was acquired for each NA (0.02, 0.03, 0.08, and 0.1) with the focal depth at approximately  $z_0$ . Scale bars = 200  $\mu\text{m}$ .

### NA variations and imaging depth in FDOCT images of air-filled pulmonary alveoli

Figure 39 and Figure 40 show a series of *en-face* images over different depths in the fixed and fresh tissue, respectively. The extended depth of focus of the 0.03 NA compared to the larger NAs is clearly visible in the fixed tissue example from a depth greater than 150  $\mu\text{m}$ . However, this extended usable imaging depth seems informative only in regions where the light had followed the airway and not interacted with air/tissue interfaces. Regions below closed airspaces or any lung tissue appear obscured independent of the depth of focus. In the fresh tissue images of subpleural alveoli, the extended depth of focus does not appear to provide any additional information. Thus, the qualitative improvement in image quality seems marginal.

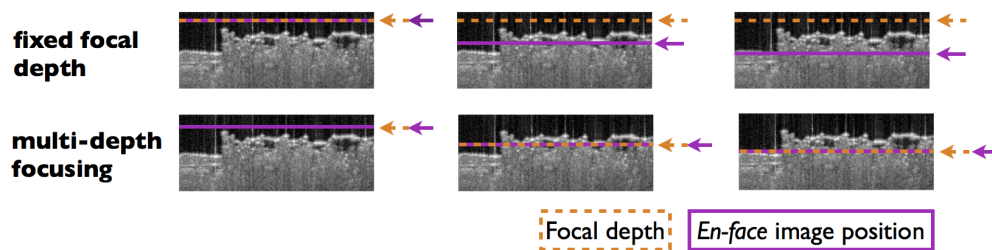


**Figure 41: Schematic illustrating multi-depth focusing. Previously, different depths in the tissue were visualized while the focus was placed at a fixed depth. In multi-depth focusing, an image stack was created by combining several different data sets acquired with different focal depths, such that every image in the resulting stack was in focus.**

### Multi-depth focusing and imaging depth in FDOCT images of air-filled pulmonary alveoli

After evaluating different depths of focus, the following experiment evaluates the influence of the focal depth (depth in the tissue where the focus is created) for a fixed depth of focus on the total imaging depth. Several three-dimensional images were acquired sequentially with the same NA, but the objective lens was translated towards the sample in discrete steps in-between the sequential image acquisitions. Thus, the depth of focus was also shifted in the axial direction between the images. Then, an image stack was created by combining several different three-dimensional images acquired with different focal depths,

such that every image in the resulting stack was in focus (Figure 41). This technique is hereinafter referred to as multi-depth focusing (MDF).

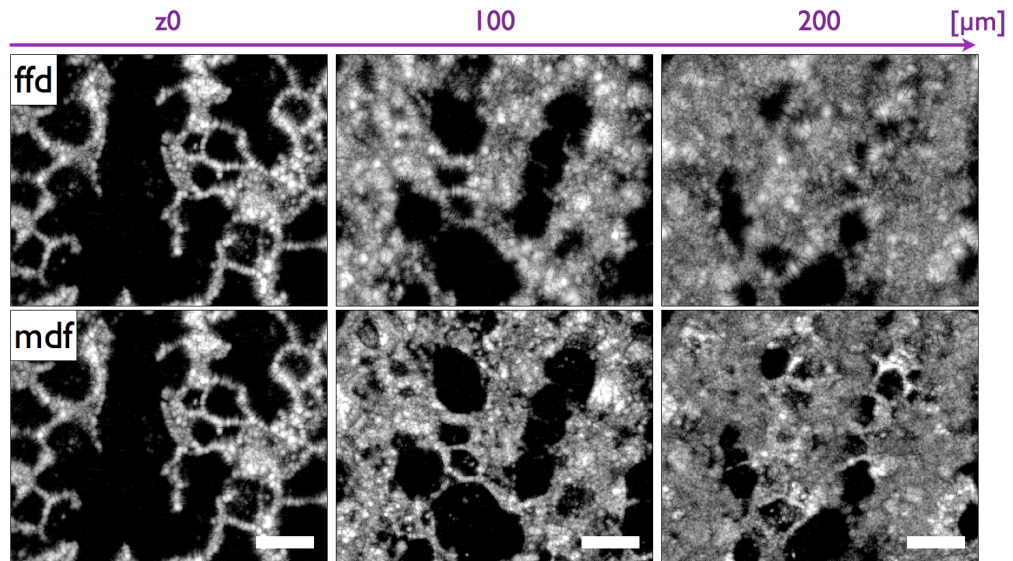


Figure 42: FDOCT *en-face* images of fixed rabbit lung tissue illustrating the improvement in usable imaging depth through multi-depth focusing (mdf) compared to imaging at a fixed focal depth (ffd). NA = 0.08. Scale bars = 200 $\mu$ m.

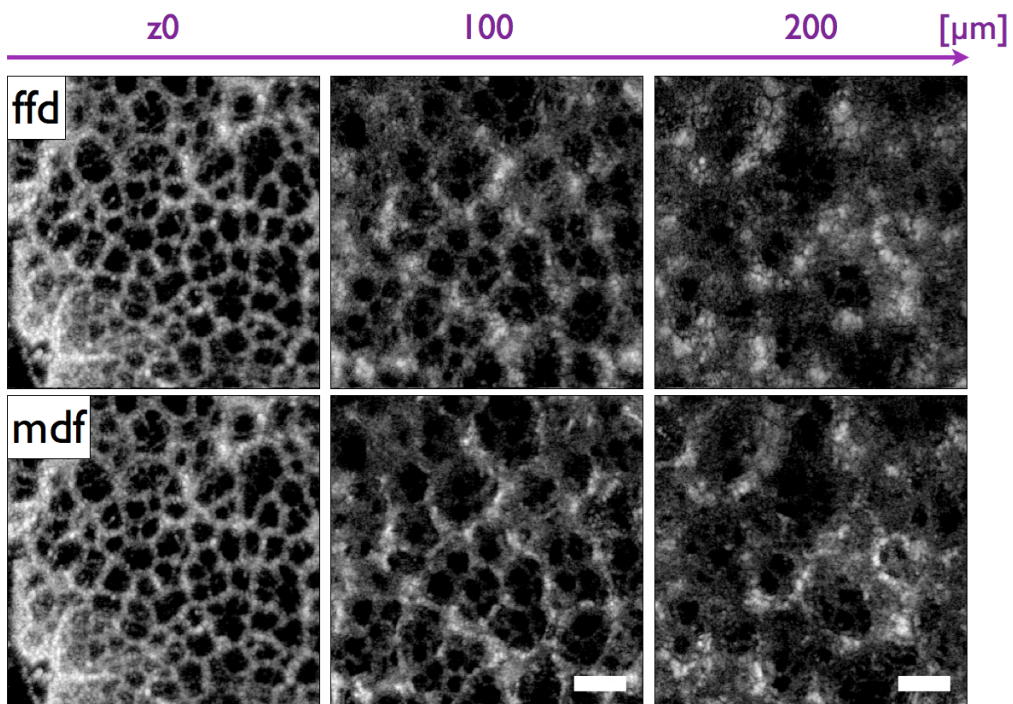


Figure 43: FDOCT *en-face* images of fresh subpleural rabbit alveoli illustrating the improvement in usable imaging depth through multi-depth focusing (mdf) compared to imaging at a fixed focal depth (ffd). NA = 0.08. Scale bars = 200 $\mu$ m.

Figure 42 and Figure 43 show the qualitative improvement of usable imaging depth achieved through MDF in fixed and freshly excised tissue, respectively. Similar to the extended depth of focus, obtained by imaging with smaller NAs, there is clear improvement in image quality for fixed tissue, but only in regions where the light was able to travel through an airway without many tissue/air interfaces. In freshly excised lung tissue, an improved focus can be seen at deeper depths, but the effect is marginal and could be explained by the fact that all light penetrates through the pleura directly in the first layer of subpleural alveoli and the amount of light-tissue interactions is similar across the entire field of view.

### **Conclusions**

In this study, variations in the imaging lens focal parameters were investigated, namely numerical aperture (NA) and multi-depth focusing, for FDOCT imaging of air-filled alveoli. It was hypothesized that an optimal set of parameters could be identified maximizing imaging depth while maintaining sufficient lateral resolution.

The influence of the NA on the lateral resolution could be shown as expected. From the evaluated NAs (0.02, 0.03, 0.08, 0.1), only the 0.02 NA did not provide the ability to identify all air spaces and is therefore insufficient for imaging alveolar networks. Alveolar wall thicknesses were also measured from the images obtained with different NAs and the median wall thickness decreased with increasing NA. A plateau was not reached, however, indicating that for a correct visualization of the wall thickness, the NA should be even higher ( $\sim 0.23$ ) than the 0.1 NA tested. However, using a larger NA will result in a smaller depth of focus as tested that could be incompatible with the depth of focus required to visualize at least one layer of alveoli in focus, especially in the presence of surface height variations.

The imaging depths at which alveolar septal walls appeared in focus varied from 80 to 200  $\mu\text{m}$  depending on the NA and the sample properties. Acquisition of images obtained at different focal locations increased the resulting depth of focus in the MDF data set for the 0.08 and 0.1 NA lenses. For an application favoring a depth of focus larger than one layer of alveoli over correct representation of the wall thickness, the 0.03 NA seemed most

appropriate. Where both the lateral resolution and the depth at which the image stack appears in focus are crucial, an adaptive focusing approach could be designed.

In air-filled peripheral lung tissue, however, the usable imaging depth seemed to be limited to only one layer of alveoli by the intrinsic tissue properties rather than the depth of focus of the imaging technique. This is especially true for imaging subpleural alveoli, where light-tissue interactions are similar across the entire field of view. Therefore, it appears advantageous to accept a short depth of focus in order to provide better lateral resolution for a realistic representation of the alveolar airspace wall thickness and size. Further, a contact imaging probe was chosen for the subsequent studies of this work to fix the distance between the objective lens and the tissue, which allows further reduction of the depth of focus compared to non-contact imaging of a moving sample. Therefore, a 0.2 NA was chosen as discussed in the following subsection.

### **3.3.3 MEMS imaging probe for dynamic *in-vivo* imaging**

To allow dynamic imaging of pulmonary alveoli *in-vivo*, it was crucial to find a scanning approach that would allow tracking of specific alveoli in spite of lung movement during breathing. This subsection explains the rationale behind developing an imaging probe that was in direct contact with the lung and gives the probe specifications. The probe was developed by Eman Namati (54).

#### **Rationale for the development of a contact-imaging probe**

So far, this work has only shown static FDOCT images of pulmonary alveoli acquired with a galvanometer scanning setup for the transverse directions. A similar scanning approach was used previously for dynamic imaging of one mouse alveolus post-mortem (107). However, the galvanometer setup is not convenient for imaging alveolar dynamics of any species larger than mice or of several alveoli per field of view, because of the translation of the alveoli of interest (AOI) during breathing. In the axial direction, the depth of focus of a system with stationary galvanometric scanner (galvo) setup would have to approximately reach the translation distance of the AOI. In small animals (mice or rats) this could possibly be achieved at the cost of reduced resolving

capacity as explained in subsection 3.3.2. In the lateral direction, the field of view would have to be larger than the lateral translation of the AOI to track a single alveolus and accordingly larger to track several alveoli. The translation distance in both directions depends mainly on the animal size, the imaging location, and the overall lung volume change. In general, small animals and the upper lobes in any species exhibit less translation. Positive end-expiratory pressures (PEEP) can be used to limit lung deflation.

For this work, the swine model was chosen to provide alveolar dynamics that approximate those in humans. The translation of an AOI during ventilation in a physiologic pressure range (5-20 cmH<sub>2</sub>O) is on the order of a few centimeters in both the lateral and axial direction making it impossible to use a fixed galvanometer scanning setup. A galvanometer scanning setup that is synchronized to the movement of the AOI could provide a solution at increased complexity of the system, requiring mechanical translation of the mirrors in three dimensions and precise synchronization to the acquisition.

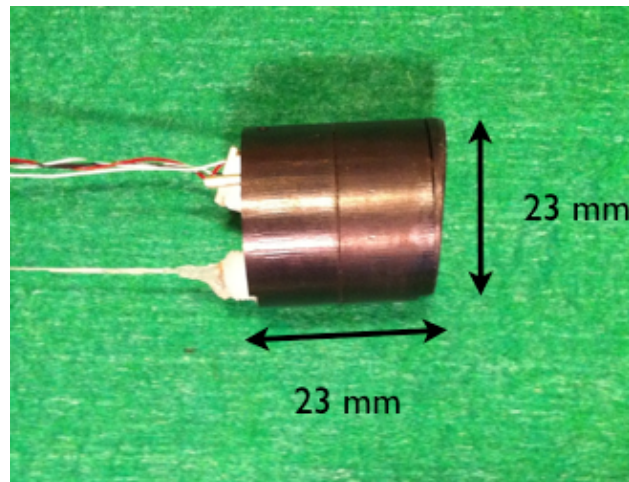
In the context of this work, an imaging probe was developed that sits directly on the moving lung during breathing and as such allows dynamic imaging of about 20 alveoli per field of view. It therefore follows the translation of the AOI and provides a fixed distance between the focusing lens and the pleura, which enables imaging with higher numerical aperture (tighter focus and shorter depth of focus). However, this approach also requires direct access to the lung and thus imaging cannot be performed through a transparent window in the closed chest wall.

### **Probe specifications**

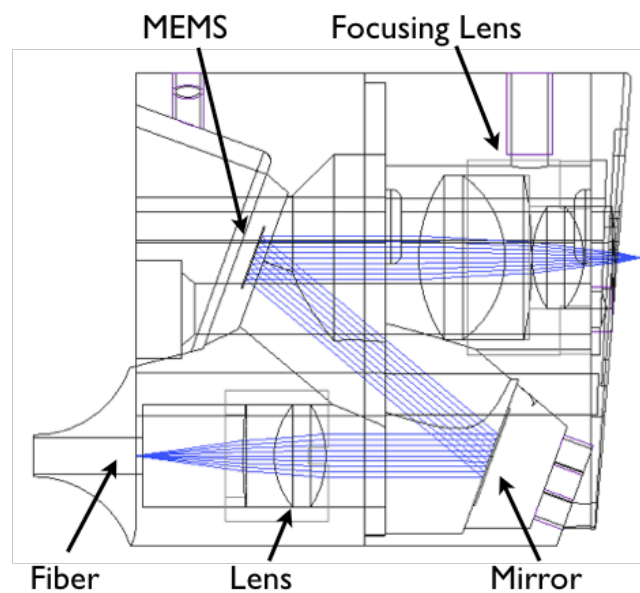
The MEMS probe specifications have been described in detail in (108) and (54):

Figure 44 shows the cylindrical MEMS probe (23 mm diameter, 23 mm tall) weighing 12g. It utilizes a dual-axis microelectromechanical systems (MEMS) mirror (Mirrorcle 4Q Development kit, Mirrorcle Technologies, Inc. Richmond, CA) to scan a 930  $\mu\text{m}$  x 930  $\mu\text{m}$  transverse field of view upon the tissue. The focusing lens provides a 0.2 NA resulting (in air) in a theoretical resolution of 3  $\mu\text{m}$  (equation (3.2)), a focal diameter of 4  $\mu\text{m}$  (equation (3.9)) and a depth of focus of 21  $\mu\text{m}$  (equation (3.10)). An open space exists between

the lens and the field of view such that no optics are in direct contact with the imaged tissue. However, it is important to note that a 3.0 cmH<sub>2</sub>O pressure was calculated to be applied to the region immediately surrounding the field of view based on the weight and cross-sectional area of the probe in contact with the lung. Note further, that an 8°-angled base plate was included to reduce the surface reflection from the tissue caused by the large change in refractive index between air and tissue. The base plate changes the illumination angle of the light such that the reflection from the surface will not be collected by the detection optics.



(a)



(b)

**Figure 44: (a) MEMS probe. (b) Wireframe of the device showing the optical path within the housing.**

### 3.3.4 Air space segmentation and measurement in four-dimensional *in-vivo* images

In order to obtain quantitative measurements of airspace size from the FDOCT images, the individual contours were traced manually on each two-dimensional image. The following describes the segmentation that was applied to the four-dimensional data sets and is adapted from (54).

The boundary of each air space was chosen as the inner alveolar wall and traced manually over 18 volume acquisitions (6 samples per breath). The analysis was limited to the first layer of subpleural alveoli due to imaging artifacts that result from the propagation of light through tissue-air interfaces and are described in detail in sections 3.4 and 4.2. An artificial boundary was created along the bottom of the air space to close any ducts or pathways to additional air spaces in the axial direction by connecting the natural incomplete curves of the alveolar walls where the bottom of the air space narrows (solid arrow in Figure 45). It is important to note that in the four-dimensional data no artificial boundaries were traced between alveoli in the transverse direction (dashed arrow in Figure 45), such that each alveolar air space may be comprised of multiple alveoli.

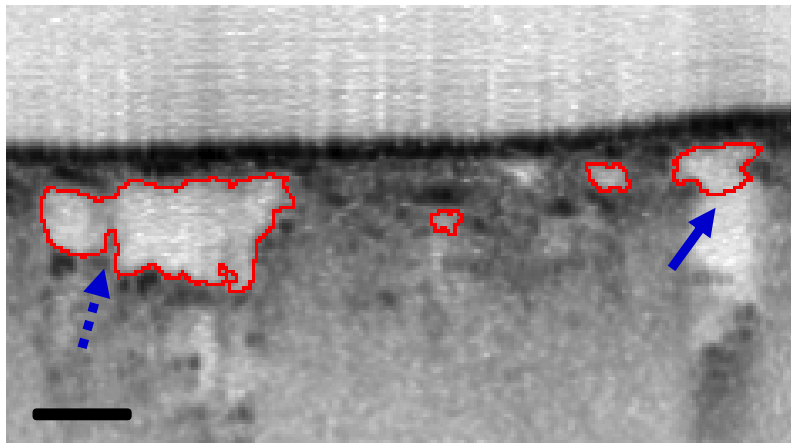


**Figure 45: Representative example of alveolar segmentation. Solid arrow: artificial boundary created to close alveolar air space from the air spaces below the top layer. Dashed arrow: clusters or alveoli were not separated within the first layer of alveoli. Scale bar = 100  $\mu\text{m}$ .**

Upon completion of the segmentation in all 2D cross-sectional planes, the resulting individual segments were stacked together to create three-

dimensional volumes. A dilation and erosion algorithm was applied in the direction orthogonal to the segmentation plane in Matlab (Mathworks: Natick, MA) to smooth any slight offset between the two-dimensional frames. Four-dimensional rendering were created with OsiriX (Pixmeo: Bernex, Switzerland). Volume and surface area were calculated for each alveolar air space by summing the number of pixels within all cross-sections and along the surface of the three-dimensional object, respectively, and then multiplying by the appropriate three-dimensional pixel size. Figure 46 illustrates schematically how the alveolar volume could be approximated as the sum of all products of cross-sectional area  $A_i$  of each segment (number of pixels in  $x$ - $y$ -plane multiplied by pixel size along  $x$  and  $y$ ) and pixel size  $d_i$  in the  $y$ -direction. Percentage change in volume ( $\Delta V\%$ ) and surface area ( $\Delta SA\%$ ) for each airspace and volume acquisition were defined as the percent change of airspace volume and surface area with respect to the minimum airspace volume acquired over three breaths.

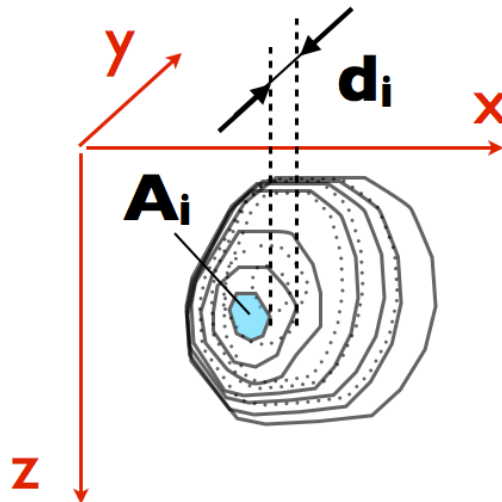


**Figure 46:** Calculation of airspace volume as the sum of all products of cross-sectional area  $A_i$  of each segment (number of pixels in  $x$ - $y$ -plane multiplied by pixel size along  $x$  and  $y$ ) and pixel size  $d_i$  along  $y$ .

### 3.4 Techniques to investigate the quantitative representation of alveolar size and shape in optical coherence tomography images

In order to validate quantitative measurements of pulmonary alveoli in FDOCT images, it was crucial to investigate the effects of refraction at the tissue-air interfaces that create artifacts in FDOCT images. Initially, the quantitative refractive index of alveolar tissue was measured with FDOCT. Secondly, size measurements of fixed, air-filled swine alveoli obtained in FDOCT were compared to measurements from micro-CT images, which are minimally influenced by refraction. Further, a two-dimensional ray-trace model was created that estimates the expected size error due to refraction and could explain the experimentally observed difference in alveolar size. The last subsection describes in detail how the agreement between alveolar sizes obtained through two different methods (FDOCT raw data *versus* micro-CT raw data or corrected FDOCT data *versus* raw micro-CT measurements) was evaluated. These approaches allowed the validation of quantitative measures of alveolar size obtained from FDOCT images (56).

#### 3.4.1 Refractive index measurement

Representative values of the mean refractive indices of fixed and fresh mammalian lung tissue were measured using FDOCT (109). Fixed and fresh rat lung tissues from the same animal were ground in a freezer mill (SPEX 6770) to create bulk lung tissue paste, warmed to 37°C and placed on a planar reflecting surface. Cross-sectional images were acquired when the tissue on the reflecting surface was visible as well as the surface on both sides of the tissue (Figure 47). A straight line connecting the unobstructed surfaces outside of the sample and traversing through the tissue paste provides a point of reference to calculate the physical thickness ( $z$ ) of the lung paste and the displacement of the razor blade surface by the tissue paste ( $z'$ ) along the A-line. The refractive index is calculated by the ratio of the optical path length of the tissue paste ( $z+z'$ ) to the actual thickness:

$$n = \frac{z+z'}{z} \quad (3.12)$$

A total of 30 measurements were recorded from each sample (10 measurements from three separate images) to provide a mean refractive index of  $1.412 \pm 0.001$  for fresh and  $1.514 \pm 0.003$  for fixed rat lung tissue.

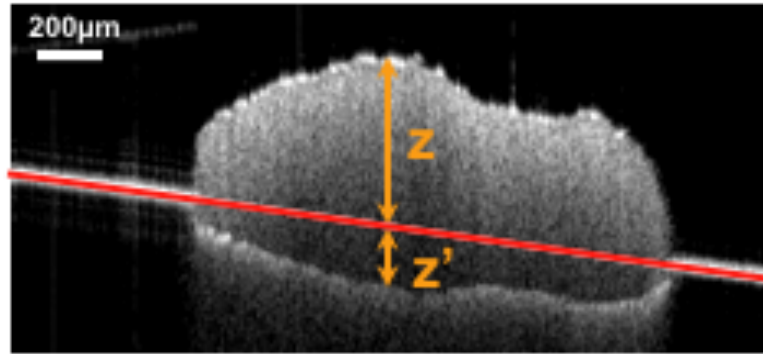


**Figure 47: Cross-sectional FDOCT image of heated (37°C) lung tissue paste placed on a razor blade illustrating the difference between the optical path length ( $z+z'$ ) and the real tissue thickness ( $z$ ). The refractive index of the tissue can thus be computed as  $(z'+z/z)$ .**

### 3.4.2 Comparison of FDOCT to micro-CT images

#### Image acquisition with FDOCT

A Fourier Domain Optical Coherence Tomography (FDOCT) system (68, 70), centered at 1310nm was used that provides  $12 \mu\text{m}$  lateral resolution and  $8 \mu\text{m}$  axial resolution. In this study, fields of view of  $1.5 \times 1.5 \text{ mm}$  ( $512 \times 512$  pixels) over a ranging depth of 6.6 mm (in air) were acquired with a bench-top galvanometric scanner through the pleural surface of the sample. The acquired voxel size was  $2.9 \times 2.9 \times 6.47 \mu\text{m}$  in air.

#### Image acquisition with micro-CT

A desktop high-resolution micro-CT system (SkyScan 1172, Kontich, Belgium) with an isotropic voxel size of  $2.9 \mu\text{m}^3$  was used to obtain three-dimensional cylindrical images with a 3 mm diameter and 0.5 mm height that contained the pleural surface. Each sample was rotated approximately  $196^\circ$  at  $0.4^\circ$  steps with 4 projection images averaged per rotation step. Source voltage and current were 40 kV and  $250 \mu\text{A}$ , respectively. No external contrast was used.

### **Segmentation and measurement of two- and three-dimensional quantitative alveolar parameters: cross-sectional area and volume, perimeter and surface area**

In order to directly compare two- and three-dimensional alveolar size parameters, a bicubic interpolation was applied to the FDOCT images to match the  $2.9\ \mu\text{m}$  isotropic pixel size of micro-CT. Both datasets were then manually reoriented in three dimensions to match a  $1.5 \times 1.5\ \text{mm}$  field of view between the *en-face* planes. Identical alveoli in both data sets were identified by shape and location, and then segmented manually in ImageJ (110). Each alveolar airspace was segmented along the leading edge of its luminal surface in order to include and measure the air inside the alveolus. Openings to a duct or to additional alveoli in the axial direction were closed by connecting the incomplete boundaries in Figure 48 (c-d) to limit the analysis to the first layer of alveoli. The closing contour was determined after careful examination of all cross-sectional planes in the three-dimensional volume of each alveolus to assure a smooth three-dimensional shape as indicated in Figure 49 (continued in Figure 50). Further, individual cross-sections were created and segmented by re-slicing the *en-face* data sets along identical line segments. The closing contours were determined analogous to the volume segmentation. An example is shown in Figure 48 (a-d), where Figure 48 (a-b) show the matched *en-face* sections from micro-CT and FDOCT, respectively, as well as the line along which cross-sections Figure 48 (c-d) were re-sliced. Figure 48 (e-f) indicate the manually segmented alveolar cross-sections from field of views Figure 48 (c-d). A total of 29 alveolar cross-sections, at least 7 from each lobe, were segmented in both data sets, and the cross-sectional area with its respective perimeter was measured in ImageJ. The maximum alveolar height and width were determined by fitting a bounding rectangle around the segment. For further analysis, the aspect ratio  $f$  of the alveolus was defined as the ratio of height over width:

$$f = \frac{h}{w} \quad (3.13)$$

Further, a total of 19 (at least 5 from each lobe) three-dimensional, closed alveoli were segmented frame by frame in the cross-sectional plane. The

volume of each alveolus was determined as the sum of all its cross-sectional areas multiplied by their slice thicknesses. In order to obtain surface area, a dilation and erosion algorithm was applied in the direction orthogonal to the segmentation plane in Matlab to smooth any slight mismatch between frames. The surface area was calculated as the sum over all pixels along the surface. The alveolar height, width, and depth were calculated in a manner that was analogous to that of the cross-sectional area procedure. The arithmetic mean of width and depth was defined as the width to compute the form factor.

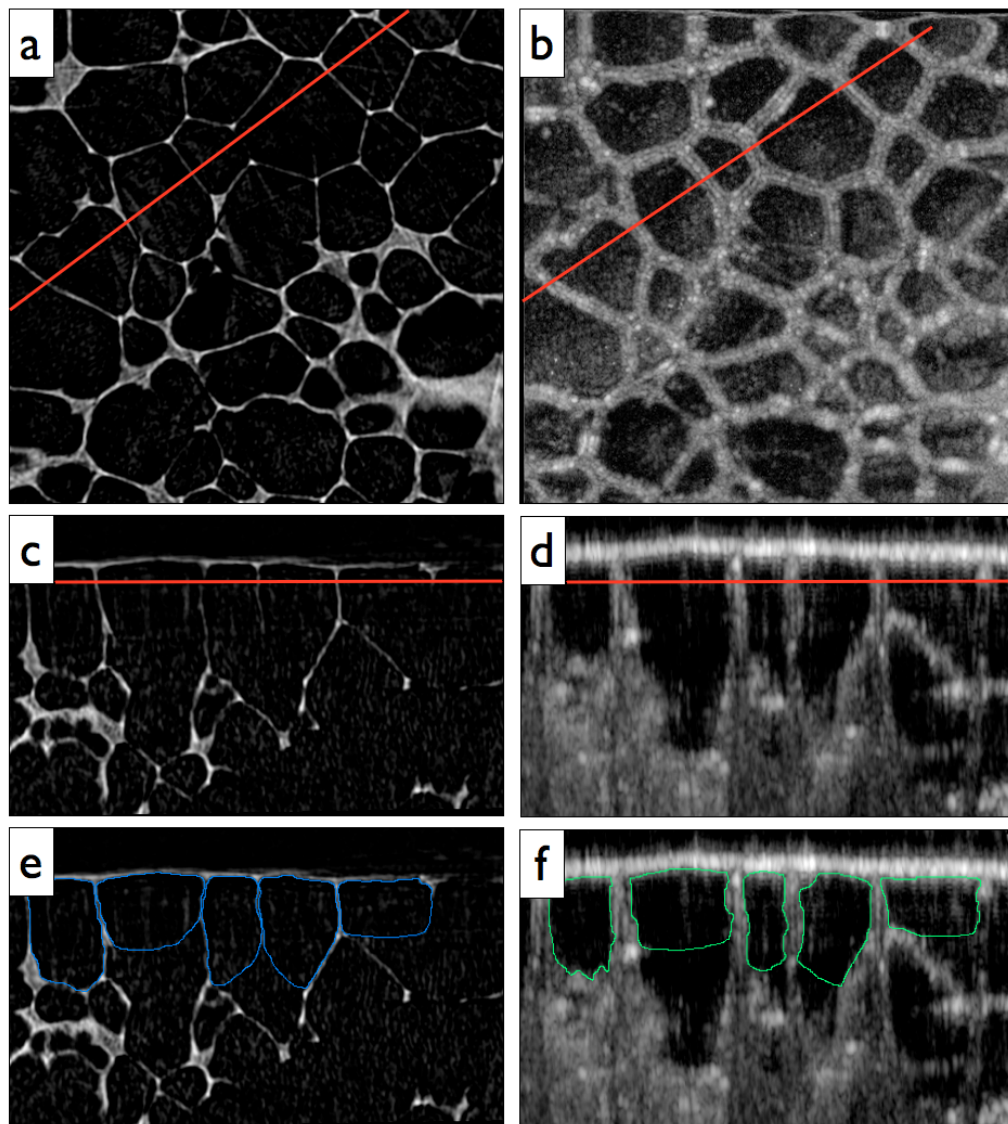


**Figure 48:** Segmentation of alveolar airspaces in micro-CT and FDOCT images of fixed swine lung. *En-face* (a) micro-CT and (b) FDOCT images where red line indicates position of axial cross-sectional (c) micro-CT and (d) FDOCT images. Comparison of segmentations from (e) micro-CT and (f) FDOCT axial cross-sections.

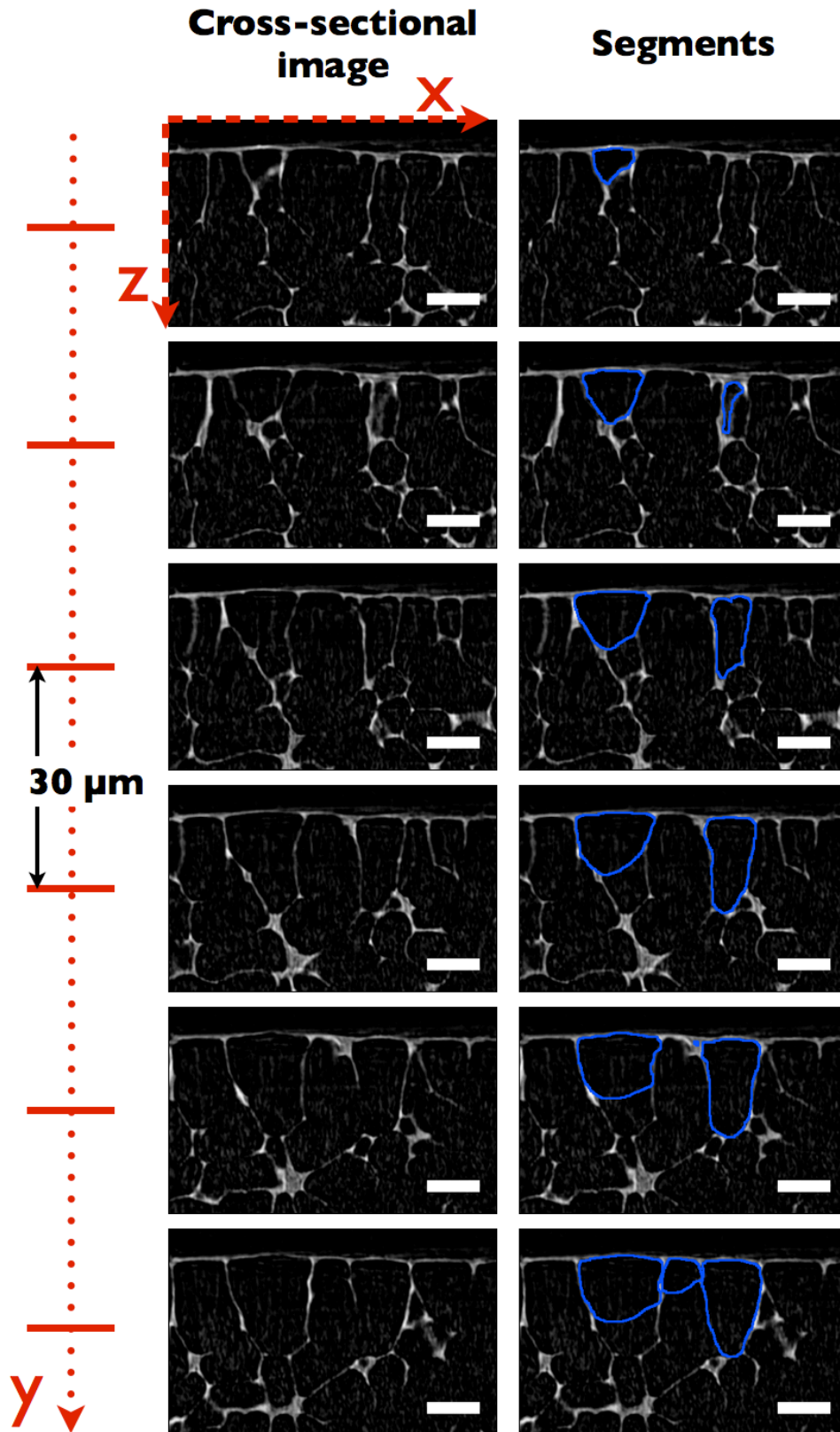


Figure 49: Sequence (along  $y$ ) of consecutive  $30 \mu\text{m}$ -spaced cross-sectional ( $x, z$ ) frames from micro-CT dataset demonstrate closing of alveolar segments with incomplete walls.

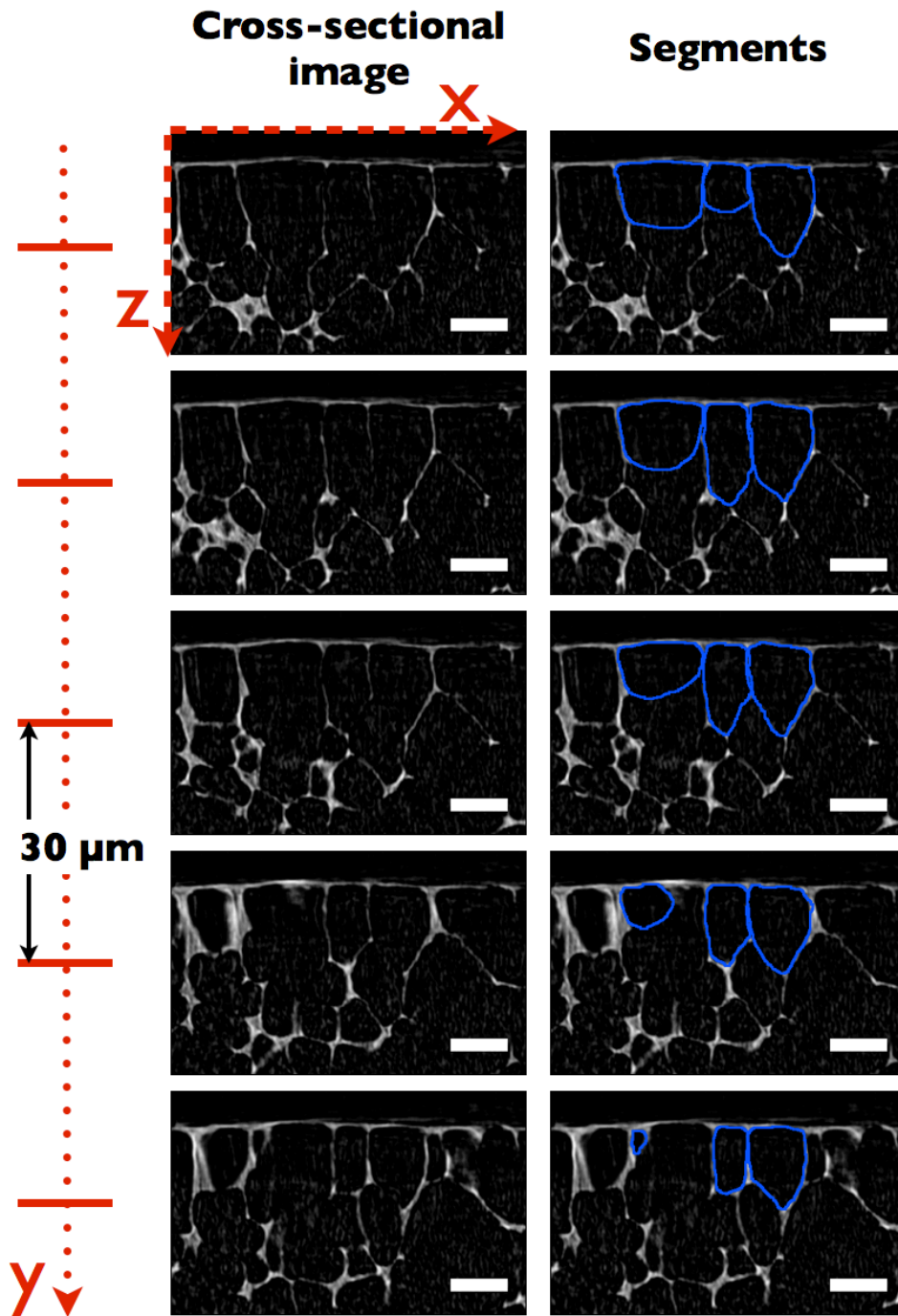
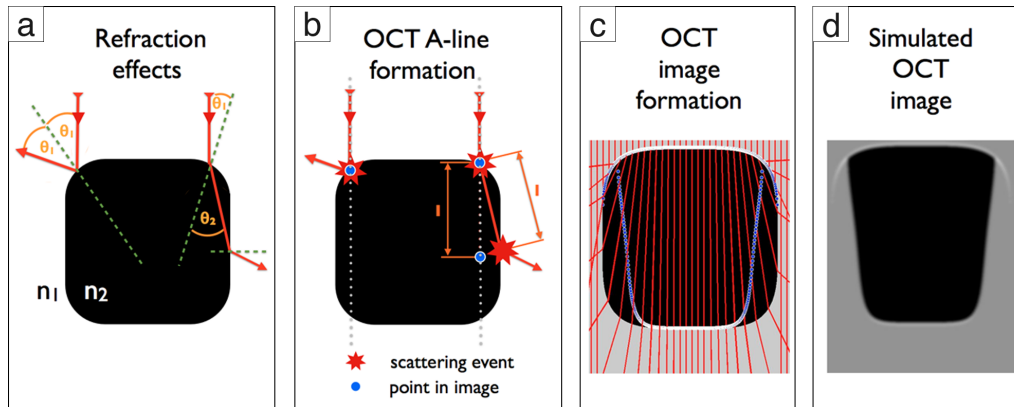


Figure 50: Sequence (along  $y$ ) of consecutive  $30 \mu\text{m}$ -spaced cross-sectional ( $x, z$ ) frames from micro-CT dataset demonstrate closing of alveolar segments with incomplete walls. (continued from Figure 49)



**Figure 51:** Image sequence illustrating the developed ray tracing model to simulate an FDOCT image based on the effects of refraction and total internal reflection.

### 3.4.3 Ray-tracing model to investigate the influence of refraction effects

An interesting property of white-light interferometry and therefore also FDOCT, is the fact that the signal is generated at equal optical path lengths (OPL) rather than equal geometrical path lengths (GPL) of the sample and reference arm. In other words, while the GPL represents the true structure of the tissue of interest, the FDOCT system visualizes this structure in terms of the OPL, which is linked to the GPL mainly through the refractive index of the tissue. In FDOCT imaging of air-filled peripheral lung tissue this difference is particularly important, due to the high refractive index mismatch between the alveolar tissue and the air inside the alveolus. Subsections 3.3.1 and 3.3.2 have shown the limited imaging depth observed in FDOCT images of air-filled pulmonary alveoli that has motivated this investigation together with the previously published appearance of double alveolar walls (83). The following subsections describe the two-dimensional ray-tracing model that was developed to investigate the difference between the true alveolar structure and the visualization of this structure in FDOCT and show some of the qualitative results obtained on hollow glass phantoms.

#### Modeling of refraction and total internal reflection

A two-dimensional ray-tracing model was created in Matlab that calculates the refraction effects (total internal reflection and refraction) for parallel incident rays on a pre-defined shape and simulates an FDOCT image based on the

obtained optical path lengths. Figure 51 illustrates the process of simulating an FDOCT image. The model calculated the refracted geometric path of each ray through the predefined sample and recorded the distance and refractive index between refraction events (Figure 51(a)). The refraction of each incident light ray is computed according to Snell's law:

$$n_1 \sin \theta_1 = n_2 \sin \theta_2 \quad (3.14)$$

where  $n_1$  and  $n_2$  are the refractive indices of the media before and after the interface, respectively, and  $\theta_1$  and  $\theta_2$  are the angles of incidence and propagation, respectively. If the incident angle equals or exceeds the critical angle  $\theta_c = \arcsin(n_2/n_1)$ , the ray will be totally internally reflected ( $\theta_2 = \theta_1$ ). Because FDOCT assumes light travels in a straight A-line, the model translated the recorded geometric path lengths into straight optical path lengths (Figure 51(b)) to create a simulated FDOCT image (Figure 51(d)). In order to visually make the borders of the modeled shapes more apparent, a point spread function (PSF) in the form of an ellipsoidal Gaussian distribution with a width equal to twice the 12  $\mu\text{m}$  lateral resolution and a height equal to twice the 8  $\mu\text{m}$  axial resolution of the FDOCT system was applied with a 2D convolution (examples: Figure 51(d), Figure 53(b)). This PSF convolution was, however, not performed at any point during the quantitative analyses.

### Validation with phantoms

In order to validate the model qualitatively, FDOCT images of glass capillaries were compared to simulated images of two concentric circles taking into account refraction and total internal reflection. The glass capillaries were filled with air or different refractive index oils (Cargille Labs). In the model, the refractive index of the surrounding medium, shell and circular area inside the shell could be defined to simulate the expected contours of an FDOCT image. The refractive index of glass was assumed to be 1.5. Figure 52 shows the excellent agreement in glass capillary contours between the actual and simulated images.

The model further provided an explanation for the streaking-effect observed on hollow glass beads in a sample containing several beads in translucent epoxy. The thin-walled ( $\sim 5$  to  $10 \mu\text{m}$ ) hollow beads were modeled as circular geometries of refractive index 1 in a surrounding of refractive index 1.5. Figure

53 shows that reflections appearing below the bead could be the result of other beads that are present in the sample at specific distances. The streaking artifact could be successfully induced in the simulated image by adding adjacent virtual beads.

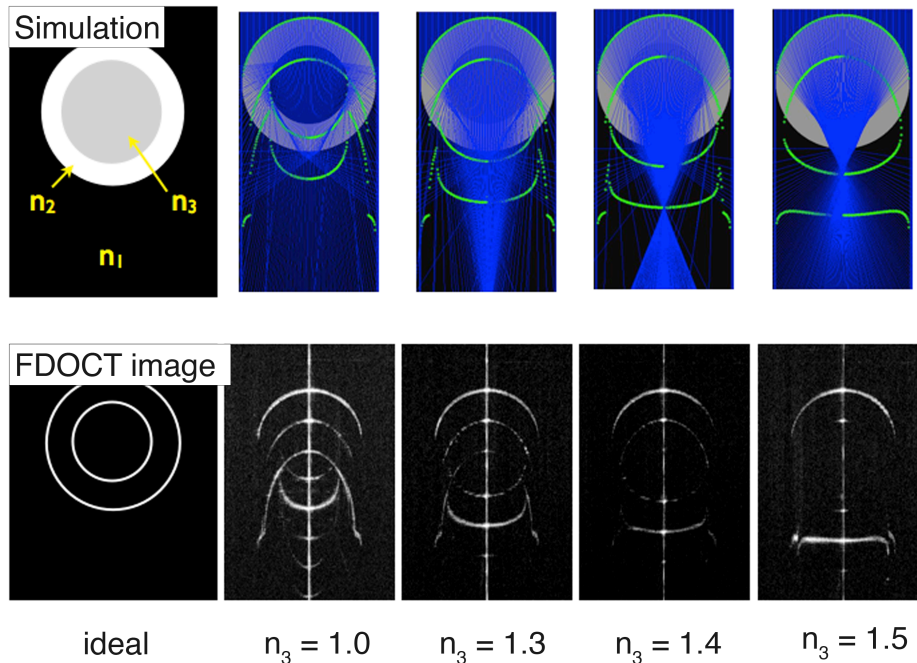


**Figure 52:** Comparison of FDOCT images of glass capillaries (gc) to the ray-trace simulation results (simulated rays in blue, simulated gc image contours in green). Gc were filled with air ( $n_3 = 1$ ) or different refractive index oils ( $n_3 = 1.3, 1.4, 1.5$ ).

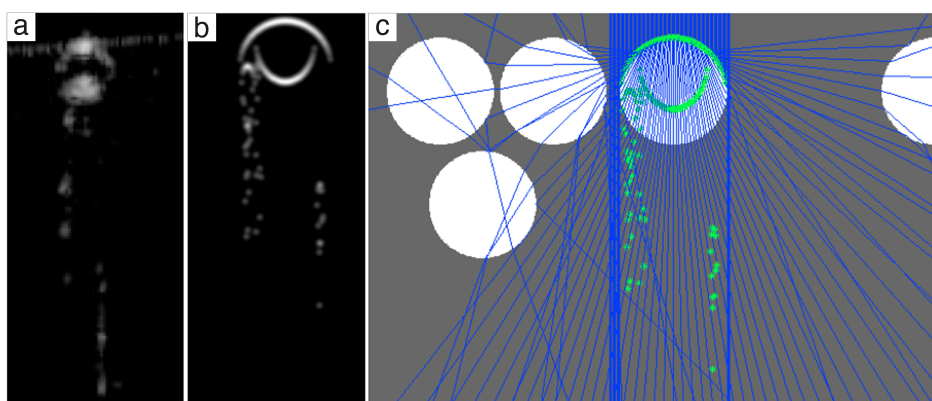


**Figure 53:** Comparison of an FDOCT image of one hollow glass bead (a) in an epoxy sample containing several beads to a simulated image (b) based on ray-trace modeling (c) assuming bead filling with air ( $n = 1$ ) and epoxy of refractive index  $n = 1.5$ . The streaking effect observed in (a) could be reproduced in (b) through virtual adding of beads at specific distances from the simulated bead.

### Modeling of refraction effects in alveolar tissue

For the simulation of alveolar cross-sections, the shape of a rounded rectangle approximated best the average cross-section observed in micro-CT images of pulmonary alveoli. Alveolar cross-sections were therefore simulated as superellipses of order 4 with height  $h$  and width  $w$ :

$$\left(\frac{x}{w}\right)^4 + \left(\frac{z}{h}\right)^4 = 1 \quad (3.15)$$

where  $x$  is the direction parallel to the *en-face* plane and  $z$  is parallel to the axial plane (Figure 54). Relations based on the shape of the superellipse can be defined by ratio of the height  $h$  to the width  $w$ , or the aspect ratio  $f$ :

$$f = \frac{h}{w} \quad (3.16)$$

Figure 54 visualizes the superellipse shape of aspect ratio  $f$ , which was modeled in two dimensions as the approximate true shape of an alveolar cross-section. The corresponding cross-sectional area (CS), perimeter (P), volume (V) and surface area (SA) were calculated directly from the discretized shape embedded in a larger two-dimensional matrix (index mask). In this index mask, the pixels of the alveolar shape and the surrounding are distinguished through their different numerical values (detail A of Figure 54). Consecutive pixels along a constant  $x$  location are referred to as columns, while pixels along the same  $y$  location are referred to as rows. Calculating the quantitative size parameters from the index mask allows direct comparison between the parameters of the original and simulated alveolar shape. The CS was determined as the number of (square) pixels inside the discretized shape. For example, the pixel inside the discretized superellipse in Figure 54 could be represented by the number 1, whereas pixel outside the superellipse are represented by a different number. Therefore, the CS in the original index mask and later also in the simulated FDOCT image can be computed by finding the number of pixels in the respective index mask that are equal to 1. The P was approximated as the sum of all the hypotenuses between the ends of subsequent rows describing the contour of the discretized shape (detail A of Figure 54) adding the radii  $r_{(1)}$  and  $r_{(h)}$  of the first and last row, respectively:

$$P = 2 \cdot \sum_{z=1}^h \sqrt{r_{(z+1)}^2 + r_{(z)}^2} + r_{(1)} + r_{(h)} \quad (3.17)$$

In order to calculate the quantitative three-dimensional size parameters  $V$  and  $SA$ , the three-dimensional alveolar shape was approximated as a rotationally symmetric object with superellipse cross-section in the axial plane and circular cross-section in the lateral plane as sketched in Figure 54. The  $V$  was computed as the sum of circular slices with area  $r_{(z)}^2 \pi$  and thickness  $\Delta z$  through the height of the superellipse:

$$V = \sum_{z=1}^h r_{(z)}^2 \pi \cdot \Delta z \quad (3.18)$$

The surface area was approximated according to the first Guldinus theorem for rationally symmetric objects:

$$SA = 2\pi \cdot L \cdot R_{grav} \quad (3.19)$$

where  $L$  is the arc length of the generating curve of the object (and equal to half of the perimeter  $P$ ) and  $R_{grav}$  the centroid of the curve  $L$  with respect to the symmetrical axis (Figure 54).  $R_{grav}$  was approximated by summing the products of the distance (from  $z$ ) and the length of the hypotenuse between rows  $r_{(z+1)}$  and  $r_{(z)}$ , normalized by the overall length  $L$ , throughout the height of the discretized shape:

$$R_{grav} = \sum_{z=1}^h \left( r_{(z)} + \frac{1}{2}(r_{(z+1)} - r_{(z)}) \right) \cdot \frac{\sqrt{1 + (r_{(z+1)} - r_{(z)})^2}}{L} \quad (3.20)$$

Lastly, the modeled quantitative size parameters ( $m$ ) between the original index mask and the simulated FDOCT image were compared and expressed as the predicted error:

$$E_{pred} = \frac{m_{original} - m_{simulated}}{m_{original}} \quad (3.21)$$

It was hypothesized that this predicted error could serve as a correction factor for measurements of alveolar size in actual FDOCT images of pulmonary alveoli. In order to establish an equation to calculate the correction factors for a given alveolar aspect ratio and refractive index ratio between the alveolar tissue and the filling, the predicted error was simulated and computed for a range of aspect ratios ( $f = 0.4$  to  $2$  with an increment of  $0.1$ ) and refractive

index ratios ( $n_{ratio} = n_{tissue}/n_{air} = 1.04$  to  $1.61$  with an increment of  $0.01$ ). Using Matlab's surface fitting toolbox, separate polynomial equations were then deducted from the discrete modeling results to approximate the correction factor as a function of  $f$  and  $n_{ratio}$  in the tested range for all size parameters. Figure 55 visualizes this process for one example parameter, namely cross-sectional area. For all parameters, the lowest orders of the polynomial were chosen that provided a fit with residuals less than 5% error. The goodness of fit of the chosen equations was characterized by  $R^2 > 0.99$ , with the exception of the perimeter, where  $R^2 > 0.91$ . The modeling predicted error is shown to depend on both  $n_{ratio}$  and the aspect ratio of the alveolus, such that alveoli with an aspect ratio below 1 (short and wide) will be visualized with less error. Equation (3.22) was derived to compute the error for the example cross-sectional area (the equations for all parameters are discussed in subsection 4.2.2):

$$E_{pred} = -93.8 - 0.901f + 129n_{ratio} - 3.01f^2 + 17.9fn_{ratio} - 44.6n_{ratio}^2 \quad (3.22)$$

Accordingly, the ray-trace modeling results predict a 22% underestimation for the cross-sectional area of the simulated FDOCT image compared to the original index mask for a superellipse with equal width and height and a refractive index ratio between the tissue and alveolar filling  $n_{ratio} = 1.53$  (fixed alveolar tissue, air-filled alveoli). For the same refractive index ratio, but an alveolar aspect ratio of 1.2 the modeling predicted percent errors is 26% for cross-sectional area.

The following sections illustrate how the modeling results compare to the experimentally observed difference in alveolar size between FDOCT and micro-CT images. Further, the established correction factors are used to rescale original size measurements from FDOCT images and the results are evaluated against the micro-CT measurements.

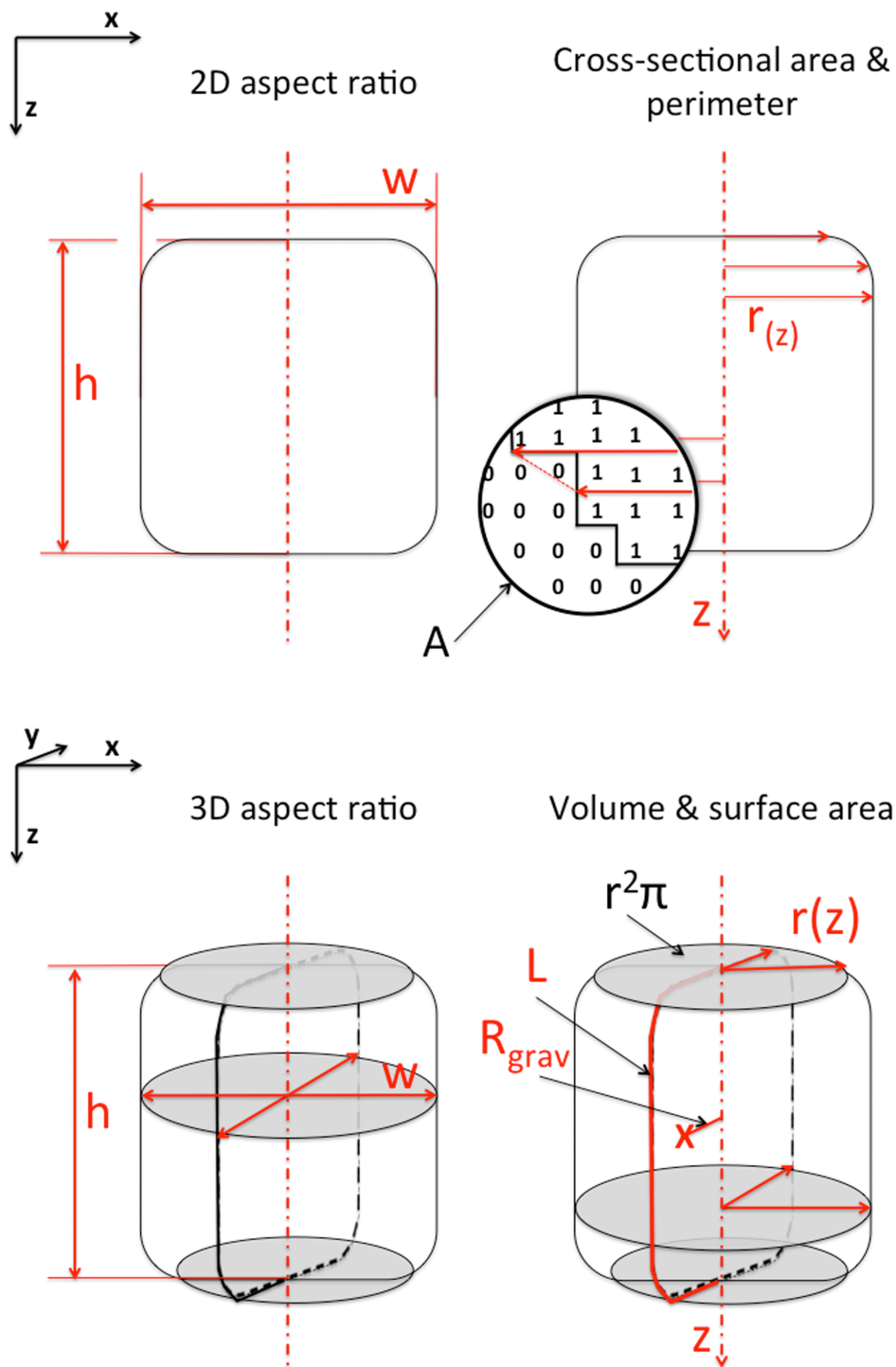


**Figure 54: Illustration of the modeled alveolar shape: A superellipse cross-section characterized through its aspect ratio and embedded in a larger matrix (index mask) was modeled in two dimensions. The three-dimensional shape was assumed rotationally symmetric around axis  $z$ . Two- and three-dimensional size parameters were calculated directly from the discretized shape (details described in the text).**

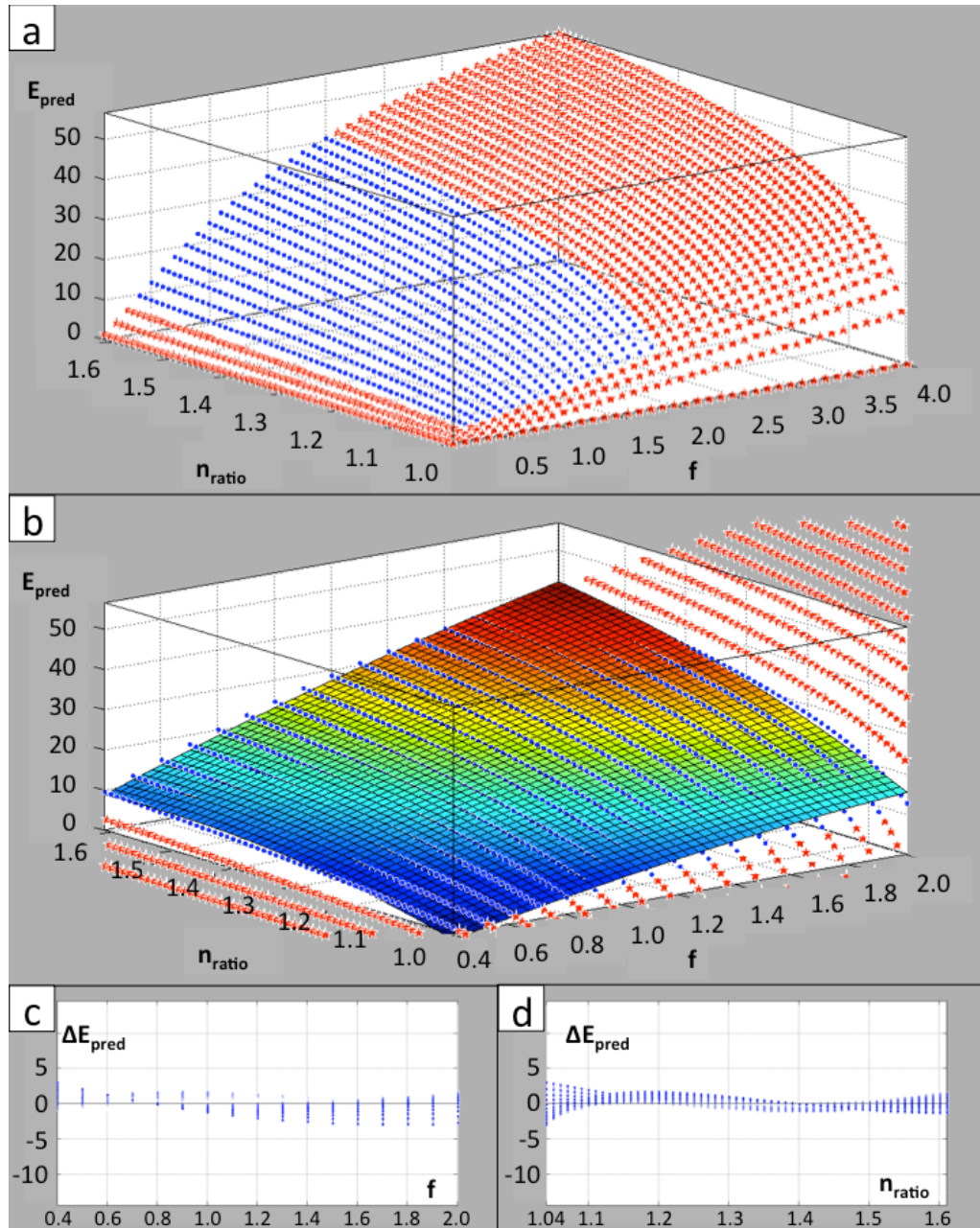


**Figure 55:** Schematic illustrating the establishment of correction factors based on ray-trace modeling for the example of cross-sectional area. A polynomial was fit to discrete modeling results of predicted cross-sectional area error  $E_{pred}$ . (a) Discrete modeling results were initially evaluated for  $f = 0.1$  to  $4.0$  and  $n_{ratio} = 1.0$  to  $1.61$ , a polynomial was fit to a restricted interval for  $f = 0.4$  to  $2.0$  and  $n_{ratio} = 1.04$  to  $1.61$  (blue dots), (b) overlay of the fitted polynomial from equation (3.22), (c-d) difference  $\Delta E_{pred}$  between actual data point and fitted polynomial visualized in the two different two-dimensional planes.  $\Delta E_{pred}$  stayed below 5% for the interval of interest.

#### **3.4.4 Statistical analysis to assess the agreement of FDOCT with micro-CT measurements of alveolar size**

As previously described, 29 alveolar cross-sectional areas from 29 different alveoli have been measured using manual segmentation of the contours of each 2D alveolar cross-section for the two different technologies, micro-CT and FDOCT. The micro-CT measurement was accepted as the true value of the specific cross-sectional area. In the context of this thesis work, it was essential to evaluate whether the other technology, FDOCT, can also provide true values of alveolar cross-sections and this is done by comparison to the gold standard. Therefore, the following questions need to be answered:

- Are and how closely are the two measurements from the different technologies related to each other?
- Could FDOCT be used to predict the same values than micro-CT?
- What is the estimated bias between the two measurements?

The following subsections illustrate how these questions are addressed on the example of alveolar cross-sectional area measurements. The same approach is used consistently to evaluate the other size parameters, namely perimeter, volume, and surface area.

##### **Correlation**

In order to evaluate the degree to which two variables are related, a correlation analysis is typically performed, where the value of the correlation coefficient  $R$  will indicate how much one variable will change with the other.  $R$  values can vary from  $-1$  to  $+1$ , where positive  $R$  values indicate that the two variables increase together, and  $R = 1$  indicates a perfect positive correlation. The software Prism offers two choices to compute the correlation coefficient, namely Pearson and Spearman correlation. The Pearson correlation will be performed in the case of Gaussian distributed samples with a linear relationship while the Spearman correlation makes no assumption about the samples' distribution, and will be relevant in the more generic case of any monotone relationship. In order to test whether the distribution of alveolar sizes were normally distributed, a Shapiro-Wilk normality test was performed. The null hypothesis of this test is that the distribution does follow a Gaussian

distribution. Thus, small p-values indicate non-normally distributed distributions. While most of the parameters analyzed in this work provided non-conclusive results with p-values  $> 0.05$ , important parameters, such as healthy alveolar volume and surface area were clearly non-normally distributed ( $p < 0.0001$ ). In order to provide a consistent and comparable analysis for all data sets, no normal distributions were assumed for the correlation analysis and the Spearman correlation coefficient  $R$  was determined for all size parameters utilizing for each measurement in the sample its rank in the sample rather than its absolute value:

$$R = \frac{\sum (x_i - \bar{x})(y_i - \bar{y})}{\sqrt{\sum (x_i - \bar{x})^2} \sqrt{\sum (y_i - \bar{y})^2}} \quad (3.23)$$

where  $x_i$  is the rank of a data point in sample  $X$ , for example the cross-sectional area of alveolus 1 measured with FDOCT, and  $y_i$  is the rank of the corresponding data point in sample  $Y$ , such as the cross-sectional area of alveolus 1 measured from the micro-CT image.  $\bar{x}$  is the average of the ranks  $x_i$ ,  $\bar{y}$  is the average of the ranks  $y_i$ .

Figure 56 shows the distribution of the 29 previously mentioned cross-sectional areas as a comparison. As a result of the non-parametric correlation analysis, the Spearman correlation coefficient  $R$  is determined to be 0.95 with a 95% confidence interval of 0.89 to 0.98 and a p-value for the correlation of  $p < 0.0001$ . The two measurements seem therefore highly correlated to one another where one increases with the other. In conclusion, a measured alveolar cross-sectional area in FDOCT will be highly correlated to the area as measured in micro-CT: FDOCT is capable of measuring relative alveolar cross-sectional area. However, it cannot be concluded that the absolute measured values are the same. In order to further investigate absolute size measurements, a linear fit between the data points was performed.

### **Linear fit**

In spite of the high correlation between the two measurements, this analysis does not allow concluding that measurements made from FDOCT images could be used to predict the micro-CT measurements. Further, no conclusion about a possible correction factor could be drawn. Therefore, the relationship

between the FDOCT ( $x$ ) and the micro-CT measurements ( $y$ ) was determined by fitting a straight line. The corresponding line equation with slope  $m$  and intercept  $t$  describes then the best way to predict  $y$  from  $x$ . The goodness of fit is described by the parameter  $R^2$ . Note that  $R^2$  is equivalent to the squared Pearson correlation coefficient ( $R$ ), and not necessarily equivalent to the squared Spearman  $R$ . In the presented case, the difference appears marginal. The following table shows these results for the cross-sectional area example:

Slope	Intercept [ $\mu\text{m}^2$ ]	$R^2$
1.19	4451	0.93

The slope of this best fit line ( $R^2 = 0.93$ ) was greater than one, and thus measurements made from FDOCT images seem to systematically underestimate the absolute true values. Figure 56 visualizes the linear fit graphically.

It is interesting to note, that this line fitting is similar to a linear regression. A full linear regression analysis, however, depends on the assumption of normally distributed data in order to provide confidence intervals of the slope, or to test whether the slope is significantly different from zero. In this test, the null hypothesis of the slope being equal to zero is tested and the probability, that, given this data, the null hypothesis would be incorrectly rejected (p-value), is determined. In other words, if the result of the linear regression analysis was a slope of 0.5, the p-value estimates the probability, that the slope was determined to be greater than zero, although it was in fact equal to zero. A p-value lower 0.05 is generally considered statistically significant.

If differences between the measurements rather than the actual measurements are compared as a function of alveolar sizes, these differences are now normally distributed and a true linear regression analysis can be performed. Compared to the very high correlation of the first linear fit, the  $R^2$  value when looking at the difference between the two measurements was much lower (around 0.25) and predicting one from the other seemed less precise. However, testing whether the slope in this relationship is statistically different from zero is equivalent to testing whether the original slope was equal to one. Since now the error in FDOCT measured values is predicted as a function of the alveolar size as measured in micro-CT, the slope  $m$  and the intercept  $t$  in the line

equation  $y = m \cdot FDOCT_{area} + t$  have to be equal to zero if the two measurements are the same. This was with high probability not the case in the given example ( $p < 0.05$ ). Consequently, it could be concluded from the linear regression that there is a significant difference between the two measurements. Further, the error was size dependent. It is important to state, however, that the conclusion of significant difference is often criticized in the context of basic science research, where the data rarely meets the required assumptions for the test (Gaussian distribution, number of data points, etc.) (111). Moreover, if the test result was “not significant”, one could not conclude that the slope and intercept are indeed equal to zero; one could solely state that the test for this specific data was not conclusive.

### **Estimation of bias**

Depending on the specific research question, a certain bias in the data could be acceptable and a difference below 10% is often considered noise. Under the assumption of normally distributed data, the range of error in the evaluated data set (intra-data variability) can be estimated using the mean error and the spread of the data characterized by the standard deviation (SD). 95% of the data can then be expected to lie between the mean  $\pm 2SD$ . Further, based on the results of this study, one could possibly want to establish correction factors to scale future measurements made with FDOCT in order to conclude absolute alveolar size. Therefore, the inter-data variability must be estimated, which will be larger than the intra-data variability and the difference will depend on the sample size of the original data set. Further, each set of initial measurement data would result in a different correction factor. In this work, correction factors were not derived from the experimental results, because they could successfully be derived from an independent model that was in good agreement with the experimental results. Nevertheless, it is interesting to further characterize the expected inter-data variability. Therefore, an additional uncertainty has to be added to the mean and to the upper and lower limits (mean  $\pm 2SD$ ). Under the assumption of normally distributed data, the bias can be estimated by calculating the 95% CIs with help of the standard error (SE) (112):

$$SE_{mean} = \frac{SD}{\sqrt{n}}, \quad SE_{mean \pm 2SD} = \sqrt{\frac{3 \cdot SD}{n}}$$

For the analysis of the bias, a method similar to what has been suggested by Bland and Altman was followed (113). In contrast to Bland and Altman, however, micro-CT measurements were here considered as the true values and thus the two measurement methods were not compared with each other, but FDOCT was evaluated against the gold standard. The error in the FDOCT data normalized by the respective micro-CT measurement was computed and the respective bias is visualized Figure 56.

The mean error for the given sample was 26.6% with a SD of 10.2%. Thus, about 95% of the data lie in the range between 6% (mean-2SD) and 47% (mean+2SD) error in this data set (intra-data variability) (113).

The inter-data variability is estimated with the help of the 95% CI of the mean and the upper and lower limit. The mean error in a hypothetical different data set would be expected between 22.8% and 30.5% as shown on the scatter dot plot on Figure 56. The upper limit would be expected to extend to about 56.7% and the lower limit could be as low as -3.5% (Table 5).

It is important to note that these calculations could be slightly conservative for high alveolar sizes and slightly optimistic for small alveolar sizes, since the spread in percent error seems to become narrower with an increase in alveolar size.

### **Possible correction factors from the experiment**

Having evaluated the expected error in FDOCT measurements with respect to the gold standard, correction factors for future measurements in similar data sets could theoretically be established. For example, the mean percent error could be used to scale future FDOCT measurements to obtain absolute values of alveolar size. The expected spread of the data would be similar to the previously evaluated 95% CI of the percent error in the here evaluated case. However, the validity of these correction factors would need to be tested in a completely independent data set to evaluate their effectiveness, precision and applicability to different alveolar sizes, shapes, tissue refractive indices, etc. Such factors would then need to be re-established for each specific situation of

interest, which is tedious and not feasible in many cases. As mentioned previously, correction factors were not derived from this experiment, because an independent ray-trace model was created in this work that successfully provided such correction factors.

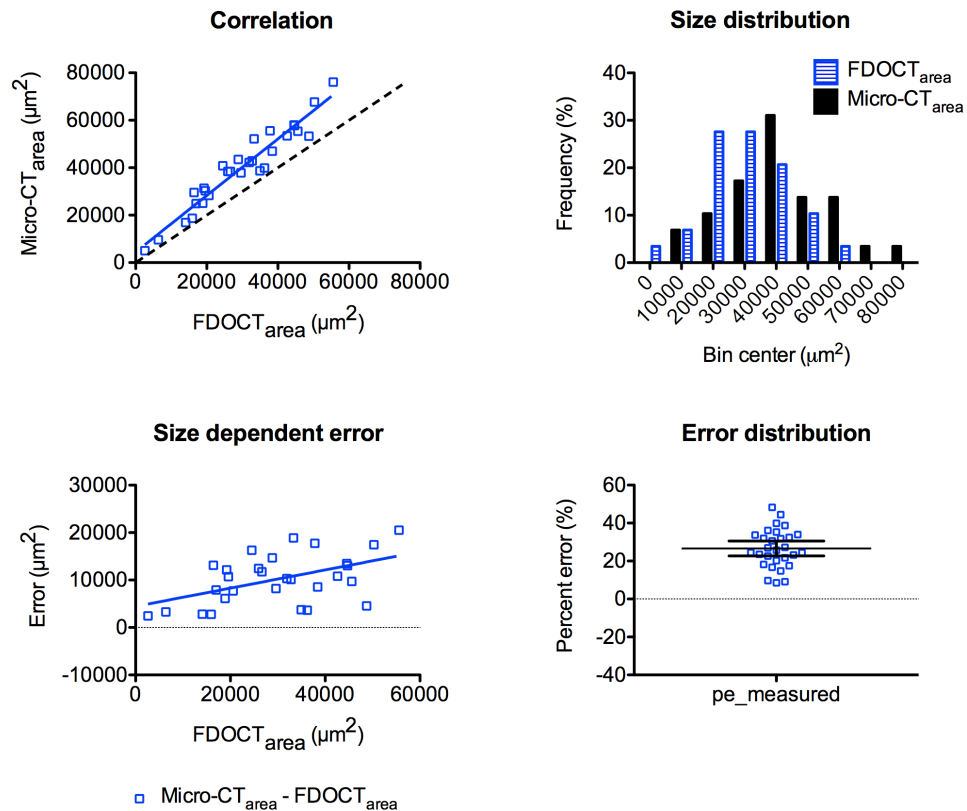


**Figure 56: Comparison of micro-CT size measurements *versus* FDOCT measurements of cross-sectional area. Upper left: micro-CT measurements *versus* FDOCT measurements and the linear fit. The dashed line represents the identity line indicating perfect agreement. Upper right: Comparison of alveolar size distributions. Lower left: Measurement errors *versus* FDOCT measurement. Lower right: Visualization of the mean percent error and 95% CI of the mean error.**

### Summary

In summary, when analyzing the agreement of FDOCT to micro-CT data of alveolar sizes, a preliminary non-parametric correlation analysis was performed to prove the correlation between the two measurements. Further, a linear regression on the representation of the measurement error in the unit of

the respective alveolar size was used to evaluate whether the two values correspond in absolute terms. The observed intra- and inter-data bias were estimated quantitatively using the mean, standard deviation and 95% CIs of the measurement error.

#### **3.4.5 Statistical analysis to assess the agreement of scaled FDOCT with micro-CT measurements of alveolar size**

In the context of this work, a ray-tracing model was developed that calculates the expected error in FDOCT measurements compared to micro-CT measurements based on the effect of refraction and provided scaling factors to approximate absolute alveolar size from FDOCT images as introduced in paragraph 3.4.3. In order to test the validity of the model, the available FDOCT measurements of alveolar size were scaled accordingly, and were then compared to the corresponding micro-CT measurements. The comparison was performed as outlined above for the original un-scaled measurements. Figure 57 and Table 5 illustrate the comparison between the original and modeling corrected data for the example of cross-sectional area measurements.

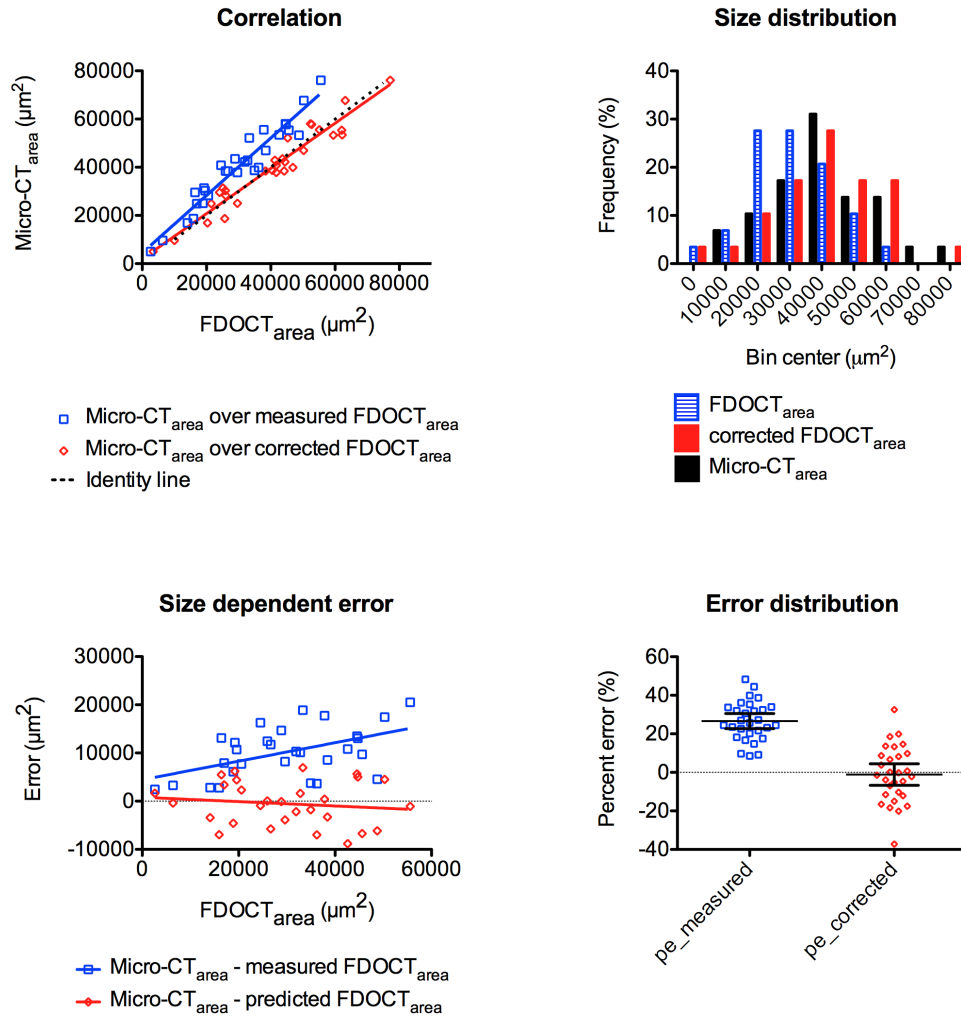


**Figure 57: Comparison of micro-CT and corrected FDOCT size measurements versus the originally measured, un-scaled FDOCT measurements of cross-sectional area. The original situation is represented by blue rectangles, the corrected situation by red diamonds. Upper left: micro-CT and scaled FDOCT measurements versus un-scaled FDOCT and the linear fits. The dashed line visualizes the identity line indicating perfect agreement. Upper right: Frequency distributions. Lower left: Measurement errors versus FDOCT measurement. Lower right: Visualization of the mean percent error and 95% CI of the mean for the originally measured and the corrected values.**

**Table 5: Overview of values comparing micro-CT versus scaled and un-scaled FDOCT measurements of cross-sectional area of fixed swine alveoli.**

	Value ranges [ $\mu\text{m}^2$ ]			Correlation		Linear fit $M_{\text{CT}} = \text{sl} * M_{\text{OCT}} + \text{t}$	
	Min	Max	Median	R	p	sl	t [ $\mu\text{m}^2$ ]
CT	5046	76102	39872	0.96	<0.0001	1.2	4451
FDOCT_ measured	2607	55582	29612				
FDOCT_ scaled	3405	77187	41715	0.93	<0.0001	0.94	1990
	Linear regression $(M_{\text{micro-CT}} - M_{\text{OCT}}) = \text{sl} * M_{\text{OCT}} + \text{t}$						
	R <sup>2</sup>	sl	p <sub>m</sub>	sig?	t	p <sub>t</sub>	sig?
FDOCT_ measured	0.25	0.19	0.006	y	4451	0.044	y
FDOCT_ scaled	0.05	-0.06	0.225	n	1990	0.37	n
	Estimated bias in percent error (%) $(M_{\text{micro-CT}} - M_{\text{OCT}}) / M_{\text{micro-CT}}$						
	Mean	SD	Mean- 2SD	Mean+2 SD	SE	95% CI mean	95% CI limits
FDOCT_ measured	26.6	10.2	6.2	47.0	1.9	22.8 to 30.5	-3.5 to 56.7
FDOCT_ scaled	-1.1	14.7	-30.6	28.3	2.7	-6.7 to 4.5	-40.3 to 38.0

## 4 RESULTS

The overall goal of this work was to develop an imaging tool to visualize and quantify mammalian pulmonary alveoli for the study of healthy and diseased alveolar structure and function. This chapter presents the results that were obtained to meet this goal. First, images of pulmonary alveoli are shown including the first *in-vivo* visualization of alveoli during uninterrupted ventilation within healthy (54) and emphysematous swine. Second, quantitative alveolar measurements obtained from FDOCT images are compared to the results of micro-CT images and ray-trace modeling results (56). The chapter closes with preliminary quantitative investigation into alveolar physiology and pathophysiology.

### 4.1 FDOCT images of pulmonary alveoli

This section demonstrates the ability of FDOCT to visualize mammalian pulmonary alveoli in different species and throughout the entire breathing cycle within healthy and emphysema swine models.

#### 4.1.1 Three-dimensional visualization of mammalian alveoli across species

Figure 58 shows example *en-face* images of subpleural alveoli from freshly excised mouse, rat, rabbit, and swine lung. Alveoli could be visualized by FDOCT in all of these four species. As expected (44, 49, 102), alveolar arrangements across species closely resemble each other and a qualitative assessment of alveolar sizes shows similar ranges for the rodents and rabbit alveoli ( $\sim 50\text{-}150\ \mu\text{m}$ ) with comparatively large alveoli in the swine model ( $\sim 100\text{-}300\ \mu\text{m}$ ). A thorough quantitative comparison of alveolar sizes would require strict consistency in image acquisition at the same inflation pressures, times, and location, and was not performed. In this work, the swine model was further investigated, because of the close resemblance in overall lung size and morphology to humans as outlined in section 3.1.

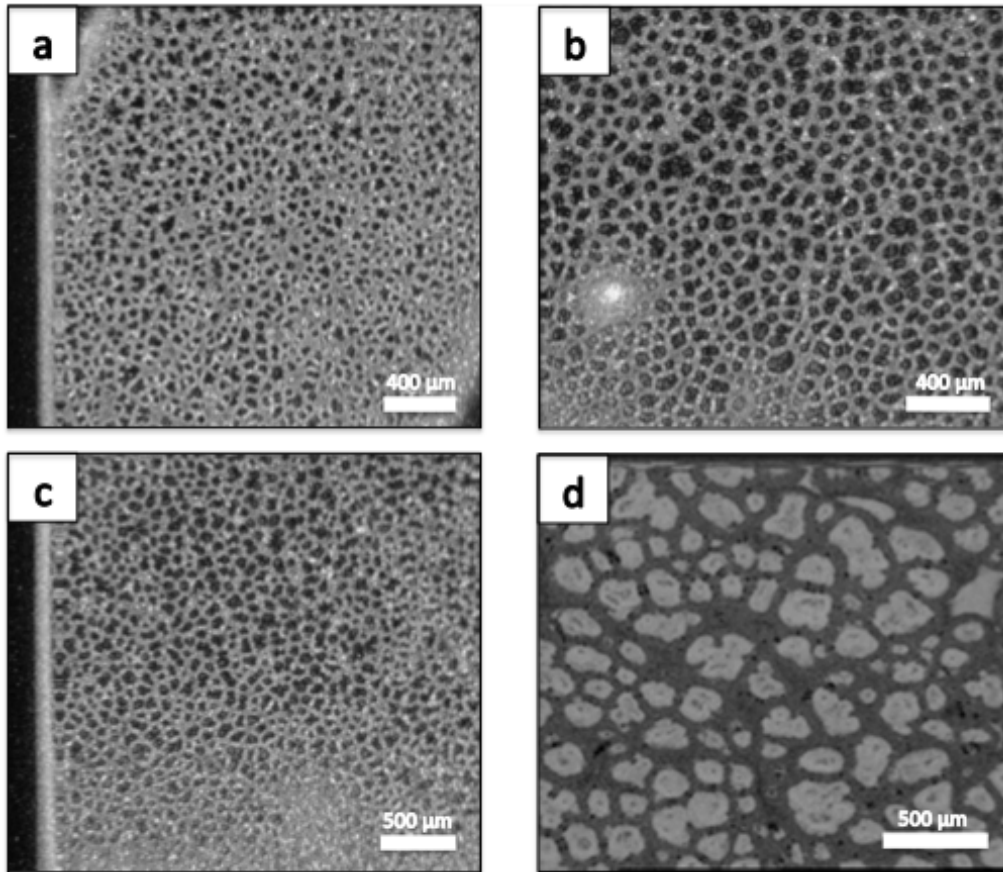


**Figure 58:** *En-face* FDOCT images of mammalian subpleural alveoli from different species: a) mouse, b) rat, c) rabbit, and d) swine. Lungs were freshly excised and inflated to airway pressures between 20 – 30 cmH<sub>2</sub>O.

#### 4.1.2 Four-dimensional visualization of healthy alveolar motion *in-vivo*

Figure 60 and Figure 59 show FDOCT images and segmentation of subpleural swine alveoli from the right middle lobe acquired *in vivo* during continuous ventilation (54). Compared to the previously presented images of fixed and freshly excised alveolar tissue, the *en-face* plane in Figure 60 shows a higher tissue/air ratio and limited appearance of the double wall effect (83). The field of view in Figure 59 contains approximately 34 air spaces that expand and contract as a function of the inflation pressure. Volume renderings were produced from the segmentation to visualize the arrangement and 3D structure of the air spaces more intuitively. Further, the volume could be calculated and the relative expansion was quantified as shown color-coded in Figure 59(d). Subsection 4.3.1 summarizes the quantified results in detail.

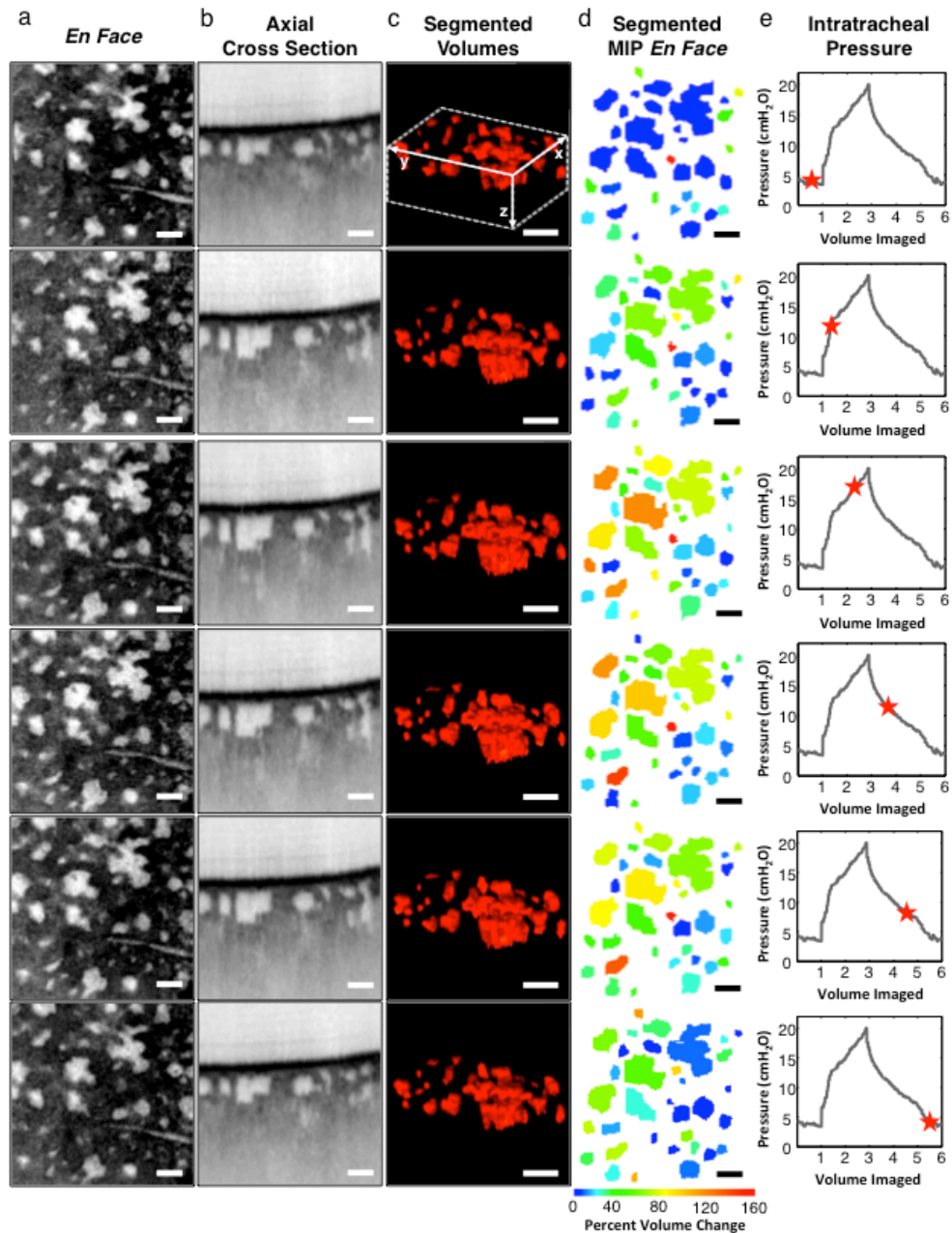


**Figure 59:** (a) *En-face* and (b) axial cross-sectional FDOCT images of subpleural swine alveoli acquired over one respiratory cycle *in vivo* during continuous ventilation with 10 bpm, 3 cmH<sub>2</sub>O PEEP, 20 cmH<sub>2</sub>O PIP. (c) Four-dimensional rendering of 34 segmented air spaces. (d) Maximum intensity projection (MIP) *en-face* visualization of color-coded percentage volume change of each air space over the respiratory cycle. (e) Intratracheal pressure trace during the respiratory cycle where the red star denotes mean intratracheal pressure during the volume acquisition. Scale bar = 100  $\mu$ m. [Adapted from (54).]

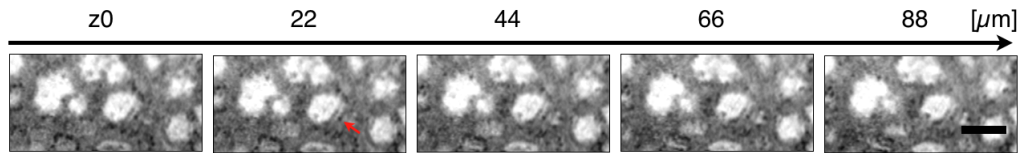


**Figure 60: Depth series of *en-face* FDOCT images of healthy swine alveoli at constant inflation state ( $\sim 15\text{-}20$  cmH<sub>2</sub>O) showing limited appearance of double walls (example highlighted with red arrow). Depth is given relative to a plane z0 directly under the pleura. Scale bar = 200  $\mu\text{m}$ .**

### 4.1.3 Four-dimensional visualization of emphysematous alveolar motion *in-vivo*

Pulmonary alveoli within the lower left lobe of three healthy (control group) and three emphysematous swine (study group) were imaged with FDOCT *in-vivo* during uninterrupted ventilation. Thus far, one emphysematous swine could be analyzed and compared to the healthy *in-vivo* data previously shown. Figure 61 shows the expansion and contraction of the emphysematous swine alveoli as a function of the inflation pressure similar to the results from healthy swine in Figure 59. The color-coded volume change in Figure 61(d) visualizes the restricted relative expansion (volume change normalized to minimum volume during three breaths) compared to the expansion seen in healthy alveoli. Further, the relative expansion is more uniform. However, because of the generally larger size of the emphysematous air spaces, the absolute expansion (in units of nl) is larger. Subsection 4.3.2 summarizes the quantified results in detail. Figure 62 shows a direct qualitative comparison of FDOCT images of healthy and emphysematous subpleural swine alveoli acquired *in vivo* during continuous ventilation. The tissue/air ratio in the emphysematous alveoli appears lower than in the healthy swine and double walls can be frequently observed in Figure 63 approximating previous results in fixed and freshly excised lungs.

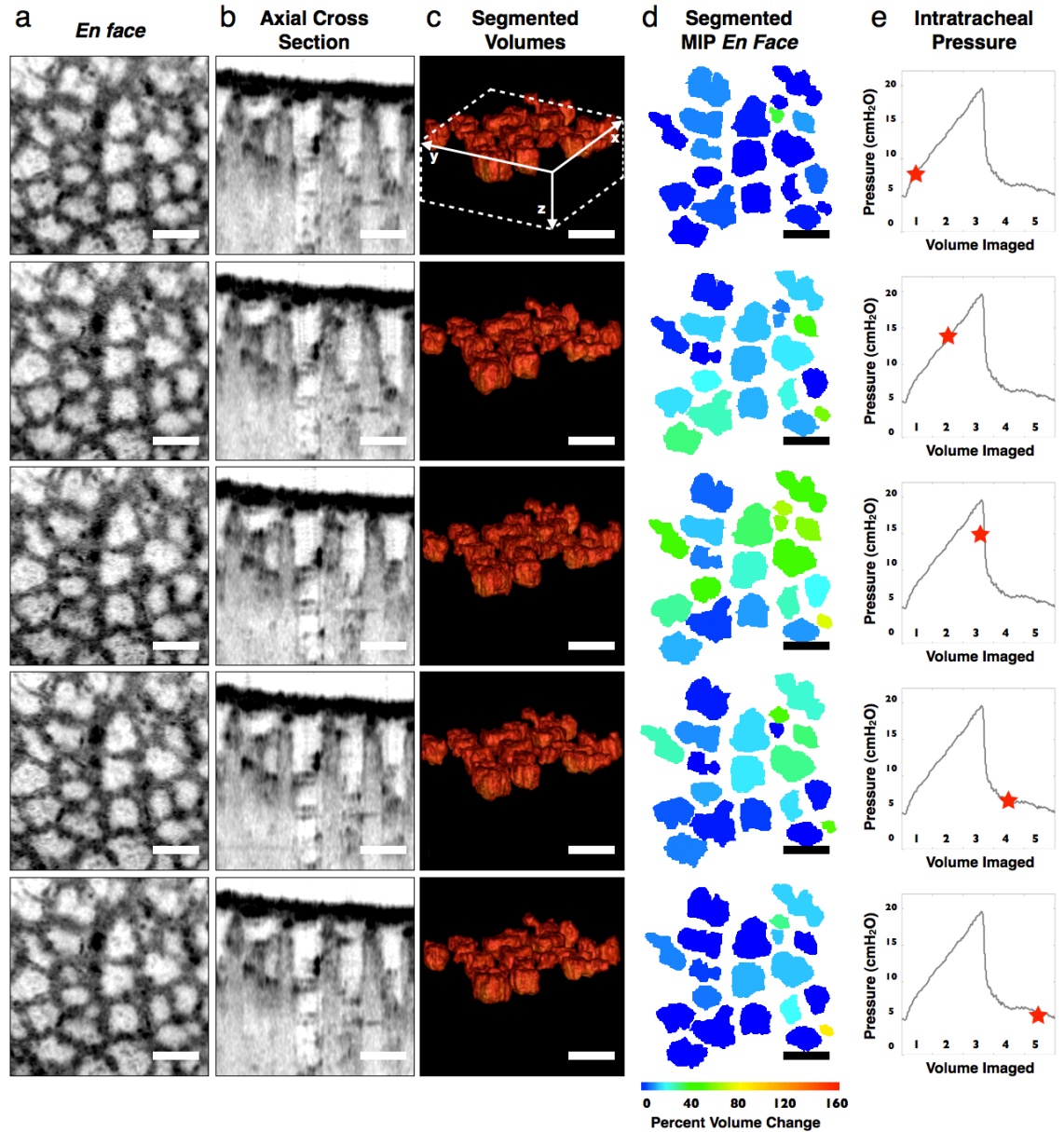


**Figure 61:** (a) *En-face* and (b) axial cross-sectional FDOCT images of subpleural emphysematous swine alveoli acquired over one respiratory cycle in vivo during continuous ventilation at 11 bpm, 4.7 cmH<sub>2</sub>O PEEP, 20 cmH<sub>2</sub>O PIP. (c) Four-dimensional rendering of 20 segmented subpleural alveolar air spaces. (d) Maximum intensity projection (MIP) en-face visualization of color-coded percentage volume change of each alveolar air space over the respiratory cycle. (e) Intratracheal pressure trace during the respiratory cycle where \* denotes mean intratracheal pressure during the volume acquisition. Scale bar = 200  $\mu$ m.

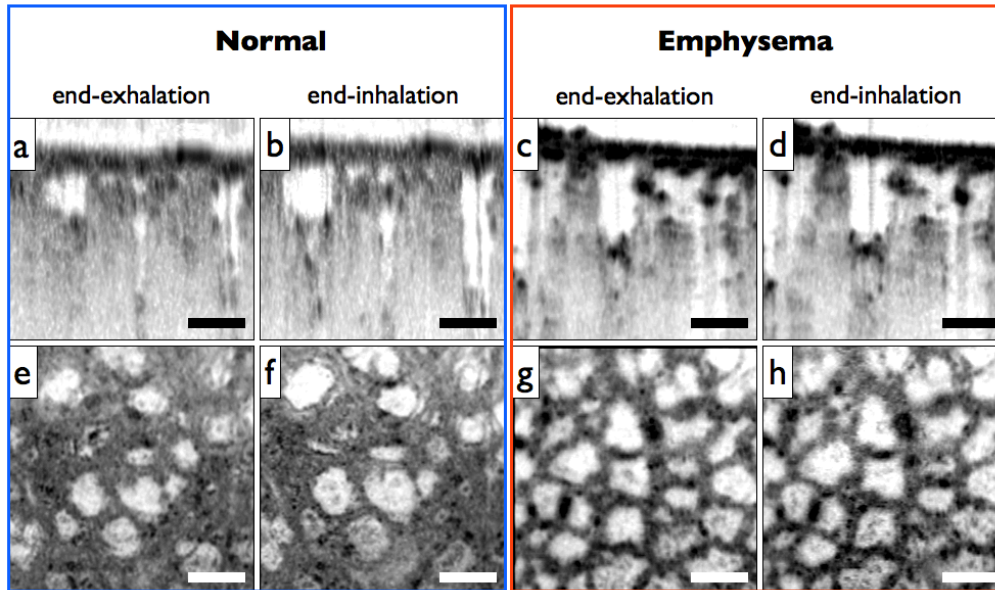


**Figure 62:** Comparison of cross-sectional (top row) and respective *en-face* (bottom row) FDOCT images of normal (left, blue frame) and emphysematous (right, red frame) subpleural swine alveoli at end-exhalation (low alveolar volume) and end-inhalation (high alveolar volume). Scale bars = 200  $\mu\text{m}$ .

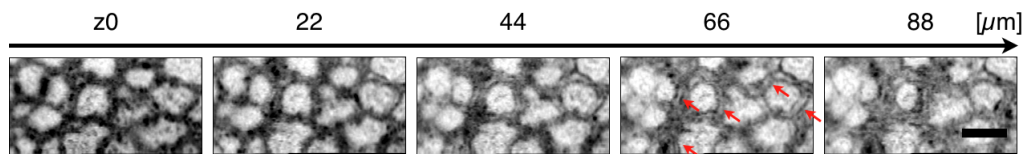


**Figure 63:** Depth series of *en-face* FDOCT images of emphysematous swine alveoli showing the increasing appearance of double walls with increasing depth from a plane  $z_0$  directly under the pleura (examples highlighted with red arrows). Scale bar = 200  $\mu\text{m}$ .

To confirm the clinical appearance of emphysema in the study group compared to the control, X-ray images of healthy and emphysematous lungs were acquired of the freshly excised lungs following the FDOCT imaging procedures. The lungs were then fixed and CT scans were obtained. Figure 64 and Figure 65 show example X-ray and CT images, respectively. While the two-dimensional projection X-ray images fail to show clear signs (decreased density) of an emphysematous lower left lobe in the study lung, the CT images reveal a heterogeneous density pattern in the diseased lobes with large air bullae characterized by low absorption of X-rays.

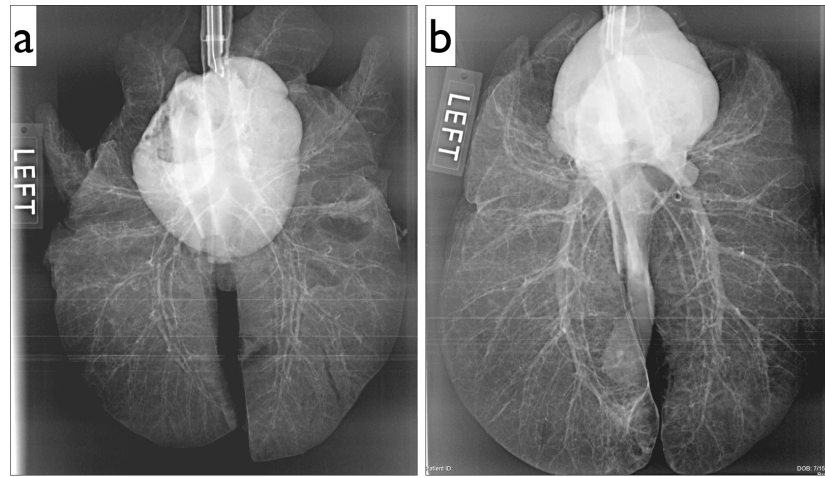


**Figure 64:** X-ray images of freshly excised normal (a) and emphysematous (b) swine lung. Tissue density appears uniform in both lungs in these 2D projection images.

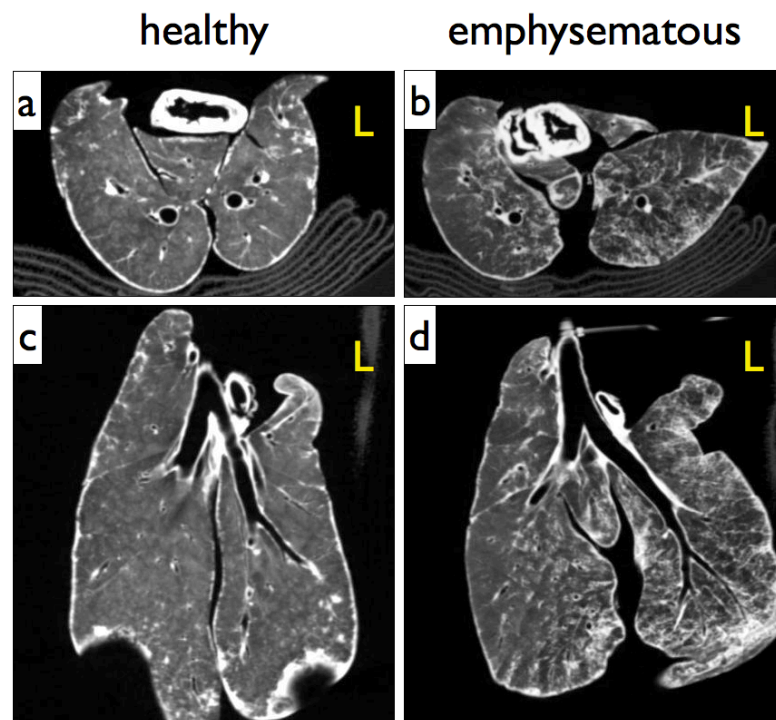


**Figure 65:** CT images of normal and emphysematous fixed swine lungs, L indicating the left side. (a) axial and (c) coronal view of a healthy swine showing uniform tissue density. (b) axial and (d) coronal view of a swine lung fixed 3 weeks after instillation of porcine pancreatic elastase into the left lower lobe showing heterogeneous tissue density in the left lung compared to the right lung and compared to the control left lung in (a-c).

## 4.2 Validation of two- and three-dimensional measurements of subpleural alveolar size by optical coherence tomography

To validate quantitative measurements of pulmonary alveoli within FDOCT images, it was crucial to investigate the effects of refraction at the tissue-air interfaces that were known to create artifacts in FDOCT images (83, 114). Thus far there has been limited quantitative studies on individual alveolar areas (115, 116) and the validity of alveolar volume measures within FDOCT images has not been shown.

The goal of this study was to investigate the representation of air-filled subpleural alveolar sizes in FDOCT images to enable quantitative measurements of alveolar cross-sectional area, perimeter, volume, and surface area. Swept-source FDOCT images were compared to X-ray micro-computed tomography (micro-CT) images of fixed swine lung to quantify the influence of refraction on alveolar shapes as outlined in subsection 3.4.2. Micro-CT was used as the gold standard for imaging air-filled peripheral lung tissue because it is subject to minimal refraction artifacts. The alveolar reconstruction within FDOCT images was confirmed with a two-dimensional ray-tracing model that calculates the refraction of light at tissue-air interfaces (subsection 3.4.3). The refractive indices used in the model were experimentally determined from the analysis of fixed and fresh lung tissue using FDOCT (shown in subsection 3.4.1).

### 4.2.1 FDOCT *versus* micro-CT comparison of segmented alveolar sizes

Identical alveoli as represented in FDOCT *versus* the gold standard micro-CT were identified and the cross-sectional area (CS) and perimeter (P) of 31 cross-sections and the volume (V) and surface area (SA) of 19 alveoli were compared between the two imaging modalities. Table 6 provides the respective size distributions. A correlation analysis showed that FDOCT provides highly representative measures of relative alveolar cross-sectional area ( $R = 0.95$ ,  $p < 0.001$ ), perimeter ( $R = 0.93$ ,  $p < 0.001$ ), volume ( $R = 0.91$ ,  $p < 0.001$ ), and surface area ( $R = 0.93$ ,  $p < 0.001$ ) without further scaling or correction. However, when FDOCT measurements were plotted as a function of micro-CT measurements, the slope of the linear fit was smaller than one for all size

parameters, equal to 0.78 for cross-sectional area, 0.88 for perimeter, 0.62 for volume, and 0.78 for surface area, indicating that FDOCT systematically underestimated the absolute alveolar sizes when compared to micro-CT. Consequently, FDOCT did not allow the prediction of absolute alveolar sizes as measured by micro-CT as visualized in Figure 66 and confirmed by a linear regression analysis showing that the slope  $s$  in Figure 66 was significantly different from one with the y-intercept  $t$  significantly different from zero for cross-sectional area ( $p_s = 0.006$ ,  $p_t = 0.044$ ,  $R^2 = 0.25$ ) and volume ( $p_s = 0.003$ ,  $p_t = 0.016$ ,  $R^2 = 0.42$ ). The relationship was not significant for perimeter ( $p_s = 0.61$ ,  $p_t = 0.477$ ,  $R^2 = 0.01$ ) and surface area ( $p_s = 0.27$ ,  $p_t = 0.08$ ,  $R^2 = 0.07$ ). The intra-data variability as a function of alveolar size can be observed in Figure 67 from the mean  $\pm$  2SD of the error  $E_{exp}$  from equation (4.1) for: cross-sectional area ( $27\% \pm 20\%$ ), perimeter ( $7\% \pm 16\%$ ), volume ( $46\% \pm 22\%$ ), and surface area ( $25\% \pm 18\%$ ).

$$E_{exp} = \frac{M_{micro-CT} - M_{FDOCT}}{M_{micro-CT}} \quad (4.1)$$

Based on this data, future FDOCT measurement error of alveoli from a similar data set (inter-data variability, 95% confidence interval) can then be expected to lie within -3.5% to 56.7% for area, -14.3% to 28.8% for perimeter, 13.8% to 78.3% for volume and -1.6% to 51.6% for surface area with 95% confidence (Table 10) (113). The difference between the FDOCT and micro-CT measurements could not be correlated significantly to the respective alveolar sizes (Figure 67), but the data suggests a statistically-significant increase in error with increasing aspect ratio of the alveolus (from equation 3.13) for area ( $p = 0.008$ ,  $R^2 = 0.234$ ), volume ( $p = 0.0004$ ,  $R^2 = 0.53$ ), and surface area ( $p = 0.029$ ,  $R^2 = 0.27$ ). A plot of the percent error *versus*  $f_{CT}$  is shown in Figure 68 in the following section, where the experimental results are compared to the modeling. The relationship for the perimeter was not significant but the plot is provided for completeness.

The results of this direct comparison between FDOCT and micro-CT measurements show that FDOCT does not provide exact quantification of alveolar sizes (referred to as absolute sizes in contrast to relative sizes). Specific applications, however, such as models of gas exchange, would profit from absolute size measurements. The following section therefore investigates

whether the underestimation of alveolar size in FDOCT images can be explained and subsequently corrected with ray-trace modeling.

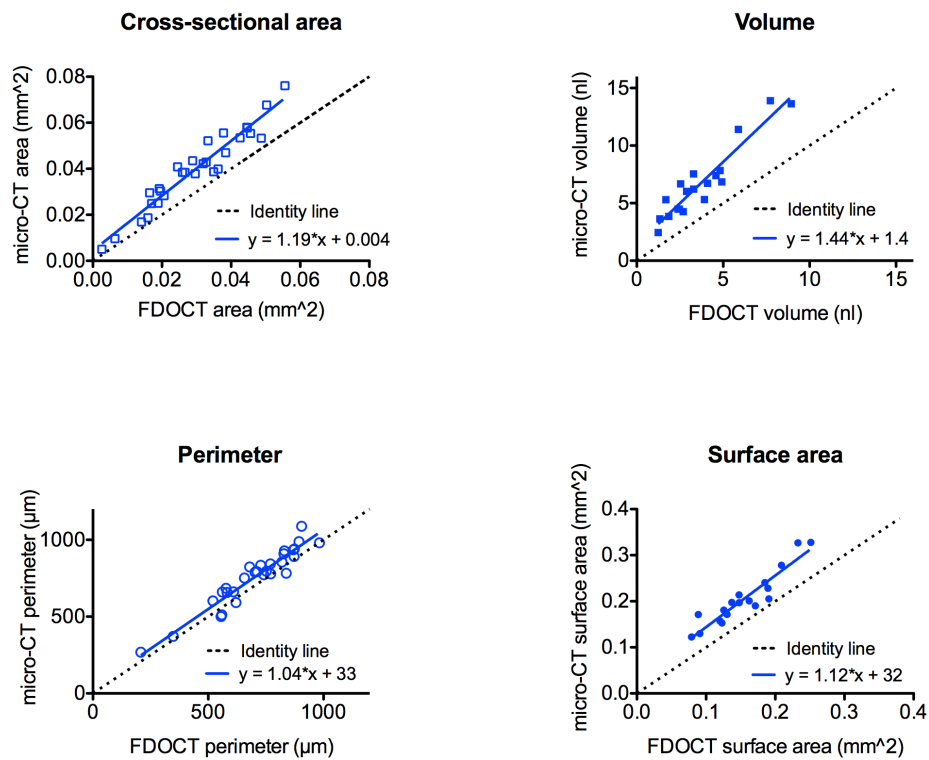


**Figure 66:** Comparison of alveolar size measurements (cross-sectional area, volume, perimeter, and surface area) obtained from micro-CT images (y-axis) and FDOCT images (x-axis) showing systematic underrepresentation of alveolar size in FDOCT images compared to micro-CT. Linear fit ( $R^2 \geq 0.88$ ) shown for all parameters compares to identity line (dotted black line), which indicates perfect agreement.

**Table 6: Overview of alveolar cross-sectional area (CS), perimeter, volume, and surface area (SA) measured from FDOCT images *versus* micro-CT images from three samples, each of a different lobe from one fixed swine lung. CS and perimeter were measured on 31 alveolar cross-sections, 19 alveoli were evaluated for volume and SA.**

		CS	Perimeter	Volume	SA
		[10 <sup>-3</sup> mm <sup>2</sup> ]	[μm]	[nl]	[10 <sup>-3</sup> mm <sup>2</sup> ]
FDOCT	min – max	2 - 56	208 – 982	1 – 9	79 – 251
	25% percentile	19.05	579.5	2.389	122.4
	median	29.61	727.0	3.286	147.8
	75% percentile	40.52	834.0	4.825	189.7
Micro-CT	min - max	5 – 76	269 – 1088	2 – 15	123 – 328
	25% percentile	28.91	659.0	4.477	167.6
	median	39.87	790.0	6.220	197.1
	75% percentile	53.37	900.5	7.539	231.2

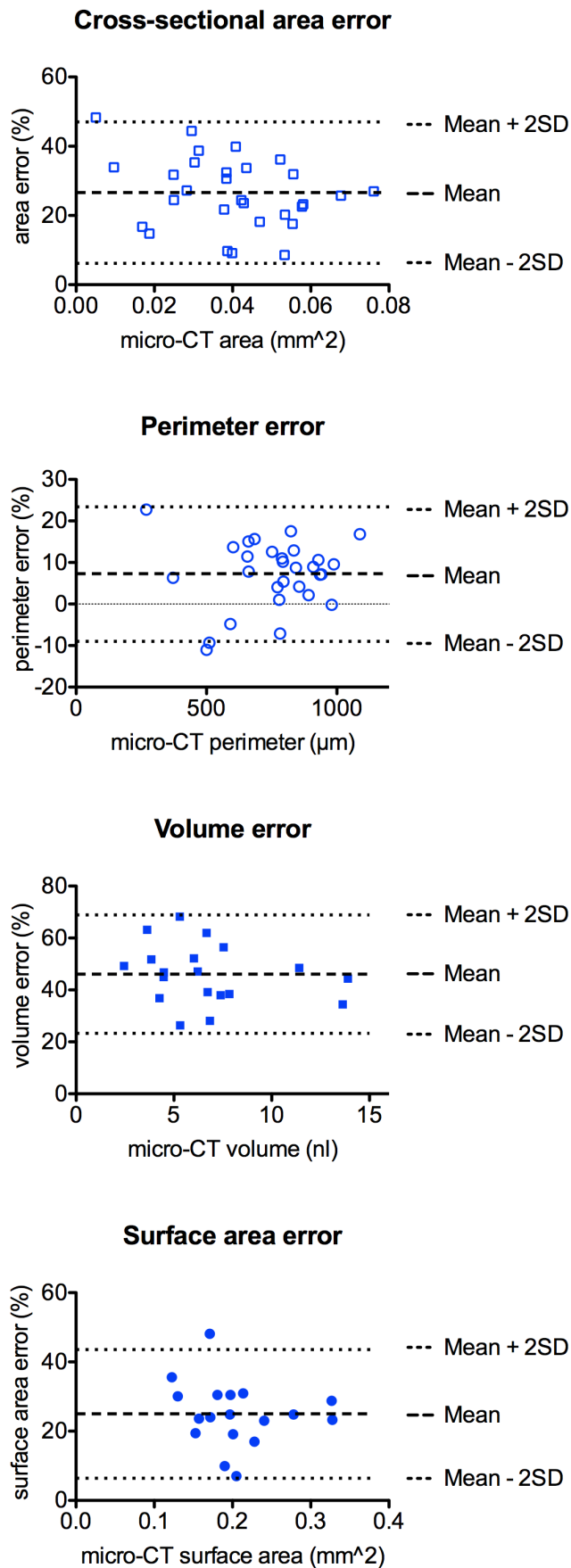


**Figure 67: FDOCT measurement error for alveolar size measurements (cross-sectional area, volume, perimeter, and surface area) as a function of micro-CT measurements of alveolar size showing intra-data variability and alveolar size independence of the error.**

**Table 7: Polynomial coefficients ( $P_{fn}$ ) to be inserted into equation (4.2) to compute correction factors for alveolar superellipse measurements with  $n_{ratio} = 1.04$  to  $1.61$  and  $f = 0.4$  to  $2.0$ .**

Coefficients	$P_{00}$	$P_{10}$	$P_{01}$	$P_{20}$	$P_{11}$	$P_{02}$
Cross-section	-93.76	-0.9008	128.9	-3.012	17.88	-44.63
Perimeter ( $f \leq 1$ )	2.749	0.7287	1.083	0	0	0
Perimeter ( $f > 1$ )	3.707	-0.0683	1.258	0	0	0
Volume	-179.9	15.77	242.9	-7.272	19.86	-81.55
Surface area	-105.7	-0.09633	147.2	-3.317	17.20	-50.42

#### 4.2.2 Modeled influence of refraction

Subsection 3.4.3 introduced the ray-trace model and showed the qualitative effect of refraction and total internal reflection due to the curvature of the upper surface and the refractive index difference between tissue and air for an alveolar cross section approximated by a superellipse (compare Figure 51 and Figure 54). Rays incident upon the upper surface either refract or totally internally reflect. The refracted rays that traverse through the alveoli result in a narrowed visualization below the top surface because the detected light from the refractive index mismatches project along a straight A-line regardless of the true propagation direction within the sample. Total internal reflection of incident rays prevents the visualization of any surfaces below the top surface at the expected transverse location. The size of these non-sampled regions is dependent on the curvature of the top surface where a circle would contain the largest region and a high order superellipse would contain the least. Consequently, the refraction effects result in an underrepresentation of alveolar size in the simulated compared to the original image. Quantitatively, the modeling results predict a 23% underestimation for cross-sectional area and 5% underestimation for the perimeter of a superellipse with equal width and height. The model further predicts an underestimation of 40% for the volume and 25% for the surface area of a circularly symmetric superellipsoid with equal width and height. The modeling predicted error  $E_{pred}$  is shown to depend on both  $n_{ratio}$ , the ratio of the tissue refractive index to the refractive index of

the alveolar filling, and the aspect ratio of the alveolus (alveolar width over height, equation (3.16)), such that alveoli with an aspect ratio below 1 (short and wide) will be visualized with less error. Equation (4.2) was derived through a surface fitting to discrete modeling results (discussed in paragraph 3.4.3) to compute  $E_{pred}$ :

$$E_{pred} = P_{00} + P_{10}f + P_{01}n_{ratio} + P_{20}f^2 + P_{11}fn_{ratio} + P_{02}n_{ratio}^2 \quad (4.2)$$

for the cross-sectional area, perimeter, volume, and surface area for an alveolar superellipse as a function of  $f$  and  $n_{ratio}$  with the polynomial coefficients from Table 7.

Figure 68 shows the experimentally obtained errors as a function of the aspect ratio and compares the results to the modeling predicted error for a refractive index ratio of 1.53. The mean aspect ratio as measured in micro-CT images  $f_{CT}$  of the alveoli segmented in this study was 1.2, corresponding to modeling predicted percent errors of 26% for cross-sectional area, 5% for perimeter, 46% for volume, and 28% for surface area. For comparison, the experimentally obtained mean errors were 27% (area), 7% (perimeter), 46% (volume), and 25% (surface area).

**Table 8: Overview of the experimentally determined error (mean) in alveolar cross-sectional area (CS), perimeter, volume, and surface area (SA) measurement versus the modeling predicted error for an alveolar aspect ratio  $f = 1.2$  (mean aspect ratio of investigated alveoli in micro-CT images)**

Alveolar size measurement error in FDOCT image	CS	Perimeter	Volume	SA
Mean experimental error (mean $f_{CT} = 1.2$ )	27%	7%	46%	25%
Modeling predicted error $f = 1.2$	26%	5%	45%	28%

Figure 68 shows the experimentally obtained errors as a function of the form factor and compares these results to the model for a refractive index of 1.53. The mean  $f_{CT}$  of the alveoli segmented in this study was 1.2, corresponding to modeling predicted percent errors of 26% for cross-sectional area, 5% for

perimeter, 45% for volume, and 28% for surface area. For comparison, the experimentally obtained respective means were 27% (area), 7% (perimeter), 46% (volume), and 25% (surface area).

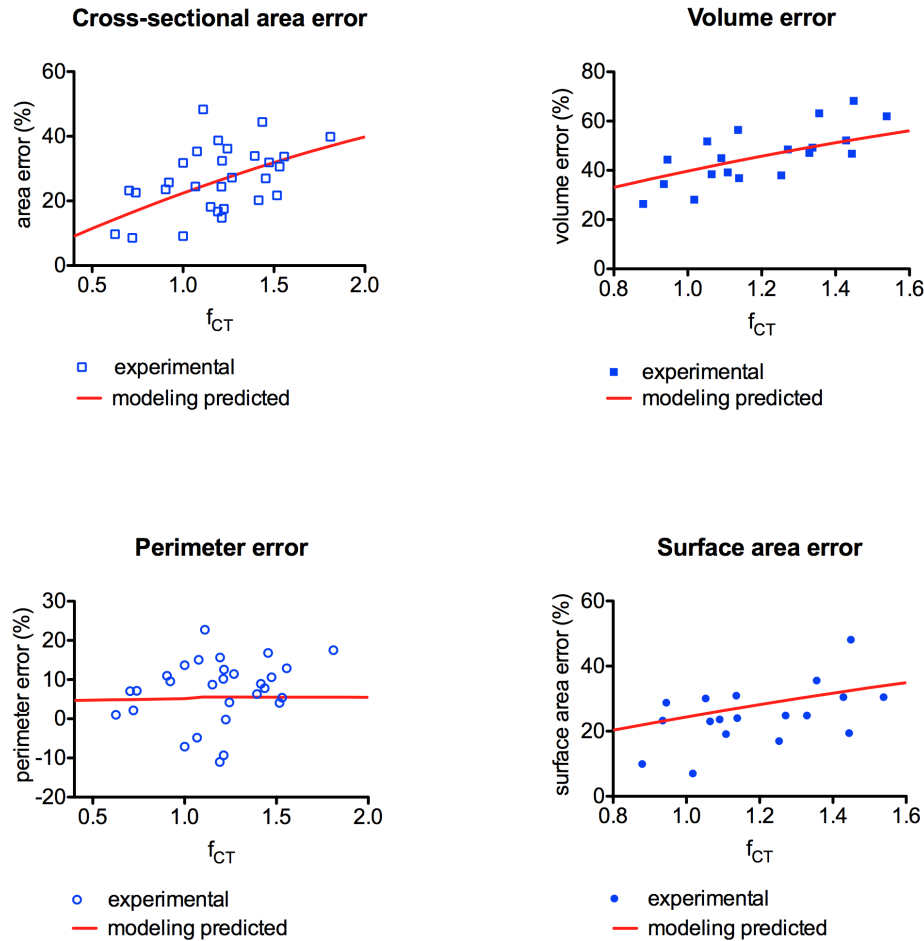


**Figure 68:** Comparison of experimental FDOCT measurement error (blue datapoints) vs. predicted modeling results (red line) as a function of alveolar aspect ratio for cross-sectional area, volume, perimeter, and surface area. Predicted result (red line) calculated from equation (4.2), polynomial coefficients in Table 7, and  $n_{ratio} = 1.53$

### 4.2.3 Correction of alveolar size measurements

In order to test whether the modeling predicted error ( $E_{pred}$ ) from paragraph 4.2.2 could be used as a correction factor to compute absolute measures ( $M_{pred}$ ) of alveolar size from the originally segmented FDOCT data,  $f_{OCT}$  of each alveolus was determined from the FDOCT images and scaled the originally measured sizes ( $M_{FDOCT}$ ):

$$M_{pred} = \frac{M_{FDOCT}}{1 - E_{pred}} \quad (4.3)$$

The mean error between the newly predicted FDOCT measurements and the original micro-CT measurements was -1% for cross-sectional area, 2% for perimeter, -11% for volume, and -9% for surface area. The distribution of the error and the confidence intervals for the inter-data variability were similar to the previous measurements (Table 9). Figure 69 illustrates the comparison of alveolar sizes as measured with micro-CT *versus* the predicted values analogous to Figure 66. Neither slopes nor intercepts could be shown to be statistically significant from one and zero, respectively (Table 9).

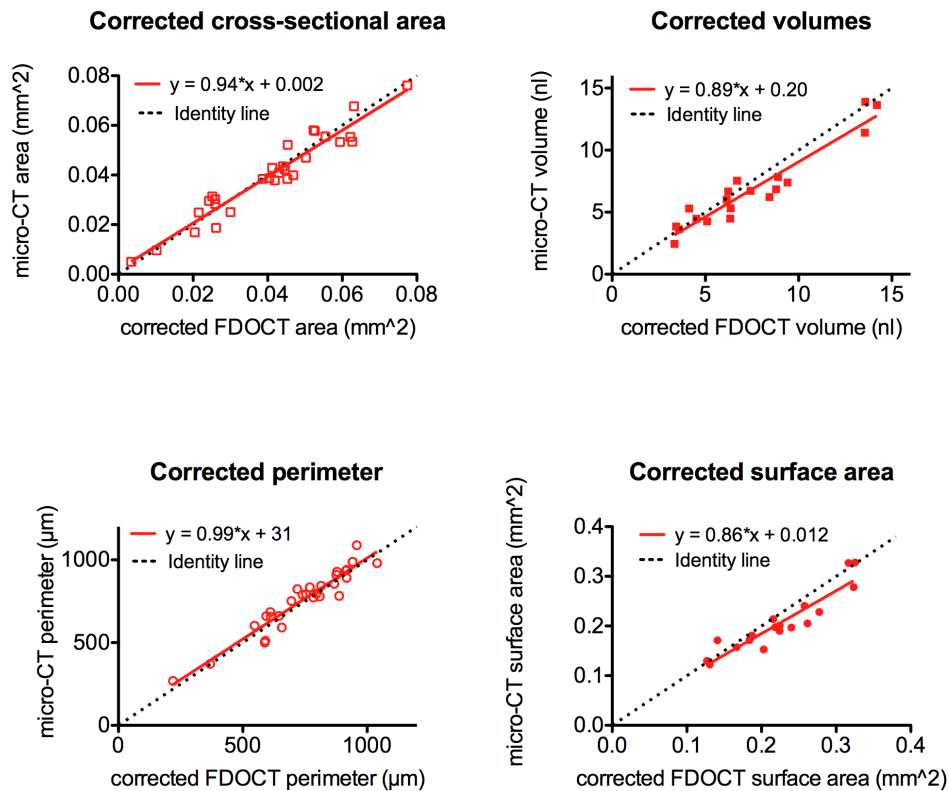


**Figure 69:** Comparison of alveolar size measurements (cross-sectional area, volume, perimeter, and surface area) obtained from micro-CT images (y-axis) and corrected FDOCT measurements according to modeling predicted error (x-axis). A linear fit ( $R^2 \geq 0.85$ ) shown for all parameters compares to identity line (dotted black line), which indicates perfect agreement.

These results indicate that FDOCT images provide correct measurements of absolute alveolar size, when corrected for refraction effects. The presented

two-dimensional ray-trace model allowed a correction of alveolar size (CS, P, V, and SA) with less than 12% average error for the alveoli in this study.

**Table 9: Results of the linear regression analyses testing the slopes and intercepts of the differences in measurement values obtained from micro-CT versus FDOCT measurements, for the originally measured values and FDOCT values scaled according to the modeling results. CS = cross-sectional area**

	Linear regression						
	$(M_{micro-CT} - M_{OCT}) = s * M_{OCT} + t$						
CS	R <sup>2</sup>	s	p <sub>s</sub>	p<0.05	t	p <sub>t</sub>	p<0.05
FDOCT_meas	0.25	0.19	0.006	y	0.005	0.044	y
FDOCT_scaled	0.05	-0.06	0.225	n	0.002	0.37	n
<b>Perimeter</b>							
FDOCT_meas	0.01	0.033	0.61	n	33.10	0.477	n
FDOCT_scaled	0.001	-0.012	0.85	n	31.29	0.499	n
<b>Volume</b>							
FDOCT_meas	0.42	0.44	0.003	y	1.41	0.016	y
FDOCT_scaled	0.14	-0.11	0.07	n	0.27	0.63	n
<b>Surface area</b>							
FDOCT_meas	0.07	0.12	0.27	n	0.03 2	0.08	n
FDOCT_scaled	0.13	-0.13	0.15	n	0.01 3	0.54	n

**Table 10: Overview of the estimated bias in percent error in FDOCT cross-sectional area (CS), perimeter, volume, and surface area (SA) compared to micro-CT images, for the originally measured values and FDOCT values scaled according to the modeling results.**

	Estimated bias in percent error (%)					
	$(M_{micro-CT} - M_{OCT}) / M_{micro-CT}$					
	Mean	Limits		SE	95% CI mean	95% CI limits
Mean -2SD		Mean +2SD				
<b>CS</b>						
FDOCT_meas	26.6	6.2	47.0	1.9	22.8 to 30.5	-3.5 to 56.7
FDOCT_scaled	-1.1	-30.6	28.3	2.7	-6.7 to 4.5	-40.3 to 38.0
<b>Perimeter</b>						
FDOCT_meas	7.3	-9.0	23.4	1.5	4.2 to 10.3	-14.3 to 28.8
FDOCT_scaled	2.8	-14.0	19.7	1.6	-0.4 to 6.0	-19.6 to 25.3
<b>Volume</b>						
FDOCT_meas	46.1	23.3	68.9	2.6	40.6 to 51.6	13.8 to 78.3
FDOCT_scaled	-8.9	-43.3	25.6	4.0	-17.2 to - 0.6	-57.7 to 40.01
<b>SA</b>						
FDOCT_meas	25.0	6.4	43.6	2.2	20.4 to 29.7	-1.6 to 51.6
FDOCT_scaled	-8.5	-32.7	15.6	2.8	-14.5 to - 2.5	-43.1 to 26.0

### 4.3 Preliminary quantitative studies of uncorrected alveolar structure and motion *in vivo*

The previous section demonstrated that uncorrected measurements of fixed, subpleural alveoli obtained directly with FDOCT were strongly correlated to micro-CT measurements. Consequently, this section presents quantitative measurements of alveolar volumes and volume changes. Limitations of the validation studies and subsequent necessary corrections to provide exact quantitative data will be discussed in the following chapter.

#### 4.3.1 Healthy alveolar airspace sizes in a swine model during continuous mechanical ventilation

A total of 90 alveolar air spaces were segmented and measured from *in-vivo* images of healthy swine, 30 of which were ventilated between 2 and 11 cmH<sub>2</sub>O and 60 between 3 and 20 cmH<sub>2</sub>O, measured intratracheally. Alveolar volume (V), the radius of a sphere that would contain the same volume (spherical radius, SR), and surface area (SA) were calculated. The scatter plots in Figure 70 show the observed heterogeneous distribution of V and SA over the intratracheal pressure and suggest no clear pressure dependence. The median alveolar V was 0.2 nl, corresponding to a median SR of 40  $\mu$ m and the median SA was 0.023 mm<sup>2</sup>. Figure 74 in the next section, where normal alveoli are compared to emphysematous alveoli, visualizes the distributions fully characterized in Table 13.

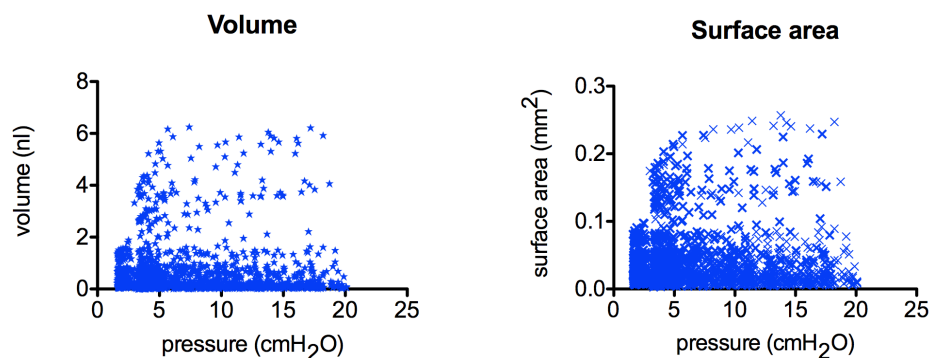


**Figure 70: Volume (left) and surface area (right) of 90 subpleural airspaces from three healthy swine as a function of the intratracheally measured pressure at airspace acquisition.**

In addition to investigating alveolar size at a specific pressure, the observed change in airspace size was evaluated. Therefore, the volume increase was first characterized dependent on the maximum intratracheal pressure difference measured between inspiration and expiration. Further, the corresponding change in surface area during that volume increase was calculated. Figure 71 shows the variation in volume and surface area as a function of the applied intratracheal pressure difference. Surface area decreased with increasing volume in approximately 20% of the evaluated air spaces due to flattening/smoothing of the segment at higher volumes. Further, no clear dependency of volume or surface area change with increased intratracheal pressure difference could be shown, but the plot visually suggests the possibility of increased volume changes with increased pressure difference. Further studies would be needed to confirm the statistical significance of this result. As a consequence, however, the following analyses in this and subsequent sections include only 60 airspaces exposed to intratracheal pressures between 3 and 20 cmH<sub>2</sub>O.

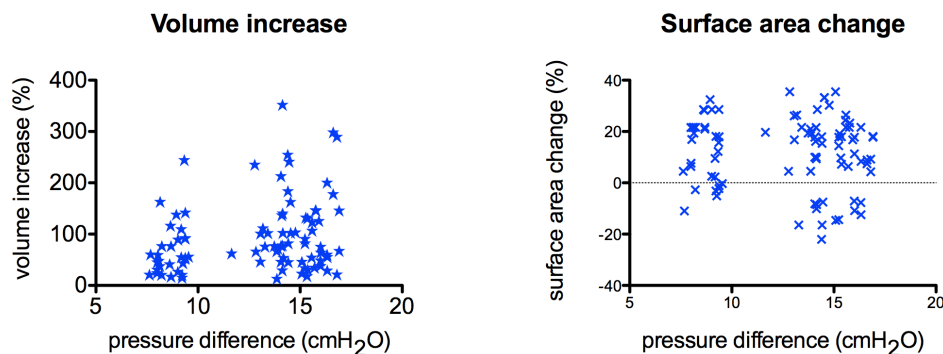


**Figure 71: Volume increase and surface area change from minimum to maximum alveolar airspace volume over the difference of intratracheal pressures applied during airspace volume acquisition.**

The increase in airspace volume over this pressure range (3 - 20 cmH<sub>2</sub>O) as a function of maximum alveolar volume is shown in Figure 72. The volume increase was heterogeneous and independent of the maximum size ranging from 13% to 352% with a median increase of 80%. The change in surface area from minimum to maximum alveolar volume ranged from -22% to 36% with a median increase of 16%. Figure 75 in the next subsection visualizes the overall

distribution and Table 14 characterizes it quantitatively. A subset of twelve airspaces reached a maximum volume greater than 1 nl during the breathing cycle and presented with a relatively constant volume increase and surface area change compared to alveoli smaller than 1 nl. The volume increase of this subset was normally distributed and 51% in average (6.7% standard error) with a spread of 23% standard deviation. Their increase in surface area from minimum to maximum volume was 20% in average (3.1% standard error) with a spread of 11% standard deviation. It is possible that airspaces from this subset represent cluster of alveoli rather than single alveoli. In order to investigate the connectivity of alveoli, however, an improved image quality and imaging depth would be necessary.

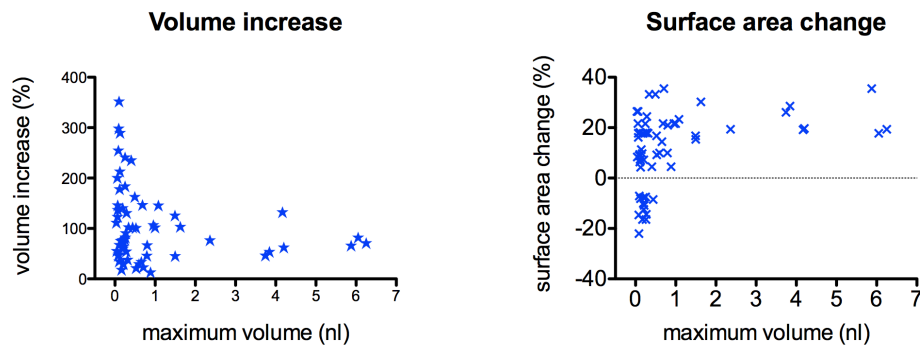


**Figure 72: Volume increase and surface area change from minimum to maximum alveolar airspace volume over maximum alveolar volume.**

Finally, for all alveoli, the ratio of maximum airspace volume increase  $\Delta V_{alv}$  over the maximum intratracheally applied pressure difference  $\Delta P_{intratracheal}$  was calculated as an approximate measure of alveolar compliance  $C_{max}$ :

$$C_{max} = \frac{\Delta V_{alv}}{\Delta P_{intratracheal}} \quad (4.4)$$

Actual alveolar tissue compliance measurements would require knowledge about the pressure experienced by each alveolus, which was not available. The median alveolar compliance in the evaluated set of 60 airspaces was 0.008 nl/cmH<sub>2</sub>O. While the overall lung compliance is an important clinical measurement for the characterization of diseased lungs and the adjustment of mechanical ventilation parameters (typical values for swine approximately 21 – 24 ml/cmH<sub>2</sub>O (117)), the compliance at the alveolar level could not be investigated with current techniques and is therefore not available in the

literature. This work presents a measure of alveolar compliance for the first time and Figure 76 in the next paragraph compares compliance measurements from healthy alveoli ( $n = 60$ ) to emphysematous alveoli ( $n = 20$ ). Table 11 characterizes the full distribution.

#### 4.3.2 Emphysematous alveolar structure and motion in an elastase swine model

A total of 20 alveolar air spaces were segmented and measured from *in-vivo* images of one emphysematous swine ventilated between 5 and 20 cmH<sub>2</sub>O intratracheal pressure. Similar to the healthy airspaces, airspace size did not clearly depend on the measured intratracheal pressure as shown in Figure 73.

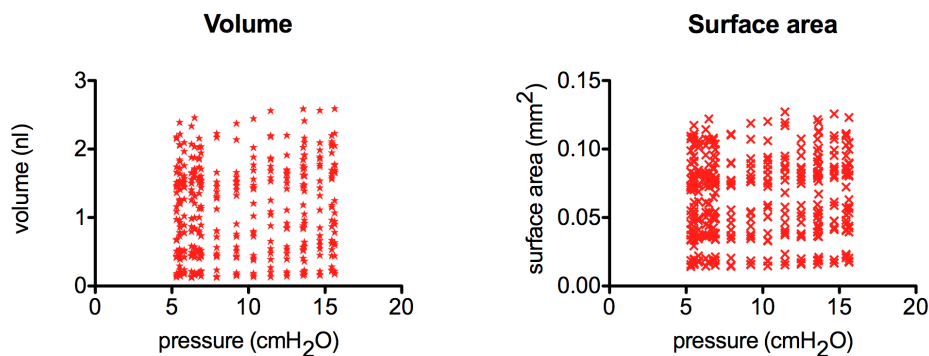


**Figure 73: Volume (left) and surface area (right) of 20 subpleural alveolar airspaces from one emphysematous swine at mean inflation pressure during acquisition of airspace.**

Alveolar volumes ranged from 0.1 nl (min) to 2.6 nl (max) with a median of 1.1 nl, corresponding to a range in SR from 31  $\mu$ m (min) to 85  $\mu$ m (max) with a median of 62  $\mu$ m. The median SA was 0.068 mm<sup>2</sup> (min – max: 0.014 mm<sup>2</sup> – 0.127 mm<sup>2</sup>). Compared to the 90 alveoli measured in healthy swine, the median airspace volume was increased by a factor of 4.7 and the median surface area was increased by a factor of 2.9. However, the spread in uncorrected alveolar volume and surface area was smaller compared to healthy alveoli as visualized in Figure 74. For example, the difference between the 75<sup>th</sup> and 25<sup>th</sup> percentile in the volume of healthy alveoli (0.59 nl) was almost 250% of the median volume, whereas the same difference in the emphysematous alveoli (1.143 nl) represented only 100% of the median volume. Table 12

characterizes the distributions for these three-dimensional measurements in detail.

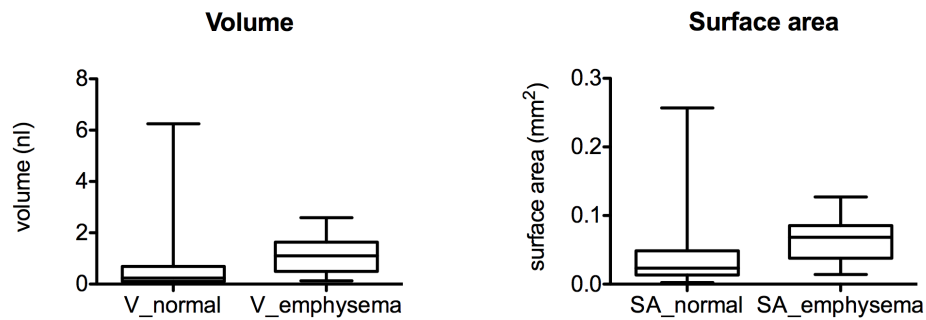


**Figure 74: Comparison of the volume and surface area distribution of healthy (n = 90) vs. emphysematous (n = 20) alveolar airspaces.**

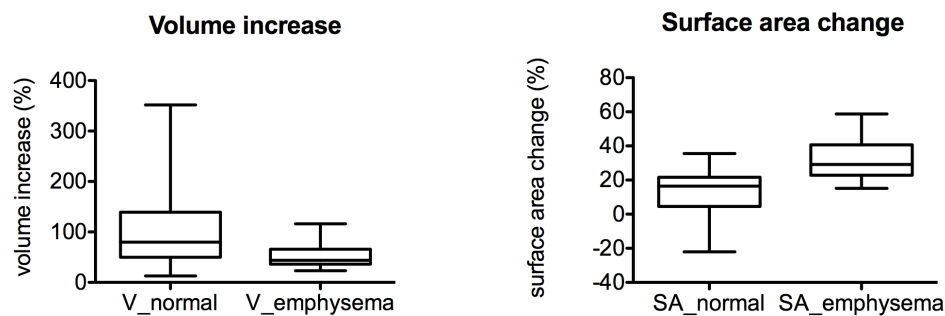


**Figure 75: Comparison of the increase in volume and change in surface area of healthy (n = 60) vs. emphysematous (n = 20) alveolar airspaces for an intratracheal pressure difference of approximately 5 to 20 cmH<sub>2</sub>O.**

Further, the variations in volume and surface area over the breathing cycle between the intratracheally measured pressures of 5 to 20 cmH<sub>2</sub>O were evaluated. The median change in volume and surface area of the emphysematous alveoli was 44% and 29% (compared to 80% and 16% in healthy alveoli for a similar pressure range of 3 to 20 cmH<sub>2</sub>O), respectively. Compared to the 60 normal alveoli that were exposed to a similar pressure range, the range in percent volume increase was narrower both in absolute and in relative terms. While the difference between the 75<sup>th</sup> and 25<sup>th</sup> percentile in the volume increase of healthy alveoli was 89% and represented 112% of the median volume increase, the same difference in the emphysematous alveoli was 66% and represented only 68% of the median volume increase. Further, in contrast to the healthy alveoli, the change in surface in the emphysematous

airspace was always positive. Figure 75 provides a visual comparison of changes in volume and surface area for healthy *versus* emphysematous alveoli and Table 14 fully characterizes the distributions.

The alveolar compliance, approximated as the maximum volume change per alveolar airspace over the maximum pressure difference applied at the trachea, was increased in the emphysema model except for 10 out of the 60 investigated healthy alveolar airspaces. The median compliance in emphysematous alveoli was approximately three-fold increased compared to the healthy alveoli. Figure 76 and Table 11 characterize the compliance distributions in detail.

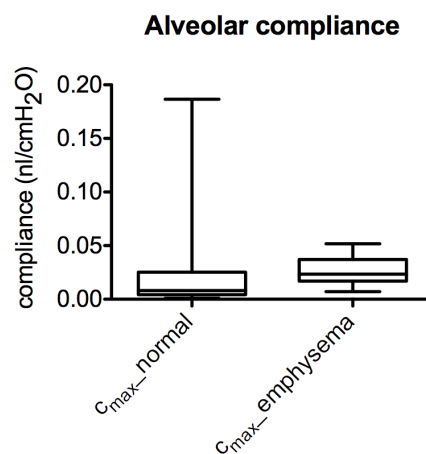


**Figure 76: Comparison of healthy (n = 60) *versus* emphysematous (n = 20) alveolar airspace compliance, approximated as the maximum volume change per airspace over the maximum intratracheally measured pressure difference during the breathing cycle.**

In summary, the three-dimensional structure and structure change of 60 healthy (from two swine) and 20 emphysematous alveoli (from a single swine) were compared over an intratracheal inflation pressure range of approximately 5 to 20 cmH<sub>2</sub>O. No systematic dependence of alveolar volume on pressure was found in either model. However, the emphysematous alveoli in this limited data set were clearly larger (5-fold median volume increase, 3-fold median surface area increase) than the healthy alveoli with less relative variation in size between the alveoli. Further, their median volume increase relative to each alveolus smallest volume was reduced by a factor of 2 with less variation in absolute and relative volume change, and their surface area systematically increased with volume increase in contrast to the healthy alveoli, where

segmented surface area could be smaller at higher alveolar volumes. Lastly, median emphysematous alveolar compliance was calculated to be larger (factor of 3) than the median compliance of healthy alveoli.

**Table 11: Comparison of the overall lung and uncorrected alveolar compliance of 60 normal and 20 emphysematous alveoli evaluated over a physiologic inflation pressure range.**

4D alveolar function		normal (n = 60)	emphysema (n = 20)
tracheal pressure range [cmH <sub>2</sub> O]		3.0 – 20	4.7 - 20
alveolar compliance [nl/cmH <sub>2</sub> O]	Minimum	0.0009717	0.007120
	25% Percentile	0.004217	0.01689
	Median	0.008027	0.02343
	75% Percentile	0.02517	0.03708
	Maximum	0.1866	0.05173

**Table 12: Overview of alveolar airspace volume (V), equivalent spherical radius (SR) and surface area (SA) distributions of 90 healthy and 20 emphysematous alveoli evaluated over 18 time points.**

3D alveolar structure		normal (n = 90*18)	emphysema (n = 20*18)
tracheal pressure range [cmH <sub>2</sub> O]		1.6 – 20	4.7 - 20
alveolar V [nl]	Minimum	0.009378	0.1270
	25% Percentile	0.1058	0.4949
	Median	0.2357	1.100
	75% Percentile	0.6908	1.638
	Maximum	6.253	2.590
alveolar SR [ $\mu$ m]	Minimum	13.08	31.19
	25% Percentile	29.34	49.07
	Median	38.32	64.04
	75% Percentile	54.84	73.13
	Maximum	114.3	85.19
alveolar SA [mm <sup>2</sup> ]	Minimum	0.002475	0.01424
	25% Percentile	0.01336	0.03796
	Median	0.02341	0.06849
	75% Percentile	0.04855	0.08547
	Maximum	0.2570	0.1272

**Table 13: Overview of the maximum alveolar airspace volume (V), equivalent spherical radius (SR) and surface area (SA) distributions of 60 healthy and 20 emphysematous alveoli exposed to tracheal pressures of 20 cmH<sub>2</sub>O.**

3D alveolar structure		normal (n = 60)	emphysema (n = 20)
tracheal pressure [cmH <sub>2</sub> O]		20	20
max alveolar V [nl]	Minimum	0.03359	1.945
	25% Percentile	0.1243	2.163
	Median	0.2758	2.282
	75% Percentile	0.8626	2.454
	Maximum	6.253	2.590
max alveolar SR [ $\mu$ m]	Minimum	20.02	77.43
	25% Percentile	30.96	80.23
	Median	40.38	81.67
	75% Percentile	59.04	83.68
	Maximum	114.3	85.19
alveolar SA at max V [mm <sup>2</sup> ]	Minimum	0.1452	0.09208
	25% Percentile	0.1631	0.09982
	Median	0.1847	0.1072
	75% Percentile	0.1923	0.1095
	Maximum	0.1968	0.1194

**Table 14: Overview of the increase in airspace volume (V), equivalent spherical radius (SR) and surface area (SA) of 60 healthy and 20 emphysematous alveoli relative to their minimum size.**

4D alveolar function		normal (n = 60)	emphysema (n = 20)
tracheal pressure range [cmH <sub>2</sub> O]		3.0 – 20	4.7 - 20
alveolar V increase (%)	Minimum	12.84	23.18
	25% Percentile	49.85	36.10
	Median	79.77	43.95
	75% Percentile	139.2	65.93
	Maximum	351.8	116.2
alveolar SR increase (%)	Minimum	4.110	15.16
	25% Percentile	14.43	22.81
	Median	21.59	29.10
	75% Percentile	33.73	40.66
	Maximum	65.32	58.78
SA change from minimum to maximum alveolar V (%)	Minimum	-22.02	15.16
	25% Percentile	4.519	22.81
	Median	16.47	29.10
	75% Percentile	21.60	40.66
	Maximum	35.52	58.78

## 5 DISCUSSION

The goal of this thesis was to develop an imaging technique for the four-dimensional visualization and quantification of pulmonary alveoli *in-vivo*. While *in-vivo* imaging was demonstrated, the validation of the obtained quantitative size measurements was performed on fixed *ex-vivo* tissue, due to the lack of an alternative gold standard for imaging *in-vivo* alveolar movement. This chapter therefore discusses the findings of this validation approach, their applicability to the *in-vivo* data, and the consequences for the quantitative assessment of alveolar physiology and pathophysiology *in vivo* (56). Secondly, future work is discussed that is merited to leverage the achievements of this work and to address its current limitations.

### 5.1 Validation of two- and three- dimensional measurements of subpleural alveolar size by optical coherence tomography

This section discusses the results of the comparison of FDOCT measurements of alveolar size to micro-CT measurements and ray-trace modeling as presented in section 4.2.

#### 5.1.1 Summary of results

In this study, the effect of refraction and total internal reflection on the representation of subpleural alveolar cross-sectional area, perimeter, volume, and surface area within FDOCT images was investigated.

FDOCT images of an identical sample of fixed swine lung were compared to micro-CT images, where micro-CT was considered a gold standard for visualization of the true alveolar size. Under this assumption, the study showed that FDOCT provides alveolar size measurements (relative sizes) that are highly correlated to measurements from micro-CT. The absolute alveolar size parameters, however, were significantly underestimated, independent of alveolar size. Secondly, the results of a ray-tracing model were shown that calculated the expected error of FDOCT size measurements resulting from refraction artifacts. The predicted underestimation of alveolar size from the

model corresponded very well to the experimentally determined mean error, and both showed an increasing error with increasing aspect ratio (elongation of the alveoli in depth) indicating that refraction and total internal reflection at the tissue-air interfaces are the primary reasons for the underrepresentation of alveolar size in FDOCT images. Further, the modeling results provided scaling factors that were used to correct the initial FDOCT measurements and successfully approximate the absolute average micro-CT values.

### **5.1.2 Differences between *in-vivo* and fixed subpleural alveolar tissue**

This study was conducted as a crucial step towards validating alveolar size measurements made from FDOCT images of subpleural alveoli *in vivo*. FDOCT measurements were compared against micro-CT measurements on small samples of fixed, swine lung in order to image the same field of view with both technologies at the same inflation state and with similar spatial resolution. Adequate resolution could not have been obtained in micro-CT images of an entire swine lung since the resolution of micro-CT depends on the transmission of the X-rays through the sample to capture the absorption profile, while FDOCT collects the back-scattered light. Further, the samples could be easily transported between imaging technologies without creating morphologic changes to the sample.

Three main differences can be expected between fixed tissue and *in-vivo* mammalian subpleural alveoli. First, the lower refractive index of the living tissue, and therefore the lower refractive index difference at the tissue-air interfaces, will reduce the refraction artifacts within the FDOCT measurements. According to the presented measurements of the group refractive indices of fixed and fresh healthy lung parenchyma, the refractive index would decrease from 1.53 to 1.41. Therefore, conclusions drawn from fixed tissue can be expected to remain proportional when transitioning to fresh tissue, and this difference can be modeled for absolute measurements. It is important to note, that in diseased lungs, both the refractive index of the lung tissue as well as the refractive index of the alveolar space could be altered. For example, the alveoli could be fluid filled in pulmonary edema or the alveolar tissue could contain an excess of collagen in interstitial fibrosis.

Secondly, the *in-vivo* alveolar size of a specific alveolus is expected to change dynamically during inflation and deflation of the lung. In contrast, the alveoli in this study were representative of a single inflation pressure (20 cmH<sub>2</sub>O) and were fixed outside of the body where they were not subject to the effects of the chest wall. Both the experimental and modeling results indicate that the percent measurement error caused by refraction artifacts were independent of alveolar size. Therefore, the results from different sized alveoli at a single inflation state are considered representative of the change in alveolar size *in vivo*.

Lastly, the alveolar shape changes dynamically during the breathing cycle. For example, the upper surface of subpleural alveoli could flatten out as overall lung volume increases. The modeling results showed that the error is significantly dependent on the alveolar shape. More specifically, the error increases with increasing curvature of the upper surface of the alveolus and increasing aspect ratio. A circular cross-section of air-filled fresh tissue ( $n_{ratio} = 1.41$ ), for example, would have an error of 29.3%, which corresponds to the error expected for a superellipse of  $f = 1.52$ , and compares to 20.6% error for a superellipse with equal width and height ( $f = 1$ ). This alveolar shape dependence of the measurement error could be the primary cause for the spread in the experimentally determined error values. When evaluating *in-vivo* data, the change in shape of individual alveoli and the distribution of shapes for a cluster of alveoli should be considered to decide whether the specific research question for a given study design can be answered using relative (uncorrected) or absolute (individually refraction-corrected) measurements of alveolar size.

### **5.1.3 *In-vivo* measurements of uncorrected subpleural alveolar size**

The presented study showed very high correlations between the two imaging methods for uncorrected measures of alveolar cross-sectional area, perimeter, volume, and surface area leading to the conclusion that FDOCT could be used to answer important questions about alveolar structure and function without correcting for refraction effects. However, for exact results, the alveolar shape change must be assessed and the assessment will depend on the research question. For example, in order to evaluate the dynamic percent volume change of specific alveoli during the breathing cycle, isotropic expansion and contraction of each alveolus would be ideal. In order to estimate the error in the

alveolar volume change of interest, the change in alveolar aspect ratio from end-expiration to end-inhalation could be measured for all or a subset of the alveoli and the modeling predicted error for both inflation states could be compared. In another example, where relative regional differences should be quantified or clusters of alveoli in healthy and diseased lungs should be compared, the shape characteristics between the clusters of alveoli should be similar. In this case, it could be helpful to compare the distributions of alveolar aspect ratios between the two groups. Whether or not alveolar sizes should be corrected to perform analyses with absolute alveolar sizes must be decided on an individual basis depending on the research question and study design.

In addition to being based on the analysis of fixed tissue, the presented results were obtained evaluating a single species, swine, and from a single lung. However, because these experimental results could be approximately explained and validated *via* a model, the drawn conclusions can be expected to remain valid for all mammalian species where single subpleural alveoli can be identified in FDOCT images. Possible variations in refractive indices between samples, species, or pathologies can easily be modeled. In general, variations in refractive index ratio that appear probable in the case of air-filled alveoli are not significant. For example, a variation in refractive index ratio between 1.38 and 1.41 would result in a maximum (at aspect ratio  $f = 1.6$ ) difference in the predicted error for the volume measurement of a circularly symmetric superellipse of 1.2% representing only a 2% variation from the 50.2% predicted error in volume measurement.

#### **5.1.4 Correction of FDOCT measures of subpleural alveolar size**

Most studies may require evaluating absolute values of alveolar size or a quantification of the change in percent error. Computational fluid dynamic (CFD) models of aerosol deposition in the alveolar region, for example, could profit from exact data about the direction and magnitude of alveolar expansion and contraction (7).

In this study, correction factors were provided as a function of the refractive index of the tissue and the alveolar aspect ratio to account for the underrepresentation of alveolar sizes in FDOCT due to refraction effects.

These factors are based on the two-dimensional ray-trace model of a superellipse-shaped cross-section. Further, these factors were tested for correcting the previously discussed FDOCT measurements of fixed swine lung samples and could reduce the absolute mean error compared to micro-CT below 12% for all size parameters. The wavelength dependence of the refractive index was not considered in the analysis because the difference in refractive index over the 100 nm bandwidth of the utilized light source was estimated to be approximately 0.1% based on the 0.2% change in index for water between 1.2 and 1.4  $\mu\text{m}$  (84). The measured refractive indices also correspond well to previously published results. The refractive index of fresh lung tissue was measured to be 1.38 at a wavelength of 632.8nm (118) and important constituents of lung tissue have been shown to have indices of 1.33 – 1.35 (interstitial liquid), 1.39 (nuclei), 1.41 (connective tissue fibers), and 1.61 – 1.66 (red blood cells) in the visible wavelength range (119). The higher refractive index of the fixed tissue could be due to the fixation solution containing PEG 400 (refractive index of 1.47) and the subsequent drying that reduced the water content of the tissue.

Based on the assumptions of the ray-trace model, these correction factors are recommended where alveolar shapes resemble superellipse cross-sections. They were computed for a range of tissue refractive index ratios between 1.04 and 1.61 and require a measure of the aspect ratio for each alveolus. Further, the scaling factors are expected to more efficiently correct two-dimensional measurements compared to three-dimensional, as discussed in more detail in the following subsections. It is also interesting to note that the correction factors for the perimeter are primarily given for completeness. In the evaluated index and aspect ratio ranges, the modeling predicted perimeter error did not exceed 6%.

### **Alveolar shape**

The superellipse shape was chosen because it seemed to provide the most accurate representation of the general subpleural alveolar shape within the micro-CT images. It is important to note, however, that the superellipse was a large simplification for the individual cross-sections. The upper surface of the alveoli within the micro-CT images ranged from almost completely rounded to

completely flat, and the walls could be vertical or inclined. Cross-sectional shapes of the same alveolus also varied depending on the location and angle they were evaluated. Further, the correction factors were based on fully closed alveoli. In reality, none of the fixed alveoli are completely closed in three dimensions and even single two-dimensional cross-sections must often be closed manually during segmentation to compute cross-sectional area. The spread of percent error in corrected measurements for a given size or aspect ratio could in part be caused by the discrepancy between the real and modeled shape.

*In-vivo* alveolar shapes could potentially differ more significantly from the superellipse and the correction factors would have to be re-evaluated accordingly. For a circular cross-section or spherical alveolus, for example, correction factors could be calculated according to equation (2.1) and Table 15. While any specific shape could in principle be modeled to obtain exact correction factors, alveolar shapes can only be evaluated under the influence of refraction artifacts within *in-vivo* FDOCT images due to the lack of comparable micro-CT data. However, refraction artifacts are expected to be less severe *in vivo* due to the smaller refractive index ratio.

$$E_{pred} = P_0 + P_1 n_{ratio} + P_2 n_{ratio}^2 \quad (5.1)$$

### Aspect ratio

Similar to the general appearance of the alveolar shape, the aspect ratio evaluated within *in-vivo* FDOCT images is also subject to refraction artifacts. This could be problematic if alveolar sizes are corrected according to correction factors calculated with the use of the observed aspect ratio. For the alveoli segmented in this study, however, the FDOCT aspect ratio was found to be closely related to the micro-CT aspect ratio ( $p < 0.0001$ ,  $R^2 = 0.69$  for area and perimeter,  $p < 0.0001$ ,  $R^2 = 0.80$  for volume and surface area). Using the micro-CT aspect ratio instead of the FDOCT aspect ratio for the calculation of the correction factor would have only slightly improved the analysis of the scaled measures compared to micro-CT: 1% mean error (compared to -2%) for cross-sectional area, 2% mean error (compared to 2%) for the perimeter, 2% mean error (compared to -11%) for volume, and -4% mean error (compared to

-9%) for surface area. It therefore seems reasonable to correct FDOCT measurements of alveolar size based on the aspect ratio visualized in the same images.

**Table 15: Polynomial coefficients ( $P_n$ ) to be inserted into equation (2.1) for circular alveoli with  $n_{\text{ratio}} = 1.00-1.61$  to calculate correction factors for alveolar size measurements.**

<b>Coefficients</b>	$P_0$	$P_1$	$P_2$
Cross-section	-136.4	184.2	-47.29
Perimeter	-41.86	58.53	-16.26
Volume	-275.8	389.7	-112.4
Surface area	-170.8	236.5	-64.55

### **2D versus 3D alveolar sizes**

While the absolute mean error for all sizes was reduced to less than 12%, the correction factors performed better for the two-dimensional cross-sectional area and perimeter than for the three-dimensional volume and surface area. This could be explained by two approximations that were made for the 3D case. First, the simulated FDOCT image was directly modeled for the two-dimensional case and the three-dimensional error was inferred assuming the two-dimensional result was circularly symmetric throughout the height of the alveolus. This stronger discrepancy between the real and modeled shape for the three-dimensional case could explain the larger difference between the actual and the modeling predicted measurement error. Second, in order to calculate the appropriate correction factor, the three-dimensional aspect ratio was reduced to two dimensions. The alveolar width of the 3D aspect ratio was defined as the mean of the alveolar width and depth as measured from the two transverse planes. In order to determine the exact correction factor per alveolus, each specific alveolar shape should be modeled in three dimensions.

### Fluid filled alveoli

It is interesting to note, that some studies have chosen to minimize refraction artifacts by filling the alveolus with fluid, such as saline, ethanol or perfluorodecalin (83, 95, 105). The presented modeling results confirm the efficacy of this approach. According to equation (4.2) and Table 7, assuming a superellipse shape with an aspect ratio of 1.2, a tissue refractive index of 1.41 and a fluid-filled refractive index of 1.30 ( $n_{ratio} = 1.085$ ), the expected error is 11% for cross-sectional area, 5% for perimeter, 22% for volume, and 12% for surface area. Compared to the air-filled case, the error in alveolar size measures from fluid-filled alveoli would be more than halved.

#### 5.1.5 Alternative segmentation to obtain absolute alveolar sizes

FDOCT measurements of alveolar size were shown to be correctable to yield absolute values using modeling predictive factors. For exact results, however, the correction factors should be determined by modeling the specific three-dimensional shape of each alveolus. It could therefore be advantageous to obtain correct absolute alveolar sizes directly through segmentation that accounts for the primary refraction artifacts, such as the appearance of two walls per alveolus (83). Triple walls between adjacent alveoli were also frequently observed in the FDOCT images of this work and the additional walls were confirmed as artifacts through the comparison of the same alveolar wall in FDOCT and micro-CT images (Figure 77(a-d)) and *via* ray-trace modeling of two adjacent airspaces (Figure 77(e)). Further, the hypothesis that the outer two of three walls would be artifacts in FDOCT images and could be excluded from segmentation was quantitatively confirmed. Therefore, the original alveoli were re-segmented in the FDOCT images by tracing the boundary along the central of three apparent alveolar walls and comparing the newly segmented alveolar sizes to those measured in micro-CT images. Alveolar cross-sections were re-segmented within the cross-sectional plane and alveolar volumes within the *en-face* plane. Where no three clear walls could be identified, the boundary was traced near the center of the wall between alveoli. Figure 77(f-g) illustrate the alternative segmentation methods. Figure 78 shows the micro-CT sizes over the newly segmented FDOCT values and compares

the linear fit to the experimental data points to the line of identity similar to Figure 66 and Figure 69.

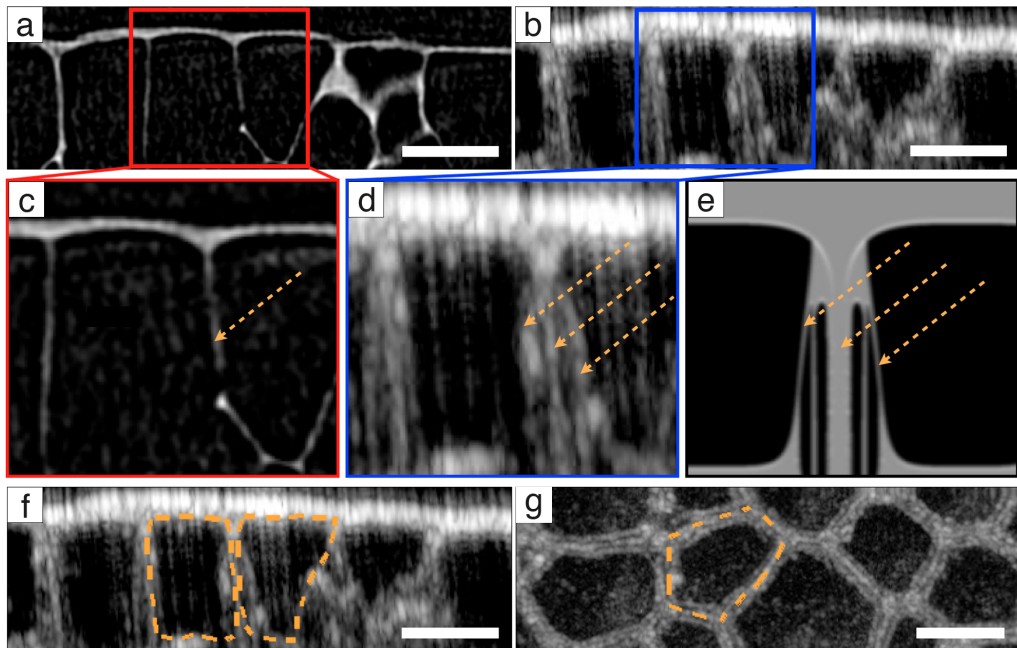


**Figure 77: Illustration of triple-wall artifacts and an alternative segmentation method. A single alveolar wall (dashed arrow) in (a, c) micro-CT image appears as three separate walls (dashed arrows) in the corresponding (d, e) FDOCT image. (e) Ray-trace simulation of two adjacent alveoli confirms outer two of three walls can result from refraction artifacts. Alveoli were alternatively segmented at middle of alveolar wall in (f) axial cross-sectional and (g) *en-face* planes.**

Mean errors for this alternative segmentation technique in cross-sectional area and perimeter were reduced from 27% and 7% (original segmentation method) to 7% and 0%, respectively. Mean errors in volume and surface area were reduced from 46% and 25% to 5% and -6%, respectively. Statistically, the slope of the linear fit remained significantly different from one for cross-sectional area and surface area, but could not be shown to be different from one for volume. The y-intercept was only statistically different from zero for surface area. The non-parametric correlations of size measurements between the techniques remained equally high for cross-sections ( $R = 0.96$ ,  $p < 0.0001$ ), perimeter ( $R = 0.91$ ,  $p < 0.0001$ ), volumes ( $R = 0.93$ ,  $p < 0.0001$ ), and surface area ( $R = 0.91$ ,  $p < 0.0001$ ).

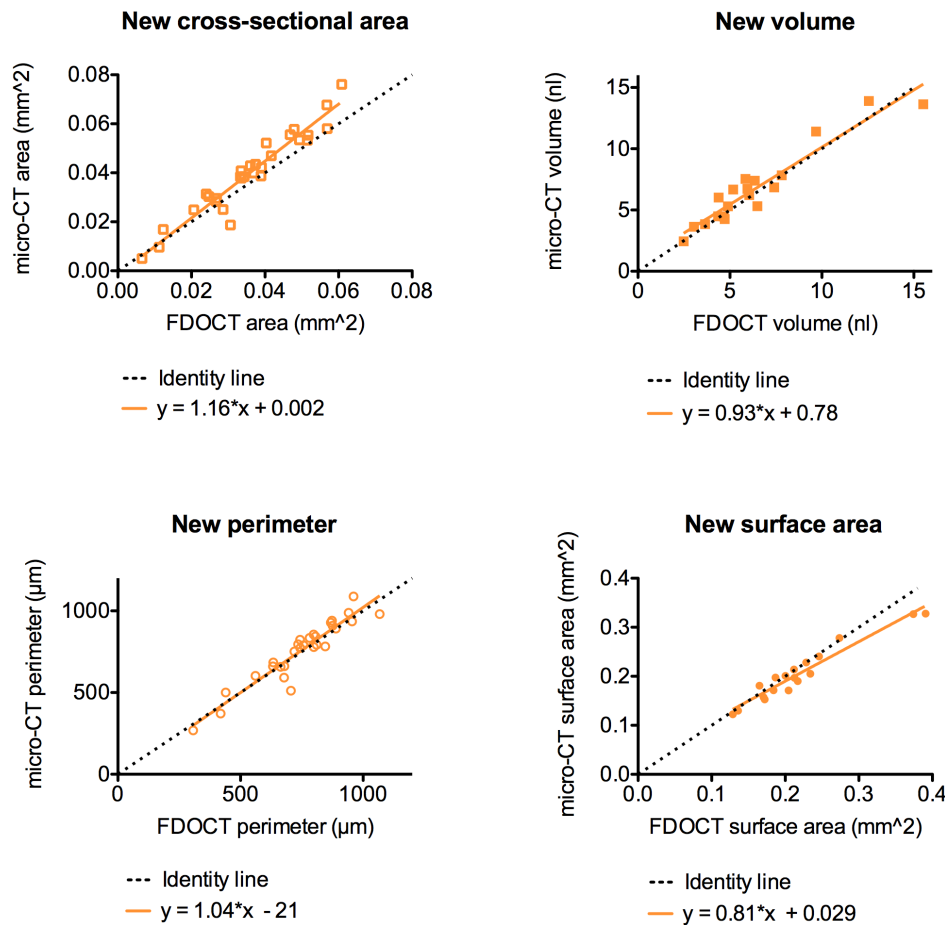


**Figure 78:** Comparison of alveolar size measurements (cross-sectional area, volume, perimeter, and surface area) obtained from micro-CT images (y-axis) and alternatively segmented FDOCT images (x-axis). A linear fit ( $R^2 \geq 0.88$ ) shown for all parameters compares to identity line (dotted black line), which indicates perfect agreement.

As expected, this alternative segmentation could be advantageous over a correction of sizes according to the modeling results for three-dimensional measurements, since the exact three-dimensional shape of each individual alveolus as well as the three-dimensional effect of refraction are considered. However, this approach requires that the refraction effects result in distinguishable real and artificial alveolar walls. Although these multiple walls were frequently observed in fixed excised lungs, it is unclear under which circumstances the effect would be seen *in-vivo* and whether it could be misinterpreted in the case of de-recruited alveoli in between recruited alveoli. The segmentation can therefore be recommended over the correction approach

where absolute alveolar volumes and surface area must be determined in images showing triple walls.

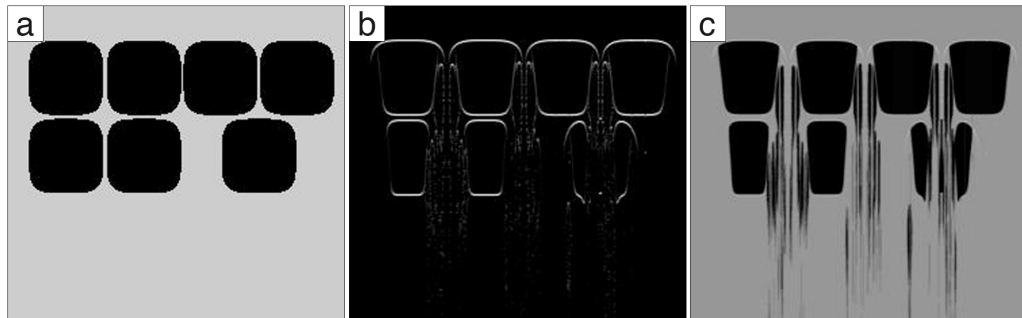


**Figure 79: Illustration of refraction effects that limit analysis to single layer of air-filled alveoli. (a) Original alveolar shapes input into ray-tracing model. (b) Outlines of alveolar shapes calculated by ray-tracing model. (c) Resultant simulated FDOCT image.**

### 5.1.6 Applicability to non-subpleural alveoli

It is important to emphasize that the analysis was limited to the first layer of alveoli beneath the pleura. As previously described (83), the imaging depth in air-filled alveolar tissue is significantly compromised compared to fluid-filled alveoli. Figure 79 shows a simulated image of two layers of alveoli created by the ray-tracing model with the refractive indices for fixed tissue and air. While the first layer reconstructs with little distortion, the second layer of alveoli appears extremely distorted and would require complex correction to provide meaningful results.

However, any first layer of alveoli could potentially be imaged and analyzed deeper in the lung parenchyma through endoscopic or needle probes (95, 120). Because these more internal alveoli are not limited in their expansion by the pleura, they could have a significantly different shape compared to the alveoli analyzed within this study.

## 5.2 Preliminary quantitative studies of subpleural alveolar structure and motion *in-vivo*

This work provided quantitative alveolar sizes and size changes measured directly from FDOCT images of subpleural alveoli obtained in an *in-vivo* swine model at six acquisitions of a three-dimensional data set per breath (subsection

4.3.1). The validity of similar relative measurements along with potential correction factors was also demonstrated, however in fixed tissue (section 4.2). The previous section 5.1 discussed the precision and application of these correction factors and the central role of the alveolar shape in determining whether uncorrected alveolar sizes should be evaluated to answer a specific research question *versus* the use of corrected, absolute values. This section discusses the alveolar shapes and shape changes that were observed *in-vivo* and investigates the potential benefit of correcting the directly measured size parameters to yield absolute alveolar sizes.

### **5.2.1 Assessment of uncorrected *versus* corrected sizes and size changes**

The alveolar shape is the single most important parameter influencing the error in absolute size measurement provided by FDOCT, as discussed previously. As two critical parameters describing the alveolar shape, the curvature of the upper surface and the aspect ratio of the alveolus should be evaluated in particular before scaling alveolar sizes according to the provided correction factors. Visual inspection of the *in-vivo* images of subpleural airspaces shown in this work confirms the superellipse as an appropriate choice as a simplified shape to represent alveolar cross-sections for both the relatively deflated and inflated states. A more precise assessment of the curvature of the upper surface is hindered primarily by strong back-reflections at the pleural surface but also by the pleural thickness ( $\sim 10 - 20 \mu\text{m}$ ) being comparable to the axial resolution of the FDOCT imaging system. The discussion of the aspect ratio depends on the research question. The following paragraphs outline two examples.

#### **Volume and surface area distributions**

One of the analyses provided within this work, for example, addresses the general question of alveolar volume and surface area in a living swine model. Depending on the aspect ratios of the alveoli, the distribution of the directly measured, uncorrected sizes could or could not differ significantly from the distribution of corrected, absolute alveolar sizes. In order to compare these two distributions in a reduced, easier-to-handle data set, the alveolar sizes originally acquired and measured over 18 time points were evaluated in a

reduced data set of alveolar sizes at two time points corresponding to the minimum (alveolar end-expiration) and maximum (alveolar end-inspiration) alveolar volume during three breaths. All of the 60 investigated alveoli were exposed to cyclic breathing driven by the same intratracheal pressures range of 3 to 20 cmH<sub>2</sub>O. The aspect ratio of all 60 alveoli was determined at alveolar end-expiration and end-inspiration and the corresponding originally measured volumes and surface areas were scaled to obtain absolute values. In order to confirm that reducing the data set from 18 to two time points did not have a significant effect on the overall distribution of uncorrected alveolar sizes, a non-parametric comparison was performed with the software Prism (Mann-Whitney test) and showed no significant difference for volume ( $p = 0.38$ ) or surface area ( $p = 0.47$ ). The same test was then performed to compare the distribution of uncorrected alveolar sizes in the reduced data set to the corresponding distributions of corrected, absolute alveolar sizes, which were found to be statistically significantly different from each other for both volume and surface area ( $p < 0.001$ ).

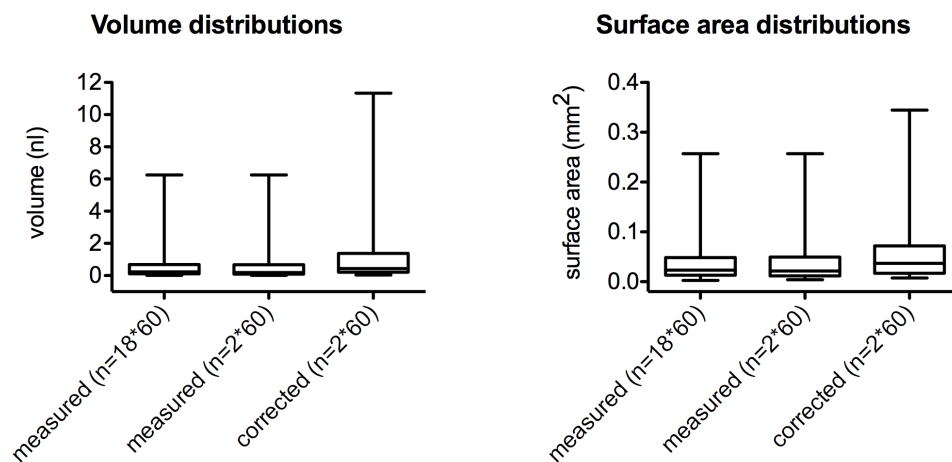


**Figure 80:** Alveolar size distributions are similar in a full ( $n = 18 \cdot 60$ ) versus reduced ( $n = 2 \cdot 60$ ) dataset and differ between measured, relative sizes and corrected, absolute sizes. Measured, uncorrected volume and surface area of 60 alveoli were evaluated either for 18 time points (over three breaths) or 2 time points (maximum end-expiration and maximum end-inspiration over three breaths). Measured, relative volume and surface area of the reduced data set were corrected.

Figure 80 compares visually the original, full distribution of directly measured, uncorrected alveolar sizes including all 18 time points to the distribution of directly measured, uncorrected alveolar sizes in the reduced data set and to the distribution of the corresponding corrected, absolute alveolar sizes. It is important to note that, although the statistical test as well as the graphically presented difference show a difference in uncorrected and corrected size values, using uncorrected *versus* corrected, absolute alveolar size measurements must be decided on an individual basis for each specific research question. Table 16 characterizes the distribution of corrected alveolar sizes to provide reference values for the experiments performed within this work.

### **Alveolar shape and size changes during breathing**

A second analysis performed within this work quantified alveolar size changes during the breathing cycle from FDOCT images based on uncorrected measurements, an assessment that is only exactly valid if the alveolar airspace undergoes isotropic change changes. As an indicator of shape change, the change  $f_{ratio}$  in aspect ratio  $f$  of a breathing alveolus from the lower (end-expiration) to the higher (end-inspiration) alveolar volume can be used.

Figure 81 shows the distributions of  $f$  at low and high alveolar volume as well as the evolution of  $f_{ratio}$  as a function of  $f$  at end-expiration. Approximately 10% of the assessed alveoli presented with equal width and height ( $f = 1$ ) at the low alveolar volume. All others were elongated in depth, perpendicular to the pleura ( $f > 1$ ). During the breath, only 25% of airspaces expanded more in the transverse than in the depth direction ( $f_{ratio} \leq 0.98$ ), and the median  $f_{ratio}$  was 1.12. This trend towards a slight elongation in depth appears confirmed by the increase in median aspect ratio from low ( $f = 1.39$ ) to high ( $f = 1.69$ ) alveolar volume, which was not found to be statistically significant ( $p = 0.056$ , Mann-Whitney test). It remains unclear whether the observed alveolar elongation in depth during inspiration is due to the outward expanding chest wall or is artificially introduced by the experimental design where the lung is no longer constrained by the chest wall at the site of imaging. Whether this non-isotropic shape change necessitates the correction of alveolar sizes to evaluate the size increase, however, will again depend on the exact research question. When

correcting alveolar sizes at low and high volume for refraction effects and comparing the change in alveolar volume and surface area to the uncorrected values, the distributions in Figure 82 are found remarkably similar (exact values in Table 17).

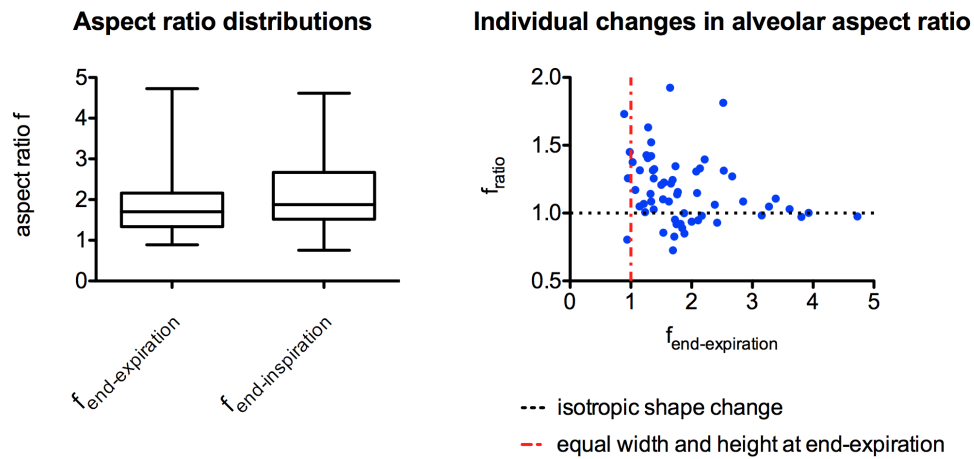


**Figure 81: Shape change of 60 supleural alveolar airspaces from end-expiration to end-inspiration as evaluated by change in aspect ratio  $f$ . (Intratracheal pressure range 3 to 20 cmH<sub>2</sub>O.) Left: The median alveolar airspace elongates in depth, perpendicular to the pleura. Right: Only 25% of airspaces expand in the transverse direction relative to the pleura ( $f < 1$ ).**

When applying the correction factors established *ex vivo* to the *in-vivo* case, two points should be noted: First, the alveolar aspect ratio itself is also subject to refraction artifacts. For the *ex vivo* study, this influence was discussed and found to have a minor effect. Ideally, however, the correction factors could be directly validated in *in-vivo* tissue in the future. Secondly, the alveolar aspect ratios in the evaluated alveolar airspaces from living swine ( $f$ : 0.8 - 4.7) were wide compared to the fixed swine alveoli from section 4.2 ( $f$ : 0.4 - 1.6). This difference could be due to the fixation process inducing unwanted unphysiologically high pressures that destroyed fine alveolar walls perpendicular to the pleura while the pleura resisted well to the pressures. Consequently, several alveoli could have been combined in the fixed tissue to one apparent and wide ( $f < 1$ ) airspace. Correction factors, however, needed not to be reassessed to correct the range of aspect ratios of *in-vivo* alveoli, because the error of discrete simulations for the wider range with respect to the fitted polynomial remained under 5%.

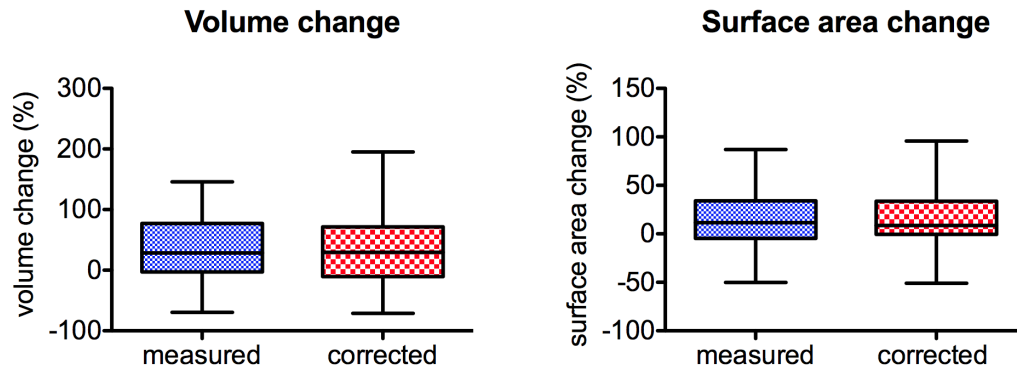


**Figure 82: Comparison of alveolar size changes during breathing when assessed using directly measured, uncorrected values *versus* corrected, absolute values for volume and surface area.**

In conclusion, correcting alveolar size parameters from FDOCT measurements in this study was merited to obtain the most precise absolute values of alveolar size. Evaluating the degree of alveolar size changes, such as percent increase in volume, however, lead to similar results when assessing uncorrected versus corrected measurements.

**Table 16: Original and scaled, absolute values of alveolar airspace volume (V), equivalent spherical radius (SR) and surface area (SA) distributions of 60 healthy alveoli evaluated over 2 time points.**

<b>3D alveolar structure</b>		<b>normal (n = 60*2)</b>	<b>scaled (n = 60*2)</b>
tracheal pressure range [cmH <sub>2</sub> O]		3 – 20	3 – 20
alveolar V [nl]	Minimum	0.01591	0.03367
	25% Percentile	0.09098	0.2042
	Median	0.1911	0.4302
	75% Percentile	0.6742	1.382
	Maximum	6.253	11.33
alveolar SR [μm]	Minimum	15.60	20.03
	25% Percentile	27.90	36.53
	Median	35.73	46.83
	75% Percentile	54.40	69.10
	Maximum	114.3	139.3
alveolar SA [mm <sup>2</sup> ]	Minimum	0.004108	0.007344
	25% Percentile	0.01171	0.01679
	Median	0.02161	0.03684
	75% Percentile	0.04958	0.07203
	Maximum	0.2570	0.3445

**Table 17: Overview of the change in airspace volume (V), equivalent spherical radius (SR) and surface area (SA) of 60 healthy alveoli relative to their corrected size at minimum tracheal pressure.**

4D alveolar function		normal (n = 60)	scaled (n = 60)
tracheal pressure range [cmH <sub>2</sub> O]		3.0 – 20	4.7 - 20
alveolar V change (%)	Minimum	-69.48	-71.11
	25% Percentile	-2.964	-10.56
	Median	28.47	29.51
	75% Percentile	77.02	71.50
	Maximum	145.9	195.1
alveolar SR change (%)	Minimum	-32.68	-33.89
	25% Percentile	-0.9982	-3.653
	Median	8.705	8.998
	75% Percentile	20.97	19.70
	Maximum	34.98	43.43
SA change for respective V change (%)	Minimum	-50.05	-50.86
	25% Percentile	-4.585	-0.6022
	Median	11.66	8.741
	75% Percentile	33.98	33.74
	Maximum	86.92	95.68

### **5.2.2 Translation of results into models simulating airflow in human alveoli**

This work presents to the best of our knowledge the first quantitative, four-dimensional data about alveolar sizes and size changes evaluated in a large animal *in-vivo* (54). Modeling studies of alveolar gas flow and particle deposition could immediately integrate these results to adjust or confirm assumptions made about three-dimensional alveolar shapes and four-dimensional alveolar shape changes (6). However, the presented study has a couple of limitations compared to potentially ideal data that would be representative of all alveoli per generation in spontaneously breathing humans. First, a swine model was studied and it is not clear to what extent the obtained results are representative of human alveolar structure and function. Although this model is popular for respiratory research because of the similarity in lung size, lung functional capacity, and even cardiac output to humans, obvious differences exist including an accessory lobe, more monopodial branching, and higher pulmonary blood pressure (121).

Secondly, a limited number of subpleurally located alveoli were evaluated and the technique does not provide information about the generation rank these alveoli could belong to. Potential differences in alveolar shape between subpleural and non-subpleural alveoli have been discussed previously within this work (subsection 5.1.6).

Finally, in comparison to the physiologic movement of healthy alveoli, the investigated airspaces were mechanically ventilated at a partly open chest. Instead of being pulled open by the descending diaphragm and expanding chest, they were inflated by positive pressures.

Subsections 5.3.3 to 5.3.5 will discuss in more detail how future developmental efforts could mitigate the effects of the mentioned limitations.

## **5.3 Future opportunities and challenges for FDOCT imaging of pulmonary alveoli**

This subsection discusses the achievements and limitations of the presented techniques with respect to answering important scientific and clinical questions in the future. It starts with an outlook on studies of alveolar physiology and

pathophysiology that this work may enable. Secondly, the main current limitations are discussed, namely the time-consuming manual segmentation of alveolar airspaces, the current probe design requiring an invasive procedure with an open chest for imaging, and the limited sample size of the optical imaging tool. Finally, the resulting potential clinical impact is outlined.

### **5.3.1 New pathways to studying alveolar physiology and pathophysiology**

The techniques presented within this work should open new venues for studying respiration at the alveolar level, the site where the exchange of O<sub>2</sub> and CO<sub>2</sub> between the freshly inhaled air and the circulating blood occurs.

This work provides a first look at the quantitative expansion and contraction of healthy, mechanically ventilated alveoli in swine, and further studies will strengthen the drawn conclusions. Further, fundamental questions about the mechanisms of alveolar recruitment and de-recruitment can now be addressed four-dimensionally, *in vivo*, and in a large animal respiratory system that closely resembles the human respiratory system. Local differences and other potential heterogeneities in alveolar movement could also be characterized. The results of such studies can then serve to improve models of gas exchange and aerosol deposition, for example. By replacing assumptions about alveolar movement in these models with experimental data, the resulting gas flow can be simulated and the deposition of particles can be calculated more realistically. Although spontaneously breathing animals cannot be investigated at the current stage of development due to the required thoracotomy, this limitation is not intrinsic to the imaging technology itself. The ongoing development of intrabronchial and needle probes (95, 99) could enable studies of alveolar dynamics in spontaneous breathing.

Secondly, this work demonstrated that individual enlarged air spaces characteristic for emphysema can be visualized and quantified *in vivo* rather than post-mortem or post-excision. In future studies, the progression of pathologies involving the pulmonary alveoli could therefore be monitored in a single animal rather than sacrificing numerous animals at different disease stages or time points after exposure to a pathogen. Similarly, the short- and long-term responses to therapy could be assessed at the level of single alveoli in the same animal. Such a study design would not only be more cost- and

time-efficient by reducing the number of animals required, but would also reduce conflicting factors due to each animal's individual response to the pathogen or therapy. Further alveolar disease models to be explored in swine could include a bleomycin-induced fibrosis model (122) or any respiratory distress model resulting from repetitive saline lavage or instillation of oleic acid (123).

Finally, the effects of mechanical ventilation on healthy and diseased lungs and particularly different mechanical ventilation strategies or inhalation gases can now be quantified at the alveolar level. Current hypotheses of ventilator induced damage to the alveoli through overdistension or collapse as a result of excessive tidal volumes or insufficient opening pressures can be investigated (4). More precise explanations could be reached or optimally safe ventilation parameters could be discovered.

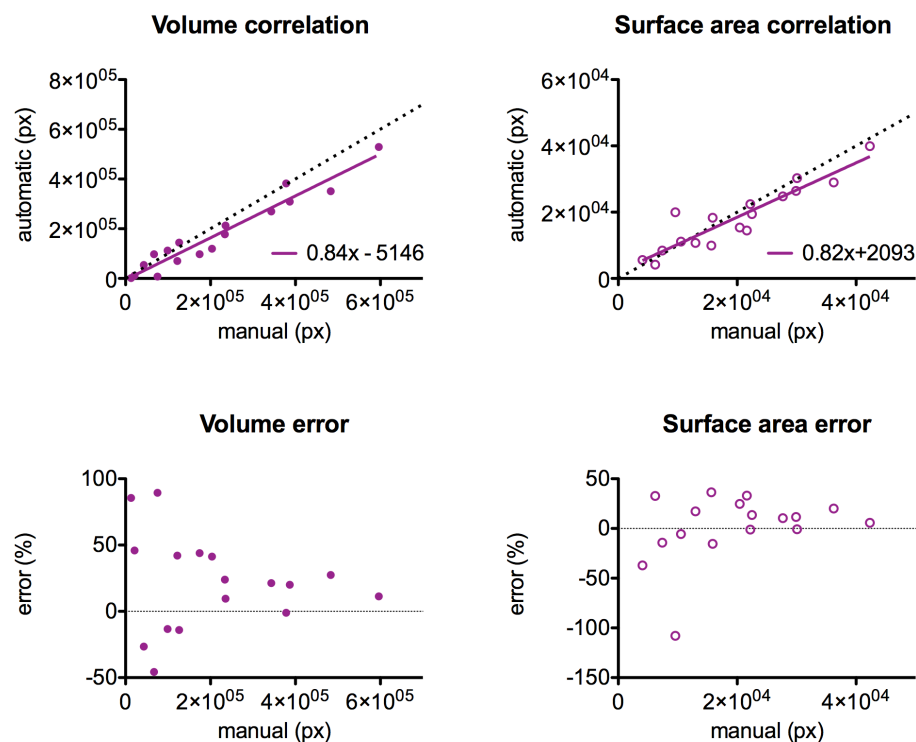


**Figure 83: Comparison of correlations (upper row) and percent error (lower row) for alveolar volume (left) and surface area (right) measurements in manual versus semi-automatic segmentation (ALAlveoliSeg). Upper left: linear fit for volumes ( $0.84x-5146$ ); upper right: linear fit for surface areas ( $0.82x+2093$ ).**

### 5.3.2 Development of automatic segmentation methods

All quantitative results presented in this work were obtained through manual segmentation, which required the user to display the image and trace individual alveolar boundaries with use of a computer mouse or tablet. In a four-dimensional image containing 20 alveoli, where each alveolus is represented by roughly 40 two-dimensional slices and tracked over three breaths with 6 volume acquisitions per breath, the user then needs to manually segment about 15 000 contours to analyze the single data set. The future success of FDOCT for imaging pulmonary alveoli therefore depends highly on the development of automatic or semi-automatic segmentation algorithms that allow correct segmentation and calculation of alveolar volumes. This subsection introduces promising existing approaches and specific challenges for automatic segmentation of pulmonary alveoli.

Recently, a semi-automatic algorithm for segmentation of alveolar area changes over time has been developed for *en-face* video microscopy images of closed alveolar contours (124). The algorithm requires manual tracing of the initial boundary of each alveolar *en-face* area to iteratively adapt this boundary to fit it to the contour of the same alveolus in the subsequent time point's frame. This adaptive fitting process is achieved using an active contours approach based on image gradients (125).

In imaging techniques that capture the three-dimensional structure of pulmonary alveoli, such as optical coherence tomography (FDOCT) or micro-computed tomography (micro-CT), however, alveolar openings to a duct are often observed as an interruption of the air space contour, even in the two-dimensional planes. This discontinuity represents a challenge for automatic segmentation algorithms, such as gradient-based active contours, because the image itself does not contain a gradient at the “visually best” completion of the contour, which is easily identifiable for human vision.

A second promising semi-automatic segmentation algorithm has been developed by Air Liquide Medical Gases R&D. In contrary to the previously described approach, the algorithm extracts three-dimensional contours and manual segmentation of the first contour is replaced by a semi-automatic segmentation. Because this second algorithm also employs gradient-based

active contours, the current implementation requires the user to identify visual contours and to set a virtual bounding box around the area-of-interest to limit expansion of the contour across the bounding box. Figure 83 illustrates the correlation between alveolar sizes segmented manually as shown earlier in this work *versus* corresponding results of the semi-automatic segmentation in three-dimensional FDOCT images of fixed subpleural swine alveoli. The volumes and surface areas of the tested 17 alveoli were highly correlated between the two segmentation methods ( $R > 0.9$ ,  $p < 0.0001$ ). Considering the measurement values derived from manual segmentation as true values, the mean errors in volume and surface area derived from the semi-automatic segmentation were 21% and 1%, respectively. The estimated bias seems high (up to 125% error to expect for the 95% confidence interval of measurements in a future data set), but further studies are needed to provide a meaningful quantitative analysis. A larger scale study needs to be performed to confirm these preliminary results and to validate the technique before it can be used as a stand-alone technique for the segmentation of FDOCT images of pulmonary alveoli. Future work should also include a thorough analysis of the different parameters driving the iterative evolution of the active contour in order to assure a segmentation that is consistent, robust, and provides similar results as the manual segmentation.

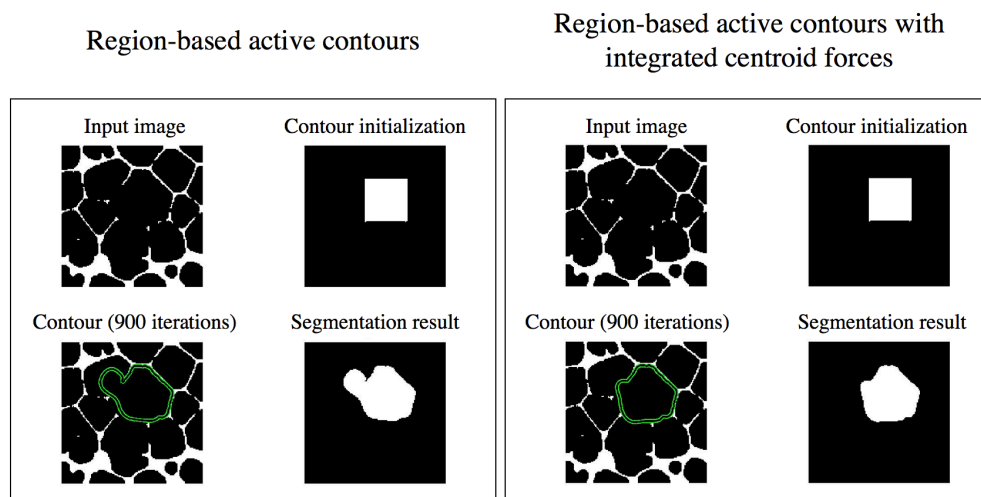


**Figure 84: Integration of centroid forces enables the active contour to converge after 900 iterations without protruding across a visual contour. Left: Classic region-based active contour approach continues to integrate a second airspace. Right: Convergence after 900 iterations.**

Lastly, a semi-automatic two-dimensional segmentation algorithm was tested that would respect visual contours at the interface of two airspaces while requiring only a single point input from the user corresponding to the approximate center of gravity of the wanted segment. A region-based rather than gradient-based active contour segmentation approach (126) was modified to penalize contour evolution that would result in a segment with a centroid shifted from to the pre-defined location. Figure 84 shows the successful segmentation result in an *en-face* micro-CT image that was binarized (threshold 0.15) and underwent morphological opening with a disk of radius 1 and closing with a disk of radius 7. While interesting, centroid-based curve evolution is only one exemplary opportunity to improve existing active contour segmentation algorithms to respect visual contours and the active contour method in general remains sensitive to numerous input parameters (size and position of initial contour, number of iterations, weight of different force parameters, etc).

In summary, promising approaches for semi-automatic segmentation are in development. However, future work to provide robust, exact, and fast segmentation approaches for the incomplete contours of pulmonary alveoli in medical images is highly merited.

### **5.3.3 Future probe developments to image alveoli in a closed chest**

The presented MEMS probe for imaging subpleural alveoli is unique in its approach of following the unrestricted movement of the lung during inflation and deflation and maintaining the same field of view despite the displacement, which enabled the continuous imaging of 20 to 30 alveoli per probe position over several breaths. It is therefore superior to previous approaches in the literature capturing the movement of individual alveoli. These approaches included placing a cover glass on the lung (127) restricting alveolar movement or creating optical windows (93) in the chest, requiring that both the window size and the field of view of the imaging system are large enough to track at least one alveolus.

However, the presented MEMS approach required thoracotomy for imaging. During the procedure, the ribs have to be spread apart to give enough space for imaging (~15 to 20 cm) and air enters the pleural space breaking the natural

connection between the lung and the chest wall. As a result, the natural outward recoil of the chest wall at rest can no longer keep the lungs inflated and expansion of the chest wall fails to drive lung inflation. Thus, the swine has to be mechanically ventilated. The approach described in this work can therefore not provide images of spontaneously breathing animals. Secondly, the lung inflates into the free space at the opening instead of sliding along the rib cage. It is unclear to what extent the natural alveolar movement is altered by these changes. Further, in order to image different locations on the same lung, several incisions have to be made, which is time consuming and increases the risk of complications for the animal, and not all lobes (cardiac lobe) and locations (especially close to the apex or to the base) can be reached with the current approach. Lastly, the procedure itself has to be performed extremely carefully to limit damage to the region of interest before any images can even be obtained.

An ideal imaging probe would follow the natural movement of the lung and track specific alveoli during breathing in a closed chest. In order to image similar locations as studied in this work, such a probe must be an integral part of the approximately 20  $\mu\text{m}$ -thick (128) fluid layer between the lung and the chest wall to allow the lungs sliding motion without breaking the connection to the chest wall or creating damage to either side. The exacting constraints include a small, ideally completely wireless probe of smooth surfaces. An alternative and possibly more suitable approach for an implantable imaging probe in a small animal (mouse or rat) could be the attachment of the probe to the diaphragm from the abdominal side. The diaphragm in small animals is nearly transparent and the abdominal cavity provides sufficient space so that a imaging probe could capture movement of sub-diaphragmatic alveoli within a closed chest wall and thus potentially even in spontaneously breathing animals. Other ways of accessing pulmonary alveoli in a closed chest model could be through needle probes or intrabronchially as discussed in previously (subsection 3.2.3). These ways of access, however, do in turn not intrinsically maintain the same field of view during breathing, as does the presented MEMS probe.

### 5.3.4 Sample size

FDOCT is currently the only method demonstrated to be capable of visualizing alveolar dynamics *in vivo* due to its uniquely well-suited spatial and temporal resolution. The provided sample size, however, is small compared to the estimated total number of alveoli in a human lung of almost 500 million (10). The here-presented methods, for example, allowed visualization of about 20 – 30 alveoli in a field of view of approximately 1 x 1 mm and only the first layer of alveoli was assessed due to refraction artifacts. Current developments of increasingly fast FDOCT systems (MHz A-line range) (86) should enable imaging of larger field of views at comparable spatial resolution in the future. Depending on the scanning mechanism, lateral fields of view of several mm<sup>2</sup> could thus be visualized at a specific probe location. In addition, a preliminary algorithm was recently demonstrated to correct for refraction effects in the visualization of the first layer of alveoli (114), and further work is merited to allow reconstruction of the second layer of alveoli to increase the sample size. Depending on the application, additional CT imaging or other whole organ imaging technologies to guide FDOCT could complement the obtained information and mitigate the limitations due to sample size. For example, the appearance of emphysema on CT as diagnosed in the clinic could be confirmed at the alveolar level with FDOCT.

### 5.3.5 Clinical relevance

Subsection 5.3.1 discussed the great potential of the techniques presented within this work to serve as a research tool to improve the current understanding of alveolar physiologic and patho-physiologic mechanisms. Subsequently, subsections 5.3.2 to 5.3.4 suggested future work to accelerate quantification of alveoli through automatic segmentation algorithms, potential avenues to developing less invasive imaging probes, as well as possibilities to increase the sample size provided by the technique. This subsection concludes with discussing the achieved progress and potential roadmaps towards achieving three exemplary clinically relevant research goals (as outlined in section 2.2) that would benefit from the development of an imaging tool for visualization and quantification of pulmonary alveoli: To improve models of

gas exchange and aerosol deposition through quantitative data about alveolar movement during breathing, to enable better phenotyping of COPD patients to facilitate the development of new therapies, and to accelerate the development of protective mechanical ventilation strategies. This work described the development of the desired tool and provided preliminary quantitative data about alveolar volumes and surface areas in mechanically ventilated healthy and emphysematous swine as a function of airway pressure.

The obtained data can already be integrated into models of gas exchange and aerosol deposition as discussed in subsection 5.2.2 to validate or refute previously made assumptions about alveolar motion and to improve deposition analyses by these models. Further, quantitative results from a greater number of airspaces as well as from non-subpleural airspaces are expected to be available in the near future as automatic segmentation algorithms as well as intrabronchial and needle probes will be developed. Mechanically ventilated patients receiving inhaled drugs, for example, could eventually profit from the improved modeling results, if these were used to design the specific therapy.

The second goal of this work was to contribute to a more specific diagnosis of COPD or other lung diseases involving the distal alveoli. This work demonstrated that FDOCT is capable of visualizing differences between healthy and emphysematous alveoli, a crucial first step towards distinguishing COPD caused primarily by destruction of alveolar walls (emphysema) *versus* mucus obstructed airways (chronic bronchitis). In order to improve phenotyping of patients, future efforts should particularly be directed towards developing a non-invasive procedure in which the limited sample size provided by FDOCT could yield the necessary relevant information, possibly through CT guided FDOCT imaging of specific regions of interest. Potentially, such improved diagnostics could also contribute to novel therapies for selected groups of patients to eventually impact patient care.

Finally, it is now possible to investigate alveolar behavior *in-vivo* under different mechanical ventilation strategies that are thought of as harmful or protective, and to confirm or refute current hypotheses about their mechanisms. It may also be possible to link alveolar behavior to important parameters indicating overall success of the procedures, such as oxygenation or pre-

cursors of inflammation. If such links can be established in animal models, non-invasive imaging tools will be key to translating the gained knowledge into improved patient care. Further research in this area is highly merited.

## 6 SUMMARY AND CONCLUSION

This work has described the successful development of a method to visualize and quantify subpleural alveolar sizes in healthy and emphysematous swine *in vivo*.

During the first step, three optical reflectance imaging techniques, namely FDOCT, SECM, and FFOCM, were identified as having the potential to provide four-dimensional imaging with sufficient spatial resolution to clearly delineate alveolar morphology ( $\leq 10 \mu\text{m}$ ) or cellular detail ( $\leq 5 \mu\text{m}$ ) across species without the need for contrast agents or ionizing radiation. All three techniques were evaluated with fixed, fluid-immersed rat lung samples. Optical reflectance images were successfully matched to hematoxylin & eosin (H&E) stained histology slides of the same sample to confirm the resolved structures, including the outlines of individual alveoli and blood vessels (all techniques), type II pneumocytes within the alveolar epithelium (SECM and FFOCM), and crenated red blood cells (FFOCM). Images from all three technologies were further matched to each other allowing a direct comparison of the respective contrast and resolution to determine the capabilities and limitations of each technique. While SECM and FFOCM were found most suitable to visualize the true thickness of the alveolar wall and cellular structures, FDOCT was identified for further development within the scope of this thesis work because of the fast imaging speed ( $> 100 \text{ fps}$ ) and the current potential to integrate within miniaturized probes.

FDOCT was then integrated into a light-weight (12 g), miniaturized (23 mm diameter) cylindrical contact probe to sit upon the lung and follow the natural dynamic movement during the ventilation cycle. This technique allows dynamic imaging of individual air-filled subpleural pulmonary alveoli in a swine model *in vivo*. The transition from fluid-filled to air-filled samples resulted in a dramatic reduction in imaging depth as confirmed previously (83). Consequently, a comparative study was performed on fixed and freshly-

excised air-filled lung samples with the goal to identify optimal focal parameters to achieve maximum imaging depth while maintaining sufficient lateral resolution. The angle with which the light was focused upon the sample (numerical aperture, NA) was varied and the inverse relationship between transverse resolution and depth-of-focus was demonstrated. Of the four tested NAs (0.02, 0.03, 0.08, 0.1), the 0.03 NA provided the best compromise between usable imaging depth ( $\sim 150 \mu\text{m}$ ) and lateral resolution ( $\sim 25 \mu\text{m}$ ) to identify individual alveoli within the evaluated section of fixed air-filled rabbit lung. For the freshly excised tissue, where subpleural alveoli were visualized, the imaging depth was similar across all NAs. The depth location of the focus within the sample was also evaluated to further increase the usable imaging depth. The acquisition and combination of images obtained at different focal locations substantially increased imaging depths in the fixed sample for the 0.08 and 0.1 NA lenses to achieve similar imaging depths compared to the 0.03 NA with improved lateral resolution ( $\sim 12 \mu\text{m}$ ). However, the improvement in imaging depth within the freshly excised subpleural tissue seemed marginal. Recommendations for focusing parameters and methods therefore depend on the specific research question and study design. In subpleural tissue, which was the focus of this work, the overall imaging depth remained unchanged across the imaging parameters and corresponded to approximately one layer of alveoli suggesting that the inherent optical properties of the lung architecture are the primary limitation to the imaging depth. The miniaturized probe was therefore designed for this exact application by integrating a high NA (0.2) to leverage improved lateral resolution ( $3 \mu\text{m}$  diffraction limited) at no significant cost to imaging depth.

It was further hypothesized that the multiple tissue-air interfaces intrinsic to the structure of the peripheral lung strongly refract the light such that the signal reconstructed over a single axial column (A-line) results from various regions within the tissue. The resultant shape of even the first layer of alveoli will then be distorted and the effect could explain additional artifacts that have been observed, such as a double-wall effect (83). In order to validate quantitative measurements of pulmonary alveoli in FDOCT images, it was crucial to

investigate the effects of refraction at the tissue-air interfaces, which was done both experimentally and *via* ray-trace modeling. Measurements of fixed, air-filled swine alveoli obtained from FDOCT were compared to measurements from micro-CT images of the same alveoli, which are minimally influenced by refraction. Alveolar cross-sectional area, perimeter, volume, and surface area were evaluated and measurements from the two techniques were found to be highly correlated ( $R^2 > 0.9$ ) for all size parameters. However, the absolute values were systematically underestimated by FDOCT compared to micro-CT, independent of alveolar size. The mean average underestimation was 27% (area), 7% (perimeter), 46% (volume), and 25% (surface area). In addition to the described experimental comparison, a ray-tracing model was developed that calculated the expected error of FDOCT size measurements resulting from refraction artifacts. The predicted error from the model corresponded very well to the experimentally determined mean underestimation, and both showed an increasing error with increasing aspect ratio of the alveolar shape indicating that refraction and total internal reflection at the tissue-air interfaces are the primary reasons for the underrepresentation of alveolar size in FDOCT images. Based on the modeling results, scaling factors were derived and validated to correct the initial FDOCT measurements and successfully approximate the absolute average micro-CT values. Because the experimental results of this study could be approximately explained with the model, the conclusions from the *ex-vivo* study are expected to transfer to *in-vivo* subpleural alveolar tissue.

The developed methodologies therefore enabled the first visualization and quantification of alveolar structure and motion in three healthy and one emphysematous swine *in-vivo*. A large heterogeneity in alveolar size and size change was observed for 90 healthy alveoli and the 20 emphysematous alveoli. Compared to the healthy alveoli, the emphysematous alveoli had a larger median volume and surface area with less relative variation in size between the alveoli. Further, the median volume increase relative to the alveolar volume was reduced with less variation in absolute and relative volume change. Lastly, this work presents first quantitative values for the compliance of individual alveoli, and emphysematous airspaces were shown to be more compliant than

healthy airspaces. A measure of volume increase for a given pressure increase, the compliance evaluated for an entire lung is an important clinical measure characterizing pulmonary diseases, even though these pathologies may occur at the alveolar level. The techniques presented in this work are a first step towards new avenues of studying pulmonary pathologies and regional differences therein.

Specifically challenging in the analysis of alveolar size from FDOCT images is defining the contours of single alveoli and their segmentation. Preliminary algorithms for semi-automatic segmentation have shown promise but still require user input. Another major limitation of this technique is the invasiveness of the procedure and the limitation of visualizing only the first layer of subpleural alveoli. Further development of intrabronchial probes to access different intact regions in the peripheral lung is highly merited.

In conclusion, this thesis work provides an array of qualitative and quantitative analyses to characterize subpleural alveolar structure and movements in mammalian lungs. A panoply of unique validation techniques has been demonstrated to justify the use of FDOCT for alveolar imaging including the: 1) assessment of optical reflectance imaging techniques correlated and validated with histopathology, 2) validation of alveolar size measurements through the qualitative and quantitative comparison of measurements obtained from the combination of FDOCT, micro-CT, and a ray-tracing model, 3) fabrication of a novel FDOCT imaging probe to image subpleural alveolar dynamics *in vivo*, and 4) development and imaging of an emphysema swine model to compare healthy and diseased alveolar dynamics. While the presented experiments were sample limited, the results from the presented pilot studies demonstrate great potential for characterizing four-dimensional alveolar dynamics *in vivo* during uninterrupted ventilation with the use of FDOCT. The continuation of this work has the potential to develop a more complete understanding of pulmonary physiology and pathophysiology to eventually improve patient care through more precise models for gas exchange and aerosol deposition, more protective ventilation strategies, more refined

phenotyping of COPD patients, and new therapies for lung diseases involving the alveoli.

## 7 DISSEMINATION OF RESULTS

To date, the work described in this thesis has resulted in three peer-reviewed journal papers published or in preparation, six presentations at international conferences, two invited talks, and one patent application:

### **Peer-reviewed journals:**

1. **C. I. Unglert**, E. Namati, W. C. Warger II, L. Liu, H. Yoo, D. K. Kang, B. E. Bouma, G. J. Tearney. *Evaluation of optical reflectance techniques for imaging of alveolar structure*. J Biomed Opt 2012;17:071303.
2. **C. I. Unglert**, W. C. Warger II, J. Hostens, E. Namati, R. Birngruber, B. E. Bouma, G. J. Tearney. *Validation of two- and three-dimensional measurements of subpleural alveolar size parameters by optical coherence tomography*. J Biomed Opt (accepted for publication December 2012).
3. E. Namati, W. C. Warger II, **C. I. Unglert**, J. E. Eckert, J. Jostens, B. E. Bouma, G. J. Tearney. *Four-dimensional visualization of subpleural alveolar dynamics in vivo during uninterrupted mechanical ventilation*. J Appl Physiol (in preparation).

### **International conferences**

#### Oral presentations:

1. **C. I. Unglert**, W. C. Warger II, J. Hostens, E. Namati, R. Birngruber, B. E. Bouma, and G. J. Tearney. Modeling of light refraction to investigate the validity of alveolar shape and volume visualized by optical frequency domain imaging. SPIE Photonics West; 2012 January 20– 26, San Francisco, CA
2. **C. I. Unglert**, E. Namati, W. C. Warger II, B. E. Bouma, and G. J. Tearney. Optimization of focal parameters for three-dimensional Optical Frequency Domain Imaging of air-filled alveoli. SPIE Photonics West; 2011 January 21– 27, San Francisco, CA

3. **C. I. Unglert**, E. Namati, H. Yoo, L. Liu, D. K. Kang, B. E. Bouma, and G. J. Tearney. High Resolution Reflectance Microscopy Techniques for 3-Dimensional Imaging of the Alveolar Structure. American Thoracic Society; 2010 May 15 - 20, New Orleans, LA.

4. **C. I. Unglert**, E. Namati, H. Yoo, L. Liu, D. K. Kang, B. E. Bouma, and G. J. Tearney. Reflectance Microscopy Techniques for Three-Dimensional Optical Frequency Domain Imaging of the Alveolar Structure. SPIE Photonics West; 2010 January 22 – 28, San Francisco, CA.

Poster presentations:

5. **C. I. Unglert**, W. C. Warger II, J. Hostens, E. Namati, R. Birngruber, E. B. Bouma, and G. J. Tearney. *Optical coherence tomography measurements of subpleural alveolar size compared to micro-CT and ray-trace modeling*. ERS; 2012 September 1-5, Vienna, Austria

6. **C. I. Unglert**, E. Namati, B. E. Bouma, and G. J. Tearney. Variation of the Focal Parameters for Three-Dimensional Optical Frequency Domain Imaging of the Peripheral Lung. European Respiratory Society; 2010 September 18 – 22, Barcelona, Spain.

**Invited talks:**

1. Feb 2011: 2011 International Pulmonary Imaging Workshop, University of Pennsylvania, PA

2. May 2010: Center for Pulmonary Functional Imaging, Brigham and Women's Hospital & Harvard Medical School, Boston, MA

**Patent application:**

1. W. C. Warger II, E. Namati, **C. I. Unglert**, B. E. Bouma, G. J. Tearney, "Implantable imaging arrangement and method for using the same", U.S. provisional patent application number 61/549.567, filed October 20, 2011

## 8 BIBLIOGRAPHY

1. K. R. Chapman, D. M. Mannino, J. B. Soriano, P. A. Vermeire, A. S. Buist, M. J. Thun, C. Connell, A. Jemal, T. A. Lee, M. Miravitlles, S. Aldington and R. Beasley, "Epidemiology and costs of chronic obstructive pulmonary disease," *The European respiratory journal : official journal of the European Society for Clinical Respiratory Physiology* 27(1), 188-207 (2006)
2. C. J. Murray and A. D. Lopez, "Alternative projections of mortality and disability by cause 1990-2020: Global Burden of Disease Study," *Lancet* 349(9064), 1498-1504 (1997)
3. M. B. Amato, C. S. Barbas, D. M. Medeiros, R. B. Magaldi, G. P. Schettino, G. Lorenzi-Filho, R. A. Kairalla, D. Deheinzelin, C. Munoz, R. Oliveira, T. Y. Takagaki and C. R. Carvalho, "Effect of a protective-ventilation strategy on mortality in the acute respiratory distress syndrome," *The New England journal of medicine* 338(6), 347-354 (1998)
4. L. Gattinoni, A. Protti, P. Caironi and E. Carlesso, "Ventilator-induced lung injury: the anatomical and physiological framework," *Critical care medicine* 38(10 Suppl), S539-548 (2010)
5. D. Talmor, T. Sarge, A. Malhotra, C. R. O'Donnell, R. Ritz, A. Lisbon, V. Novack and S. H. Loring, "Mechanical ventilation guided by esophageal pressure in acute lung injury," *The New England journal of medicine* 359(20), 2095-2104 (2008)
6. P. Muller, M. Pichelin, R. Fodil, G. Apiou, B. Louis, I. Katz, G. Caillibotte and D. Isabey, "The role of flow irreversibility in the convective dispersion of an aerosol bolus in the pulmonary acinus," *Journal of biomechanical engineering* *under review*((2012)
7. A. A. Rostami, "Computational modeling of aerosol deposition in respiratory tract: a review," *Inhalation toxicology* 21(4), 262-290 (2009)
8. J. B. West, *Respiratory Physiology*, Lippincott Williams & Williams (2007).
9. E. Weibel, *Morphometry of the Human Lung*, Springer, Heidelberg (1963).

10. M. Ochs, J. R. Nyengaard, A. Jung, L. Knudsen, M. Voigt, T. Wahlers, J. Richter and H. J. Gundersen, "The number of alveoli in the human lung," *American journal of respiratory and critical care medicine* 169(1), 120-124 (2004)
11. A. N. Husain, "The Lung," in *Pathologic Basis of Disease R. a. Cotran, Ed.*, pp. 677 - 738, Elsevier (2010).
12. E. R. Weibel, "Morphological basis of alveolar-capillary gas exchange," *Physiological reviews* 53(2), 419-495 (1973)
13. L. Thiberville, M. Salaun, S. Lachkar, S. Dominique, S. Moreno-Swiric, C. Vever-Bizet and G. Bourg-Heckly, "Human in vivo fluorescence microimaging of the alveolar ducts and sacs during bronchoscopy," *The European respiratory journal : official journal of the European Society for Clinical Respiratory Physiology* 33(5), 974-985 (2009)
14. R. C. Wagner and F. E. Hosseler, "Respiratory System Ultrastructure," (2012).
15. S. P. Albert, J. DiRocco, G. B. Allen, J. H. Bates, R. Lafollette, B. D. Kubiak, J. Fischer, S. Maroney and G. F. Nieman, "The role of time and pressure on alveolar recruitment," *Journal of applied physiology* 106(3), 757-765 (2009)
16. J. D. Escolar and A. Escolar, "Lung hysteresis: a morphological view," *Histol Histopathol* 19(1), 159-166 (2004)
17. H. Kitaoka, G. F. Nieman, Y. Fujino, D. Carney, J. DiRocco and I. Kawase, "A 4-dimensional model of the alveolar structure," *J Physiol Sci* 57(3), 175-185 (2007)
18. M. Mertens, A. Tabuchi, S. Meissner, A. Krueger, K. Schirrmann, U. Kertzsch, A. R. Pries, A. S. Slutsky, E. Koch and W. M. Kuebler, "Alveolar dynamics in acute lung injury: heterogeneous distension rather than cyclic opening and collapse," *Crit Care Med* 37(9), 2604-2611 (2009)
19. M. E. Hanley and C. H. Welsh, *Current diagnosis & treatment in pulmonary medicine*.
20. H. Tavana, D. Huh, J. B. Grotberg and S. Takayama, "Microfluidics, Lung Surfactant, and Respiratory Disorders," *Lab Medicine* 40), 203 - 209 (2009)

21. "From the Global Strategy for the Diagnosis, Management and Prevention of COPD, Global Initiative for Chronic Obstructive Lung Disease (GOLD) 2011. Available from: <http://www.goldcopd.org/>," (2011).
22. P. W. Jones, "Health status and the spiral of decline," *Copd* 6(1), 59-63 (2009)
23. J. B. West, *Pulmonary Pathophysiology*, Lippincott Williams & Wilkins (2008).
24. J. M. Drazen, S. H. Loring and A. Malhotra, "Pulmonary Physiology and Pathophysiology," in HST-100 SYLLABUS, Harvard Medical School, Boston (2012).
25. C. Fletcher and R. Peto, "The natural history of chronic airflow obstruction," *Br Med J* 1(6077), 1645-1648 (1977)
26. B. L. Tjep, "Long-term home oxygen therapy," *Clinics in chest medicine* 11(3), 505-521 (1990)
27. F. C. Sciruba, A. Ernst, F. J. Herth, C. Strange, G. J. Criner, C. H. Marquette, K. L. Kovitz, R. P. Chiacchierini, J. Goldin and G. McLennan, "A randomized study of endobronchial valves for advanced emphysema," *The New England journal of medicine* 363(13), 1233-1244 (2010)
28. O. C. Brantigan and E. Mueller, "Surgical treatment of pulmonary emphysema," *Am Surg* 23(9), 789-804 (1957)
29. I. Y. Wan, T. P. Toma, D. M. Geddes, G. Snell, T. Williams, F. Venuta and A. P. Yim, "Bronchoscopic lung volume reduction for end-stage emphysema: report on the first 98 patients," *Chest* 129(3), 518-526 (2006)
30. H. F. Lausberg, K. Chino, G. A. Patterson, B. F. Meyers, P. D. Toeniskoetter and J. D. Cooper, "Bronchial fenestration improves expiratory flow in emphysematous human lungs," *The Annals of thoracic surgery* 75(2), 393-397; discussion 398 (2003)
31. "Ventilation with lower tidal volumes as compared with traditional tidal volumes for acute lung injury and the acute respiratory distress syndrome. The Acute Respiratory Distress Syndrome Network," *N Engl J Med* 342(18), 1301-1308 (2000)
32. L. Brochard, F. Roudot-Thoraval, E. Roupie, C. Delclaux, J. Chastre, E. Fernandez-Mondejar, E. Clementi, J. Mancebo, P. Factor, D. Matamis, M.

- Ranieri, L. Blanch, G. Rodi, H. Mentec, D. Dreyfuss, M. Ferrer, C. Brun-Buisson, M. Tobin and F. Lemaire, "Tidal volume reduction for prevention of ventilator-induced lung injury in acute respiratory distress syndrome. The Multicenter Trail Group on Tidal Volume reduction in ARDS," *American journal of respiratory and critical care medicine* 158(6), 1831-1838 (1998)
33. E. K. Hartmann, S. Boehme, A. Bentley, B. Duenges, K. U. Klein, A. Elsaesser, J. E. Baumgardner, M. David and K. Markstaller, "Influence of respiratory rate and end-expiratory pressure variation on cyclic alveolar recruitment in an experimental lung injury model," *Critical care* 16(1), R8 (2012)
34. M. David, J. Karmrodt, C. Bletz, S. David, A. Herweling, H. U. Kauczor and K. Markstaller, "Analysis of atelectasis, ventilated, and hyperinflated lung during mechanical ventilation by dynamic CT," *Chest* 128(5), 3757-3770 (2005)
35. G. Apiou-Sbirlea, I. M. Katz and T. B. Martonen, "The effects of simulated airway diseases and affected flow distributions on aerosol deposition," *Respiratory care* 55(6), 707-718 (2010)
36. S. Miyawaki, M. H. Tawhai, E. A. Hoffman and C. L. Lin, "Effect of carrier gas properties on aerosol distribution in a CT-based human airway numerical model," *Annals of biomedical engineering* 40(7), 1495-1507 (2012)
37. J. W. De Backer, W. G. Vos, S. C. Vinchurkar, R. Claes, A. Drollmann, D. Wulfrank, P. M. Parizel, P. Germonpre and W. De Backer, "Validation of computational fluid dynamics in CT-based airway models with SPECT/CT," *Radiology* 257(3), 854-862 (2010)
38. T. B. Martonen, "Mathematical model for the selective deposition of inhaled pharmaceuticals," *J Pharm Sci* 82(12), 1191-1199 (1993)
39. J. Fleming, J. Conway, C. Majoral, L. Tossici-Bolt, I. Katz, G. Caillibotte, D. Perchet, M. Pichelin, B. Muellinger, T. Martonen, P. Kroneberg and G. Apiou-Sbirlea, "The use of combined single photon emission computed tomography and X-ray computed tomography to assess the fate of inhaled aerosol," *Journal of aerosol medicine and pulmonary drug delivery* 24(1), 49-60 (2011)

40. B. Haefeli-Bleuer and E. R. Weibel, "Morphometry of the human pulmonary acinus," *Anat Rec* 220(4), 401-414 (1988)
41. A. Tsuda, R. A. Rogers, P. E. Hydon and J. P. Butler, "Chaotic mixing deep in the lung," *Proceedings of the National Academy of Sciences of the United States of America* 99(15), 10173-10178 (2002)
42. S. E. Soutiere, C. G. Tankersley and W. Mitzner, "Differences in alveolar size in inbred mouse strains," *Respiratory physiology & neurobiology* 140(3), 283-291 (2004)
43. E. D'Angelo, "Local alveolar size and transpulmonary pressure in situ and in isolated lungs," *Respiration physiology* 14(3), 251-266 (1972)
44. R. R. Mercer, J. M. Laco and J. D. Crapo, "Three-dimensional reconstruction of alveoli in the rat lung for pressure-volume relationships," *J Appl Physiol* 62(4), 1480-1487 (1987)
45. J. L. Wright, M. Cosio and A. Churg, "Animal models of chronic obstructive pulmonary disease," *Am J Physiol Lung Cell Mol Physiol* 295(1), L1-15 (2008)
46. D. O. Slauson and F. F. Hahn, "Criteria for development of animal models of diseases of the respiratory system: the comparative approach in respiratory disease model development," *Am J Pathol* 101(3 Suppl), S103-122 (1980)
47. G. R. Zosky and P. D. Sly, "Animal models of asthma," *Clin Exp Allergy* 37(7), 973-988 (2007)
48. C. S. Rogers, W. M. Abraham, K. A. Brogden, J. F. Engelhardt, J. T. Fisher, P. B. McCray, Jr., G. McLennan, D. K. Meyerholz, E. Namati, L. S. Ostedgaard, R. S. Prather, J. R. Sabater, D. A. Stoltz, J. Zabner and M. J. Welsh, "The porcine lung as a potential model for cystic fibrosis," *American journal of physiology. Lung cellular and molecular physiology* 295(2), L240-263 (2008)
49. B. R. Wallau, A. Schmitz and S. F. Perry, "Lung morphology in rodents (Mammalia, Rodentia) and its implications for systematics," *Journal of morphology* 246(3), 228-248 (2000)
50. J. W. De Backer, W. G. Vos, P. Burnell, S. L. Verhulst, P. Salmon, N. De Clerck and W. De Backer, "Study of the variability in upper and lower

- airway morphology in Sprague-Dawley rats using modern micro-CT scan-based segmentation techniques," *Anatomical record* 292(5), 720-727 (2009)
51. C. C. Hsia, D. M. Hyde, M. Ochs and E. R. Weibel, "An official research policy statement of the American Thoracic Society/European Respiratory Society: standards for quantitative assessment of lung structure," *Am J Respir Crit Care Med* 181(4), 394-418 (2010)
52. E. Namati, J. De Ryk, J. Thiesse, Z. Towfic, E. Hoffman and G. McLennan, "Large image microscope array for the compilation of multimodality whole organ image databases," *Anat Rec (Hoboken)* 290(11), 1377-1387 (2007)
53. E. R. Heitzman, *The lung; radiologic-pathologic correlations*, Mosby, Saint Louis (1973).
54. E. Namati, W. C. Warger II, C. I. Unglert, J. E. Eckert, J. Hostens, B. Bouma and G. J. Tearney, "Four-dimensional visualization of peripheral alveolar dynamics within living swine during uninterrupted mechanical ventilation," (*in preparation*)
55. C. I. Unglert, E. Namati, W. C. Warger, L. Liu, H. Yoo, D. Kang, B. E. Bouma and G. J. Tearney, "Evaluation of optical reflectance techniques for imaging of alveolar structure," *Journal of Biomedical Optics* 17(7), 071303 (2012)
56. C. I. Unglert, W. C. Warger II, J. Hostens, E. Namati, R. Birngruber, B. E. Bouma and G. J. Tearney, "Validation of two- and three-dimensional measurements of subpleural alveolar size parameters by optical coherence tomography," *Journal of Biomedical Optics* 17(12), (2012)
57. M. E. Wohl, J. Turner and J. Mead, "Static volume-pressure curves of dog lungs--in vivo and in vitro," *Journal of applied physiology* 24(3), 348-354 (1968)
58. H. Inoue, C. Inoue and J. Hildebrandt, "Temperature effects on lung mechanics in air- and liquid-filled rabbit lungs," *Journal of applied physiology: respiratory, environmental and exercise physiology* 53(3), 567-575 (1982)
59. D. Engelberts, A. Malhotra, J. P. Butler, G. P. Topulos, S. H. Loring and B. P. Kavanagh, "Relative effects of negative versus positive pressure

ventilation depend on applied conditions," *Intensive Care Med* 38(5), 879-885 (2012)

60. K. Raymondos, U. Molitoris, M. Capewell, B. Sander, T. Dieck, J. Ahrens, C. Weilbach, W. Knitsch and A. Corrado, "Negative- versus positive-pressure ventilation in intubated patients with acute respiratory distress syndrome," *Critical care* 16(2), R37 (2012)

61. H. Parameswaran, E. Bartolak-Suki, H. Hamakawa, A. Majumdar, P. G. Allen and B. Suki, "Three-dimensional measurement of alveolar airspace volumes in normal and emphysematous lungs using micro-CT," *J Appl Physiol* 107(2), 583-592 (2009)

62. S. Noma, G. W. Moskowitz, P. G. Herman, A. Khan and K. A. Rojas, "Pulmonary scintigraphy in elastase-induced emphysema in pigs. Correlation with high-resolution computed tomography and histology," *Invest Radiol* 27(6), 429-435 (1992)

63. S. Noma, P. G. Herman, A. Khan, K. A. Rojas and Y. Pipman, "Sequential morphologic changes of elastase-induced pulmonary emphysema in pig lungs. Evaluation by high-resolution computed tomography," *Invest Radiol* 26(5), 446-453 (1991)

64. J. C. Fox and M. F. Fitzgerald, "The role of animal models in the pharmacological evaluation of emerging anti-inflammatory agents for the treatment of COPD," *Curr Opin Pharmacol* 9(3), 231-242 (2009)

65. J. Fujimoto and W. Drexler, "Introduction to Optical Coherence Tomography," in *Optical Coherence Tomography: Technology and Applications* W. Drexler and J. Fujimoto, Eds., pp. 1-40, Springer (2008).

66. J. A. Izatt and M. A. Choma, "Theory of Optical Coherence Tomography," in *Optical Coherence Tomography Technology and Applications* W. Drexler and J. Fujimoto, Eds., pp. 47-72, Springer (2008).

67. R. Leitgeb, C. Hitzenberger and A. Fercher, "Performance of fourier domain vs. time domain optical coherence tomography," *Opt Express* 11(8), 889-894 (2003)

68. J. G. Fujimoto, M. E. Brezinski, G. J. Tearney, S. A. Boppart, B. Bouma, M. R. Hee, J. F. Southern and E. A. Swanson, "Optical biopsy and imaging using optical coherence tomography," *Nat Med* 1(9), 970-972 (1995)

69. G. J. Tearney, M. E. Brezinski, B. E. Bouma, S. A. Boppart, C. Pitris, J. F. Southern and J. G. Fujimoto, "In vivo endoscopic optical biopsy with optical coherence tomography," *Science* 276(5321), 2037-2039 (1997)
70. S. Yun, G. Tearney, J. de Boer, N. Iftimia and B. Bouma, "High-speed optical frequency-domain imaging," *Opt Express* 11(22), 2953-2963 (2003)
71. D. Huang, E. A. Swanson, C. P. Lin, J. S. Schuman, W. G. Stinson, W. Chang, M. R. Hee, T. Flotte, K. Gregory, C. A. Puliafito and et al., "Optical coherence tomography," *Science* 254(5035), 1178-1181 (1991)
72. W. C. Warger II, C. A. DiMarzio and M. Rajadhyaksha, "Confocal Microscopy," in *Handbook of Biomedical Optics* D. A. Boas, C. Pitris and N. Ramanujam, Eds., pp. 517-541, Taylor & Francis Group (2011).
73. C. Boudoux, S. Yun, W. Oh, W. White, N. Iftimia, M. Shishkov, B. Bouma and G. Tearney, "Rapid wavelength-swept spectrally encoded confocal microscopy," *Opt Express* 13(20), 8214-8221 (2005)
74. G. J. Tearney, R. H. Webb and B. E. Bouma, "Spectrally encoded confocal microscopy," *Opt Lett* 23(15), 1152-1154 (1998)
75. D. Kang, H. Yoo, P. Jillella, B. E. Bouma and G. J. Tearney, "Comprehensive volumetric confocal microscopy with adaptive focusing," *Biomed Opt Express* 2(6), 1412-1422 (2011)
76. Y. K. Tao and J. A. Izatt, "Spectrally encoded confocal scanning laser ophthalmoscopy," *Opt Lett* 35(4), 574-576 (2010)
77. E. Beaurepaire, A. C. Boccara, M. Lebec, L. Blanchot and H. Saint-Jalmes, "Full-field optical coherence microscopy," *Opt Lett* 23(4), 244-246 (1998)
78. A. Dubois, K. Grieve, G. Moneron, R. Lecaque, L. Vabre and C. Boccara, "Ultrahigh-resolution full-field optical coherence tomography," *Appl Opt* 43(14), 2874-2883 (2004)
79. W. Y. Oh, B. E. Bouma, N. Iftimia, S. H. Yun, R. Yelin and G. J. Tearney, "Ultrahigh-resolution full-field optical coherence microscopy using InGaAs camera," *Opt Express* 14(2), 726-735 (2006)
80. C. Boudoux, "Wavelength Swept Spectrally Encoded Confocal Microscopy for Biological and Clinical Applications," in *Health Sciences and Technology*, MIT, Boston (2007).

81. A. Dubois and A. Boccara, "Full-Field Optical Coherence Tomography," in *Optical Coherence Tomography: Technology and Applications* W. Drexler and J. Fujimoto, Eds., pp. 565-591, Springer (2008).
82. M. R. Hamblin, "Mechanisms of low level light therapy," (2008).
83. S. Meissner, L. Knels and E. Koch, "Improved three-dimensional Fourier domain optical coherence tomography by index matching in alveolar structures," *J Biomed Opt* 14(6), 064037 (2009)
84. G. M. Hale and M. R. Querry, "Optical Constants of Water in the 200-nm to 200-microm Wavelength Region," *Applied optics* 12(3), 555-563 (1973)
85. M. E. Brezinski, G. J. Tearney, B. E. Bouma, J. A. Izatt, M. R. Hee, E. A. Swanson, J. F. Southern and J. G. Fujimoto, "Optical coherence tomography for optical biopsy. Properties and demonstration of vascular pathology," *Circulation* 93(6), 1206-1213 (1996)
86. W. Wieser, B. R. Biedermann, T. Klein, C. M. Eigenwillig and R. Huber, "Multi-megahertz OCT: High quality 3D imaging at 20 million A-scans and 4.5 GVoxels per second," *Optics express* 18(14), 14685-14704 (2010)
87. B. E. Bouma and G. J. Tearney, "Power-efficient nonreciprocal interferometer and linear-scanning fiber-optic catheter for optical coherence tomography," *Optics Letters* 24(8), 531-533 (1999)
88. X. Li, J. H. Han, X. Liu and J. U. Kang, "Signal-to-noise ratio analysis of all-fiber common-path optical coherence tomography," *Applied optics* 47(27), 4833-4840 (2008)
89. A. Latrive and A. C. Boccara, "In vivo and in situ cellular imaging full-field optical coherence tomography with a rigid endoscopic probe," *Biomed Opt Express* 2(10), 2897-2904 (2011)
90. K. R. Stenmark, B. Meyrick, N. Galie, W. J. Mooi and I. F. McMurtry, "Animal models of pulmonary arterial hypertension: the hope for etiological discovery and pharmacological cure," *Am J Physiol Lung Cell Mol Physiol* 297(6), L1013-1032 (2009)
91. H. O. Coxson, J. Mayo, S. Lam, G. Santyr, G. Parraga and D. D. Sin, "New and current clinical imaging techniques to study chronic obstructive pulmonary disease," *Am J Respir Crit Care Med* 180(7), 588-597 (2009)

92. G. J. Tearney and B. E. Bouma, "Shedding light on bioabsorbable stent struts seen by optical coherence tomography in the ABSORB trial," *Circulation* 122(22), 2234-2235 (2010)
93. S. Meissner, L. Knels, C. Schnabel, T. Koch and E. Koch, "Three-dimensional Fourier domain optical coherence tomography in vivo imaging of alveolar tissue in the intact thorax using the parietal pleura as a window," *J Biomed Opt* 15(1), 016030 (2010)
94. R. A. a. S. McLaughlin, D. D., "Clinical applications of fiber-optic probes in optical coherence tomography," *Optical Fiber Technology* 16(467-475) (2010)
95. B. C. Quirk, R. A. McLaughlin, A. Curatolo, R. W. Kirk, P. B. Noble and D. D. Sampson, "In situ imaging of lung alveoli with an optical coherence tomography needle probe," *J Biomed Opt* 16(3), 036009 (2011)
96. C. Boudoux, S. C. Leuin, W. Y. Oh, M. J. Suter, A. E. Desjardins, B. J. Vakoc, B. E. Bouma, C. J. Hartnick and G. J. Tearney, "Optical microscopy of the pediatric vocal fold," *Arch Otolaryngol Head Neck Surg* 135(1), 53-64 (2009)
97. C. Pitris, B. Bouma, M. Shiskov and G. Tearney, "A GRISM-based probe for spectrally encoded confocal microscopy," *Opt Express* 11(2), 120-124 (2003)
98. M. Czaplík, R. Rossaint, E. Koch, A. Fahlenkamp, W. Schroder, P. Pelosi, W. M. Kubler and J. Bickenbach, "Methods for quantitative evaluation of alveolar structure during in vivo microscopy," *Respir Physiol Neurobiol* 176(3), 123-129 (2011)
99. L. Thiberville, M. Salaun, S. Lachkar, S. Dominique, S. Moreno-Swirc, C. Vever-Bizet and G. Bourg-Heckly, "Confocal fluorescence endomicroscopy of the human airways," *Proc Am Thorac Soc* 6(5), 444-449 (2009)
100. R. S. Pillai, D. Lorensen and D. D. Sampson, "Deep-tissue access with confocal fluorescence microendoscopy through hypodermic needles," *Opt Express* 19(8), 7213-7221 (2011)
101. T. Bonin, G. Franke, M. Hagen-Eggert, P. Koch and G. Huttmann, "In vivo Fourier-domain full-field OCT of the human retina with 1.5 million A-lines/s," *Opt Lett* 35(20), 3432-3434 (2010)

102. R. R. Mercer, M. L. Russell and J. D. Crapo, "Alveolar septal structure in different species," *J Appl Physiol* 77(3), 1060-1066 (1994)
103. M. Brezinski, K. Saunders, C. Jesser, X. Li and J. Fujimoto, "Index matching to improve optical coherence tomography imaging through blood," *Circulation* 103(15), 1999-2003 (2001)
104. D. Lorensen, X. Yang, R. W. Kirk, B. C. Quirk, R. A. McLaughlin and D. D. Sampson, "Ultrathin side-viewing needle probe for optical coherence tomography," *Opt Lett* 36(19), 3894-3896 (2011)
105. C. Schnabel, M. Gaertner, S. Meissner and E. Koch, "Quantitative investigation of alveolar structures with OCT using total liquid ventilation during mechanical ventilation," in *SPIE 8207* (2012).
106. L. V. Wang and H.-I. Wu, *Biomedical Optics*, Wiley & Sons, Hoboken, NJ (2007).
107. L. Kirsten, M. Gaertner, C. Schnabel, S. Meissner and E. Koch, "Four-dimensional imaging of murine subpleural alveoli using high-speed optical coherence tomography," *J Biophotonics* (2012)
108. E. Namati, C. I. Unglert, W. C. Warger II and G. J. Tearney, "Imaging of alveolar structure and function - second year review," in *Annual progress report*, Wellman Center for Photomedicine, MGH (2010).
109. G. J. Tearney, M. E. Brezinski, J. F. Southern, B. E. Bouma, M. R. Hee and J. G. Fujimoto, "Determination of the refractive index of highly scattering human tissue by optical coherence tomography," *Opt Lett* 20(21), 2258 (1995)
110. M. D. Abramoff, P. J. Magelhaes and S. J. Ram, "Image Processing with ImageJ," *Biophotonics International* 11(7), 36-42 (2004)
111. J. M. Bland and D. G. Altman, "Measuring agreement in method comparison studies," *Stat Methods Med Res* 8(2), 135-160 (1999)
112. D. G. Altman and J. M. Bland, "Standard deviations and standard errors," *Bmj* 331(7521), 903 (2005)
113. J. M. Bland and D. G. Altman, "Statistical methods for assessing agreement between two methods of clinical measurement," *Lancet* 1(8476), 307-310 (1986)

114. A. Golabchi, J. Faust, F. N. Golabchi, D. H. Brooks, A. Gouldstone and C. A. Dimarzio, "Refractive errors and corrections for OCT images in an inflated lung phantom," *Biomedical optics express* 3(5), 1101-1109 (2012)
115. J. Bickenbach, R. Dembinski, M. Czaplík, S. Meissner, A. Tabuchi, M. Mertens, L. Knels, W. Schroeder, P. Pelosi, E. Koch, W. M. Kuebler, R. Rossaint and R. Kuhlen, "Comparison of two in vivo microscopy techniques to visualize alveolar mechanics," *J Clin Monit Comput* 23(5), 323-332 (2009)
116. S. Meissner, L. Knels, A. Krueger, T. Koch and E. Koch, "Simultaneous three-dimensional optical coherence tomography and intravital microscopy for imaging subpleural pulmonary alveoli in isolated rabbit lungs," *J Biomed Opt* 14(5), 054020 (2009)
117. J. Kytta, T. Randell, P. Tanskanen, Y. Kajimoto and P. H. Rosenberg, "Monitoring lung compliance and end-tidal oxygen content for the detection of venous air embolism," *British journal of anaesthesia* 75(4), 447-451 (1995)
118. F. P. Bolin, L. E. Preuss, R. C. Taylor and R. J. Ference, "Refractive index of some mammalian tissues using a fiber optic cladding method," *Applied optics* 28(12), 2297-2303 (1989)
119. E. A. Genina, A. N. Bashkatov and V. V. Tuchin, "Tissue optical immersion clearing," *Expert Rev Med Devices* 7(6), 825-842 (2010)
120. R. A. McLaughlin, X. Yang, B. C. Quirk, D. Lorensen, R. W. Kirk, P. B. Noble and D. D. Sampson, "Static and dynamic imaging of alveoli using optical coherence tomography needle probes," *Journal of applied physiology* (2012)
121. W. University, "Swine, Animal Models for Human Disease," St. Louis.
122. G. Balazs, S. Noma, A. Khan, T. Eacobacci and P. G. Herman, "Bleomycin-induced fibrosis in pigs: evaluation with CT," *Radiology* 191(1), 269-272 (1994)
123. J. Karmrodt, C. Bletz, S. Yuan, M. David, C. P. Heussel and K. Markstaller, "Quantification of atelectatic lung volumes in two different porcine models of ARDS," *British journal of anaesthesia* 97(6), 883-895 (2006)

124. D. Schwenninger, K. Moller, H. Liu and J. Guttman, "Automated analysis of intratidal dynamics of alveolar geometry from microscopic endoscopy," *IEEE Trans Biomed Eng* 57(2), 415-421 (2010)
125. C. Xu and J. L. Prince, "Snakes, shapes, and gradient vector flow," *IEEE Trans Image Process* 7(3), 359-369 (1998)
126. S. Lankton and A. Tannenbaum, "Localizing region-based active contours," *IEEE Trans Image Process* 17(11), 2029-2039 (2008)
127. G. F. Nieman, C. E. Bredenberg, W. R. Clark and N. R. West, "Alveolar function following surfactant deactivation," *J Appl Physiol* 51(4), 895-904 (1981)
128. J. Lai, A. Gouldstone, J. P. Butler, W. J. Federspiel and S. H. Loring, "Relative motion of lung and chest wall promotes uniform pleural space thickness," *Respiratory physiology & neurobiology* 131(3), 233-243 (2002)